HYBRID MAGNETIC AND SEMICONDUCTING MATERIALS BASED ON METAL COMPLEXES AND ORGANOCYANIDE ELECTRON ACCEPTORS

A Dissertation

by

XUAN ZHANG

Submitted to the Office of Graduate and Professional Studies of
Texas A&M University
in partial fulfillment of the requirements for the degree of

DOCTOR OF PHILOSOPHY

Chair of Committee,	Kim R. Dunbar
Committee Members,	Fran ̧ois P. Gabba ï
	Timothy R. Hughbanks
	Joseph H. Ross
Head of Department,	Simon North

August 2016

Major Subject: Chemistry

ABSTRACT

Multifunctional molecular materials are of high interest because of the coexistence of two or more functionalities such as magnetism, electrical conductivity, and ferroelectric and optical properties. The radical anion of tetracyanoquinodimethane (TCNQ) can serve as a spin-carrying bridge to enhance magnetic exchange interactions between paramagnetic metal ions and electrical conducting columnar stacks that allow for conduction electrons to travel over long distances. In this vein, coordination compounds with metal ions and TCNQ are excellent candidates for combining magnetic properties with electrical conductivity. The goal of my research is to synthesize new bifunctional materials based on organocyanides and to study their structure-property relationships, which will serve as guidelines for the synthesis of molecular materials with enhanced properties that are promising for applications in electronic devices.

A facile modular synthetic approach has been developed to introduce partially charged TCNQ species in hybrid inorganic-organic bifunctional magnetic and electrical conducting materials. By taking advantage of the structural breathing features of the metal-organic cations in conjunction with the π-stacking interactions of partially charged TCNQ radicals, an anomalous conducting behavior has been observed in $[Co(terpy)_2](TCNQ)_3 \bullet CH_3CN$, which is composed of alternating semiconducting and spin-crossover layers. A series of isostructural compounds [Ln(TPMA)(μ-TCNQ)(μ-OH)]$(TCNQ)_2$ CH_3CN (Ln = Dy, Gd, Y) with partially charged TCNQ have also been synthesized and it has been found that the Dy(III) compound exhibited slow relaxation

of the magnetization and semiconductivity. This procedure was further generalized to systems containing single-molecule magnets and other functional cationic species with partially charged TCNQ radicals, indicating that this method is highly promising for the synthesis of a variety of bifunctional materials with electrical conducting properties.

Magnetic metal-organic frameworks are promising for applications in high density data storage and small molecule recognition and sensors. TCNQ dianion can be employed as a substitute for carboxylate anions in the formation of MOFs that exhibit interesting interactions between the host framework and guest molecules. It has been found that aromatic guest molecules can induce distinct magnetic ordering in the family of magnetic MOFs Fe(TCNQ)(4,4'-bpy)⊃guest. The flexibility of dicyanamidobenzene dianions allows them to be bridging ligands for the formation of interesting structures, including a quadruple helical aperiodic structure.

DEDICATION

To my wife and our daughter Emily

ACKNOWLEDGEMENTS

First of all, I would like to thank my advisor, Dr. Dunbar, for her guidance and tremendous support throughout the course of this research. I am extremely grateful for her mentorship

I am grateful to my committee members, Dr. Gabba ̈ı Dr. Hughbanks, and Dr. Ross, for their helpful discussions and suggestions to this work. I also would like to extend my gratitude to my collaborators Dr. Mario Wriedt (Clarkson University), Dr. Kevin Gagnon (ALS, LBNL), Dr. Lukas Palatinus (Institute of Physics of the AS, CR), Dr. John Bacsa (Emory University), and Dr. Joseph Reibenspies.

I also acknowledge the previous and current group members of the Dunbar group for their help during my graduate career here. They include Dr. Hanhua Zhao, Dr. Zhongyue Zhang, Dr. Helen Chifotides, Dr. Andrey Prosvirin, Dr. Zhao-Xi Wang, Dr. Maria Ballesteros Rivas, Dr. Yuan-Zhu Zhang, Dr. Silvia Gomez, Dr. Yue Ma, Dr. Dawid Pinkowicz, Dr. Ian Giles, Dr. Heather Southerland, Dr. Bruno Pena, Dr. Zhanyong Li, Dr. Andrew Brown, Dr. Amanda David, Dr. Mohamed Saber, Dr. Codi Sanders, Dr. Toby Woods, Dr. Jill Ellenbarger, as well as Haomiao Xie, Charles Culbertson, Zhilin, Guo, Zhe Shen, Ryan Coll, Francisco Birk, David Kempe, Sayan Saha, Kelsey Schulte, Augustin Millet, and Carolyn Gunthardt.

Finally, I would like to thank my family for their encouragement and support, especially my wife, for her love and bringing our daughter to us.

TABLE OF CONTENTS

Page

LIST OF FIGURES

Page

LIST OF TABLES

CHAPTER I

INTRODUCTION AND LITERATURE REVIEW*

Multifunctional Molecular Materials

Functional materials in chemistry, physics, biology and materials research have played an important role in the evolution of technology for mankind. Molecule-based functional materials have recently emerged as a new class of hybrid materials owing to their advantages of pre-designed bottom up synthesis, the facile tuning of their properties, their well-defined structures, and possibility of multifunctionalities.[1,2]

Multifunctional molecular materials are of high interest to chemists and material scientists because of the potential coexistence of two or more functionalities such as magnetic, conducting, ferroelectric and optical properties.[3,4,5] What is more interesting is that the interactions between these functionalities is not like those in a Swiss army knife, where the different functionalities are just incorporated in one object. We are after the synergy between these functionalities where, for example, one can use a magnetic field to control the electrical conducting behavior of a material or use an electrical field to control the magnetic responses of a material. One of the prototypical examples is the combination of metallic conductivity with ferromangnetic ordering in [BEDT-TTF]$_3$[$Mn^{II}Cr^{III}(ox)_3$], as reported by Coronado and coworkers in 2000. This

* A portion of this chapter is reprinted with permission from "Structural distortions of the spin-crossover material [Co(pyterpy)$_2$](TCNQ)$_2$ mediated by supramolecular interactions", by Xuan Zhang, Haomiao Xie, Maria Ballesteros-Rivas, Zhao-Xi Wang and Kim R. Dunbar, *Journal of Materials Chemistry C*, **2015**, 3, 9292-9298, DOI: 10.1039/C5TC01851J, Copyright 2015 by Royal Society of Chemistry.

bifunctional crystalline molecular material was obtained through an electrocrystallization method and the BEDT-TTF and metal-oxalate species are responsible for the electrical conductivity and magnetic properties respectively.

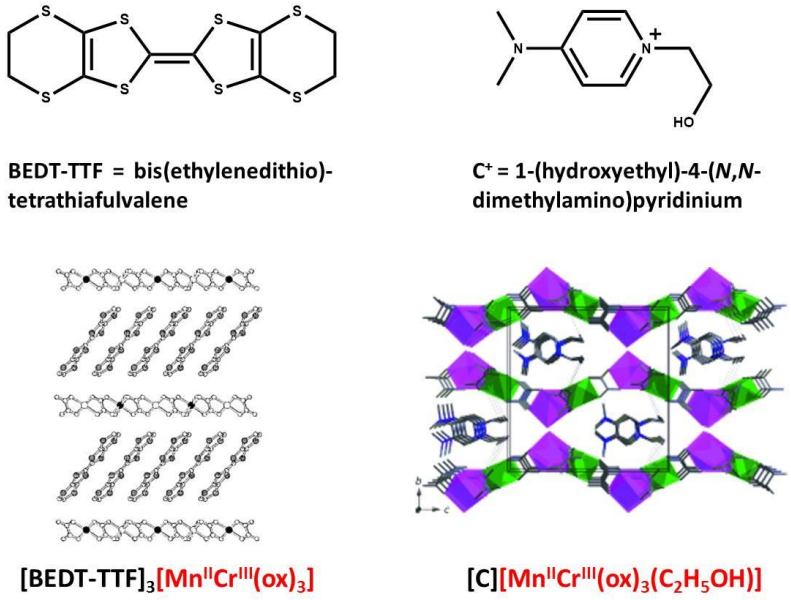

Figure 1. Packing diagram of the crystal structures of $[BEDT\text{-}TTF]_3[Mn^{II}Cr^{III}(ox)_3]$ (left) and $[C][Mn^{II}Cr^{III}(ox)_3(C_2H_5OH)]$ (right).

Moore's law asserts that the number of transistors on a given microprocessor chip is expected to double every two years. This law is projected to approach the physical miniaturization limit of conventional materials by the mid-2020s, by which time the smallest features in a chip will be on the scale of 2-3 nm. Molecular materials are promising alternatives to these traditional materials, as they usually exhibit sizes of below 3 nm. These intriguing characteristics make them promising for applications in quantum computing, data storage, and magnetic refrigeration.[6,7,8]

Molecular Magnetism

Spin-crossover

Spin-crossover, also known as a spin transition, is a magnetic bistable phenomenon generally observed in transition metal ions of octahedral geometries that have d^4-d^7 electron configurations. The spin states of these complexes can be switched between high spin (HS) and low spin (LS) states with changes in temperature or upon application of external stimuli such as light and pressure. Such magnetic bistability renders them excellent candidates for applications as sensors as well as memory and display devices.[9-12]

A first approximation of these two states in their respective equilibrium geometries requires that the high spin state have a slightly higher quantum mechanical energy than the low spin state so that it is thermodynamically favorable above a certain temperature.[13] The underlying principle is that such a spin transition (low spin to high spin) needs to be induced by a certain amount of energy to compensate for the increase in entropy from the low spin to high spin states, which has more unpaired electrons and a higher degeneracy than the former. From the view of ligand field theory, the splitting energy (Δ) between the e_g and t_{2g} orbitals as well as the electron pairing energy (P) determine whether a complex is in LS or HS states (Figure 2, left). That is to say, if the ligand field splitting is larger than the electron pairing energy, the electrons will prefer the t_{2g} orbitals to the e_g orbitals and the LS state of the metal complex will be more favorable.[14] On the other hand, when the splitting energy is smaller than the electron pairing energy, which is in accordance with Hund's rule, the electrons will begin to

occupy the e_g orbitals before filling the t_{2g} orbitals to allow for as many unpaired electrons as possible to result in a HS state of the metal complex. At the stage where the splitting energy and the electron pairing energy is of similar magnitude, thermal energy (k_BT) will be sufficient to trigger the transitions between the HS and LS states of the metal complexes.

Accompanying these theoretical explanations are the differences in the magnetic susceptibility of the compounds (Figure 2, right) and in the bond distances between the metal ions and the donor atoms. The bond distances of the metal coordination sphere are longer for HS states than the LS states due to the antibonding character of the e_g orbitals and the non-bonding character of the t_{2g} orbitals. The shorter and longer bond distances will, at the same time, apply a larger and a smaller ligand field splitting, respectively, to the d orbitals of the metal ions. On average, the changes in metal-ligand bond distances are about 0.10, 0.15 and 0.20 Å for Co(II), Fe(III) and Fe(II) systems respectively.[15] As a result, the metal coordination sphere will exhibit a significant change in the size of the molecules, which can also be transmitted to the macroscale as the unit cell, or even the size of the crystals expands and contracts with increasing and decreasing temperatures, which is known as a structural breathing behavior due to the population of the HS and LS states, respectively.

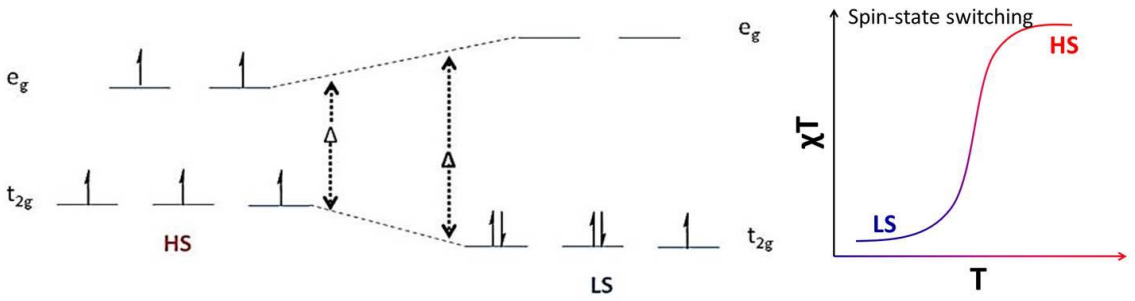

Figure 2. The d orbital splitting diagrams of octahedral d^5 electron configurations showing the two different electronic ground states (left) and the magnetic characterization of spin-crossover showing the distinct HS and LS states in the χT vs. T plot (right, χ is the magnetic susceptibility).

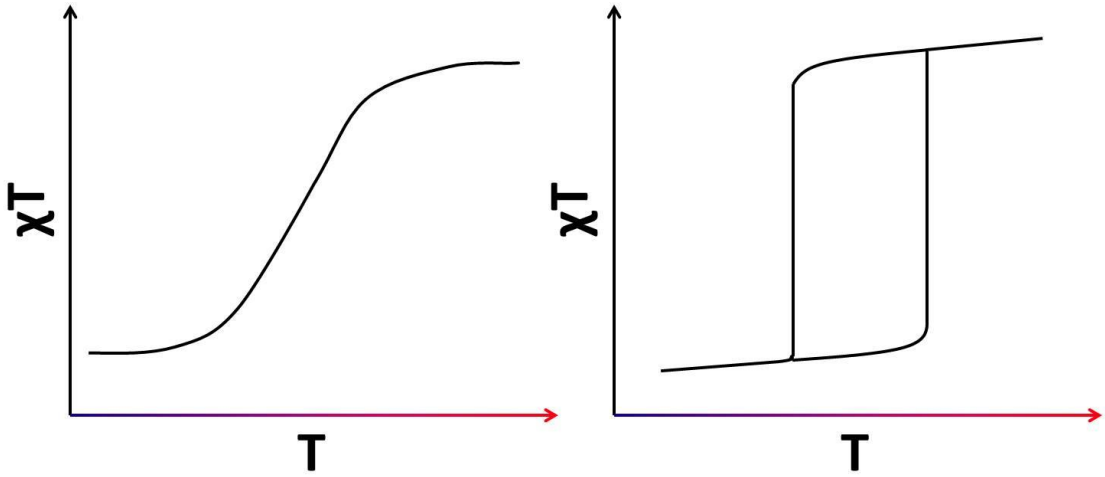

Figure 3. Typical spin-crossover behavior of a gradual spin transition (left) and an abrupt spin transition with hysteresis (right).

Despite the fact that SCO originates from changes in the volumes of the molecules, intermolecular interactions such as π-π stacking and hydrogen bonding play an important role in the cooperative behaviors of the spin transition processes. When the changes in the molecules are effectively transmitted to the crystals, this cooperativity will be exhibited as an abrupt spin transition; otherwise, a gradual spin transition is observed (Figure 3). SCO behaviors with hysteresis are desirable due to the potential

application of these materials as memory devices. In addition, SCO systems with larger structural variations such as Fe(II) and Fe(III) are generally more likely to exhibit steep spin transitions as compared to Co(II) systems for which it is difficult to engender abrupt spin transitions with hysteresis.

SCO was first discovered by Cambi and coworkers in a Fe(III) thiocarbomate system in the early 1930s.[16] The most commonly encountered spin-crossover (SCO) materials are octahedral Fe(II) compounds in which the spin transition involves a change in electronic structure from $t_{2g}^6e_g^0 \leftrightarrow t_{2g}^4e_g^2$.[17,18] The spin transitions can be abrupt and exhibit hysteresis if strong cooperative interactions between the spin centers are present.[19,20]

In stark contrast to the plethora of known Fe(II) SCO species, Co(II)-based SCO materials are more scarce and their spin state transformation is generally more gradual because only one electron is involved in the spin-transition in an octahedral geometry, *viz*., from $t_{2g}^6eg^1 \leftrightarrow t_{2g}^5e_g^2$).[21,22] Another difference is that Co(II) SCO systems usually require stronger field ligands as compared to Fe(II) systems, the ligands sets of which solely lead to LS states in Co(II).[23] Among the most widely studied Co(II)-based SCO materials are salts of $[Co(terpy)_2]^{2+}$ (terpy = 2,2';6',2''-terpyridine) for which it is known that counterion identity and the presence of interstitial solvent both affect the magnetic properties.[24-27] For example, $[Co(terpy)_2](ClO_4)_2$ and $[Co(terpy)_2](BF_4)_2$ exhibit SCO behavior but $[Co(terpy)_2](PF_6)_2$ does not; instead, the latter exists in a HS ground state with a small fraction of LS states being populated even at room temperature.[28,29] The 4'-substituted terpy derivatives with hydroxyl, alkyl, alkoxyl groups have also been

extensively investigated and it was found that the presence of long alkyl chains promote interesting properties and/or phase such as reverse spin-transition, re-entrant spin-transition, liquid crystalline SCO materials and SCO films.[30-36]

Spin-canted antiferromagnetism

According to the different types of magnetic interactions between the spins, the magnetic states of bulk magnetic materials are traditionally categorized into paramagnetic, ferromagnetic, antiferromagnetic and ferrimagnetic states (Figure 4). In a paramagnet, the spins are randomly oriented in the material and no long-range ordering is present. Spins of equal magnitude are long-range ordered in ferromagnets and antiferromagnets; in the former case the spins are aligned in a parallel fashion to exhibit an increase in the magnetic moment when these spin are ordered whereas in the latter situation the spins are aligned in an antiparallel manner to reach a zero magnetization upon ordering. A ferrimagnetic state is a special case stemming from the antiparallel (antiferromagnetic) alignment of spins, which will show a non-zero magnetization when the spins are not of equal magnitude.

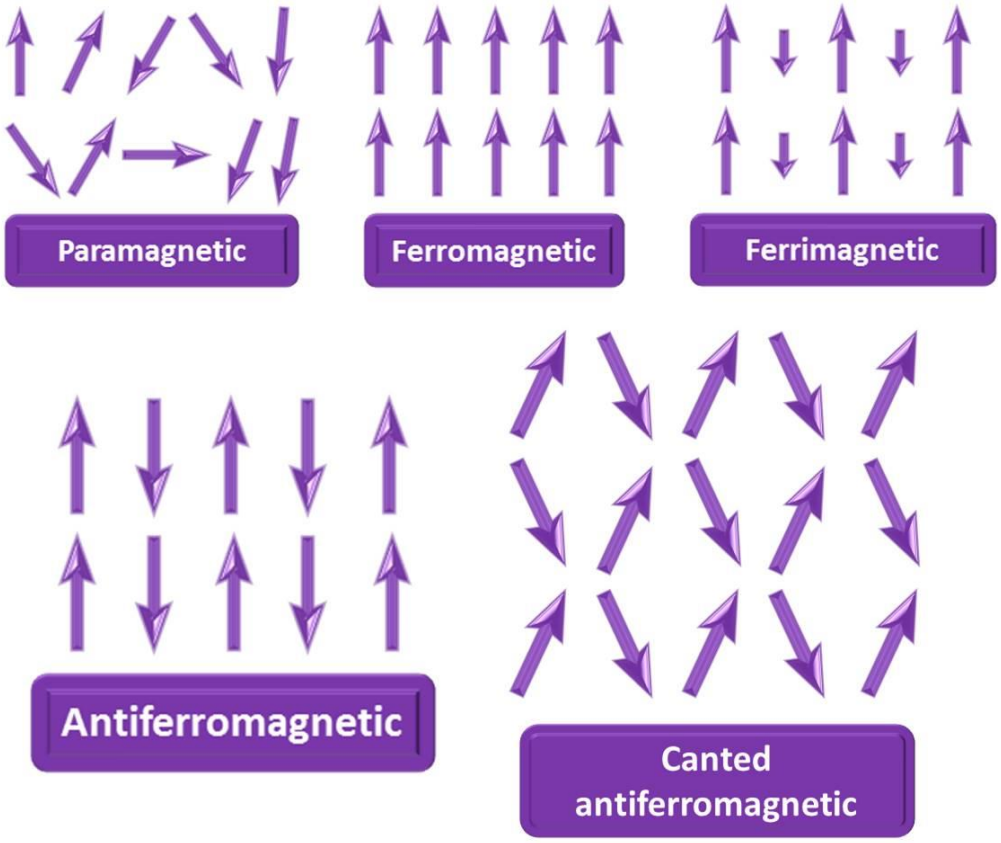

Figure 4. Different types of magnetic states between the spins in bulk magnetic materials.

Another interesting case that results from antiferromagnetic interactions of equal spins is a spin-canted antiferromagnetic state where the adjacent spins are tilted at a certain angle from each other. Due to the fact that the spins are not total cancelled, a non-zero magnetization is observed similar to the ferrimagnetic state. Therefore, spin-canted antiferromagnets will be observed as a phenomenological "weak ferromagnetic" response.

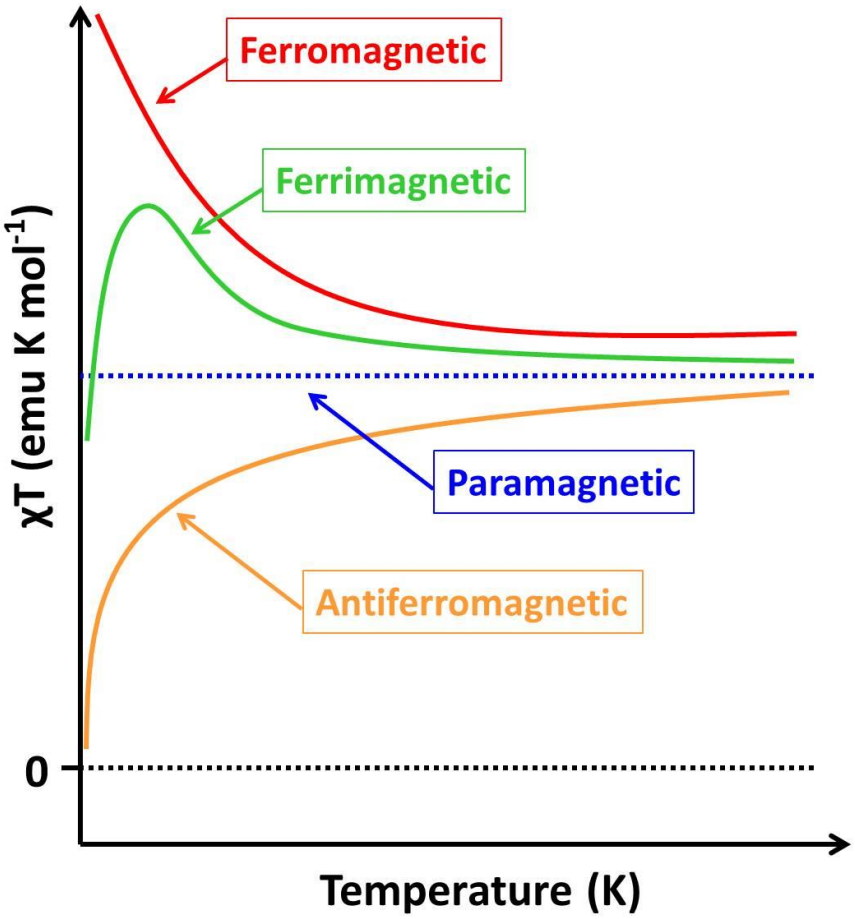

Figure 5. Magnetic characterization of the different types of magnetic states as shown in the χT versus T plot.

Single-molecule magnets

As the traditional semiconducting and magnetic materials are reaching their miniaturization limits in the near future, alternative molecular materials are receiving more attention due to the fact that they are readily available in the size regime below the 2-3 nm limits. Single-molecule magnets (SMMs), also known as molecular nanomagnets, are a type of molecular compounds that exhibit slow relaxation of the magnetization and magnetic hysteresis, which are of a molecular origin rather than a

collective effect of long-range magnetic ordering in conventional bulk magnets. These superparamagnetic-like properties are observed below a certain temperature, known as the blocking temperature.

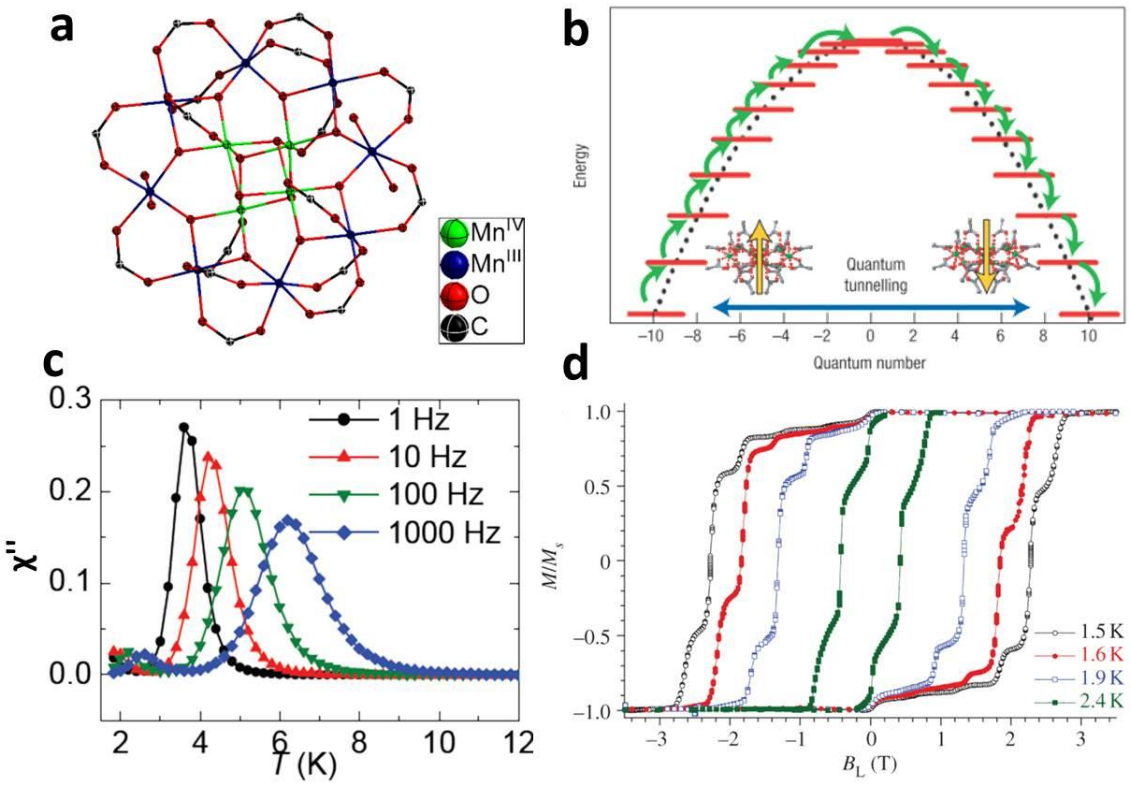

Figure 6. a). Structure of the Mn12 acetate molecule. Hydrogen atoms and the crystallizing solvent molecules are omitted for the sake of clarity. b). The potential energy scheme shows the different energy levels of Mn12 acetate. The green arrows represent the thermally activated process where the spins have to go through the highest energy barrier as depicted. The blue arrow indicates quantum tunneling processes where the spin states can go through instead of over the barrier.[37,38]

SMM behavior was first identified in a dodecanuclear manganese complex, $[Mn_{12}O_{12}(CH_3COO)_{16}(H_2O)_4]\cdot 2CH_3COOH\cdot 4H_2O$, which is also known as "Mn12 acetate" (Figure 6).[7,39-41] This prototypical SMM consists of twelve manganese ions connected by oxide and carboxylate bridges, in which the spins of the four Mn(IV) in the

middle of the molecule are antiparallel to the spins of the eight peripheral Mn(III) ions, to exhibit an S = 10 spin ground state. Mn12 acetate has an effective energy barrier of 66 K for the reversal of the spin magnetization with a negative magnetic anisotropy of -0.66 K.

Two of the key parameters in SMMs are spin and magnetic anisotropy, as the energy barrier for the reversal of magnetization is defined as $U = |D|S^2$ for integer spin systems and $U = |D|(S^2-1/4)$ for half integer spin systems. Current efforts for the enhancement of the energy barrier focus mainly on single-ion anisotropy, isotropic exchange interactions and anisotropic exchange interactions.[42]

The observation of SMM behaviors is usually conducted through the measurement of AC magnetic susceptibility, where frequency-dependent peaks of the out-of-phase (χ") magnetic susceptibility are often a good indicator of slow relaxation of the magnetization. For a thermally activated relaxation process, the relaxation time τ follows the Arrhenius law ($\tau = 1/(2\pi\nu) = \tau_0\exp(U_{eff}/k_BT)$), ν is the AC frequency and k_B is the Boltzmann constant) and fitting of the experimental data to the Arrhenius law can be used to obtain the effective energy barrier.

Apart from the thermally activated relaxation processes, other relaxation processes must also be considered for the realization of SMMs with high blocking temperatures.[43] In many cases the frequency-dependent alternating current (ac) susceptibility signals are not observed under a zero applied direct current (dc) magnetic field due to predominant quantum tunneling processes which are facilitated by inter-molecular dipole-dipole interactions. In such a case, a dc field can be applied to lift the

degeneracies between the microstates as it stabilizes the spins that are in the same direction and destabilizes the spins in the opposite orientations (Figure 7).

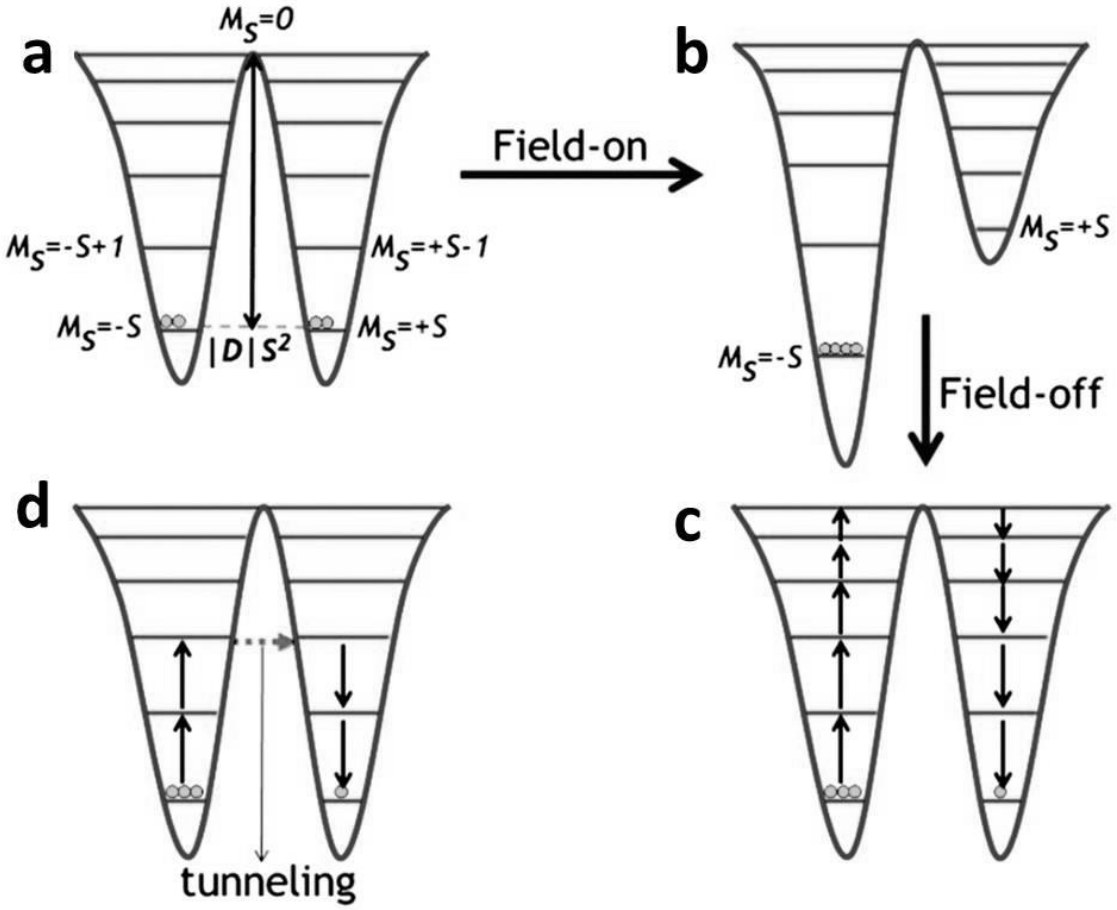

Figure 7. Schematic representation of effect of external magnetic field on the the thermal and quantum tunneling relaxation of the magnetization in SMMs. a). Under a zero dc field, the degenerate spin states are equally populated in the two potential wells due to zero-field splitting. b). Upon the application of an external magnetic field, the Zeeman effect breaks the degeneracy to result in a selective population of spin states. When the external magnetic field is removed, the relaxation of the magnetization can take place either through the anisotropy energy barrier (c) or through quantum tunneling (d). Adapted from reference.[42]

Applications of single-molecule magnets

Applications of SMMs have been demonstrated in spin valves where the preferred direction spin of the molecular valve can either allow the current to pass

through or resist the current (Figure 8, top left). Another feature of SMMs is that they can behave as potential quantum bits (qubits). As opposed to classic bits, where the smallest information storage unit can exist in either "0" or "1" states, SMMs can behave as qubits, which can exist in states that are superpositions of the "0" and "1" states due to quantum entanglement (Figure 8, bottom left). Wernsdorfer and coworkers have successfully demonstrated the read-out of the nuclear spin trajectories in a molecular spin transistor (Figure 8, right).[44]

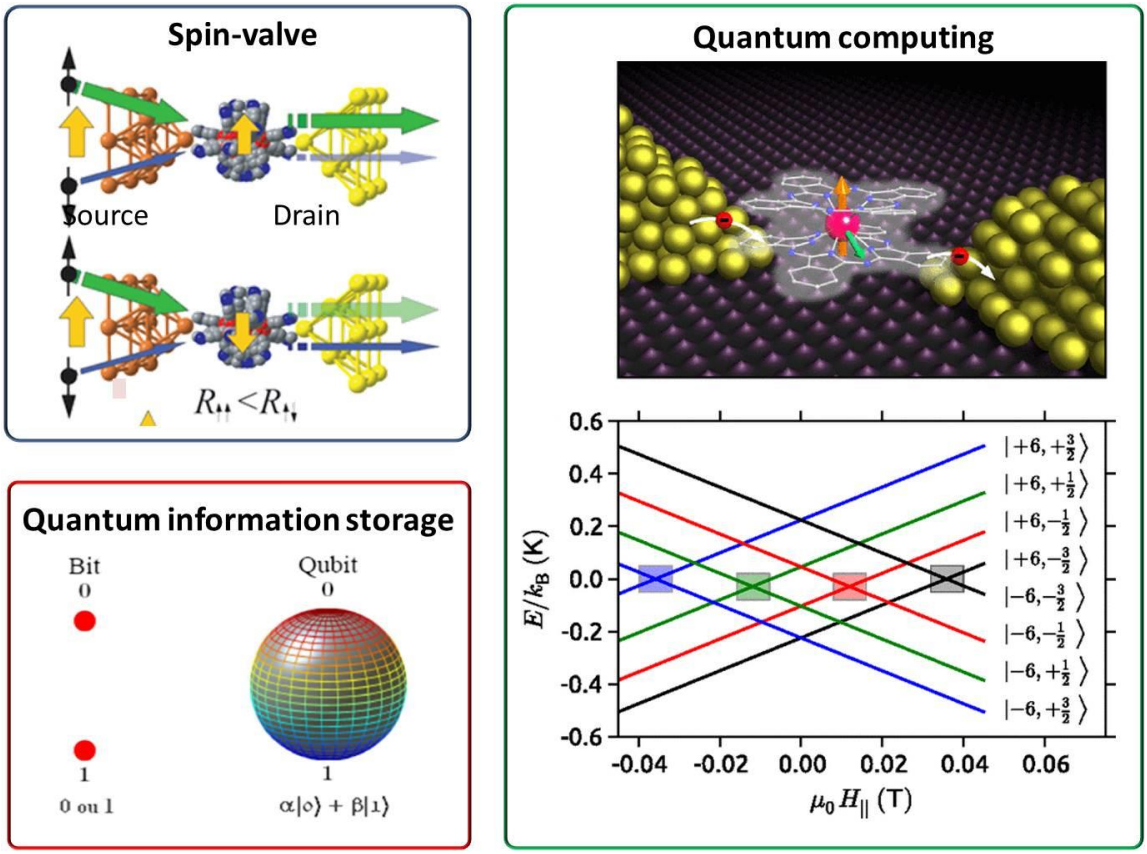

Figure 8. Applications of SMMs as spin-valves (top left) for transitors, qubits for quantum information storage (bottom left) and quantum computing (right, an SMM junction with the read-out of different energy levels).

While it is of utmost importance to synthesize and design SMMs that have higher blocking temperatures and stability, one of the biggest practical challenges for the applications of these molecular nanomagnets is the control and read-out of individual SMM information. On a practical note, however, it is more feasible at the moment to organize SMMs in ordered arrays such as quasi-1-D chains or 2-D layers for device applications instead of attempting to control all the individual molecules.

As part of a collaborative effort between the Dunbar group and the Wriedt group at Clarkson University, the prototypical SMM $[Mn_{12}O_{12}(O_2CCH_3)_{16}(OH_2)_4]$ was incorporated under mild conditions into a highly porous metal–organic framework (MOF) matrix as a "proof-of-concept" for controlled nanostructuring of SMMs. Four independent experiments revealed that the SMM clusters were successfully loaded in the MOF pores, namely synchrotron-based powder diffraction, physisorption analysis, and in-depth magnetic and thermal analyses. The results provide incontrovertible evidence that the magnetic composite, SMM@MOF, combines key SMM properties with the functional properties of MOFs. Most importantly, the incorporated SMMs exhibit a significantly enhanced thermal stability with SMM loading advantageously occurring at the periphery of the bulk MOF crystals with only a single SMM molecule isolated in the transverse direction of the pores.[45]

In another vein, a promising series of quasi-1-D compounds was formed by the self-assembly of organic $TCNQF^{-}\bullet$ radicals and the anisotropic $[Ln(valpn)Cu]^{3+}$ dinuclear cations. Magnetic characterization revealed that the effective energy barrier for the reversal of the magnetization in this rare hetero-tri-spin compound is significantly

larger than the reported single-molecule magnet with the isolated 'TbCu' dinuclear cores and the supramolecular stacking interactions of $TCNQF^{-}\bullet$ radicals were found to be essential for the 1-D correlation of the magnetic behavior.[46] It is promising to induce electrical conductivity of the TCNQ radical stacks and to study the effect of electric field on the magnetic properties of these potential bifunctional materials.

Organocyanide-Based Functional Molecular Materials

Organocyanides[47] such as tetracyanoethylene (TCNE), 7,7,8,8-tetracyanoquinodimethane (TCNQ) and dicyanoquinodiimine (DCNQI) (Figure 1) are excellent electron acceptors that have been extensively studied as radical units in magnetic,[48] semiconducting,[49] catalytic[50] and electrically bistable 'switching'[51] materials. They can be easily reduced to monoanionic radicals through a reversible one-electron reduction process. These radicals are generally stable in air in the solid state and can stack into conducting columns in semiconductors or produce a ferrimagnetic state in magnetic materials by bridging metal ions with while mediating antiferromagnetic coupling.[52,53] The organocyanide ligands can also form dianions that are stronger coordinating ligands than the radical monoanion forms, a fact that leads to robust framework solids that can undergo ligand-to-metal charge transfer and charge transfer to guest molecules.[54,55]

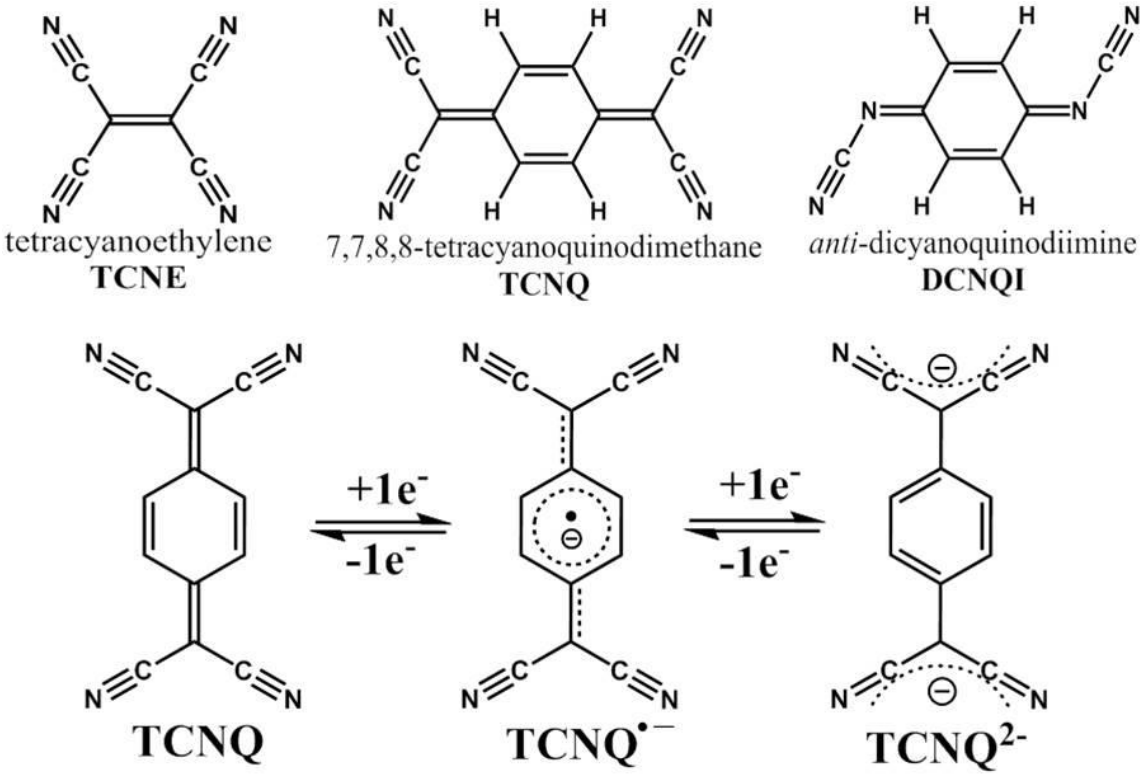

Figure 9. Molecular structures of organocyanide acceptors (top) and the reduction of TCNQ to the monoanionic radical and dianionic forms (bottom).

Two important examples of the remarkable organocyanide-based materials that have appeared include the report in 1991[56] of $V(TCNE)_x \bullet yCH_2Cl_2$ ($x \approx 2$, $y \approx 0.5$), which is a room temperature magnet with a Tc of ~400 K (albeit amorphous in nature), and Cu(TCNQ) which has been under intense investigation since 1979 as an excellent candidate for electronic memory devices.[51] The latter type of semiconducting material is renowned for its "switching" properties which involves a large enhancement of the conductivity properties upon the application of a threshold voltage. Apart from the non-volatile memory-type switching materials, there are other fascinating metallic conductors such as $Cu(DM\text{-}DCNQI)_2$ (DM-DCNQI = 2,5-dimethyl-DCNQI) and related

derivatives that exhibit room temperature conductivities as high as 800 S•cm^{-1} which is on the order of graphite.[57]

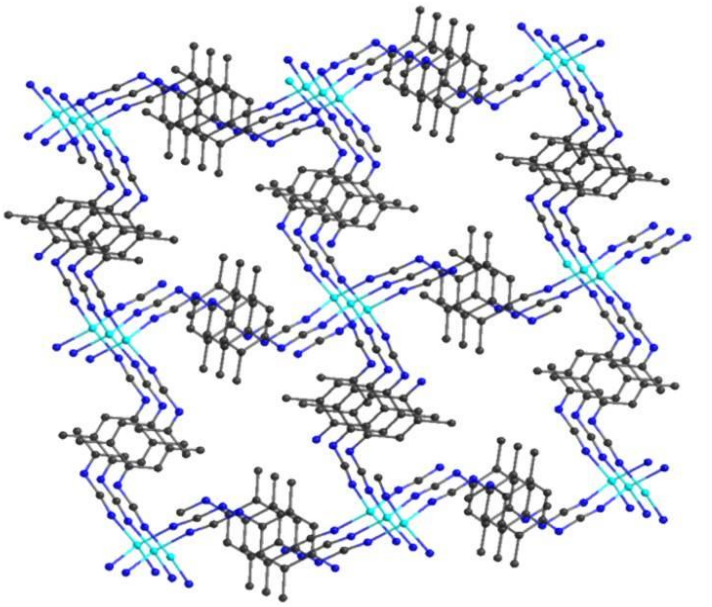

Figure 10. Packing diagram of the crystal structure of Cu(DM-DCNQI)$_2$ showing the stacked DM-DCNQI moieties.

Since the discovery of the metallic and superconducting properties of organic conductors such as TTF-TCNQ,[58] BEDT-TTF-TCNQ,[59] and the room temperature magnet V(TCNE)$_x$•yCH_2Cl_2 (x ≈ 2, y ≈ 0.5),[56] considerable efforts have been directed towards the study of organocyanide-based molecular materials and devices. In the aforementioned solid state metal-organocyanide compounds with electrical conducting properties, partially charged TCNQ and DCNQI, and their monoanionic radicals are commonly encountered, with the organocyanide moieties stacked in a columnar fashion through supramolecular interactions to form an electron-conducting pathway via coordination to diamagnetic late transition metals and main group ions such as Cu(I), Ag(I), Cd(II) and Tl(I).[60-63] Apart from being charge carriers in electrically conducting

materials, the singly charged organocyanide anion radicals are excellent spin carriers for mediating magnetic interactions. Due to the unpaired electrons with S =1/2 on these organocyanide radicals, ferrimagnetic states are obtained when they function as bridging ligands between two metal ions with higher spin states and can propagate long-range magnetic interactions. For example, in the ferrimagnet Gd-TCNQ, the larger Gd^{III} spins ($S_1 = 7/2$) are mediated through the spins on the TCNQ radicals ($S_2 = 1/2$). The spins on the metal centers and the radicals are antiparallel with parallel spins on the alternating metal ions, which results in a non-zero magnetization of the material in its ordered state (Scheme 2a).[64] By comparison, if the two paramagnetic metal ions are bridged by a diamagnetic ligand, the spins on the metal centers tend to align in an antiparallel fashion (antiferromagnetic coupling), which results in zero net magnetization in its ordered state (Scheme 2b).

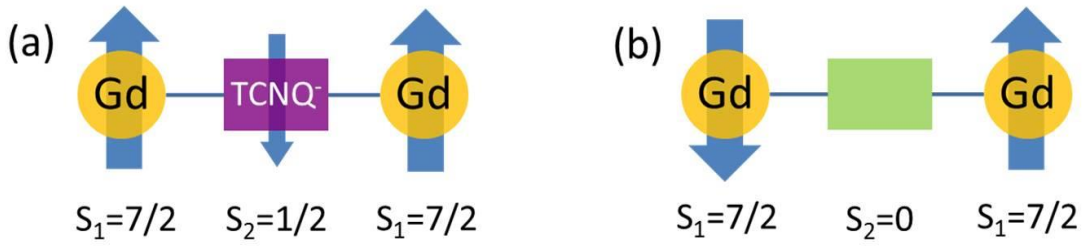

Figure 11. Schematic presentation of the magnetic coupling between Gd(III) ions through: (a) $TCNQ^-$ radical bridge, (b) diamagnetic bridge.

Table 1. Characteristic infrared *ν*(CN) stretching frequencies and electrochemical potentials of substituted TCNQ molecules (at a Pt working electrode vs. Ag/AgCl in acetonitrile with 0.2 M $[Bu_4N][PF_6]$ as the electrolyte).

Organocyanide	***ν* (CN) /cm^{-1}**	**$E^1_{1/2(red)}$ /V**	**$E^2_{1/2(red)}$ /V**
$TCNQ(OMe)_2$	2217,2175	+0.06	-0.41
$TCNQMe_2$	2222,2164	+0.15	-0.33
TCNQ	2221	+0.25	-0.29
$TCNQI_2$	2213,2201	+0.46	+0.01
$TCNQBr_2$	2223,2150	+0.49	0.00
$TCNQCl_2$	2226,2209	+0.48	-0.03
$TCNQF_4$	2226	+0.60	+0.09

In addition to the electronic properties and the supramolecular π-stacking interactions of organocyanide radicals, the rational tuning of their electron-accepting ability renders them ideal for controlling the electronic and magnetic properties of the ensuing materials. For example, substitution of the TCNQ quinoid ring with a series of electron-donating or withdrawing groups allows for tuning of electron-accepting properties by systematic control of the reduction potentials over a wide range (Table 1).[65] The substituents not only affect the electrochemical potentials of the TCNQ derivatives, but they can also induce steric effects or halogen bonding if involved in π- π stacking interactions; the combination of these interactions can give rise to other diverse properties that are not otherwise easily accessible.[46,61,63,66]

Another important aspect of these organocyanide molecules is the presence of multiple cyanide groups, which confer to them versatile bridging modes with metal ions. In this context, TCNQ has been reported to exhibit all four possible bridging modes, i.e., monodentate, μ_2-, μ_3- and μ_4-TCNQ. Moreover, the μ_2-TCNQ units in the structure of $Cd_2TCNQ_{3.5}$•$2H_2O$ are in the *syn*- and *anti*-conformations with the Cd(II) ions on the same or opposite sides of the TCNQ plane, respectively.[62] The ensuing structures have the potential to give rise to materials with versatile properties, and thus, the investigation of structure-property relationships is crucial for the design, synthesis and development of metal-organocyanide-based functional materials.

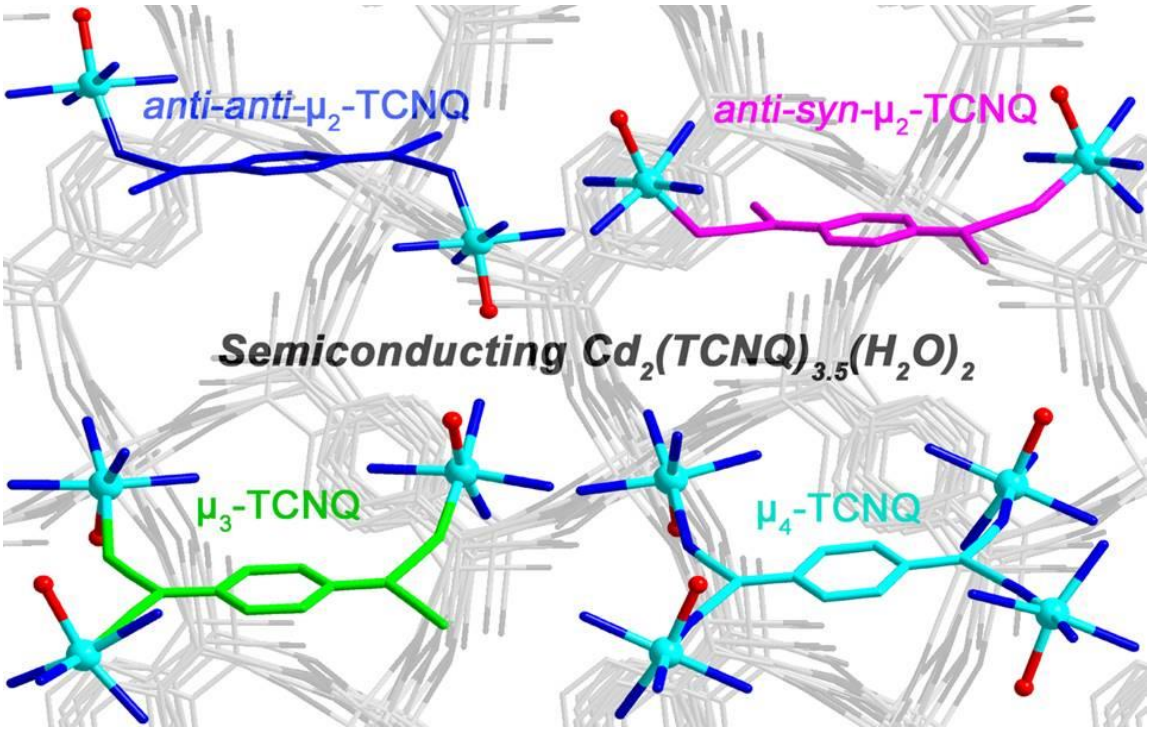

Figure 12. The semiconductor $Cd_2(TCNQ)_{3.5}(H_2O)_2$ exhibits a 3-D framework structure with four different bridging modes of TCNQ. Reproduced with permission from reference 62.[62] Copyright Royal Society of Chemistry 2014.

Whereas the radicals are fundamental for the electronic and magnetic properties of organocyanide-based materials, the organocyanide dianons can be used in place of polycarboxylate anions to form porous metal-organic frameworks that exhibit selective gas adsorption and magnetic properties.[54,67,68] In addition, as reported by our group and others, σ-dimerized $(TCNQ)_2^{2-}$ units can serve as longer and robust linkers in MOFs.[69] In one study, Kitagawa and coworkers reported selective adsorption of NO and O_2 in MOFs incorporating $(TCNQ)_2^{2-}$ units; the selective adsorption of the gases was attributed to the dynamic charge-transfer interactions between TCNQ and the guests, and the flexible gate opening and closing of the framework pores.[70]

In the aforementioned examples, the degree of charge-transfer plays a critical role in the resulting properties of the materials. The compounds with monoanion radicals of TCNQ, DCNQI, their partially charged moieties, and their derivatives exhibit higher conductivity when engaged in stacked structures. The partial charges render the electrons highly delocalized throughout the stacks and therefore enhance the conductivity. For example, in the TCNQ infiltrated HKUST-1 thin films, the presence of partially charged TCNQ moieties induces a substantial increase in the conductivity of the material.[71]

Spectroscopic and structural data are good indicators of the charges on organocyanide molecules.[72] From a molecular orbital point of view, when TCNQ molecules are reduced, the additional electrons are placed in the antibonding π* orbital, which weakens the CN triple bonds. The reduction of TCNQ results in a red shift of the ν(CN) stretching frequency as compared to that of a neutral TCNQ (2221 cm^{-1}). It

should be noted, however, that coordination to metal ions may also affect the ν(CN) stretching frequency as back donation from the metal results in a red shift as well.[73] With regard to structural studies, Kistenmacher and coworkers developed an empirical formula, which has proved to be particularly helpful in estimating the charge on TCNQ molecules in the solid state from selected bond distances in the crystal structures.[62,74,75] The charge is $\rho = A[c/(b + d)] + B$ (A = -41.667 and B = 19.833, as established from neutral TCNQ[76] (ρ = 0) and RbTCNQ[77] (ρ = -1)), and the corresponding bond distances b, c and d are depicted in Figure 13. Similar formulae for TCNQ derivatives such as $TCNQF_4$, BTDA-TCNQ and DM-DCNQI have also been developed in the literature.[78,79] In this dissertation, the charges on TCNQ molecules in the solid state are estimated from the Kistenmacher relationship unless otherwise stated.

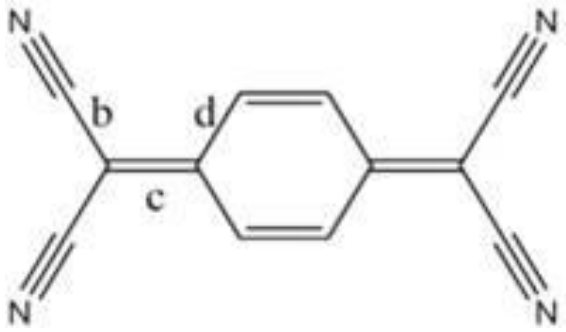

Figure 13. Molecular structure of TCNQ and the labelling of selected C-C bonds.

In general, TCNQ salts are described as narrow band intrinsic semiconductors whose density of states are independent of the temperature and their charge carrier mobility is inversely proportional to the temperature.[80] In the semiconducting region, the electrical conductivity follows an activated process governed by the Arrhenius law ($\sigma = \sigma_0 \exp(-\Delta E_a/kT)$) as the temperature changes.[81]

Research in the Dunbar group in the area of metal-organocyanide compounds focuses on the overarching goal of mapping out structure-property relationships in magnets and conductors.[69,82,66] One of the early benchmarks in our research was the discovery of polymorphism in Cu^{I}(TCNQ) which resolved a decades-long enigma surrounding the irreproducibility of the switching behavior of devices[83] composed of microcrystalline Cu(TCNQ) films grown from redox reactions of copper foil with neutral TCNQ in acetonitrile. Two polymorphs of Cu(TCNQ) have been identified with distinct conductivities, referred to as Phase I and Phase II, and it was determined that the former phase is the one responsible for the switching behavior.

Main group metal-TCNQ compounds have also been under investigation in the Dunbar group because of the resemblance of Tl^{I} to alkali metals which have been studied extensively as charge-transfer salts with TCNQ anions.[49] The difference is that thallium is coordinated to eight cyanide groups of the TCNQ radicals. A poor semiconductor referred to as the Phase I polymorph of Tl(TCNQ) was found to undergo a crystal-to-crystal phase transition in the presence of water into a much better semiconducting Phase II with a room temperature conductivity of 0.54 $S \bullet cm^{-1}$. This was the first observation of an irreversible solid-state transformation in such materials that does not involve the exchange of solvent molecules.

One of the primary goals in the study of molecule-based functional materials is the synergistic response of multiple physical properties. In this vein, our group is interested in multifunctional molecular materials that show the coexistence of properties including magnetism, conductivity and, if possible, ferroelectricity. The series of

transition metal-TCNQ compounds, $M^{II}(TCNQ)_2$ (M=Mn, Fe, Co, Ni) prepared by us over ten years ago led to the realization that open shell (paramagnetic) metal ions bridged by TCNQ radicals resulted in ferrimagnetic ground states which undergo magnetic ordering albeit of a glassy nature.[48] More interestingly, these glassy magnets also behave as semiconductors with room temperature conductivities as high as 1.4×10^{-3} $S\bullet cm^{-1}$. The semiconducting state is expected to originate from the stacks of TCNQ radicals formed through π-π interactions in the compounds along which charge carriers can be mobile, but, due to the lack of structural information, the exact details of the nanocrystalline materials is still elusive and requires further investigation.

Another example of the strategies being used to integrate magnetic interactions through bridging ligands with electron conducting pathways via stacks of partially reduced TCNQ anions was reported by our group in 2011.[74] The compound {[Mn(4,4'-bpy)(η^1-TCNQ)$_2$(CH_3OH)$_2$]TCNQ} 0.5H_2O holds the room temperature conductivity record of 3.8 S cm^{-1} for TCNQ-coordinated materials, with formal non-integer charges of -2/3 on the coordinated and uncoordinated TCNQ species. In spite of its metallic conductivity, this prototype suffers from the fact that the 4,4'-bpy (4,4'-bipyridine) which acts as a spacer is not able to transmit strong superexchange coupling between the paramagnetic S=5/2 Mn^{II} ions.

In general, it is logical to expect that magnetic coupling of paramagnetic metal ions through longer linkers such as 4,4'-bpy are not as effective as when bridges of shorter exchange pathways like cyanide (CN^-), oxide (O^{2-}) and azide (N_3^-) are used. Indeed, it was reported in the studies of dinulear Ru^{III} compounds that coupling through

bridging pyrazine was very small ($|J|<0.2$ cm^{-1})[84, 85] but, importantly for the present topic, it was later demonstrated by Crutchley and coworkers that Ru(III) ions could couple effectively through a bridging diamagnetic $DCNQI^{2-}$ with a coupling constant of $J= -53$ cm^{-1}, despite the long distance between the metal spin centers of ~13 Å.[86]

One of the goals in this research is to take advantage of what is known to date as described in the previous paragraphs to study the magnetic coupling of paramagnetic metal ions in metal-organic frameworks (MOFs), which are also commonly known as porous coordination polymers (PCPs). Such materials have been extensively studied for their potential applications in gas separation/storage, catalysis and as sensors.[87] The structures of MOFs, typically involve carboxylic acid linkers to connect secondary building units, but it is known that these ligands are not efficient at transmitting magnetic coupling. It was our hypothesis that organocyanide dianions can be used in place of carboxylic acids in the construction of MOFs and, indeed, there is some precedent for this idea from independent work from the Robson and Kitagawa groups.[54,67,88] In these separate efforts, the $TCNQ^{2-}$ dianion was generated by the disproportionation of $TCNQ^{-}$ or from the direct deprotonation of H_2TCNQ. Nevertheless, the series of MOFs that resulted exhibit similar 3D structures composed of 2D M^{II}-$TCNQ^{2-}$ (M=Zn, Cd, Mn, Fe, Co) neutral networks pillared by 4,4'-bpy bridges, with the adjacent $TCNQ^{2-}$ anions perpendicular to each other. In was also found that these redox active MOFs exhibited charge transfer (CT) between guest solvent molecules and the host frameworks.

By taking advantage of the versatility of the organocyanides in forming radical monoanions and dianions, we assert that coordination compounds with transition metals that combine several properties are possible to access. Both the monoanionic radical and the dianion can serve as bridges, but they differ in that the former leads to semiconducting properties when involved in stacking interactions whereas the latter is a good electron donor ligand for the formation of more robust metal-organic frameworks, allowing for post-synthetic interactions with small electron acceptors involving charge and/or electron transfer. By substituting electron donating or withdrawing groups in place of the hydrogen atoms on the phenyl/quinoid rings of the organocyanides (Table 1), further tunability and fine control over the corresponding properties can be achieved in these multifunctional molecular materials.

CHAPTER II

ELECTRICALLY CONDUCTING AND SPIN-CROSSOVER BIFUNCTIONAL MATERIALS*

Introduction

Hybrid inorganic-organic materials are attractive owing to the flexibility in the choice of building blocks with tunable functionalities and their potential applications in memory devices and field-effect transistors.[89-93] An important subset of these materials is magnetic molecule-based compounds that hold promise for significant miniaturization of future devices.[3,40,94] Crystalline molecular materials are also advantageous for engendering multifunctionality through the use of modular synthetic procedures which is an ideal approach for elucidating structure-property relationships.[1] Some notable examples are conducting magnets exhibiting bulk/single-molecule magnetic properties[5,95] and electrically conducting spin-crossover (SCO) complexes.[96,97]

The electron acceptor TCNQ (TCNQ = 7,7,8,8-tetracyanoquinodimethane) forms a highly stable radical which has been widely used as a building block for the design of coordination polymers and charge-transfer complexes with intriguing redox, magnetic, electrical conducting and/or switching properties.[46,55,61,62,71,98-107] The successful

* A portion of this chapter is reprinted with permission from "A cobalt(II) spin-crossover compound with partially charged TCNQ radicals and an anomalous conducting behavior", by Xuan Zhang, Zhao-Xi Wang, Haomiao Xie, Ming-Xing Li, Toby J. Woods and Kim R. Dunbar, *Chemical Science*, **2016**, **7**, 1569-1574, DOI: 10.1039/C5SC03547C, Copyright 2016 by Royal Society of Chemistry; and from "Structural distortions of the spin-crossover material $[Co(pyterpy)_2](TCNQ)_2$ mediated by supramolecular interactions", by Xuan Zhang, Haomiao Xie, Maria Ballesteros-Rivas, Zhao-Xi Wang and Kim R. Dunbar, *Journal of Materials Chemistry C,* **2015**, 3, 9292-9298, DOI: 10.1039/C5TC01851J, Copyright 2015 by Royal Society of Chemistry.

realization of molecular organic conductors requires the uniform stacking of organic molecules in addition to the presence of open-shell radicals, preferably with non-integer charges, and minimal Coulombic interactions.[108,109] In TCNQ-based electrical conducting charge-transfer compounds the TCNQ radical anions typically stack in a parallel manner, a situation that facilitates overlap between their frontier orbitals. A main challenge that remains to be addressed, however, is the design of TCNQ-based multifunctional materials that exhibit synergistic interactions, rather than the typical scenario in which the properties are observed as isolated events in separate thermal regimes.[48,74]

Spin-crossover is a form of magnetic bistability triggered by external stimuli *e.g.*, light, pressure and temperature.[20,110,111] Given that crystal packing constitutes a chemical pressure which affects metal-ligand bond distance variations that occur with spin-crossover events,[112,113] we were curious as to whether these stimuli-responsive structural changes would affect the electron transport properties of a hybrid material that contains semiconducting π-stacks of TCNQ radicals co-crystallized with a metal complex that undergoes notable structural changes under thermal perturbation. The underlying reasoning is that the transition temperature of the SCO event could be tuned over the temperature range of 100-300 K to match the thermal regime of the semiconducting behavior of the TCNQ sub-lattice.[17,19,62,111] In this context, we note that composite conducting SCO materials exhibiting synergistic interactions have been obtained by combining conducting organic polymers and SCO complexes.[114,115] Chen and coworkers reported a 1-D coordination polymer of $[Co(C_9H_6NS)_2]$ (C_9H_6NSH = 8-

mercaptoquinoline), which is a rare example of one compound with the coexistence of SCO and semiconductivity.[116] The cobalt coordination sphere is composed of two nitrogen and four sulfur donor atoms and the Co-donor bond distances have a difference of about 0.1 Å between the LS and HS states. Due to the strong π-π stacking interactions between the quinoline groups and ⋯Co-S-Co-S⋯ infinite chains, this coordination polymer was reported to behave as a semiconductor with an activation energy of 0.76 eV and a conductivity of 1.7×10^{-7} S/cm at 293 K (Figure 14).

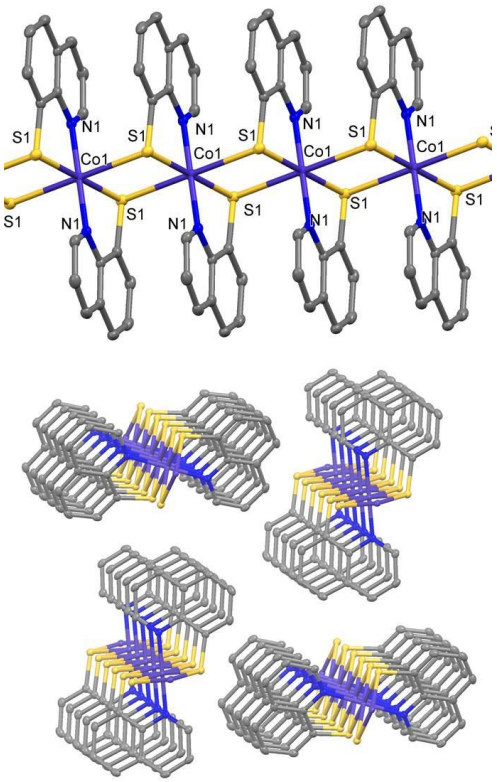

Figure 14. The chain structure (top) and the packing diagram of $[Co(C_9H_6NS)_2]$ viewed along the I axis (bottom). Color code: cobalt (purple), nitrogen (blue), sulfur (yellow), carbon (gray). Hydrogen atoms are omitted for the sake of clarity.

Galán-Mascarós and coworkers reported an excellent example of engendering the switching of electrical conductivity in a hybrid material by a combination of *p*-doped

polypyrrole and SCO coordination polymers $[Fe(trz)(Htrz)_2][BF_4]$ and $[Fe(trz\text{-}NH_2)_3][SO_4]$ (Htrz = 1,2,4-triazole, trz-NH_2 = 4-amino-1,2,4-triazole). Doped polypyrrole was chosen as a candidate for the electrically conducting component because its polymeric chains is highly dependent on pressure, which affects the inter-chain distances and hence the density of states at the Fermi level.[117] Therefore, by the incorporation of the SCO coordination polymers in the conducting polymer, the temperature dependent magnetic behavior of the former will exert a chemical pressure that affects the inter-chain interactions and the electrical conductivity. In this case, the thermal hysteresis observed in the SCO component is transmitted to the electrical conductivity of the conducting polymer matrix (Figure 15).

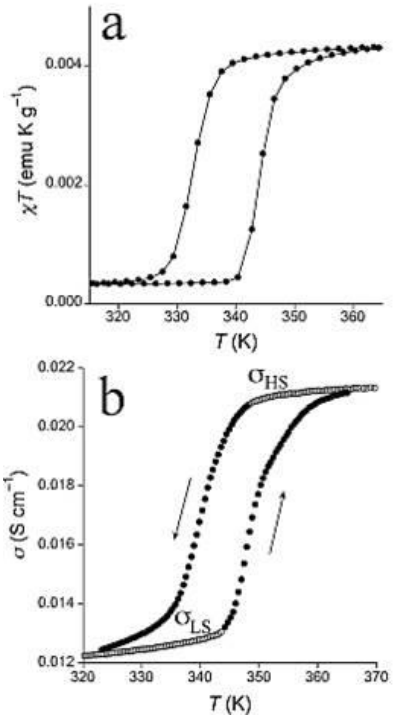

Figure 15. Thermal hysteresis of the χT and electrical conductivity of the hybrid material of $[Fe(trz\text{-}NH_2)_3][SO_4]$ and oxidized polypyrrole.

In a similar fashion, $[Fe(trz)(Htrz)_2][BF_4]$ was incorporated into a heterostructure with polycarbonate which exhibited synergistic effects between the SCO induced volume changes in the structure and the electrical conductivity of the metallic conductors.[115]

A number of crystalline conducting SCO materials have also been reported that offer an ideal platform for the investigation of structural-property relationships by the co-crystallization of Fe-based SCO complexes with metal dithiolate radicals.[96,112,118-120] In order to realize significant electrical conductivity in these materials, however, galvanostatic oxidation of the mono-anion radicals is usually performed to generate partially charged radicals, which helps to enhance the delocalization of electrons throughout the radical stacks. In comparison, reports on TCNQ-based SCO conductors have been scarce, with the most recent one being reported by Shatruk and coworkers who took advantage of the comproportionation reaction between neutral TCNQ and the mono-anion $TCNQ^{\bullet-}$ radical to yield partially charged radicals which give rise to a high room temperature conductivity of 0.2 S cm^{-1}.[121,122] Due to the extra step of combining equal equivalents of the two TCNQ sources in this comproportionation method, however, a single source of partially charged TCNQ radicals would be more desirable. In this vein, we noted that Gutierrez and coworkers reported the salt $[Et_3NH](TCNQ)_2$ as a source of partially charged TCNQ radicals for a series of electrical conducting compounds, *viz*., $[M(terpy)_2](TCNQ)_3$ (M = Ni, Cu, Zn and terpy = 2,2′;6′,2″-terpyridine). Unfortunately no structural information is available for these compounds.[123]

One of the main challenges in SCO research is the initiation of cooperative interactions between the individual spin centers the presence of which induce sharp spin transitions and a memory effect as evidenced by thermal hysteresis.[124-126] A leading strategy to this end is to incorporate SCO entities into coordination polymers with chemical linkages that assist in enhancing cooperative interactions.[127,128] Another approach is to take advantage of supramolecular interactions such as hydrogen bonding, π-stacking between the aromatic fragments and interdigitation of long alkyl chains attached to discrete SCO units.[13,32,129,130] In this study, we employed Co(II)-based SCO complexes with an expanded aromatic system with the aim of studying the effects of intermolecular π-stacking of the planar terpy ligands and TCNQ radicals on the magnetic properties of the resulted materials. In addition, we reasoned that, as TCNQ radical stacks are well known for their electrical conducting properties, inter-molecular interactions between the SCO moieties and TCNQ radicals could lead to bifunctional SCO conductors.[61-63,122,131] Of relevance to the present study is the previously demonstrated work from our group and others that organocyanide radicals such as $TCNQ^{\bullet-}$ (7,7,8,8-tetracyanoquinodimethane) effectively enhance properties through supramolecular π-stacking interactions.[46,100,132-134]

Herein we report the successful use of $[Et_3NH](TCNQ)_2$ as a readily accesible source of partially charged TCNQ radicals for the synthesis of the inorganic/organic hybrid bifunctional material, $[Co(terpy)_2](TCNQ)_3 \cdot CH_3CN$. This crystalline molecular material exhibits an impressively high electrical conductivity of 0.13 S cm^{-1} at room temperature due to the presence of partially charged TCNQ radicals despite their unusual

"cross-stacking" patterns. In addition, the observation of an unprecedented anomaly in the electrical conductivity of $[Co(terpy)_2](TCNQ)_3 \cdot CH_3CN$ at 180-190 K was observed and is attributed to the structural variations and charge fluctuations of the TCNQ stacks as evidenced by detailed temperature dependent X-ray crystallography, magnetic and electrical conductivity studies. Furtherly, we expanded the π system of the terpy ligand to incorporate an additional pyridyl ring to form the salts $[Co(pyterpy)_2](TCNQ)_2 \cdot$ solvents (pyterpy = 4'-(4'''-pyridyl)- 2,2':6',2''-terpyridine) and studied the effect of supramolecular stacking interactions of $TCNQ^{\bullet-}$ radicals on the structures and SCO behavior of the Co(II) entities.[135] As the temperature decreased from 300 to 110 K, an unusual structural "breathing behavior" was observed as the Co(II) coordination sphere exhibited a contraction from the HS-LS transition with subsequent expansion due to a Jahn-Teller distortion of the LS state of Co(II). However, due to the segregation of TCNQ radicals by the pyridyl groups of the pyterpy ligands, the conductivity of this material was not very remarkably high. $[Co(pyterpy)_2](TCNQ)_2 \cdot DMF \cdot MeOH$ (pyterpy = 4'-(4'''-pyridyl)- 2,2':6',2''-terpyridine) and its isostructural solvate $[Co(pyterpy)_2](TCNQ)_2 \cdot MeCN \cdot MeOH$ were isolated and investigated in order to probe the effect of solvent molecules on the SCO properties. The compound $[Co(pyterpy)_2](PF_6)_2$ was used as a control in this study for documenting the structural distortions and inter-molecular interactions observed in the TCNQ radical SCO materials. It was found that supramolecular π-stacking interactions exist between $TCNQ^{\bullet-}$ radicals and the aromatic pyridyl fragments of the $[Co(pyterpy)_2]^{2+}$ cations which affect the SCO events.

Experimental Section

Synthesis

The reagents terpy (2,2′;6′,2″-terpyridine, TCI america), $Co(ClO_4)_2 \cdot 6H_2O$ (Sigma-Aldrich) and the solvents THF (tetrahydrafuran, reagent grade, Alfa Aesar), acetonitrile (reagent grade, Sigma-Aldrich), N,N-dimethylformamide (reagent grade, Sigma-Aldrich) were used as received without further purification. The starting materials LiTCNQ, $(Et_3NH)(TCNQ)_2$, pyterpy and $Co(terpy)_2(ClO_4)_2 \cdot 0.5H_2O$ were synthesized according to the literature.[25,136,137] The starting material $[Co(pyterpy)_2](ClO_4)_2$ was prepared by a modified procedure from the literature.[138] Caution! Perchlorates are potentially explosive and should be handled very carefully in small amounts. Avoid heat, drying and grinding.

$(Et_3NH)(TCNQ)_2$. A solution of 1.4 g (4.9 mmol) of TCNQ in 150 mL of THF was refluxed and 0.38 mL (2.7 mmol) of trimethylamine was added. The solution turned dark green immediately and was stirred for 3 hours. The resulting solution was left to stand at room temperature overnight. Dark green black crystals were collected by filtration and washed with THF. Yield 0.45 g (65% based on TCNQ).

$[Co(terpy)_2](TCNQ)_3 \cdot CH_3CN$. A solution of $(Et_3NH)(TCNQ)_2$ (0.15 mmol) in MeCN (9 mL) was added to a solution of $Co(terpy)_2(ClO_4)_2 \cdot 0.5H_2O$ (0.1 mmol) in MeCN (2 mL). After several minutes, X-ray quality dark blue needles of **1** had already formed. The product was separated by filtration after 30 minutes. Yield 50.7 mg (45%). Elemental analysis: calculated (%) for $Co_1C_{66}N_{18}H_{34} \cdot CH_3CN$: C(69.27), H(3.16),

N(22.57); found: C(69.15), H(3.64), N(22.43). IR: Nujol mulls on KBr plates: ν(CN) 2200.1, 2171.1 and 2152.3 cm^{-1}, δ(C-H, TCNQ) 834.0 and 823.7 cm^{-1}.

$[Co(pyterpy)_2](ClO_4)_2$. $Co(ClO_4)_2 \cdot 6H_2O$ (0.6 mmol, 0.220 g) was dissolved in 9 mL of MeCN:H_2O (v:v = 1:2) solvent. A suspension of pyterpy (1.2 mmol, 0.352 g) in 5 mL of MeCN was slowly added to the solution to yield a dark red suspension. After stirring for 2 hours at room temperature, 5 mL H_2O was added. The reaction mixture was concentrated to ~10 mL by evaporation in air. The precipitate was collected by filtration, washed with water and dried in air to obtain 0.40 g (76% yield) of red powder.

$[Co(pyterpy)_2](PF_6)_2 \cdot H_2O$. A suspension of pyterpy (1 mmol, 0.310 g) in 5 mL of MeCN: MeOH (v:v = 4:1) was added into a solution of $Co(OAc)_2 \cdot 4H_2O$ (0.5 mmol, 0.125g) in 5 mL of methanol. The color of the solution turned dark red, and after stirring for 2 hours, 10 mL of an aqueous solution of KPF_6 (1.5 mmol, 0.277g) was added and the mixture was stirred for another hour. The precipitate was collected by filtration, washed with water and dried in air to afford 0.39 g (79% yield) of red-orange product. Elemental analysis: calculated (%) for $C_{40}H_{28}CoN_8P_2F_{12} \cdot H_2O$: C(48.65), H(3.06), N(11.35); found: C(48.83), H(2.99), N(11.36).

$[Co(pyterpy)_2](PF_6)_2$. Red crystals of solvent free $[Co(pyterpy)_2](PF_6)_2$ were obtained by diffusing diethyl ether vapor into a DMF solution of $[Co(pyterpy)_2](PF_6)_2 \cdot H_2O$. The phase purity of the freshly prepared bulk crystalline powder was verified by powder X-ray diffraction. See Table 6 for single crystal X-ray crystallography data.

$[Co(pyterpy)_2](TCNQ)_2 \cdot DMF \cdot MeOH$. $[Co(pyterpy)_2](PF_6)_2 \bullet H_2O$ (0.1 mmol, 97mg) in 2 mL of DMF:MeOH (v:v = 1:1) was layered with LiTCNQ (0.20 mmol, 42.2mg) in 4 mL of MeOH in a 3 dram vial. After the solution had been left undisturbed for 30 minutes, 71 mg of dark purple crystals were collected by filtration (34% yield). The phase purity of the freshly prepared bulk crystalline powder was verified by powder X-ray diffraction. See Table 1 for variable temperature single crystal X-ray crystallography data. After standing in air, the fresh sample tended to partially lose methanol and pick up water. Elemental analysis: calculated (%) for $C_{64}H_{36}CoN_{16} \cdot 0.75CH_3OH \cdot DMF \cdot 1.85H_2O$: C(66.78), H(4.11), N(19.54); found: C(66.61), H(3.97), N(19.71). IR: Nujol mulls on KBr plates: ν(OH) 3369.7 cm^{-1}, ν(CN) 2196.1, 2178.6 and 2165.9 cm^{-1}, δ(C-H, TCNQ) 822.9 cm^{-1}.

$[Co(pyterpy)_2](TCNQ)_2 \cdot MeCN \cdot MeOH$. A sample of $[Co(pyterpy)_2](ClO_4)_2$ (0.10 mmol, 87.7mg) was dissolved in 10 mL of a MeCN:MeOH (v:v = 4:1) mixture, filtered and then slowly treated with a solution of $(Et_3NH)(TCNQ)_2$ (0.10 mmol, 50 mg) in 5mL acetonitrile. After standing for 30 minutes, the reaction mixture was filtered to obtain 40 mg of dark purple crystals (61% yield). IR: Nujol mulls on KBr plates: ν(OH) 3372.4 cm^{-1}, ν(CN) 2195.1, 2178.6 and 2165.9 cm^{-1}, δ(C-H, TCNQ) 822.9 cm^{-1}. The phase purity of the freshly prepared bulk crystalline powder was verified by powder X-ray diffraction. Crystal Data for $C_{67}H_{43}CoN_{17}O$ (M =1161.11 g/mol): triclinic, space group P-1 (no. 2), a = 8.939(3) Å, b = 13.632(5) Å, c = 24.204(8) Å, α = 76.313(4)°, β = 81.950(4)°, γ = 87.007(4) °, V = 2836.8(16) Å3, Z = 2, T = 110.15 K, μ(MoKα) = 0.365 mm^{-1}, D_{calc} = 1.359 g/cm^3, 26219 reflections measured ($3.076° \leq 2\Theta \leq 48.81°$), 9330

unique (R_{int} = 0.1068, R_{sigma} = 0.0951) which were used in all calculations. The final R_1 was 0.0502 ($I > 2\sigma(I)$) and wR_2 was 0.1254 (all data).

Magnetic and conductivity measurements

Magnetic measurements were carried out using a Quantum design MPMS-XL SQUID instrument over the temperature range 2-390K. The diamagnetic contributions of the atoms and sample holders were accounted for during the data analysis process by using Pascal's constants.

A standard four-probe method was used to measure the resistivity with gold wires attached to the thin needle-like single crystals using gold paste. The measurements have been carried out on multiple samples and the general profile of temperature dependent conductivity is exemplified by the data in Figure 25b. The temperature was controlled by using the cryrogenics of a SQUID MPMS instrument at a rate of 2 K/min and stablized at each point for 60 s before the next measurement was made to allow for thermal equilibrium of the samples. For the $Co(pyterpy)_2]^{2+}$ compounds, single crystal conductivity measurements were performed by the two-probe method on the MPMS-XL SQUID magnetometer over the temperature range of 100-300K with a constant current source.

Single crystal X-ray crystallography

Single-crystal X-ray data were collected at different temperatures on a Bruker APEX CCD diffractometer equipped with a graphite monochormated MoKα radiation source (λ=0.71073 Å). Suitable crystals were affixed onto a nylon loop with paratone oil and place in a cold steam of N_2(g). The data sets were recorded by the ω-scan mehod

and integrated followed by an absorption correction in the Bruker APEX II software package. Solution and refinement of the crystal structures were carried out using the SHELXT[139] and SHELXL[140] programs and the graphical interface Olex2.[141] Hydrogen atoms were placed at calculated positions. A summary of pertinent information relating to unit cell parameters are provided in Table 2, Table 6 and Table 8. CCDC 1403742-1403750, 1049086-1049089, 1426087-1426088 contain the supplementary crystallographic data for this paper. These data can be obtained free of charge from The Cambridge Crystallographic Data Centre via www.ccdc.cam.ac.uk/data_request/cif.

Powder X-ray diffraction

Powder X-ray diffraction experiments were carried out on a Bruker D8 powder X-ray diffractometer. Phase purity of the bulk products were confirmed by the powder X-ray diffraction patterns in comparison with the simulated powder patterns obtained from the single crystal X-ray structural data. $[Co(pyterpy)_2](TCNQ)_2 \bullet DMF \bullet CH_3OH$ has also been confirmed to be isostructural with $[Co(pyterpy)_2](TCNQ)_2 \bullet CH_3CN \bullet CH_3OH$ as their powder XRD patterns matched quite well.

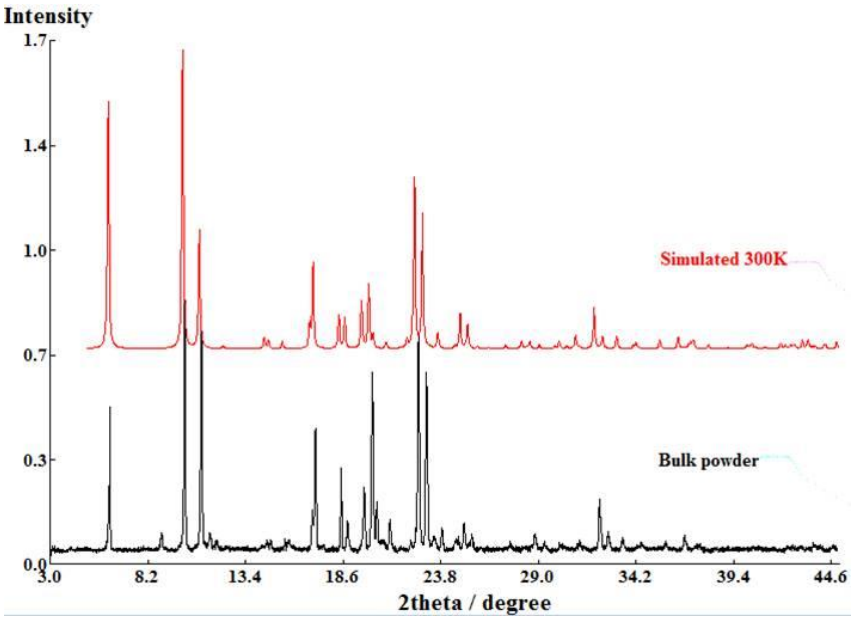

Figure 16. Bulk powder and simulated powder X-ray diffraction patterns of $[Co(terpy)](PF_6)_2$.

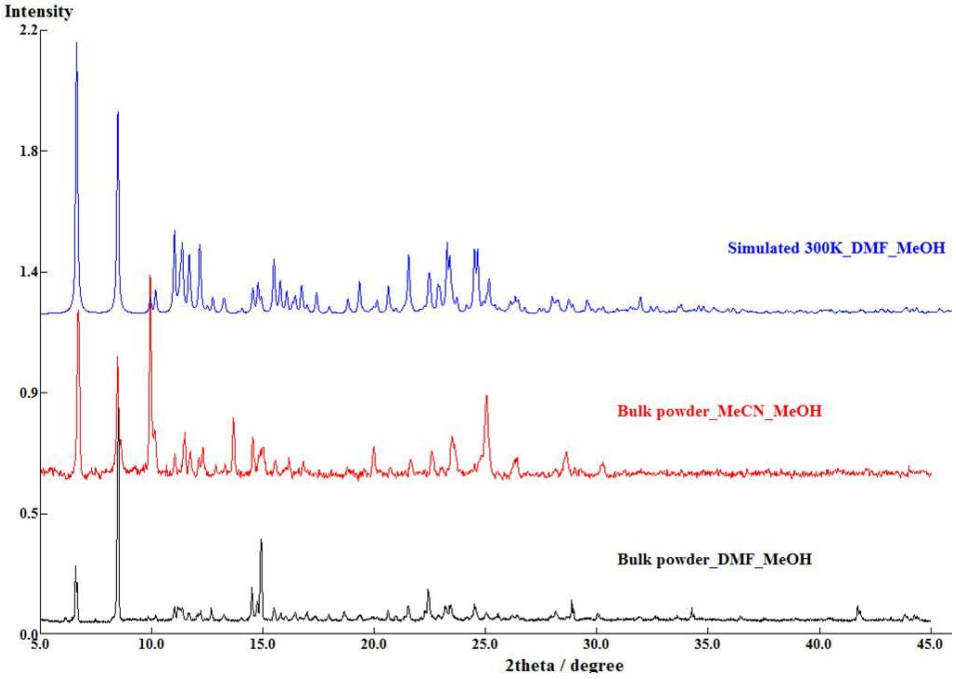

Figure 17. Overlay of the powder X-ray diffraction patterns of simulated $[Co(pyterpy)_2](TCNQ)_2 \bullet DMF \bullet CH_3OH$ (blue), bulk powder of $[Co(pyterpy)_2](TCNQ)_2 \bullet CH_3CN \bullet CH_3OH$ (red) and bulk powder of $[Co(pyterpy)_2](TCNQ)_2 \bullet DMF \bullet CH_3OH$ (black) at 300 K.

Results and Discussions

Sythesis and preparation

In the literature, two types of materials have been synthesized for the coexistence of SCO and electrical conductivity. The first examples are amorphous polymers consisting of SCO coordination polymers in conducting organic polymers such as polycarbonate and doped polypyrrole. The advantage of this amorphous material is its facile synthetic procedures as compared to the second type, which is a crystalline material prepared by the co-crystallization of SCO complexes and organic or metal-organic radicals. In order to achieve significant conductivity, howeverm charge delocalization needs to be optimized. Two general strategies have been employed for the oxidation of the monoanion radicals to partially charged anion radicals in the literature, namely galvanostatic oxidation of the anion radicals and comproportionation of the anion radicals and neutral acceptors. In this work, we have developed a new strategy that helps to combine the facile synthesis of the heterostructures and the crystallinity of the co-crystals by using a solution process that leads to crystallization in a matter of minutes.

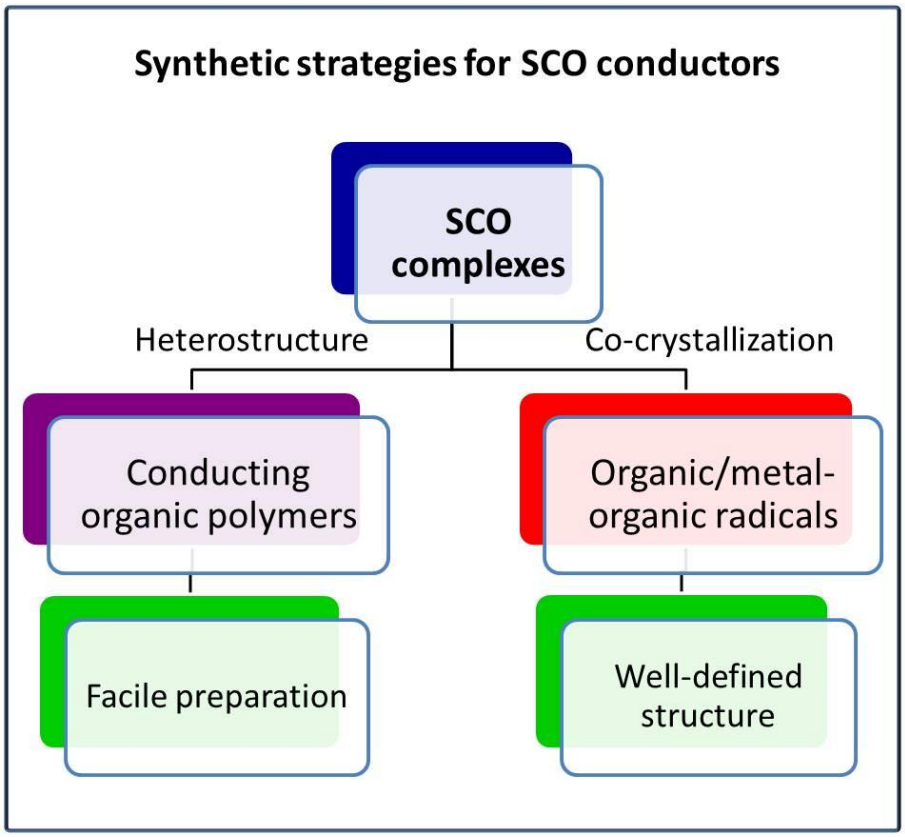

Figure 18. Two general synthetic schemes of the bifunctional SCO conductors.

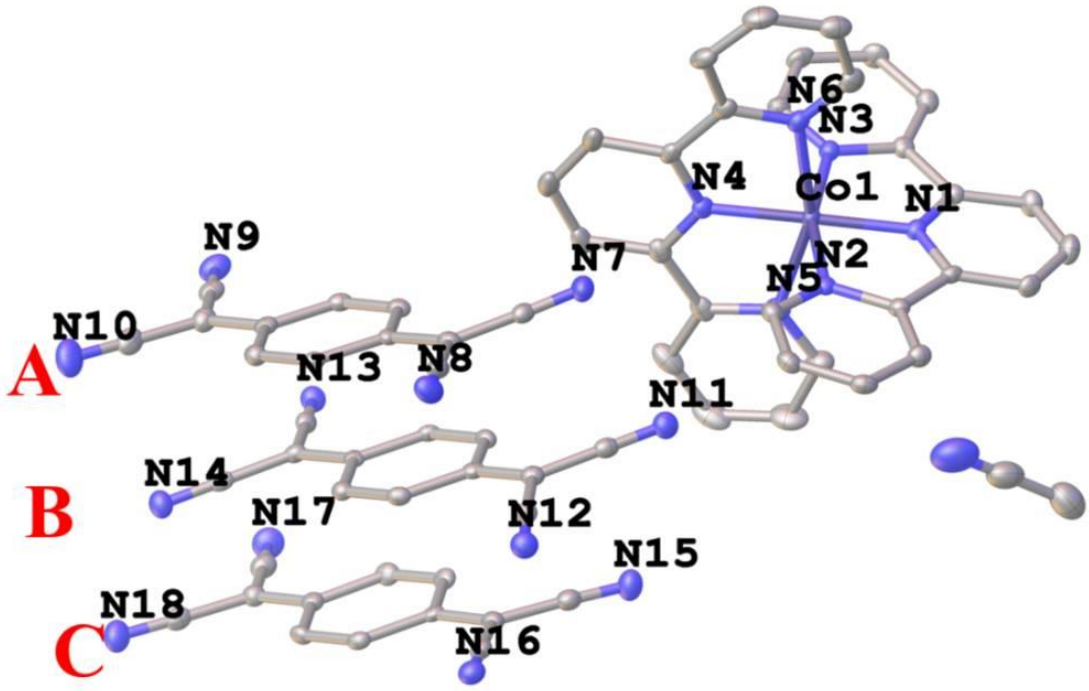

Figure 19. The asymmetric unit of the crystal structure of $[Co(terpy)_2](TCNQ)_3 \bullet CH_3CN$ with the thermal ellipsoids drawn at the 50% probability level. Hydrogen atoms are omitted for the sake of clarity.

A facile metathesis reaction between $[Co(terpy)_2](ClO_4)_2 \bullet 0.5H_2O$ and the mixed-valence salt $[Et_3NH](TCNQ)_2$ in acetonitrile produces dark blue/purple thin needle crystals of $[Co(terpy)_2](TCNQ)_3 \bullet CH_3CN$ over the course of several minutes. Variable temperature single crystal X-ray studies revealed that the structure of $[Co(terpy)_2](TCNQ)_3 \bullet CH_3CN$ remains in the non-centrosymmetric space group *Pna2₁* over the temperature range T = 300, 190, 180, 150, 130 and 100 K (Table 2). The asymmetric unit of the structure is composed of one $[Co(terpy)_2]^{2+}$ cation, three TCNQ moieties and one free acetonitrile molecule (Figure 19). The octahedral coordination environment of Co(II) is distorted in such a manner that the metal center is closer to one

of the terpy ligands (N1N2N3) than the other one (N4N5N6). This is evidenced by the shorter bond distances of Co-N1 (1.867(3) Å), Co-N3 (1.980(4) Å), and Co-N2 (1.978(4) Å) than those of Co-N4 (1.920(3) Å), Co-N5 (2.153(4) Å) and Co-N6 (2.162(3) Å), as well as the larger bond angle of N2-Co-N3 (163.4(1) °) than that of N5-Co-N6 (158.0(1) °) (100 K, Figure 20 and Table 3). The Co-N1 bond distance is relatively short as compared to those in other LS Co(II) compounds, which is attributed to a strain effect and a stronger Jahn-Teller distortion exerted by the crystal packing effects.[29,112,142] As the temperature decreases from 300 K, the Co-N bond lengths do not exhibit a significant decrease until 190 K, which is most likely due to dynamic disorder of HS and LS Co(II) entities.[29] From 190 to 180 K, when the dynamic disorder diminishes and Co(II) ions are all in the LS state (*vide infra*), an obvious decrease in the Co-N bond distances was observed (Figure 23a). From 180 to 150 K, four of the Co-N (N1, 4, 5, 6) bonds exhibit an unusual elongation (Figure 23a) instead of a contraction, which is ascribed to the Jahn-Teller distortion of the ^{2}E state of LS Co(II) ions. This unusual structural "breathing" behavior is also transmitted to the macro-scale as evidenced by a similar trend in all three unit cell axes and the unit cell volume variations (Figure 23b) upon thermal fluctuation.

Table 2. Pertinent crystallographic data for $[Co(terpy)_2](TCNQ)_3 \bullet CH_3CN$ at different temperatures.

Temperature	100 K	130 K	150 K	180 K	190 K	300 K
Empirical formula	$C_{68}H_{37}CoN_{19}$	$C_{68}H_{37}N_{19}Co$	$C_{68}H_{37}N_{19}Co$	$C_{68}H_{37}CoN_{19}$	$C_{68}H_{37}CoN_{19}$	$C_{68}CoN_{19}H_{37}$
Formula weight	1179.09	1179.09	1179.09	1179.09	1179.09	1179.09
Temperature/K	100	130	150	180	190	300
Crystal system	orthorhombic	orthorhombic	orthorhombic	orthorhombic	orthorhombic	orthorhombic
Space group	$Pna2_1$	$Pna2_1$	$Pna2_1$	$Pna2_1$	$Pna2_1$	$Pna2_1$
a/Å	18.9411(10)	18.967(3)	19.087(7)	18.969(6)	19.074(6)	19.2853(15)
b/Å	8.6917(4)	8.6864(12)	8.742(3)	8.681(3)	8.705(3)	8.7270(7)
c/Å	33.5158(17)	33.532(5)	33.634(12)	33.397(10)	33.611(10)	33.589(3)
α/°	90	90	90	90	90	90
β/°	90	90	90	90	90	90
γ/°	90	90	90	90	90	90
Volume/$Å^3$	5517.7(5)	5524.8(13)	5613(3)	5499(3)	5581(3)	5653.1(8)
Z	4	4	4	4	4	4
$\rho_{calc}g/cm^3$	1.419	1.418	1.395	1.424	1.403	1.385
μ/mm^{-1}	0.376	0.376	0.370	0.377	0.372	0.367
F(000)	2420.0	2420.0	2420.0	2420.0	2420.0	2420.0

Table 2. Continued.

Temperature	100 K	130 K	150 K	180 K	190 K	300 K
Crystal size/mm^3	0.149 × 0.038 × 0.02	0.25 × 0.15 × 0.008	0.31 × 0.06 × 0.008	0.25 × 0.15 × 0.008	0.3 × 0.12 × 0.008	0.237 × 0.035 × 0.015
Radiation	Synchrotron (λ = 0.41328 Å)	MoKα (λ = 0.71073)	MoKα (λ = 0.71073 Å)	MoKα (λ = 0.71073)	MoKα (λ = 0.71073)	Synchrotron (λ = 0.51800 Å)
2Θ range for data collection/ °	4.3 to 58.26	4.294 to 52.044	4.268 to 49.708	2.438 to 53.008	4.27 to 52.042	2.424 to 52.798
Index ranges	-25 ≤ h ≤ 25, -11 ≤ k ≤ 7, -45 ≤ l ≤ 45	-23 ≤ h ≤ 23, -10 ≤ k ≤ 10, -41 ≤ l ≤ 41	-22 ≤ h ≤ 22, -10 ≤ k ≤ 10, -39 ≤ l ≤ 39	-23 ≤ h ≤ 23, -10 ≤ k ≤ 10, -41 ≤ l ≤ 41	-23 ≤ h ≤ 23, -10 ≤ k ≤ 10, -41 ≤ l ≤ 41	-24 ≤ h ≤ 24, -10 ≤ k ≤ 6, -41 ≤ l ≤ 42
Reflections collected	77611	54108	50404	56984	55562	73630
Independent reflections	14467 [R_{int} = 0.1046, R_{sigma} = 0.1007]	10889 [R_{int} = 0.1147, R_{sigma} = 0.1092]	9665 [R_{int} = 0.1488, R_{sigma} = 0.1256]	11364 [R_{int} = 0.1606, R_{sigma} = 0.1625]	11002 [R_{int} = 0.0928, R_{sigma} = 0.0735]	11144 [R_{int} = 0.1130, R_{sigma} = 0.0977]

Table 2. Continued.

Temperature	100 K	130 K	150 K	180 K	190 K	300 K
Data/restraints/ parameters	14467/1/795	10889/1/795	9665/1/795	11364/1/795	11002/1/795	11144/1/795
Goodness-of-fit on F^2	1.010	0.872	0.864	0.845	1.018	1.044
Final R indexes [I>=2σ (I)]	R_1 = 0.0507, wR_2 = 0.1083	R_1 = 0.0451, wR_2 = 0.0783	R_1 = 0.0450, wR_2 = 0.0713	R_1 = 0.0508, wR_2 = 0.0868	R_1 = 0.0475, wR_2 = 0.0710	R_1 = 0.0482, wR_2 = 0.1173
Final R indexes [all data]	R_1 = 0.0796, wR_2 = 0.1243	R_1 = 0.0854, wR_2 = 0.0888	R_1 = 0.0838, wR_2 = 0.0817	R_1 = 0.1258, wR_2 = 0.1240	R_1 = 0.0799, wR_2 = 0.0829	R_1 = 0.0757, wR_2 = 0.1483
Largest diff. peak/hole / e $Å^{-3}$	0.49/-0.59	0.32/-0.59	0.22/-0.43	0.29/-0.30	0.23/-0.36	0.60/-0.53
Flack parameter	0.486(16)	0.437(18)	0.370(19)	0.38(2)	0.489(18)	0.46(2)

$R_1 = \Sigma||F_o| - |F_c||/ \Sigma|F_o|$. $wR_2 = [\Sigma w(|F_o| - |F_c|)^2/|\Sigma w(F_o)^2]^{1/2}$. $w = 0.75/(\sigma^2(F_o)+0.00010F_o^2)$.

Table 3. Co-N bond distances (in Å) of $[Co(terpy)_2](TCNQ)_3 \bullet CH_3CN$ at different temperatures.

Temperature	100 K	130 K	150 K	180 K	190 K	300 K
Co1-N1	1.867(3)	1.862(4)	1.874(5)	1.862(6)	1.868(4)	1.878(5)
Co1-N3	1.980(4)	1.975(4)	1.981(5)	1.983(6)	1.989(4)	2.001(5)
Co1-N2	1.978(4)	1.969(4)	1.982(5)	1.982(6)	1.991(4)	2.000(5)
Co1-N4	1.920(3)	1.923(4)	1.921(5)	1.910(6)	1.921(4)	1.909(5)
Co1-N5	2.153(4)	2.149(5)	2.151(5)	2.135(7)	2.149(4)	2.131(5)
Co1-N6	2.162(3)	2.154(4)	2.163(5)	2.145(6)	2.142(4)	2.141(4)

Table 4. Selected bond angles (in degree) in the Co(II) coordination sphere of $[Co(terpy)_2](TCNQ)_3 \bullet CH_3CN$ at different temperatures.

Temperature	100 K	130 K	150 K	180 K	190 K	300 K
N1-Co1-N2	81.53(15)	81.35(19)	81.61(19)	81.0(3)	81.79(17)	80.92(19)
N1-Co1-N3	81.99(15)	81.79(18)	81.7(2)	81.7(3)	81.24(17)	81.42(19)
N2-Co1-N3	163.36(13)	163.02(17)	163.24(19)	162.5(2)	162.94(16)	162.26(18)
N4-Co1-N5	79.19(15)	79.49(18)	79.5(2)	79.2(3)	78.91(19)	79.1(2)
N4-Co1-N6	78.84(15)	78.8(2)	78.8(2)	79.3(3)	79.25(18)	78.7(2)
N5-Co1-N6	158.01(14)	158.22(18)	158.3(2)	158.5(3)	158.15(18)	157.9(2)

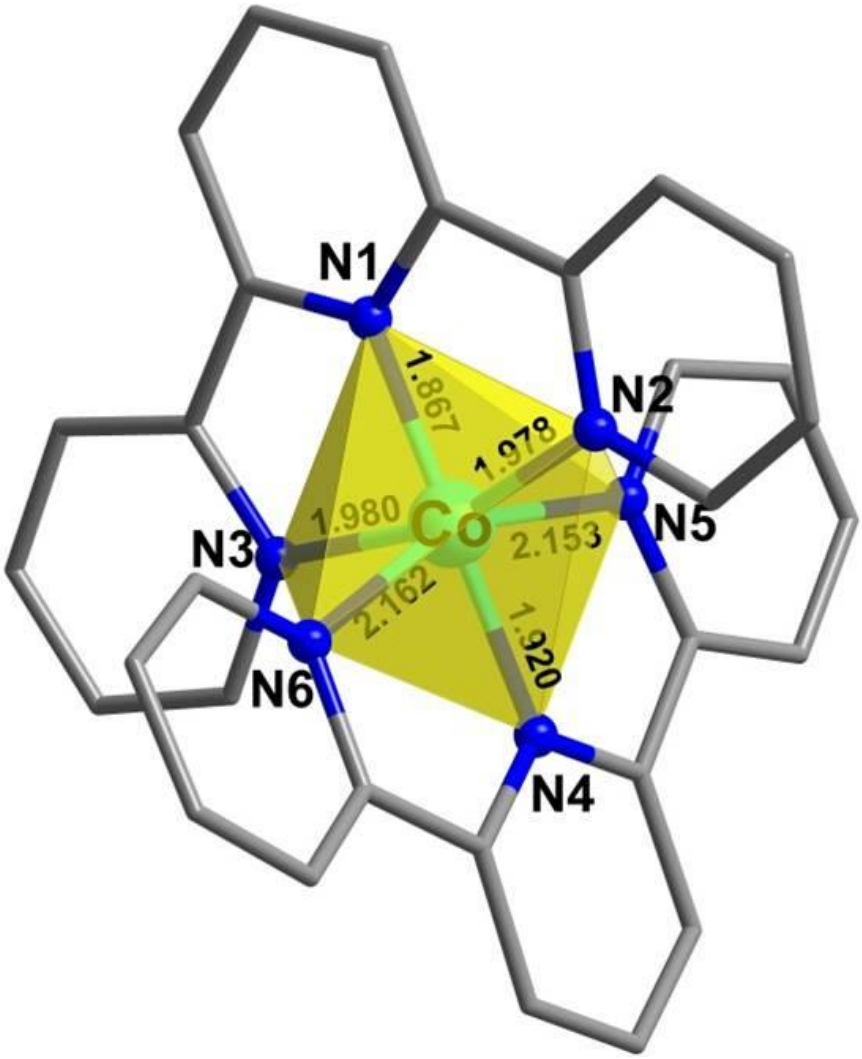

Figure 20. The coordination sphere of Co(II) in $[Co(terpy)_2](TCNQ)_3 \bullet CH_3CN$ with the Co-N bond distances measured in Å at 100 K.

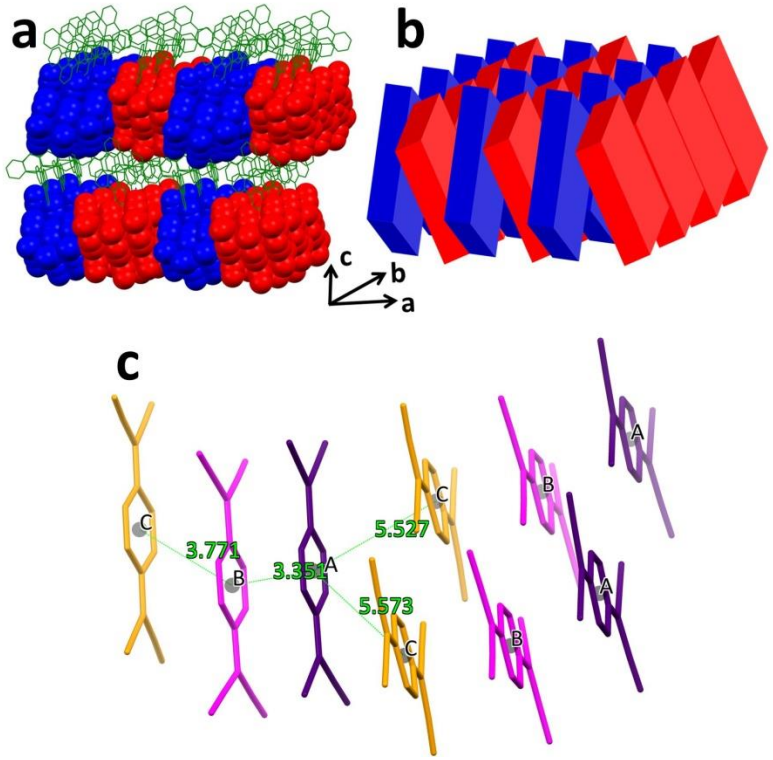

Figure 21. (a). Packing diagram of the structure of $[Co(terpy)_2](TCNQ)_3 \bullet CH_3CN$. The TCNQ triads (blue and red) are depicted in a space-filling model and the $[Co(terpy)_2]^{2+}$ cations (green) and interstitial CH_3CN molecules (black) are represented by the capped-stick models. (b). schematic presentation of the "criss-cross" pattern of the TCNQ triads. Each of the colored blocks represents one TCNQ triad. (c). Schematic representation of the *intra*- and *inter*-triad interactions at 180 K. The three distinct TCNQ species are A(purple), B(magenta) and C(orange). The centroid-centroid distances between the quinoid ring centroids of the neighboring TCNQ species are depicted in green.

The TCNQ radicals form triads (ABC as designated in Figure 19) in the structure, which are then stacked in such a manner that the adjacent triads form a hitherto unknown cross-stacking pattern of TCNQ moieties along the *a* axis, with a parallel arrangement along the *b* axis (Figure 21a and Figure 21b). At 180 K, A and B exhibit a close centroid-centroid distance of ~3.35 Å within the triad whereas the centroid-centroid distance between B and C is ~3.77 Å. The corresponding *inter*-triad distances are longer at ~5.52 and 5.57 Å (Figure 21c). The semiconducting/SCO layers

pack along the *c* axis in an alternating fashion. The stacking distances of the TCNQ units follow the same trend upon thermal perturbation as the Co-N (N1,4,5,6) bond lengths and a decrease in the centroid-centroid and shift distances from 190 to 180 K was observed (Figure 22).

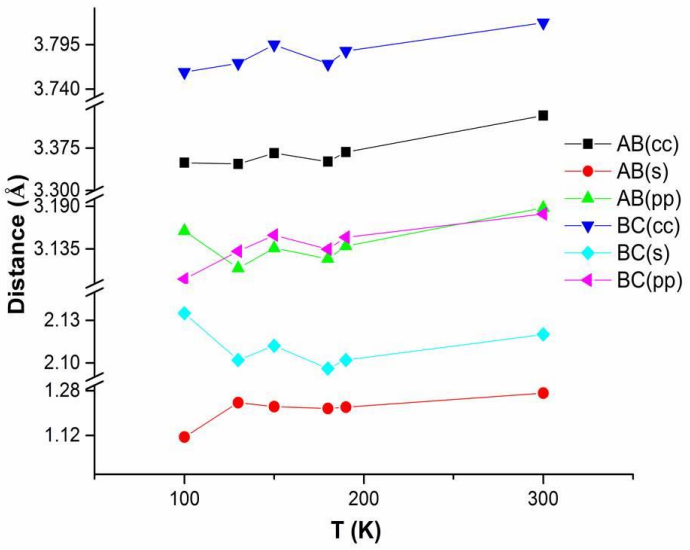

Figure 22. Temperature dependence of the π-π stacking distances of the TCNQ species in $[Co(terpy)_2](TCNQ)_3 \bullet CH_3CN$ with *cc* for centroid-centroid distances, *s* for shift distances and *pp* for plane-plane distances.

The charges on the TCNQ species have been estimated from Kistenmatcher's formula based on several signature C-C bond lengths in TCNQ (Table 5).[75] At 300 K, the negative charges on A (-1.03) and B (-0.92) are close to -1 whereas C (-0.33) is closer to the neutral form. Importantly, the charges on the different TCNQ species fluctuate as temperature changes (Figure 23c). From 190 to 180 K, the charges on A and B show a decrease toward -1 while that on C exhibits an increase toward the neutral form to result in a charge localized state of the triads.

Table 5. The charges (ρ) of different TCNQ species in $[Co(terpy)_2](TCNQ)_3 \bullet CH_3CN$ at various temperatures estimated from the Kistenmacher's formula (b, c and d are average C-C bond distances as depicted below).

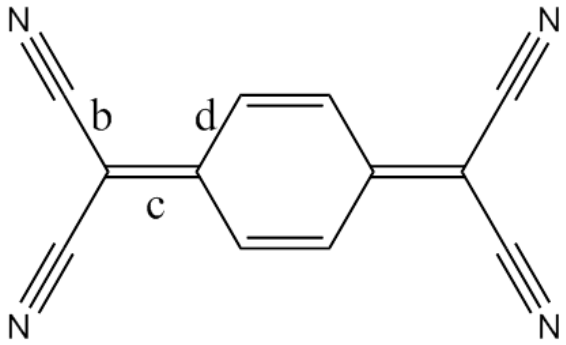

Temperature	TCNQ	b /Å	c /Å	d /Å	ρ	ρ(Triad)
100 K	A	1.424	1.423	1.420	-1.01	-2.23
	B	1.424	1.413	1.425	-0.83	
	C	1.434	1.394	1.438	-0.39	
130 K	A	1.422	1.420	1.417	-1.01	-2.05
	B	1.430	1.411	1.425	-0.76	
	C	1.437	1.388	1.437	-0.29	
150 K	A	1.427	1.420	1.427	-0.90	-1.81
	B	1.432	1.417	1.434	-0.78	
	C	1.452	1.388	1.442	-0.14	
180 K	A	1.412	1.404	1.414	-0.87	-1.90
	B	1.420	1.407	1.416	-0.84	
	C	1.428	1.373	1.429	-0.19	
190 K	A	1.427	1.410	1.419	-0.80	-1.89
	B	1.428	1.409	1.424	-0.75	
	C	1.433	1.388	1.435	-0.33	
300 K	A	1.417	1.417	1.414	-1.03	-2.27
	B	1.416	1.412	1.419	-0.92	
	C	1.433	1.385	1.429	-0.33	

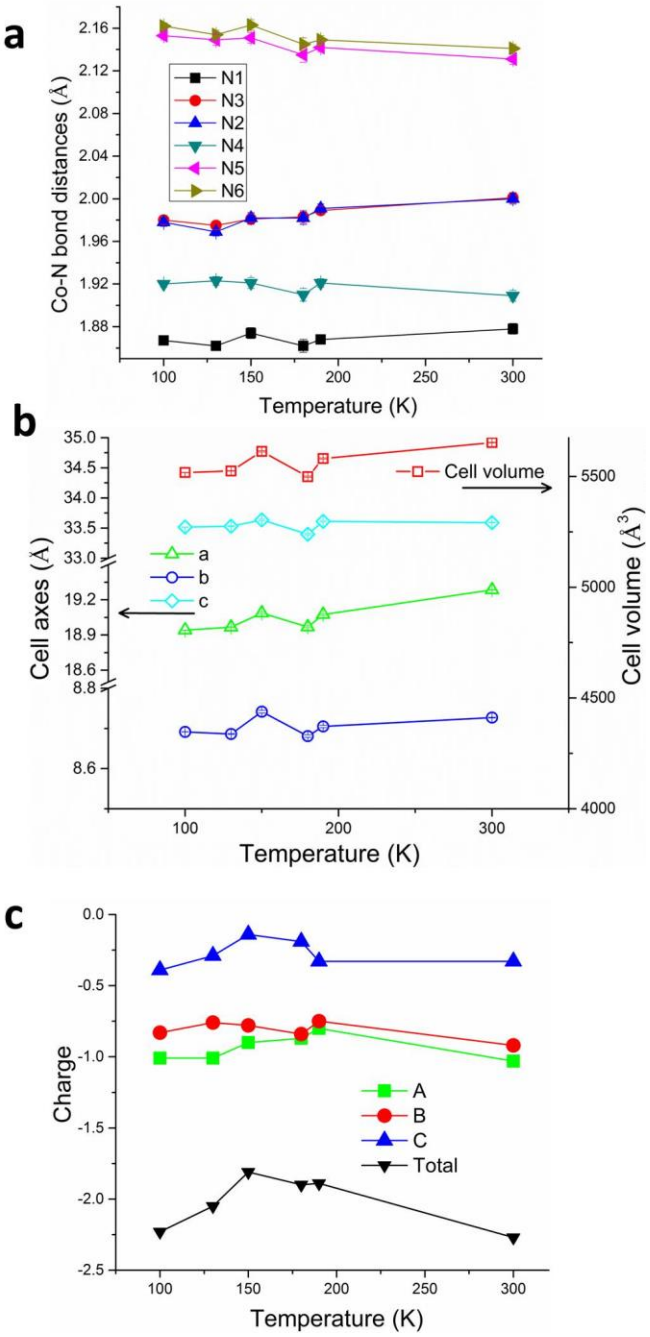

Figure 23. (a). Temperature dependence of the Co-N bond distances with corresponding error bars for compound 1. (b). Temperature dependence of the unit cell parameters and volumes with corresponding error bars of compound 1. (c). Temperature dependence of the estimated charges on individual TCNQ species (A, B, C as denoted in Figure 1) and the total charge of TCNQ triads.

Melby and coworkers reported that the charges of the TCNQ species in $[Et_3NH](TCNQ)_2$ are delocalized in the solid state. In solution, the salt dissociates into TCNQ and $TCNQ^{\bullet-}$.[136] Therefore, when employed as a starting material for the current study, $[Et_3NH](TCNQ)_2$ serves as a single source of both neutral and -1 charged TCNQ species for the triads $[(TCNQ)(TCNQ^{\bullet-})_2]^{2-}$ with two of the TCNQ charges (A and B) being close to -1 and that of the third one (C) being nearly 0. A delocalized state is observed in the solid state of **1** close to room temperature.

The temperature dependent magnetic susceptibility of **1** was measured under a 1000 Oe DC magnetic field for T = 2 - 390 K (Figure 25a). A typical Co(II) gradual SCO occurs,[135,143,144] with $\chi_M T$ gradually decreasing from 1.02 emu K mol^{-1} at 390 K to 0.41 emu K mol^{-1} at 2 K. Even at 390 K the HS state is not fully populated, as the expected $\chi_M T$ value for isolated spin-only HS Co(II) centers is ~1.88 emu K mol^{-1}. The $\chi_M T$ value at 190-180 K indicates that the Co(II) is almost all in the LS state. The TCNQ radicals give rise to a negligible contribution to the magnetic susceptibility which is typical of TCNQ materials due to radical dimerization.[131,133,145] No thermal hysteresis was observed in the SCO behavior.

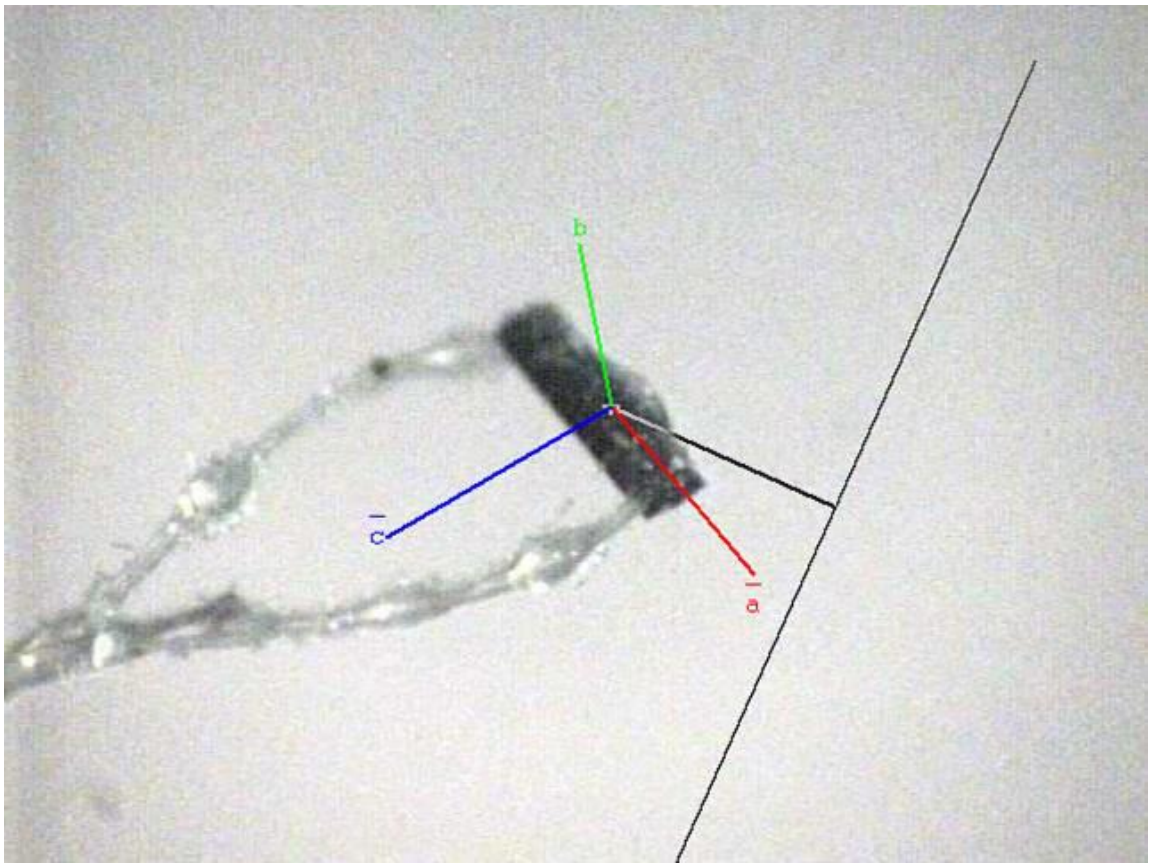

Figure 24. Face index of a single crystal of $[Co(terpy)_2](TCNQ)_3 \bullet CH_3CN$. The long direction of the thin needle crystals is along the stacking direction (a axis) of the TCNQ triads.

The temperature dependence of the electrical conductivity of compound **1** was measured on single crystals using the standard four-probe method[146] along the *a* axis (the TCNQ triad stacking direction, Figure 24) over the temperature range of 50-300 K. As is expected for partially charged radical stacks of TCNQ,[80,147,148] compound **1** exhibits a high room temperature conductivity of 0.13 S cm^{-1} and behaves as a semiconductor between 300 and ~195 K with an activation energy of 0.47 eV (Figure 25b and Figure 26).

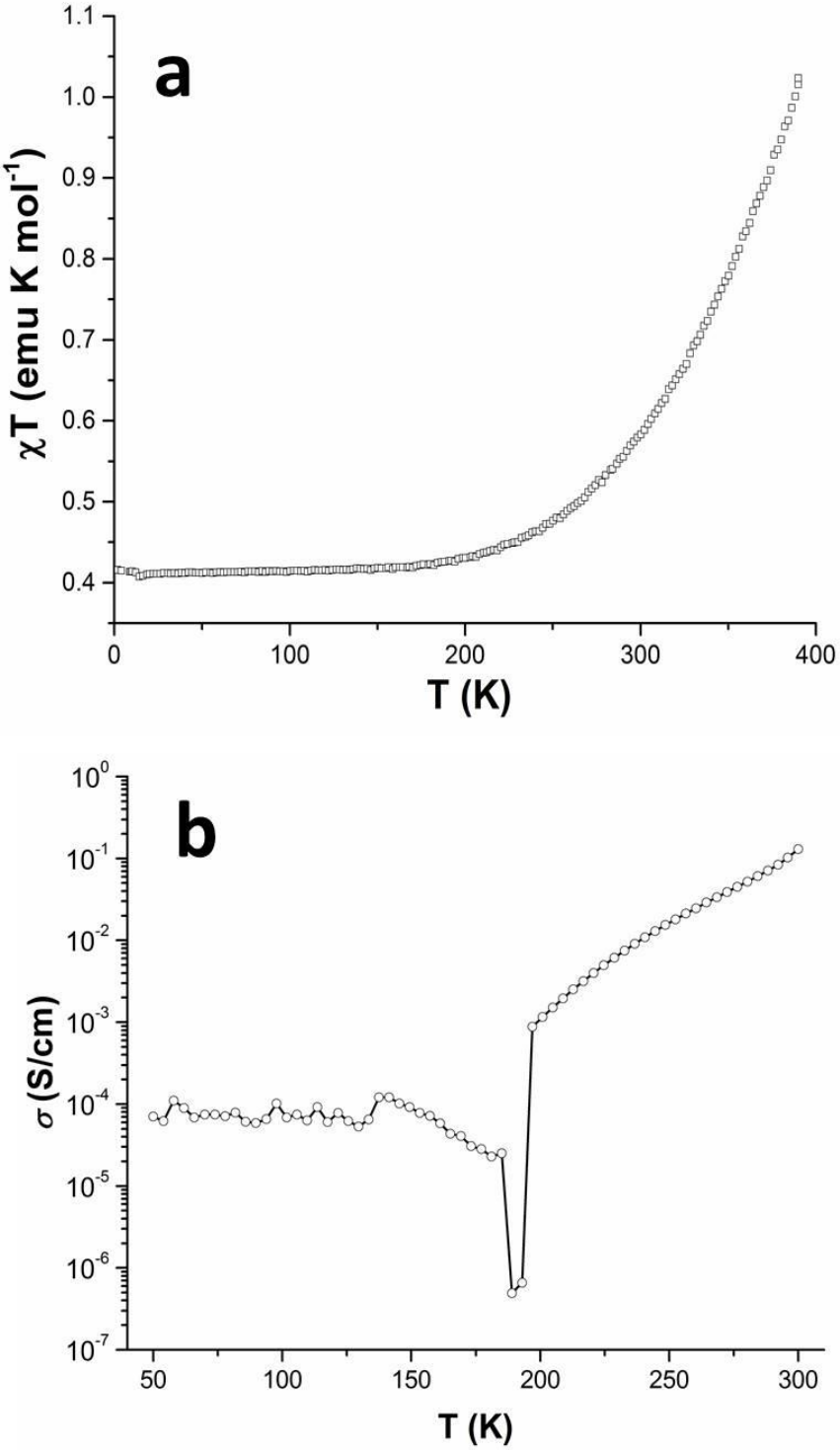

Figure 25. Temperature dependence of the (a) molar magnetic susceptibility χT product and (b) electrical conductivity of compound 1.

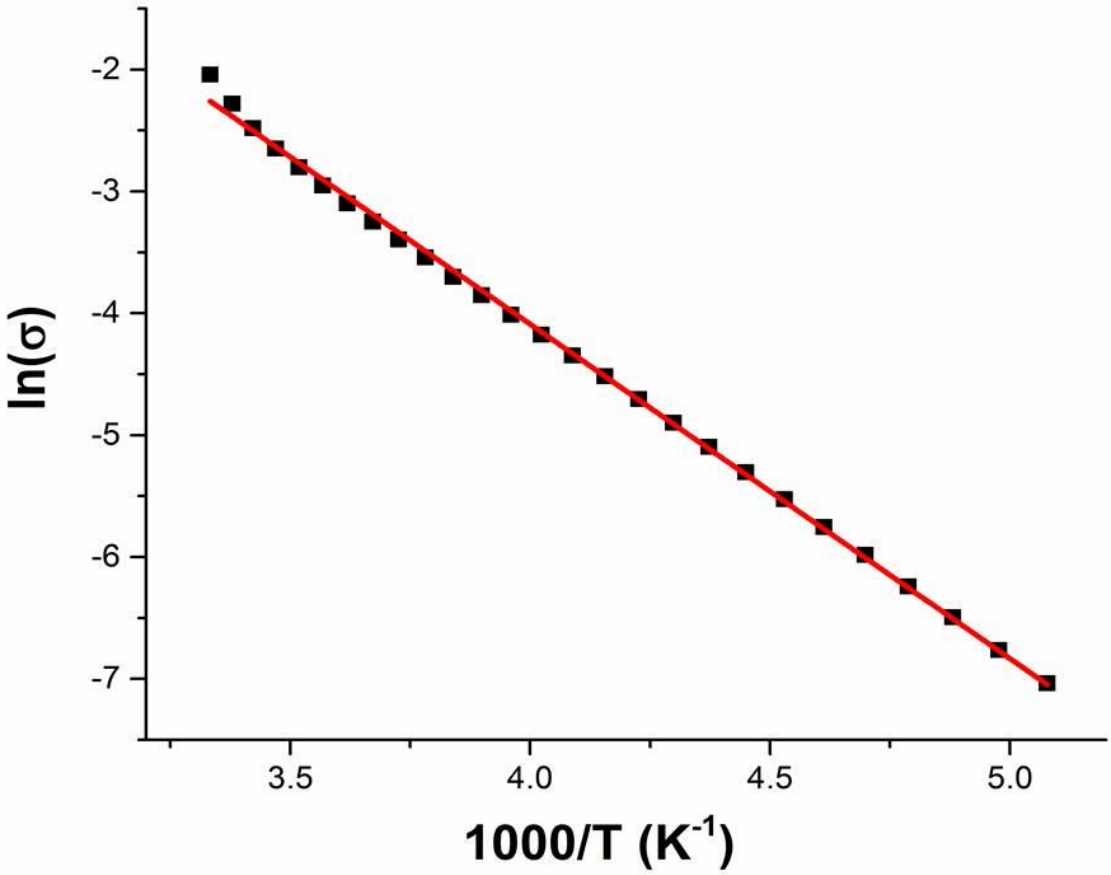

Figure 26. Arrhenius plot of the conductivity data from 195 to 300 K (the red line is a linear fit of the data).

What is most striking, however, is that the conductivity exhibits an unprecedented anomaly with a dip to ~4.9 × 10^{-7} S cm^{-1} at ~180 K from ~8.8 × 10^{-4} S cm^{-1} at ~190 K (Figure 25b). This anomaly at 180-190 K is attributed to a combination of the TCNQ radical stacking distance variations (Figure 22) and charge fluctuations (Figure 23c) as the temperature decreases from 190 to 180 K. The decrease in the TCNQ stacking distances from 190 to 180 K is correlated to the decrease in Co-N bond distances as well as to a possible Peierls distortion.[149] At the same time, the charge fluctuations of the TCNQ species result in a charge localized state of the TCNQ triads

($[(TCNQ)(TCNQ^{\bullet -})_2]^{2-}$) at 180 K that also contributes to the decrease in conductivity, as the charges on A and B become close to -1 and C is in the neutral form (*vide supra).* Below 150 K, the conductivity becomes nearly independent of temperature until 50 K which is also likely a result of the Peierls state but with slightly larger stacking distances than those at 180 K. Apart from the stacking interactions of the TCNQ moieties within the triads, the cross-stacking pattern of the TCNQ triads is also likely to be important for the conducting behavior as it disrupts continuous overlap of the frontier orbitals and at the same time minimizes Coulomb repulsion between adjacent triads. Obviously, a precise understanding of the role of the inter-triad interactions for charge transport requires in-depth theoretical studies.

Variable temperature single crystal X-ray studies

$[Co(pyterpy)_2](PF_6)_2$. Variable temperature single-crystal X-ray crystallography is a powerful tool for the investigation of structure-property relationships in SCO materials due to the fact that the metal-ligand bond distances in these "breathing" materials go through distinct changes with thermal perturbation.[150,151]

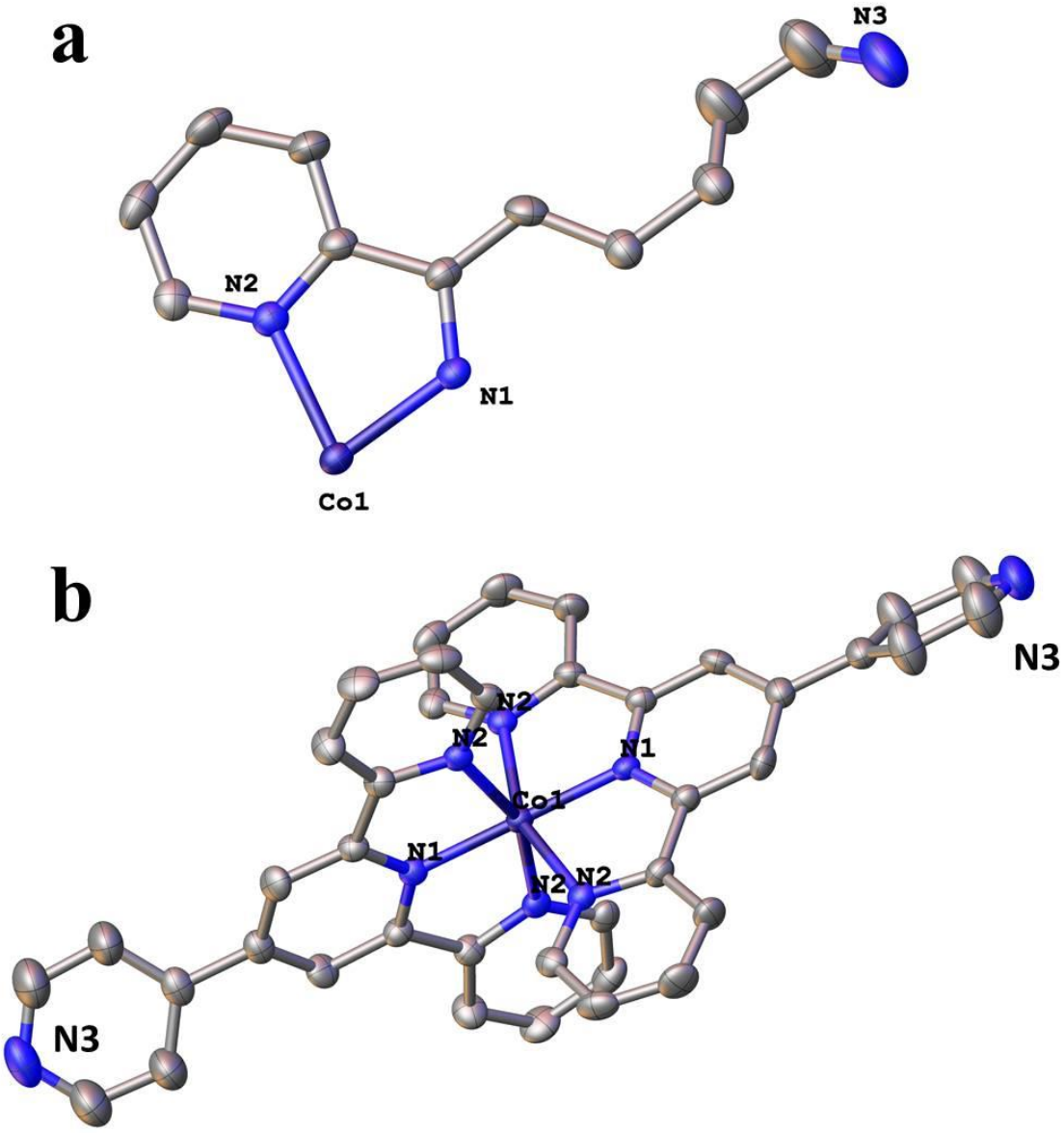

Figure 27. Asymmetric unit (a) and the cationic part (b) of the crystal structure of $[Co(pyterpy)_2](PF_6)_2$ with thermal ellipsoids drawn at the 50% probability level. The disordered $[PF_6]^-$ anions and the hydrogen atoms are omitted for the sake of clarity.

Single crystal X-ray diffraction studies reveal that $[Co(pyterpy)_2](PF_6)_2$ crystallizes in the tetragonal space group $I4_1/a$ and with an asymmetric unit composed of one-quarter of a $[Co(pyterpy)_2]^{2+}$ cation and one-half of a $[PF_6]^-$ anion (Figure 27). Variable temperature single crystal X-ray studies reveal that the space group remains the same at the temperatures 110, 150 180 and 300 K (Table 6). At 110 K, the Co(II) ion is in a compressed octahedral environment with short axial Co-N1 bond distances of 1.923(5) Å, elongated equatorial Co-(N2) distances of 2.101(3) Å and N1-Co1-N2 bond angles of 78.9(1)°. The Co1-N1 and Co1-N2 bond distances and unit cell parameters exhibit a uniform decrease from 300 to 150 K, below which temperature they display an unusual increase at 110 K (Figure 28 and Figure 29) which is the result of a Jahn-Teller distortion of the ^2E state of LS Co(II) centers as observed before by Halcrow and coworkers in $[Co(terpy)_2](BF_4)_2$ below 100 K.[29] The typical structural breathing behavior is one breathing cycle of contraction and expansion of the metal coordination sphere with temperature completes during a full cooling and warming cycle.[151] In contrast, the structural changes in compound $[Co(pyterpy)_2](PF_6)_2$ exhibits an unusual "double breathing" phenomenon in which two cycles of contractions and expansions of the Co(II) coordination sphere are completed as the temperature goes in one full cooling and warming cycle in the range of 110-300 K.

Table 6. Pertinent crystallographic data for $[Co(pyterpy)_2](PF_6)_2$ at different temperatures.

	110 K	150 K	180 K	300 K
Empirical formula	$C_{40}H_{28}CoF_{12}N_8P_2$	$C_{40}H_{28}CoF_{12}N_8P_2$	$C_{40}H_{28}CoF_{12}N_8P_2$	$C_{40}H_{28}CoF_{12}N_8P_2$
Formula weight	969.57	969.57	969.57	969.57
Temperature/K	110.15	150.15	180.15	300.15
Crystal system	tetragonal	tetragonal	tetragonal	tetragonal
Space group	$I4_1/a$	$I4_1/a$	$I4_1/a$	I41/a
a/Å	8.785(2)	8.715(2)	8.730(4)	8.888(12)
b/Å	8.785(2)	8.715(2)	8.730(4)	8.888(12)
c/Å	57.646(13)	57.026(16)	57.00(2)	57.91(8)
α/°	90	90	90	90
β/°	90	90	90	90
γ/°	90	90	90	90
Volume/$Å^3$	4449(2)	4331(3)	4344(4)	4575(13)
Z	4	4	4	4
$\rho_{calc}g/cm^3$	1.448	1.487	1.482	1.408
μ/mm^{-1}	0.547	0.562	0.560	0.532
F(000)	1956.0	1956.0	1956.0	1956.0
Crystal size/mm^3	0.14 ×0.1 ×0.05	0.14 ×0.1 ×0.05	0.14 ×0.1 ×0.05	0.12 ×0.11 ×0.06
Radiation	MoKα (λ = 0.71073)	MoKα (λ = 0.71073)	MoKα (λ = 0.71073)	MoKα (λ = 0.71073)
2Θ range for data collection/ °	2.826 to 54.338	2.856 to 53.458	2.858 to 53.464	2.814 to 51.352
Index ranges	-11 ≤ h ≤ 11, -11 ≤ k ≤ 11, -73 ≤ l ≤ 73	-10 ≤ h ≤ 11, -10 ≤ k ≤ 11, -71 ≤ l ≤ 72	-11 ≤ h ≤ 11, -11 ≤ k ≤ 10, -72 ≤ l ≤ 71	-10 ≤ h ≤ 10, -10 ≤ k ≤ 10, -70 ≤ l ≤ 70
Reflections collected	25113	23725	23554	22459
Independent reflections	2467 [R_{int} = 0.0499, R_{sigma} = 0.0261]	2301 [R_{int} = 0.0598, R_{sigma} = 0.0313]	2314 [R_{int} = 0.0771, R_{sigma} = 0.0395]	2177 [Rint = 0.1007, Rsigma = 0.0551]
Data/restraints/parameters	2467/81/170	2301/82/160	2314/81/155	2177/81/141
Goodness-of-fit on F^2	1.509	1.153	1.858	1.928
Final R indexes [I>=2σ (I)]	R_1 = 0.0991, wR_2 = 0.3183	R_1 = 0.0997, wR_2 = 0.3001	R_1 = 0.1442, wR_2 = 0.4238	R1 = 0.1643, wR2 = 0.4576
Final R indexes [all data]	R_1 = 0.1153, wR_2 = 0.3402	R_1 = 0.1175, wR_2 = 0.3178	R_1 = 0.1663, wR_2 = 0.4372	R1 = 0.1894, wR2 = 0.4708
Largest diff. peak/hole / e $Å^{-3}$	1.41/-0.69	1.26/-0.77	1.58/-0.91	1.49/-0.82

$R_1 = \Sigma||F_o| - |F_c||/ \Sigma|F_o|$. $wR_2 = [\Sigma w(|F_o| - |F_c|)^2/|\Sigma w(F_o)^2]^{1/2}$. $w = 0.75/(\sigma^2(F_o)+0.00010F_o^2)$.

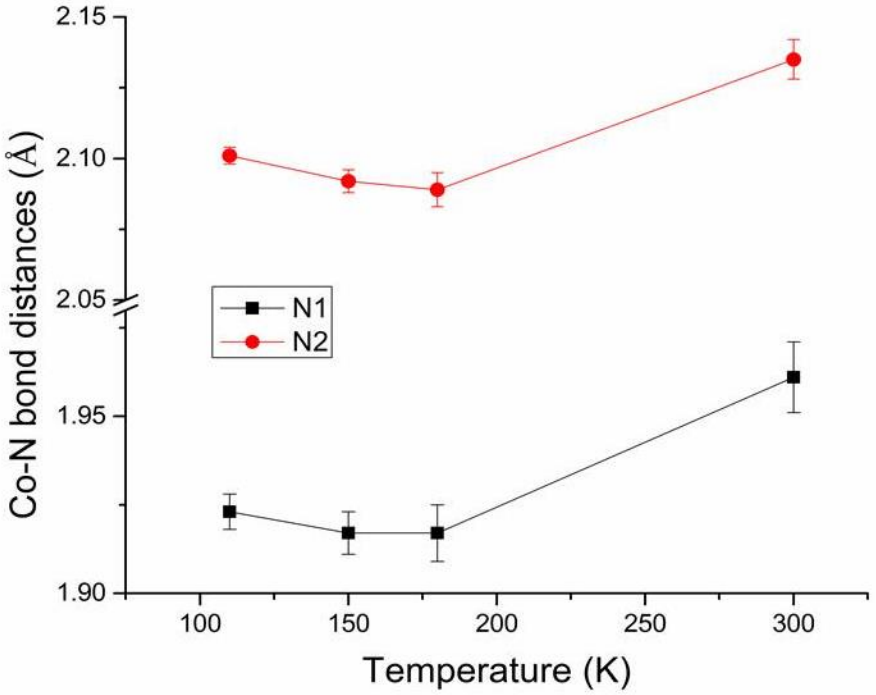

Figure 28. Temperature dependence of the Co-N bond distances in $[Co(terpy)](PF_6)_2$ with the standard deviations.

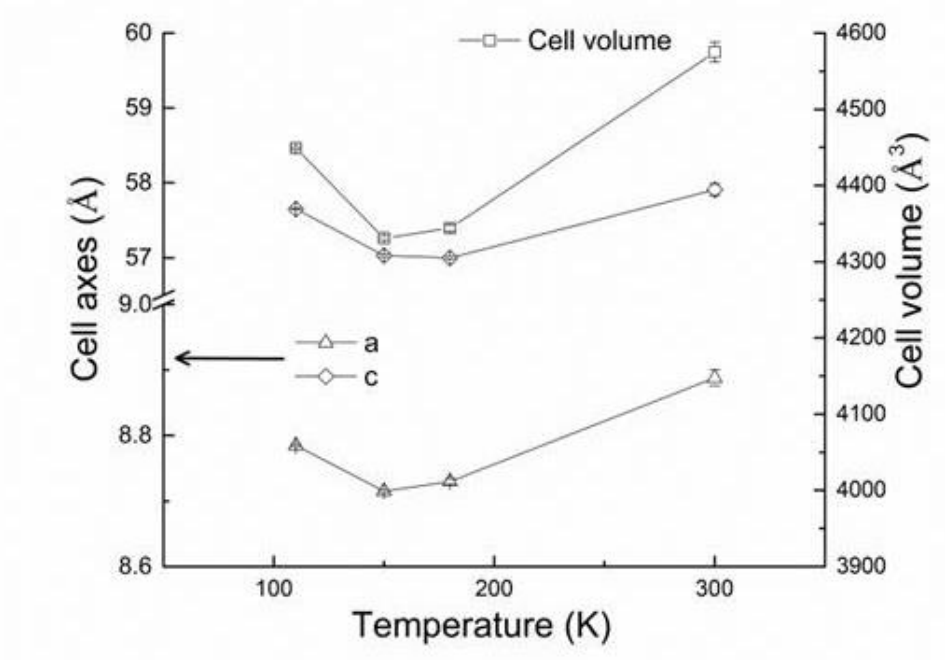

Figure 29. Temperature dependence of the unit cell parameters of $[Co(pyterpy)_2](PF_6)_2$ with the estimated standard deviation included.

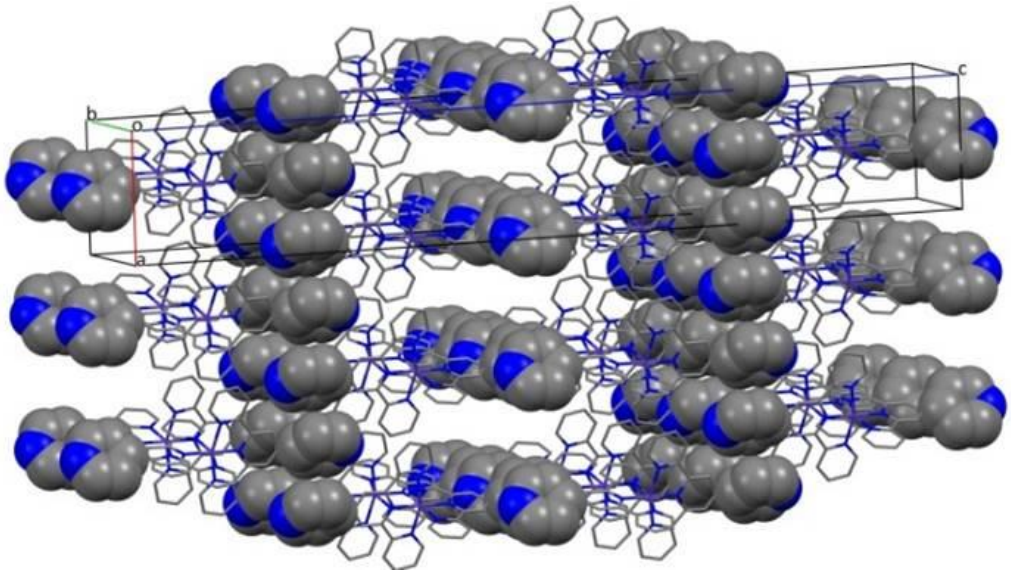

Figure 30. Packing diagram of $[Co(pyterpy)_2](PF_6)_2$ with the stacking interactions of the terminal Py(N3) rings highlighted in the space-filling model. Hydrogen atoms and disordered $[PF_6]^-$ anions are omitted for the sake of clarity.

The terminal pyridyl group (Py(N3) engages in π-stacking interactions between individual molecules along two directions (a and b axes) accompanied by the rotation of Py(N3) by 35.46 ° from the main terpy plane (Figure 30). The peripheral (Py(N2)) pyridyl rings stack with only a single nearest neighbor with no long-range stacking interactions.

$[Co(pyterpy)_2](TCNQ)_2$ solvates. Metathesis reactions of $[Co(pyterpy)_2](PF_6)_2 \cdot H_2O$ and LiTCNQ in mixtures of methanol and DMF or methanol and acetonitrile give dark purple crystalline products of $[Co(pyterpy)_2](TCNQ)_2 \cdot DMF \cdot MeOH$ or $[Co(pyterpy)_2](TCNQ)_2 \cdot MeCN \cdot MeOH$, respectively. The two products crystallize with the same space group, similar unit cell parameters and packing patterns with the only difference being the presence of interstitial DMF or acetonitrile molecules. Consequently, variable temperature X-ray

diffraction studies were conducted on a crystal of $[Co(pyterpy)_2](TCNQ)_2 \cdot DMF \cdot CH_3OH$ whose space group and packing patterns remain the same at 110, 150, 180 and 300 K. The compound crystallizes in the triclinic $P\bar{1}$ space group with a cationic $[Co(pyterpy)_2]^{2+}$ unit, two $TCNQ^{\bullet-}$ radicals, one DMF and one methanol molecules in the asymmetric unit (Figure 31). The crystals gradually lose methanol as evidenced by the single crystal X-ray diffraction data at 300 K where the methanol molecule is best refined with a partial occupancy (Table 8). The same single crystal was used for all the variable temperature X-ray diffraction studies. One of the TCNQ radical anions is engaged in hydrogen bonding with a methanol molecule with a N···O distance of 2.903(4) Å (110 K).

Table 7. Co-N bond distances (Å) of $[Co(pyterpy)_2](TCNQ)_2 \bullet DMF \bullet CH_3OH$ at difference temperatures.

	110 K	150 K	180 K	300 K
Co1-N1	1.962(2)	1.973(2)	1.957(2)	1.970(2)
Co1-N2	2.242(2)	2.244(2)	2.243(2)	2.207(2)
Co1-N3	2.215(2)	2.225(2)	2.223(2)	2.195(2)
Co1-N4	1.888(2)	1.901(2)	1.886(2)	1.918(2)
Co1-N5	2.024(2)	2.029(2)	2.021(2)	2.052(2)
Co1-N6	2.013(2)	2.037(2)	2.010(2)	2.041(2)

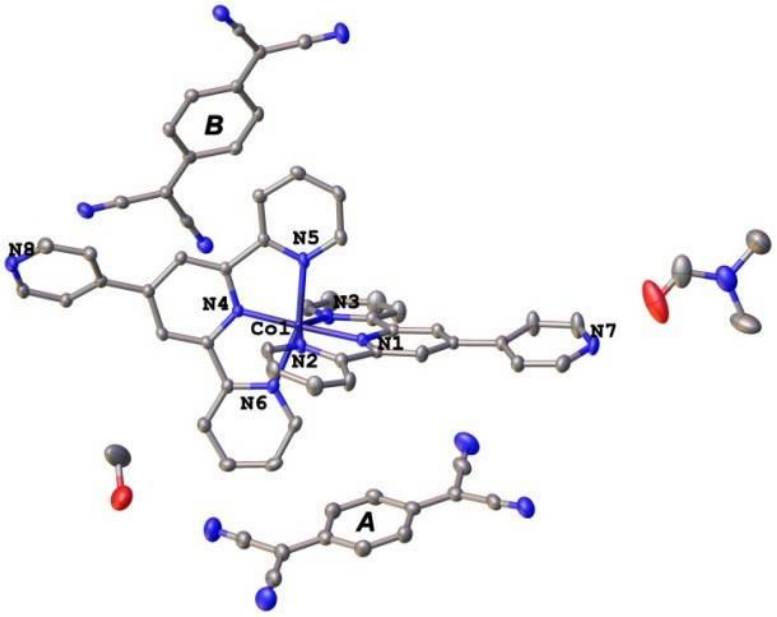

Figure 31. Asymmetric unit in the crystal structure of $[Co(pyterpy)_2](TCNQ)_2$•DMF•MeOH with thermal ellipsoids drawn at the 50% probability level. The hydrogen atoms are omitted for the sake of clarity.

The Co(II) ion is in a similar compressed octahedral geometry but is distorted in such a fashion that the metal ion is closer to the N4 in the pyterpy ligands along the N4-Co1-N1 direction as compared to the situation for $[Co(pyterpy)_2](PF_6)_2$ as evidenced by the Co-N bond distances ($[Co(pyterpy)_2](TCNQ)_2 \cdot DMF \cdot CH_3OH$ at 110 K, Co1-N1= 1.962(2) Å, Co1-N2 = 2.242(2) Å, Co1-N3 = 2.215(2) Å, Co1-N4 = 1.888(2) Å, Co1-N5 = 2.024(2) Å, Co1-N6 = 2.013(2) Å, Table 7). The two equatorial Co-N2 and Co-N3 bonds are quite elongated and thermal effects have a relatively small influence on them. The other four Co-N bond distances decrease as the temperature is lowered from 300 to 180 K and then experience an unusual increase from 180 to 150 K which is presumably due to a Jahn-Teller distortion of the ^2E state of LS Co(II) as found for $[Co(pyterpy)_2](PF_6)_2$ (Figure 32). The difference in this case is that the unusual elongation is observed below 180 K for $[Co(pyterpy)_2](TCNQ)_2 \cdot DMF \cdot CH_3OH$ as opposed to 150 K in $[Co(pyterpy)_2](PF_6)_2$. The higher temperature for the elongation in $[Co(pyterpy)_2](TCNQ)_2 \cdot DMF \cdot CH_3OH$ indicates that the lower local symmetry of the Co(II) center helps to stabilize the LS state more than does the higher local symmetry present in $[Co(pyterpy)_2](PF_6)_2$. A “double breathing” behavior is also reflected in the unit cell *b* and *c* dimensions and the contraction in the volume from 300 to 180 K and then expansion from 180 to 150 K (Figure 33).

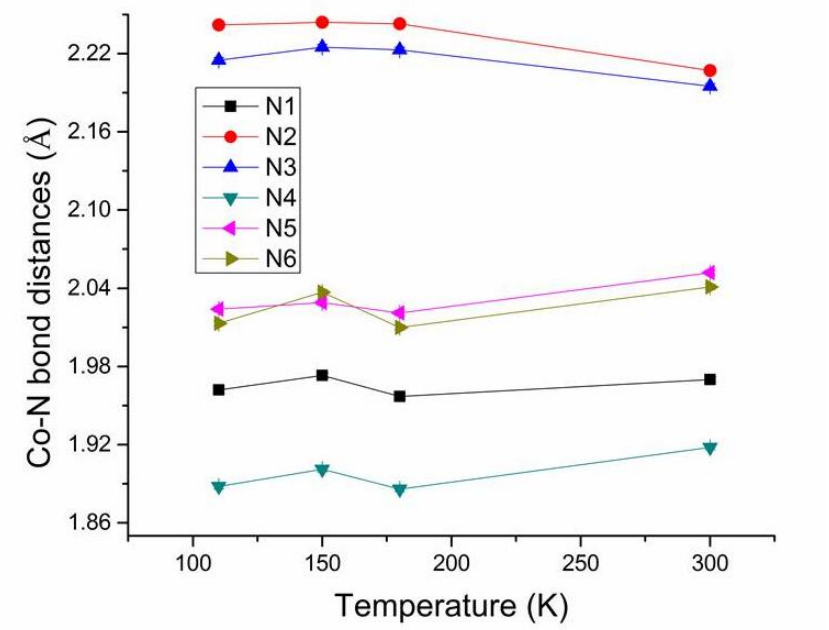

Figure 32. Temperature dependence of the Co-N bond distances of $[Co(pyterpy)_2](TCNQ)_2$•DMF•MeOH.

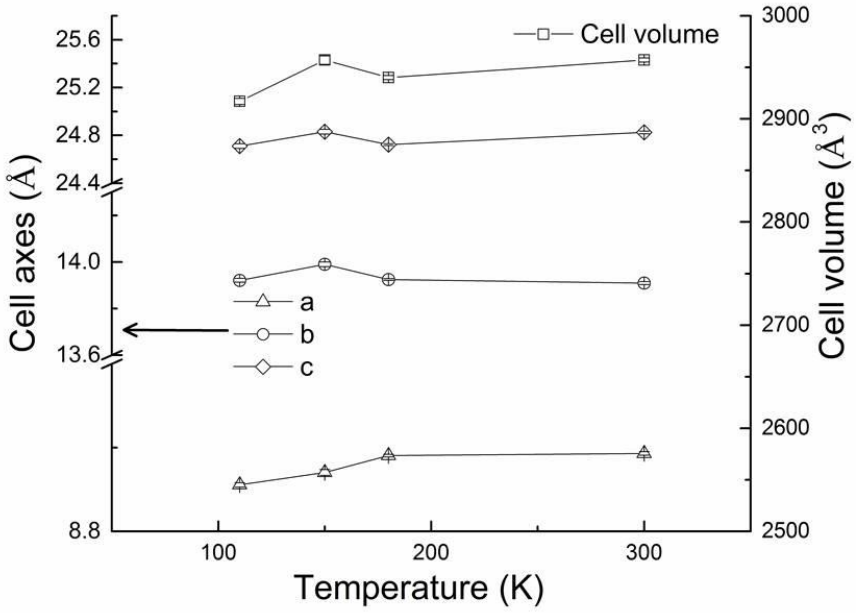

Figure 33. Cell parameters of $[Co(pyterpy)_2](TCNQ)_2$•DMF•CH_3OH at different temperatures.

Table 8. Pertinent crystallographic data for $[Co(pyterpy)_2](TCNQ)_2 \bullet DMF \bullet CH_3OH$ at different temperatures.

Temperature	100 K	150 K	180 K	300 K
Empirical formula	$C_{68}H_{47}CoN_{17}O_2$	$C_{68}H_{47}CoN_{17}O_2$	$C_{68}H_{47}CoN_{17}O_2$	$C_{67.61}H_{43}CoN_{17}O_{1.25}$
Formula weight	1193.15	1193.15	1193.15	1172.44
Temperature/K	110.15	150.15	180.15	300.15
Crystal system	triclinic	triclinic	triclinic	triclinic
Space group	P-1	P-1	P-1	P-1
a/Å	8.911(5)	8.941(7)	8.981(3)	8.986(4)
b/Å	13.921(8)	13.990(11)	13.924(4)	13.909(6)
c/Å	24.708(15)	24.828(19)	24.722(8)	24.825(11)
α/°	74.249(7)	74.116(9)	74.006(11)	105.759(6)
β/°	81.736(8)	82.082(10)	81.940(11)	95.448(6)
γ/°	85.755(7)	85.910(10)	85.735(12)	94.088(6)
Volume/$Å^3$	2917(3)	2957(4)	2940.4(16)	2957(2)
Z	2	2	2	2
$\rho_{calc}g/cm^3$	1.358	1.340	1.348	1.317
μ/mm^{-1}	0.358	0.353	0.355	0.351
F(000)	1234.0	1234.0	1234.0	1209.0
Crystal size/mm^3	0.25 × 0.13 × 0.08	0.25 × 0.13 × 0.08	0.25 × 0.13 × 0.08	0.25 × 0.13 × 0.08
Radiation	MoKα (λ = 0.71073)	MoKα (λ = 0.71073)	MoKα (λ = 0.71073)	MoKα (λ = 0.71073)
2Θ range for data collection/ °	3.042 to 52.044	3.028 to 53.464	3.07 to 52.044	3.058 to 53.466

Table 8. Continued.

Temperature	100 K	150 K	180 K	300 K
Index ranges	$-10 \le h \le 10$, $-17 \le k \le 17$, $-30 \le l \le 30$	$-11 \le h \le 11$, $-17 \le k \le 17$, $-31 \le l \le 31$	$-11 \le h \le 11$, $-17 \le k \le 16$, $-30 \le l \le 30$	$-11 \le h \le 11$, $-17 \le k \le 17$, $-31 \le l \le 31$
Reflections collected	30512	31031	25859	33075
Independent reflections	11425 [R_{int} = 0.0983, R_{sigma} = 0.0935]	12363 [R_{int} = 0.0428, R_{sigma} = 0.0538]	11436 [R_{int} = 0.0718, R_{sigma} = 0.0736]	12505 [R_{int} = 0.0424, R_{sigma} = 0.0584]
Data/restraints/parameters	11425/0/797	12363/0/797	11436/0/797	12505/0/797
Goodness-of-fit on F^2	1.058	1.091	1.049	1.024
Final R indexes [I>=2σ (I)]	R_1 = 0.0508, wR_2 = 0.1228	R_1 = 0.0461, wR_2 = 0.1388	R_1 = 0.0446, wR_2 = 0.1187	R_1 = 0.0475, wR_2 = 0.1011
Final R indexes [all data]	R_1 = 0.0759, wR_2 = 0.1379	R_1 = 0.0607, wR_2 = 0.1560	R_1 = 0.0580, wR_2 = 0.1287	R_1 = 0.0871, wR_2 = 0.1195
Largest diff. peak/hole / e $Å^{-3}$	0.99/-0.68	0.67/-0.66	0.64/-0.48	0.20/-0.30
Flack parameter	$C_{68}H_{47}CoN_{17}O_2$	$C_{68}H_{47}CoN_{17}O_2$	$C_{68}H_{47}CoN_{17}O_2$	$C_{67.61}H_{43}CoN_{17}O_{1.25}$

$R_1 = \Sigma||F_o| - |F_c||/ \Sigma|F_o|$. $wR_2 = [\Sigma w(|F_o| - |F_c|)^2/|\Sigma w(F_o)^2]^{1/2}$. $w = 0.75/(\sigma^2(F_o)+0.00010F_o^2)$.

The additional terminal pyridyl groups in $[Co(pyterpy)_2](TCNQ)_2 \cdot DMF \cdot CH_3OH$ are involved in π-stacking interactions with TCNQ radicals to varying degrees owing to the different rotational orientations present. The rotations of Py(N7) to Py(N1) and Py(N8) to Py(N4) are approximately 13.78 and 36.51 °, respectively. Due to the relatively large rotation of the Py(N8) ring, it can only stack with the Py(N8) ring of another $[Co(pyterpy)_2]^{2+}$ cation whereas the less rotated Py(N7) ring is engaged in inter-molecular stacking with closer contacts of both the Py(N1) and Py(N7) rings (Figure 34). In addition to these rotations, the structural distortion of $[Co(pyterpy)_2](TCNQ)_2 \cdot DMF \cdot CH_3OH$ as compared to $[Co(pyterpy)_2](PF_6)_2$ is reflected in the bending of the pyridyl rings (Figure 31).

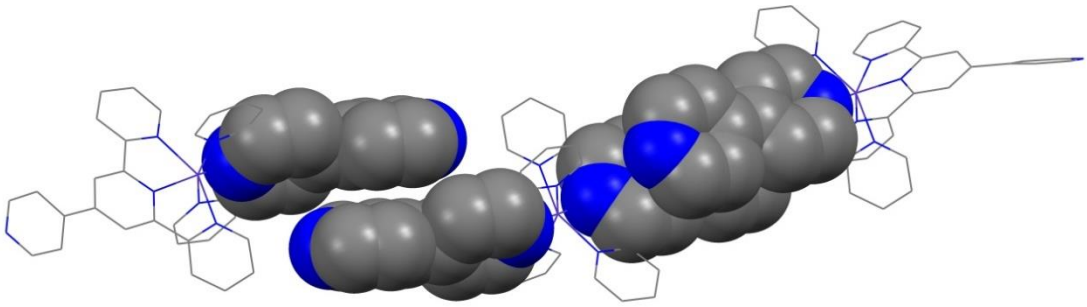

Figure 34. Packing view of the crystal structure of $[Co(pyterpy)_2](TCNQ)_2 \bullet DMF \bullet CH_3OH$ highlighting the stacking interactions between the terminal and central pyridyl groups.

As depicted in Figure 35, the two unique TCNQ radicals in the asymmetric unit designated as A and B are stacked as AA and BB dimers with inter-planar distances of ~ 3.217 and 3.088 Å, respectively. Furthermore, the TCNQ dimers AA engage in interactions with two stacked Py(8) rings of the $[Co(pyterpy)_2]^{2+}$ cations in an alternating

AA-Py(8)Py(8)-AA fashion (Figure 36). As for the TCNQ dimers BB, these are separated by the $[Co(pyterpy)_2]^{2+}$ cations (Figure S5) with no additional contacts. In contrast to $[Co(pyterpy)_2](PF_6)_2$, in which only the pyridyl groups of the $[Co(pyterpy)_2]^{2+}$ cations are available for stacking, the π-interactions between the pyridyl groups and TCNQ radical anions in $[Co(pyterpy)_2](TCNQ)_2$•DMF•CH_3OH provide secondary ligand sphere modulation effects on the $[Co(pyterpy)_2]^{2+}$ SCO units.

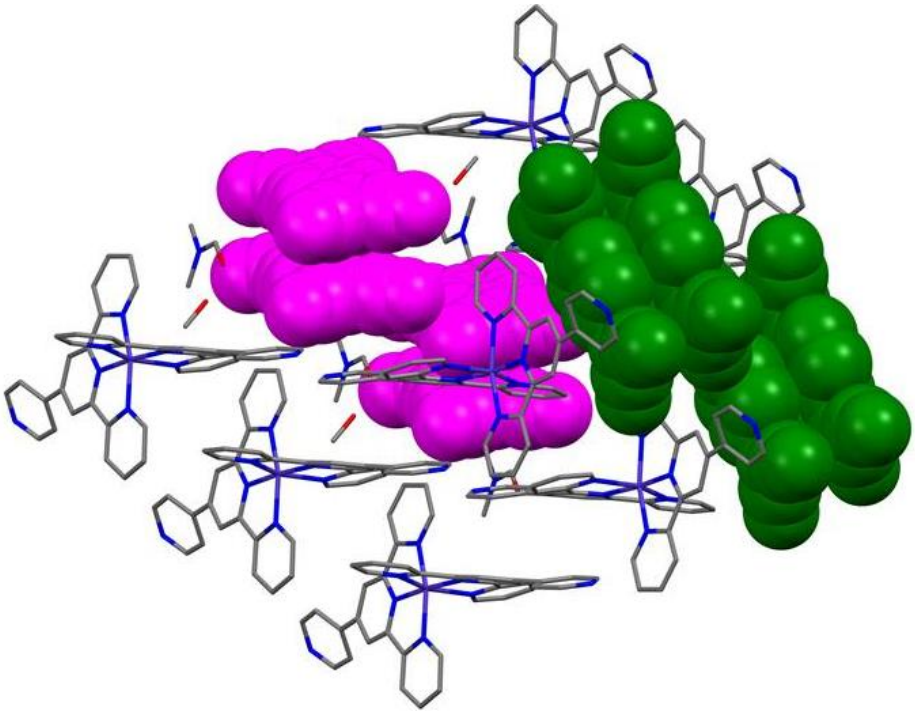

Figure 35. Packing view of the crystal structure of $[Co(pyterpy)_2](TCNQ)_2$•DMF•CH_3OH highlighting the stacking interactions between the TCNQ dimers of AA (magenta) and BB (green) in the space-filling model.

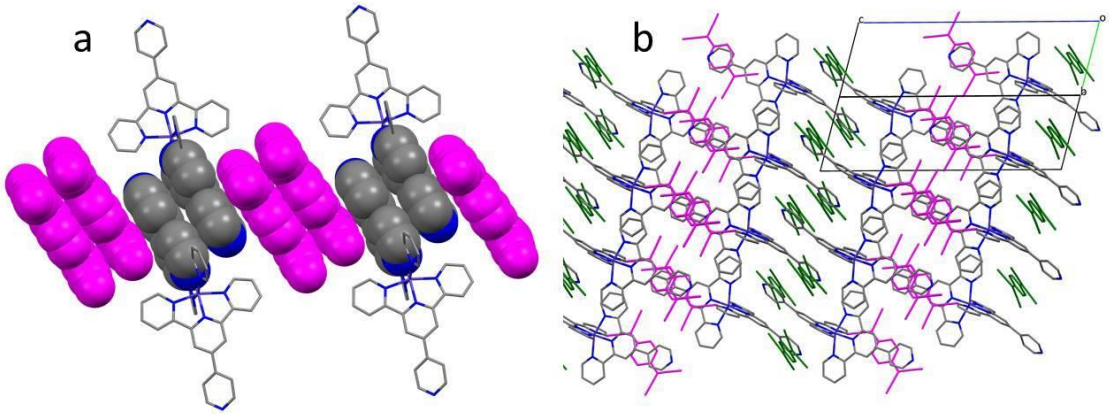

Figure 36. Side view (a) and top view (b) in the crystal structure of $[Co(pyterpy)_2](TCNQ)_2 \bullet DMF \bullet CH_3OH$ highlighting the stacking interactions between the TCNQ dimers of AA (magenta) and the Py(8)Py(8) stacked dimers.

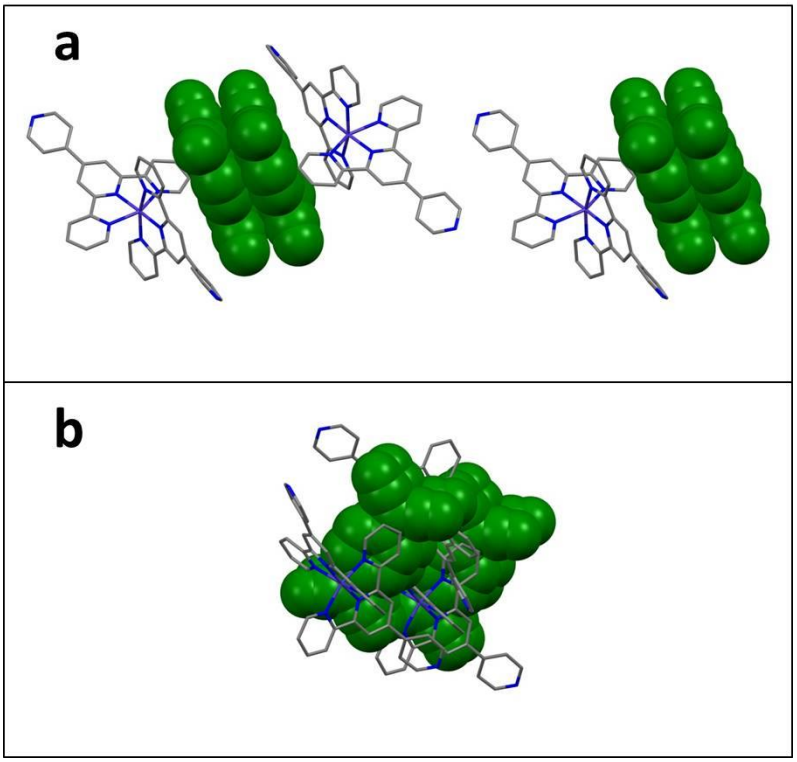

Figure 37. Side view (a) and top view (b) in the crystal structure of $[Co(pyterpy)_2](TCNQ)_2 \bullet DMF \bullet CH_3OH$ highlighting the stacking interactions between the TCNQ dimers of BB (green) and the Py(5)Py(5) stacked dimers in space-filling model.

Magnetic properties

Inorganic salts of $[Co(pyterpy)_2]^{2+}$ are known and have been investigated for their biological activities, but no magnetic properties for these compounds have been reported.[138] Magnetic measurements were carried out on freshly prepared crystalline powders of $[Co(pyterpy)_2](PF_6)_2$, $[Co(pyterpy)_2](TCNQ)_2 \cdot DMF \cdot CH_3OH$ and $[Co(pyterpy)_2](TCNQ)_2 \cdot CH_3CN \cdot CH_3OH$ in gel capsules from T = 5-390 K at a cooling/heating rate of 5 K/min. The phase purities of the freshly prepared bulk crystalline powders were verified by powder X-ray diffraction studies (Figure 16 and Figure 17). The compound $[Co(pyterpy)_2](PF_6)_2$ was measured as a control experiment for the non-innocent TCNQ radical anion salts and exhibits a very gradual spin transition that does not reach a fully populated LS state even at 5 K with a $\chi_M T$ value of 0.61(1) emu K/mol (Figure 38). At room temperature, the $\chi_M T$ value of 1.42(1) emu K/mol corresponds to ~56% of Co(II) in the HS state (assuming g = 2.16). Similar behavior was recently reported by Brooker and coworkers for a closely related compound $[Co(py\text{-}pzpypz)_2](BF_4)_2$ (py-pzpypz = (4-(4-pyridyl)-2,5-dipyrazyl-pyridine).[143]

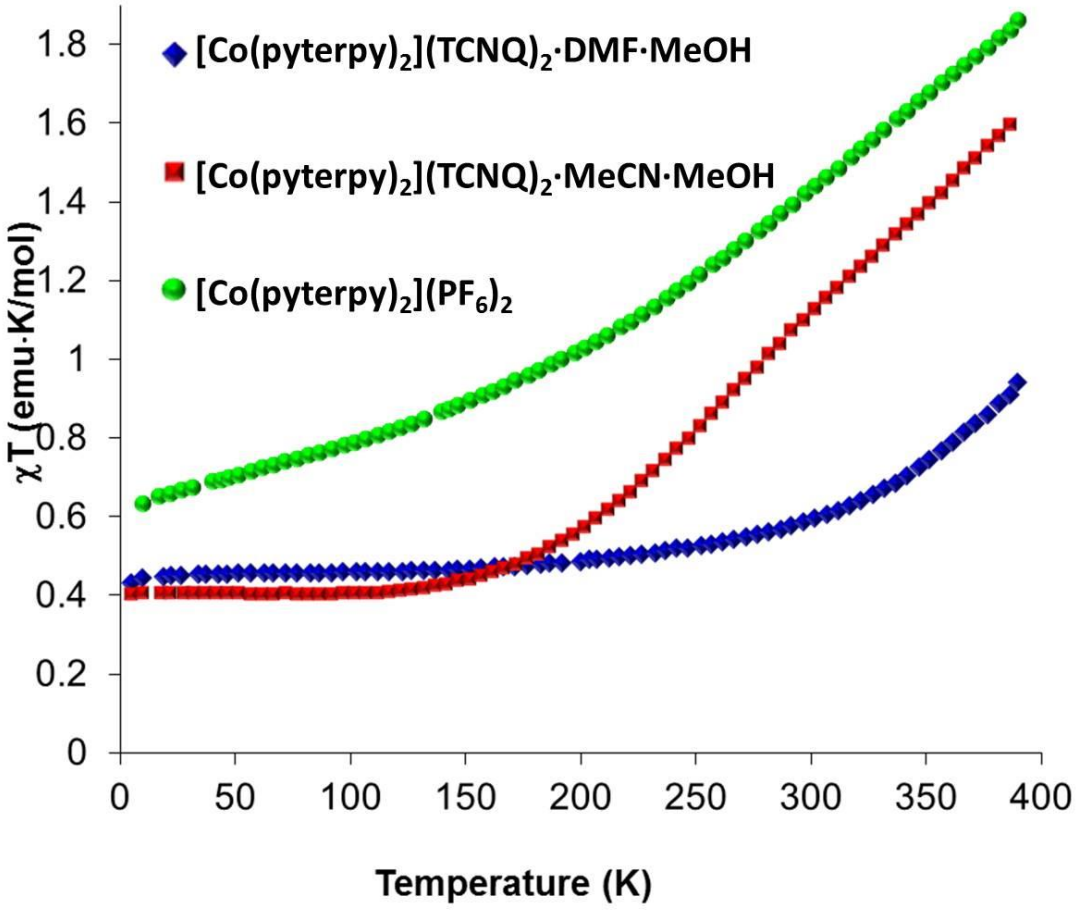

Figure 38. Temperature dependence of $\chi_M T$ versus T plots for compounds $[Co(pyterpy)_2](PF_6)_2$, $[Co(pyterpy)_2](TCNQ)_2 \cdot DMF \cdot MeOH$ and $[Co(pyterpy)_2](TCNQ)_2 \cdot MeCN \cdot MeOH$.

Compounds $[Co(pyterpy)_2](TCNQ)_2 \cdot DMF \cdot CH_3OH$ and $[Co(pyterpy)_2](TCNQ)_2 \cdot CH_3CN \cdot CH_3OH$ exhibit typical Co(II) gradual spin-crossover with LS $\chi_M T$ values of 0.45 emu K/mol and 0.41 emu K/mol, respectively. These values are higher than the spin-only values for LS Co(II), which is attributed to spin-orbit coupling. At 300 K, $[Co(pyterpy)_2](TCNQ)_2 \cdot DMF \cdot CH_3OH$ and $[Co(pyterpy)_2](TCNQ)_2 \cdot CH_3CN \cdot CH_3OH$ exhibit $\chi_M T$ values of 0.58 and 1.11 emu K/mol, corresponding to ~7% and 39% HS population of Co(II) (assuming g = 2.19),

respectively. At 390 K, $[Co(pyterpy)_2](TCNQ)_2 \cdot DMF \cdot CH_3OH$ and $[Co(pyterpy)_2](TCNQ)_2 \cdot CH_3CN \cdot CH_3OH$ exhibit $\chi_M T$ values of 0.94 and 1.63 emu K/mol, corresponding to ~27% and 67% HS population of Co(II), respectively. The $T_{1/2}$ value (the temperature at which the SCO molecules are equally populated in the HS/LS state) of compound $[Co(pyterpy)_2](TCNQ)_2 \cdot CH_3CN \cdot CH_3OH$ is ~332 K, whereas the value for $[Co(pyterpy)_2](TCNQ)_2 \cdot DMF \cdot CH_3OH$ is clearly higher than 390 K but cannot be determined from the experimental data due to instrument limitations. Below ~180 K, the Co(II) ions in compound $[Co(pyterpy)_2](TCNQ)_2 \cdot DMF \cdot CH_3OH$ are almost entirely in the LS state. The LS states of Co(II) in $[Co(pyterpy)_2](TCNQ)_2 \cdot CH_3CN \cdot CH_3OH$, however, are not fully populated until below 110 K. The spins on the TCNQ radicals are paired due to the close contacts of the TCNQ radical dimers in the structure of $[Co(pyterpy)_2](TCNQ)_2 \cdot DMF \cdot CH_3OH$ and $[Co(pyterpy)_2](TCNQ)_2 \cdot CH_3CN \cdot CH_3OH$, therefore they would not be expected to contribute to the magnetic moment.[46] The cooling and warming curves of the χT plots of all three compounds exhibit no discernible hysteresis, which is common for similar Co(II) SCO systems.[143,152]

As the structural analyses indicate, the cell parameters for crystals of $[Co(pyterpy)_2](PF_6)_2$ exhibit only one important change at ~150 K as the temperature decreases with no discernible changes down to 110 K (Figure 29). In contrast, the trend in the changes of the *b* and *c* unit cell edges and the unit cell volume for $[Co(pyterpy)_2](TCNQ)_2 \cdot DMF \cdot CH_3OH$ exhibit two anomalies at ~180 and 150 K, namely a decrease in values from ~300-180 K, an increase in the range ~180-150 K, and then a second decrease below 150 K (Figure 33). These results indicate that the Jahn-

Teller distortion in the high symmetry ($I4_1/a$) compound $[Co(pyterpy)_2](PF_6)_2$ occurs at lower temperatures as compared to $[Co(pyterpy)_2](TCNQ)_2 \cdot DMF \cdot CH_3OH$ with a lower symmetry which results in an incomplete transition from HS to LS in the former compound at 110 K, but a nearly complete transition to LS for $[Co(pyterpy)_2](TCNQ)_2 \cdot DMF \cdot CH_3OH$ below 180 K.

The effect of solvent molecules also plays an important role in the spin-transition of $[Co(pyterpy)_2](TCNQ)_2$•solvent compounds. As mentioned earlier, compounds $[Co(pyterpy)_2](TCNQ)_2 \cdot DMF \cdot CH_3OH$ and $[Co(pyterpy)_2](TCNQ)_2 \cdot CH_3CN \cdot CH_3OH$ crystallize in the same space group and exhibit similar packing patterns, with the only difference being the presence of DMF versus acetonitrile solvent molecules. It has been reported before in 3-D Fe(II) SCO frameworks that a smaller solvent molecule tends to exert a higher chemical pressure and stabilize the LS state.[153,154] However, in our case the higher $T_{1/2}$ of $[Co(pyterpy)_2](TCNQ)_2 \cdot DMF \cdot CH_3OH$ as compared to $[Co(pyterpy)_2](TCNQ)_2 \cdot CH_3CN \cdot CH_3OH$ is attributed to a higher overall chemical pressure induced by the larger DMF molecules which help to stabilize the LS states more than the smaller acetonitrile molecules in $[Co(pyterpy)_2](TCNQ)_2 \cdot CH_3CN \cdot CH_3OH$. This cannot be simply rationalized by the size of the solvent molecule because, besides the difference in SCO systems (Fe(II) *vs.* Co(II)), it is possible that in discrete molecular complexes the positions of SCO entities may move slightly to mitigate the effect of size variation in the interstitial solvents. In addition, the shape, orientation and the electronic effects of the solvent molecules are

also expected also play a role and it would be interesting in future work to systematically investigate these factors.[155,156]

Conductivity properties

Electrical conductivity studies performed on single crystal samples of $[Co(pyterpy)_2](TCNQ)_2 \cdot DMF \cdot CH_3OH$ revealed a room temperature conductivity of ~5 × 10^{-6} S/cm. It is interesting to note that the conductivity, unlike for semiconducting materials with TCNQ radicals stacks, is nearly independent of temperature between 300 and 100 K (Figure 39), which is possibly due to a compensation effect of decreased charge-carrier concentration and increased charge carrier mobility as the temperature decreases.[157]

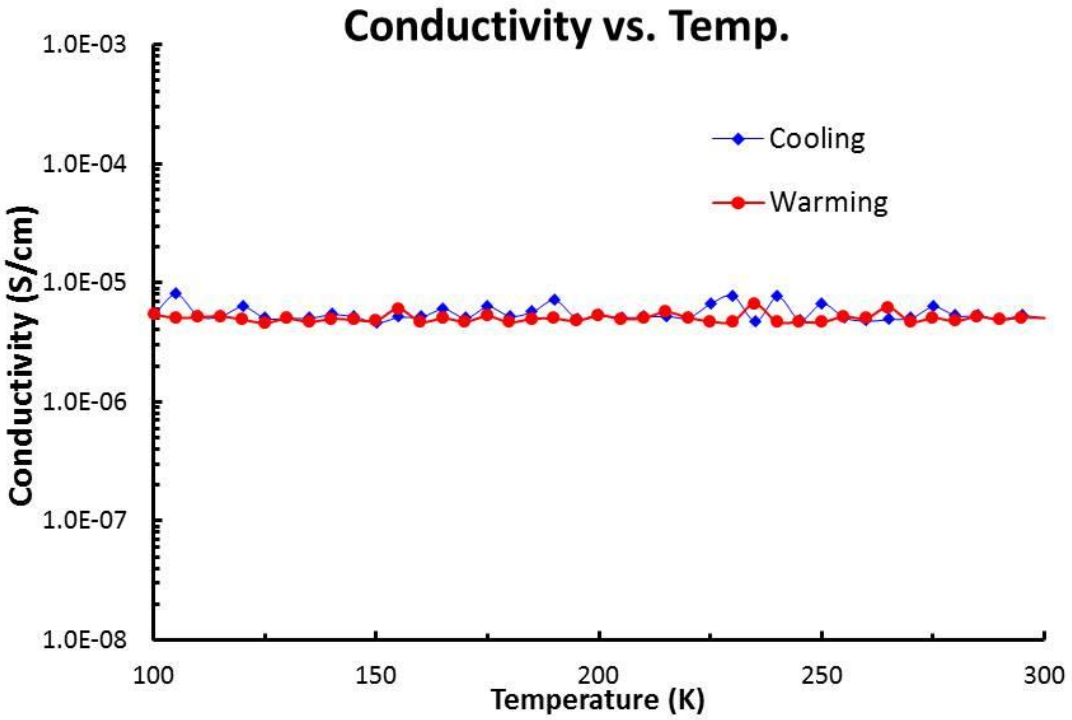

Figure 39. Temperature dependence of the conductivity of a single crystal of $[Co(pyterpy)_2](TCNQ)_2 \cdot DMF \cdot CH_3OH$.

Conclusions

In summary, an anomalous conducting behavior occurs at 180-190 K in a highly conducting hybrid inorganic/organic-radical bifunctional SCO conducting molecular material. This anomaly is directly correlated with the structural variation arising from the HS to LS transition of Co(II), subsequent Jahn-Teller distortion of LS Co(II) and concomitant charge fluctuations of the partially charged TCNQ radicals. This modular synthetic procedure for the introduction of partially charged TCNQ radicals is highly promising for the synthesis of other bifunctional materials with electrically conducting properties, efforts that are currently being explored in our laboratories.

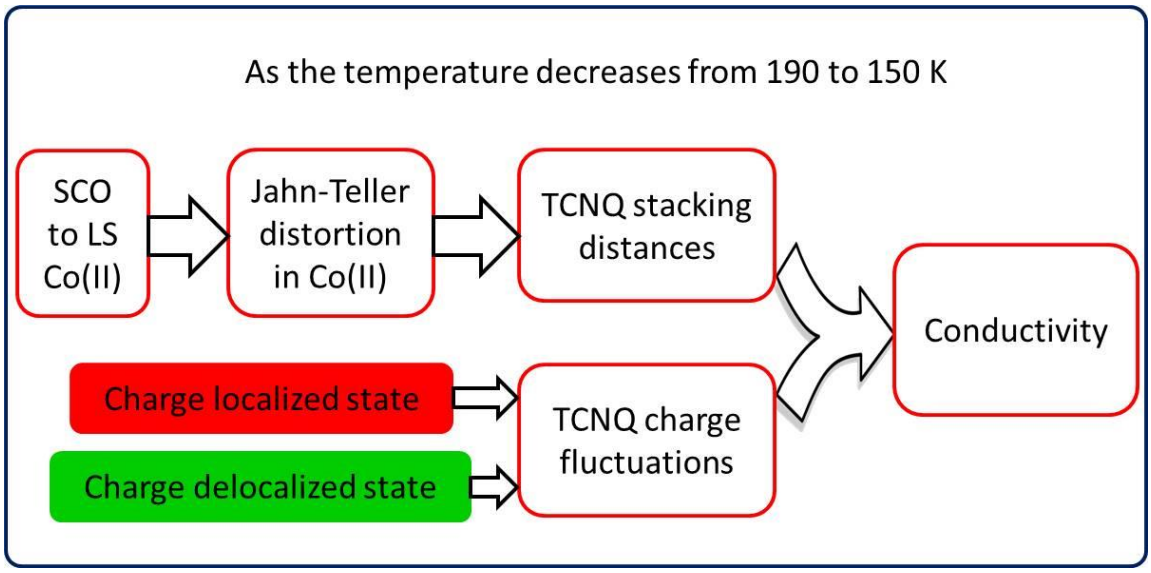

Figure 40. Schematic representation of the factors that are contributing to the electrical conductivity of $[Co(terpy)_2](TCNQ)_3\ CH_3CN$.

The bifunctional SCO materials $[Co(pyterpy)_2](TCNQ)_2$•solvent with different crystallizing solvents have been synthesized and characterized by variable temperature single crystal X-ray diffraction and magnetic measurements. Strong intermolecular interactions between the SCO centers have been realized by taking advantage of the

supramolecular π-stacking interactions between the terminal pyridyl groups of the pyterpy ligands and TCNQ radicals. In comparison to the high symmetry compound $[Co(pyterpy)_2](PF_6)_2$, in which the HS to LS transition is incomplete even at 5 K, the radical-pyridyl π-stacking interaction distorts the Co(II) coordination geometry and helps to stabilize the LS ^2E state. The design of multifunctional SCO materials with improved cooperativity may benefit from this new strategy of employing organic radicals to enhance intermolecular interactions.

CHAPTER III

COEXISTENCE OF SLOW RELAXATION OF THE MAGNETIZATION AND SEMICONDUCTING PROPERTIES

Introduction

The synthesis of nanoscale materials for electronic devices is a central theme in materials research. Given that conventional materials are estimated to approach their miniaturization limit by 2025, more efforts are being directed at the design of new types of nanoscale materials, including molecular nanomagnets that are capable of behaving as traditional magnets, but with much smaller sizes such as 1 or 2 nanometers. As a result, such molecular nanomagnets could operate at much faster speeds and require less energy than conventional devices because of the quantum effects that they exhibit.

Another intriguing aspect of the research in this disseration is the study of bifunctional magnetic and semiconducting molecular materials. By building such materials with alternating functional layers, we hope to address their magnetic behaviors through the application of an electric field, or vice versa, which will make them superior candidates for transistors and sensors. By using two distinct inorganic and organic components, we have achieved such materials and observed interactions between the different functionalities. This is a big step toward their device applications as they can be processed directly from solution and can crystallize in a matter of minutes.

In this work, a series of isostructural chain-like compounds [Ln(TPMA)(μ-TCNQ)(μ-OH)](TCNQ)$_2$ CH_3CN (Ln = Dy, Gd, Y) have been synthesized. Magnetic

and electrical conductivity studies revealed that the Dy(III) compound exhibited slow relaxation of the magnetization at 5.0-8.2 K and semiconductivity at 180-350 K.

It has also been demonstrated that other functional species such SMMs and photosensitizers such as $[Co(Tpm)_2]^{2+}$, $[Ru(terpy)_2]^{2+}$, $[Ru(bpy)_3]^{2+}$ and $[Zn(terpy)_2]^{2+}$can also be incorporated into electrically conducting bifunctional materials through a generalized modular synthetic approach by using the easily accessible TCNQ radical source of $[Et_3NH](TCNQ)_2$.

Experimental Section

Syntheses

The starting materials TPMA (tris(pyridylmethyl)amine)[158] and Tpm (tris(pyrazolyl)methane)[159] were synthesized according to literature methods. Dysprosium trifluoromethanesulfonate (triflate, Sigma-Aldrich), gadolinium trifluoromethanesulfonate (Sigma-Aldrich) and yttrium trifluoromethanesulfonate (Sigma-Aldrich) are used as received without further purification. The reagents terpy (2,2′;6′,2″-terpyridine, TCI america), $Co(ClO_4)_2\ 6H_2O$ (Sigma-Aldrich) and the solvents THF (tetrahydrafuran, reagent grade, Alfa Aesar), acetonitrile (reagent grade, Sigma-Aldrich), N,N-dimethylformamide (reagent grade, Sigma-Aldrich) were used as received without further purification. The starting materials $(Et_3NH)(TCNQ)_2$ and $Co(terpy)_2(ClO_4)_2\ 0.5H_2O$ were synthesized according to the literature.[25,136,137] The starting material $[Co(pyterpy)_2](ClO_4)_2$ was prepared by a modified procedure from the literature.[138] Caution! Perchlorates are potentially explosive and should be handled very carefully in small amounts. Avoid heat, drying and grinding.

[Dy(TPMA)(μ-TCNQ)(μ-OH)](TCNQ)$_2$ ·CH$_3$CN (1). 0.1 mmol (61.1 mg) of dysprosium trifluoromethanesulfonate and 0.15 mmol (43.5 mg) of TPMA were dissolved in 4 mL of acetonitrile and stirred for 20 min. A solution of 0.15 mmol (76 mg) of $(Et_3NH)(TCNQ)_2$ in 9 mL of acetonitrile was filtered through glass wool into the dysprosium trifluoromethanesulfonate solution. Dark blue crystals formed after a few minutes. The product was filtered and rinsed with acetonitrile after 20 min. Yield 44.2 mg (39 % based on Dy). IR: Nujol mulls on KBr plates: ν(CN) 2206.2, 2177.5 and 2153.3, 2136.6 cm^{-1}, δ(C-H, TCNQ) 826.7 cm^{-1}.

[Gd(TPMA)(μ-TCNQ)(μ-OH)](TCNQ)$_2$ ·CH$_3$CN (2). 0.1 mmol (60.5 mg) of gadolinium trifluoromethanesulfonate and 0.15 mmol (43.5 mg) of TPMA were dissolved in 4 mL of acetonitrile and stirred for 20 min. A solution of 0.15 mmol (76 mg) of $(Et_3NH)(TCNQ)_2$ in 9 mL of acetonitrile was filtered through glass wool into the dysprosium trifluoromethanesulfonate solution. Dark blue crystals formed after a few minutes. The product was filtered and rinsed with acetonitrile after 20 min. Yield 44.8 mg (40 % based on Gd). IR: Nujol mulls on KBr plates: ν(CN) 2208.1, 2173.4 and 2153.7, 2132.6 cm^{-1}, δ(C-H, TCNQ) 826.6 cm^{-1}.

[Y(TPMA)(μ-TCNQ)(μ-OH)](TCNQ)$_2$ ·CH$_3$CN (3). 0.1 mmol (53.9 mg) of yttrium trifluoromethanesulfonate and 0.15 mmol (43.5 mg) of TPMA were dissolved in 4 mL of acetonitrile and stirred for 20 min. A solution of 0.15 mmol (76 mg) of $(Et_3NH)(TCNQ)_2$ in 9 mL of acetonitrile was filtered through glass wool into the dysprosium trifluoromethanesulfonate solution. Dark blue crystals formed after a few

minutes. The product was filtered and rinsed with acetonitrile after 20 min. Yield 44 mg (39 % based on Y).

$[Co(Tpm)_2](TCNQ)_3$ (4). 0.025 mmol (12.1 mg) of Tpm and 0.0125 mmol (6.2 mg) of $CoCl_2 \cdot 6H_2O$ was dissolved in a mixture of 1 mL of CH_3CN and 1mL of CH_3OH and stirred for 10 min. To this solution was added a solution of 0.025 mmol (11.4 mg) of $(Et_3NH)(TCNQ)_2$ in 6 mL of CH_3CN through glass wool. Dark purple crystals formed after a few minutes. The product was filtered and rinsed with acetonitrile after 15 min. Yield 8.8 mg (64 % based on Co). IR: Nujol mulls on KBr plates: ν(CN) 2199.8, 2177.2 and 2156.4 cm^{-1}, δ(C-H, TCNQ) 837.4 and 856.0 cm^{-1}.

$[Fe(Tpm)_2](TCNQ)_3$ (5). 0.025 mmol (12.0 mg) of Tpm and 0.0125 mmol (6.0 mg) of $Fe(ClO_4)_2 \cdot xH_2O$ were dissolved in a mixture of 1 mL of CH_3CN, 1mL of CH_3OH and 1 mL of water and stirred for 10 min to obtain a pink solution. Then to this solution was added a solution of 0.025 mmol (11.8 mg) of $(Et_3NH)(TCNQ)_2$ in 6 mL of CH_3CN through glass wool. Dark blue crystals formed after a few minutes. The product was filtered and rinsed with acetonitrile after 15 min. Yield 9.5 mg (69 % based on Fe).

$[Ru(terpy)_2](TCNQ)_3 \cdot CH_3CN$ (6). A solution of 0.05 mmol (25.2 mg) of $(Et_3NH)(TCNQ)_2$ in 6 mL of CH_3CN was filtered through glass wool into a solution of 0.025 mmol (21.5 mg) of $[Ru(terpy)_2](PF_6)_2$ in 1 mL of CH_3CN. Dark purple crystals formed after a few minutes. The product was filtered and rinsed with acetonitrile after 15 min. Yield 11.3 mg (37 % based on Ru). IR: Nujol mulls on KBr plates: ν(CN) 2199.9, 2169.6 and 2151.0 cm^{-1}, δ(C-H, TCNQ) 834.6 and 818.6 cm^{-1}.

$[Ru(bpy)_3](TCNQ)_4$ (7). A solution of 0.05 mmol (24.7 mg) of $(Et_3NH)(TCNQ)_2$ in 3 mL of CH_3CN was filtered through glass wool into a solution of 0.025 mmol (23.6mg) of $[Ru(bpy)_2](PF_6)_2$ in 1 mL of CH_3CN. The mixture was left in air to slowly evaporate. Dark purple crystals were harvested by filtration after a day. Yield 15.2 mg (44 % based on Ru). IR: Nujol mulls on KBr plates: ν(CN) 2194.0 and 2150.3 cm^{-1}, δ(C-H, TCNQ) 831.9 and 849.0 cm^{-1}.

$[Zn(terpy)_2](TCNQ)_{2.5} \cdot 3CH_3CN$ (8). A solution of 0.11 mmol (25.1 mg) of terpy and 0.05 mmol (18.3 mg) of $Zn(ClO_4)_2 \cdot 6H_2O$ in 2 mL of CH_3CN was filtered to remove insoluble impurities. To this solution was added a solution of 0.1 mmol (51.2 mg) of $(Et_3NH)(TCNQ)_2$ in 6 mL of CH_3CN through glass wool. Dark blue crystals formed after a few minutes. The product was filtered and rinsed with acetonitrile after 60 min. Yield 24.1 mg (41 % based on Zn). IR: Nujol mulls on KBr plates: ν(CN) 2199.2 and 2149.4 cm^{-1}, δ(C-H, TCNQ) 825.0 cm^{-1}.

Magnetic and conductivity measurements

Magnetic measurements were carried out using a Quantum design MPMS-XL SQUID instrument over the temperature range 1.8-300 K. The diamagnetic contributions of the atoms and sample holders were accounted for during the data analysis process by using Pascal's constants.

The four-probe method was used on single crystal samples of $[Ru(bpy)_3](TCNQ)_4$ and $[Ru(terpy)_2](TCNQ)_3 \cdot CH_3CN$ to measure the resistivity with gold wires attached to the thin needle-like single crystals using gold paste. The temperature was controlled by using the cryrogenics of a SQUID MPMS instrument at a

rate of 2 K/min and stabilized at each point for 60 s before the next measurement was made to allow for thermal equilibration of the samples. For $[Zn(terpy)_2](TCNQ)_{2.5} \cdot 3CH_3CN$, single crystal conductivity measurements were performed by the two-probe method on the MPMS-XL SQUID magnetometer over the temperature range of 100-300K with a constant current source. Conductivity measurements on samples of $[Dy(TPMA)(\mu\text{-}TCNQ)(\mu\text{-}OH)](TCNQ)_2 \cdot CH_3CN$ and $[Co(Tpm)_2](TCNQ)_3$ was carried out on pressed pellets of polycrystalline samples with the four-probe and two-probe method respectively.

Single crystal X-ray crystallography

Single-crystal X-ray data were collected at different temperatures on a Bruker APEX CCD diffractometer equipped with a graphite monochromated MoKα radiation source (λ=0.71073 Å). Suitable crystals were affixed onto a nylon loop with Paratone oil and place in a cold steam of N_2(g). The data sets were recorded by the ω-scan mehod and integrated followed by an absorption correction in the Bruker APEX II software package. Solution and refinement of the crystal structures were carried out using the SHELXT[139] and SHELXL[140] programs and the graphical interface Olex2.[141] Hydrogen atoms were placed at calculated positions.

Powder X-ray diffraction

Powder X-ray diffraction data were measured on a Bruker D8 powder X-ray diffractometer at room temperature. Phase purity of the bulk products were confirmed by powder X-ray diffraction patterns which were compared with the simulated powder patterns obtained from the single crystal X-ray structural data.

Results and Discussions

Lanthanide-TCNQ-based electrical conducting SMM

Syntheses and structures. Dy(III)-based SMMs have been studied extensively due to superior properties of strong spin-orbit coupling and large magnetic moment. Our design strategy is to use TCNQ- radicals as bridging ligands to realize large spin ground states. A tetradentate capping ligand, tris(pyridylmethyl)amine (TPMA), was employed to restrict the number of available coordination sites of the Dy(III) ion. Dark purple crystals of [Dy(TPMA)(μ-TCNQ)(μ-OH)](TCNQ)2 ·CH3CN formed in a few minutes when a solution of (Et3NH)(TCNQ)2 in acetonitrile was added to a solution of Dy(III) trifluoromethanesulfonate and TPMA in acetonitrile. The compound crystallizes in the triclinic space group P-1 (Table 10) with the asymmetric unit being composed of one Dy(III) ion coordinated to one TPMA, one TCNQ radical and one hydroxide anion, in addition to two uncoordinated TCNQ species and one acetonitrile molecule (Figure 41).

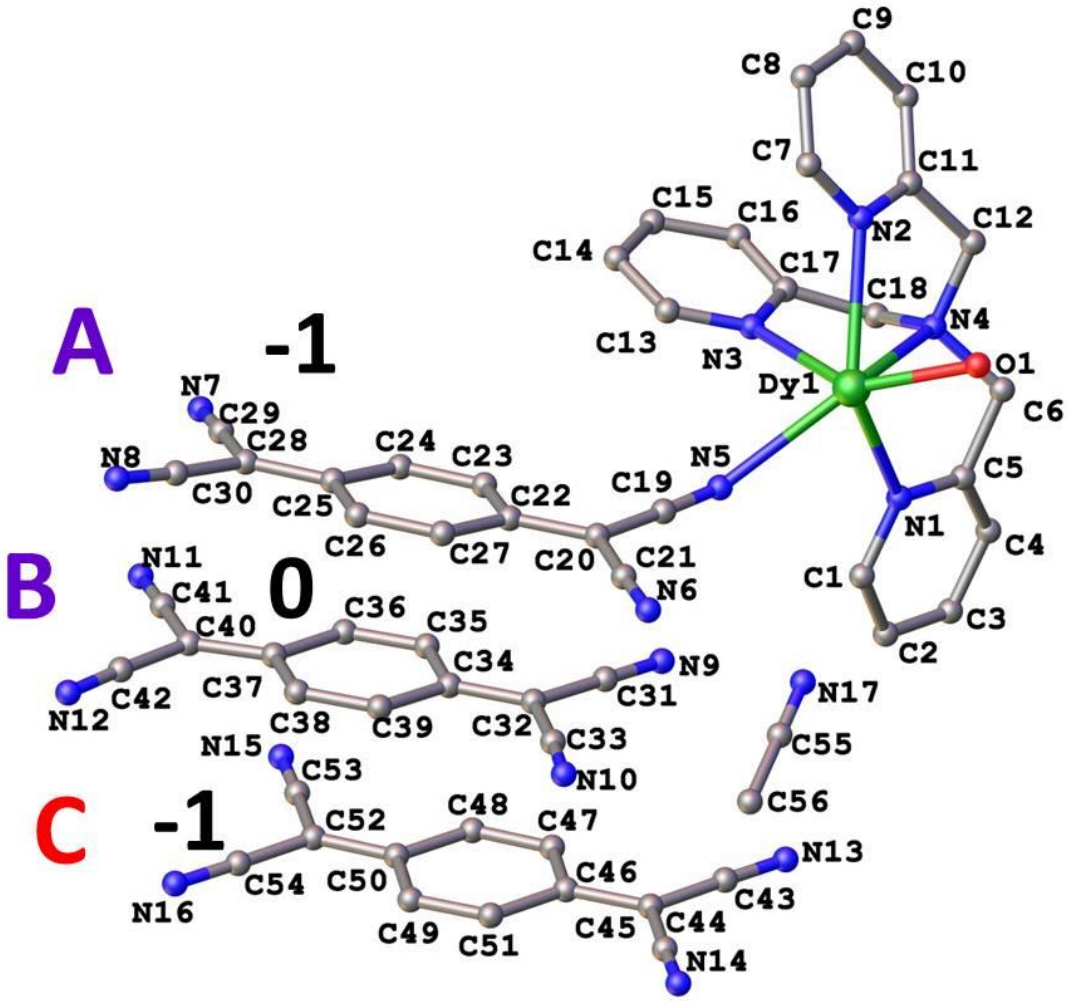

Figure 41. Asymmetric unit of **[**Dy(TPMA)(μ-TCNQ)(μ-OH)](TCNQ)$_2$ CH_3CN. Hydrogen atoms are omitted for the sake of clarity.

The presence of hydroxide groups were justified by the charge balance of the formula unit as two of the TCNQ species are monoanions and the third one is neutral (Table 9). In addition, the Dy-O bond lengths of 2.208(6) and 2.251(6) Å fall into the range of Dy-O(hydroxide) distances reported in the literature as compared to Dy-O bond distances for aqua or oxo-groups. The bond angle of Dy-O-Dy is 111.7(3)˚ and the distance between the two Dy(III) ions that are bridged by the hydroxide group is relatively short at 3.6901(8) Å. As the reactions were carried out in air, small amounts of moisture in the solvents or air can lead to hydrolysis of trifluoromethanesulfonate to result in hydroxide groups.

Table 9. The charges (ρ) of different TCNQ species in **[**Dy(TPMA)(*μ*-TCNQ)(*μ*-OH)](TCNQ)$_2$ ·CH_3CN at 100 K as estimated from the Kistenmacher's formula (A, B, C as denoted in Figure 41; b, c and d are average C-C bond distances as depicted below).

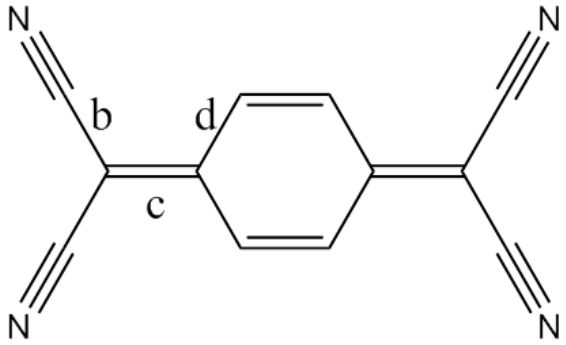

TCNQ	b /Å	c /Å	d /Å	ρ
A	1.415	1.411	1.420	-0.90
B	1.435	1.370	1.438	-0.03
C	1.416	1.406	1.426	-0.77

The Dy(III) ion is eight coordinate with four nitrogen donors from the TPMA ligand, two nitrogen atoms from two bridging TCNQ species and two oxygen atoms from the two bridging hydroxide groups. The structure can also be viewed as a chain of $[Dy(TPMA)(\mu\text{-}TCNQ)(\mu\text{-}OH)]_2$ organized via π-π stacking interactions of the TCNQ species (Figure 42 and Figure 43).

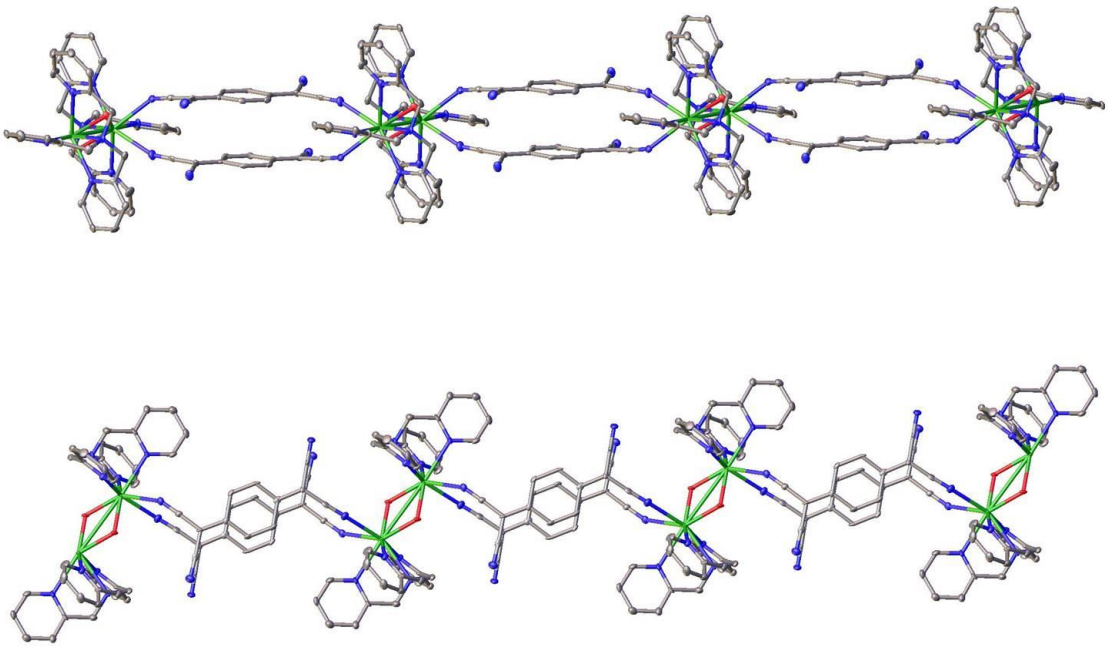

Figure 42. Perspective views of the structure of $[Dy(TPMA)(\mu\text{-}TCNQ)(\mu\text{-}OH)](TCNQ)_2 \cdot CH_3CN$ showing the bridging TCNQ radicals and the bridging hydroxide moieties.

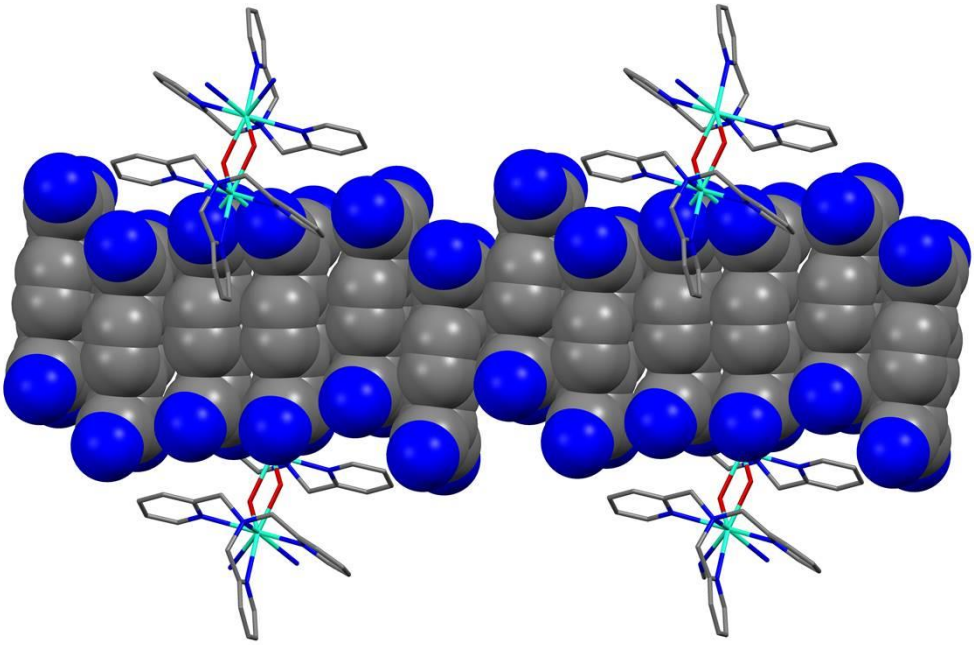

Figure 43. Packing diagram of structure of **[**Dy(TPMA)(μ-TCNQ)(μ-OH)](TCNQ)$_2$ CH_3CN showing the π-π stacking interactions between the TCNQ species.

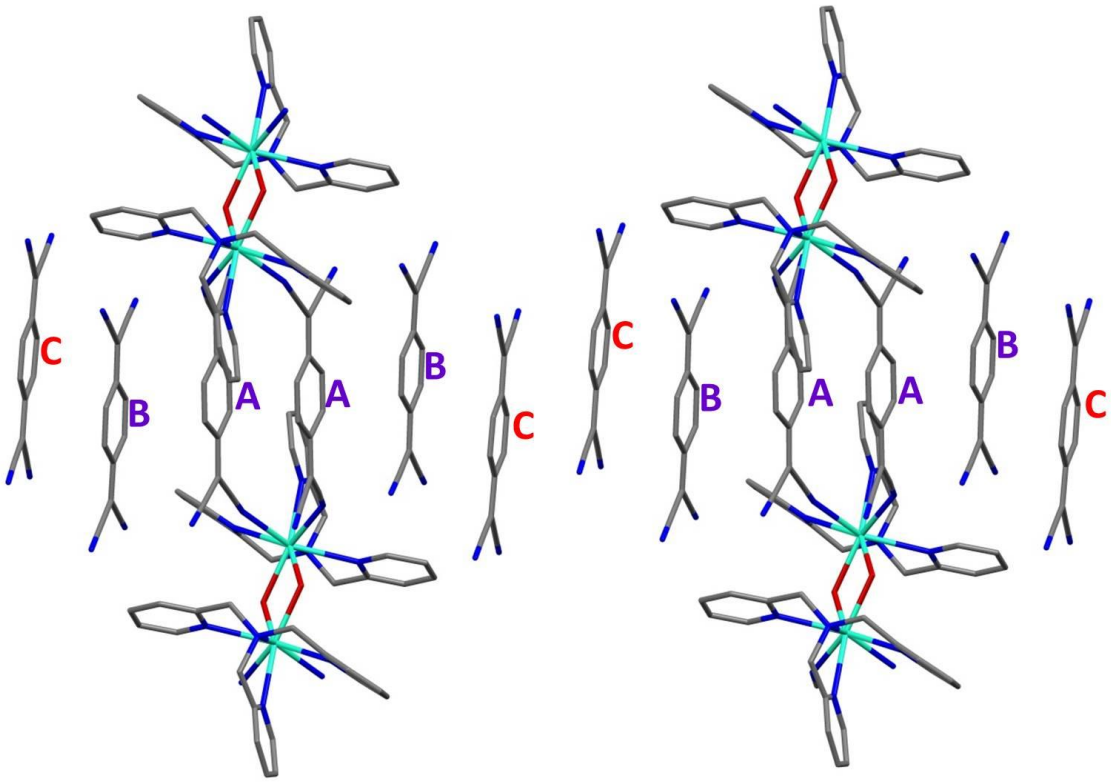

Figure 44. Packing diagram of [Dy(TPMA)(μ-TCNQ)(μ-OH)](TCNQ)$_2$ CH_3CN showing the different TCNQ species (denoted as A, B and C) stacked together.

Similar compounds of [Y(TPMA)(μ-TCNQ)(μ-OH)](TCNQ)$_2$ CH_3CN and [Gd(TPMA)(μ-TCNQ)(μ-OH)](TCNQ)$_2$ CH_3CN were prepared from the same method by using Y(III) trifluoromethanesulfonate and Gd(III) trifluoromethanesulfonate, respectively, instead of the Dy(III) trifluoromethanesulfonate in the synthesis of [Dy(TPMA)(μ-TCNQ)(μ-OH)](TCNQ)$_2$ CH_3CN. The series [Ln(TPMA)(μ-TCNQ)(μ-OH)](TCNQ)$_2$ CH_3CN (Ln = Y, Gd and Dy) is isostructural as judged by powder X-ray diffractions pattern data (Figure 45).

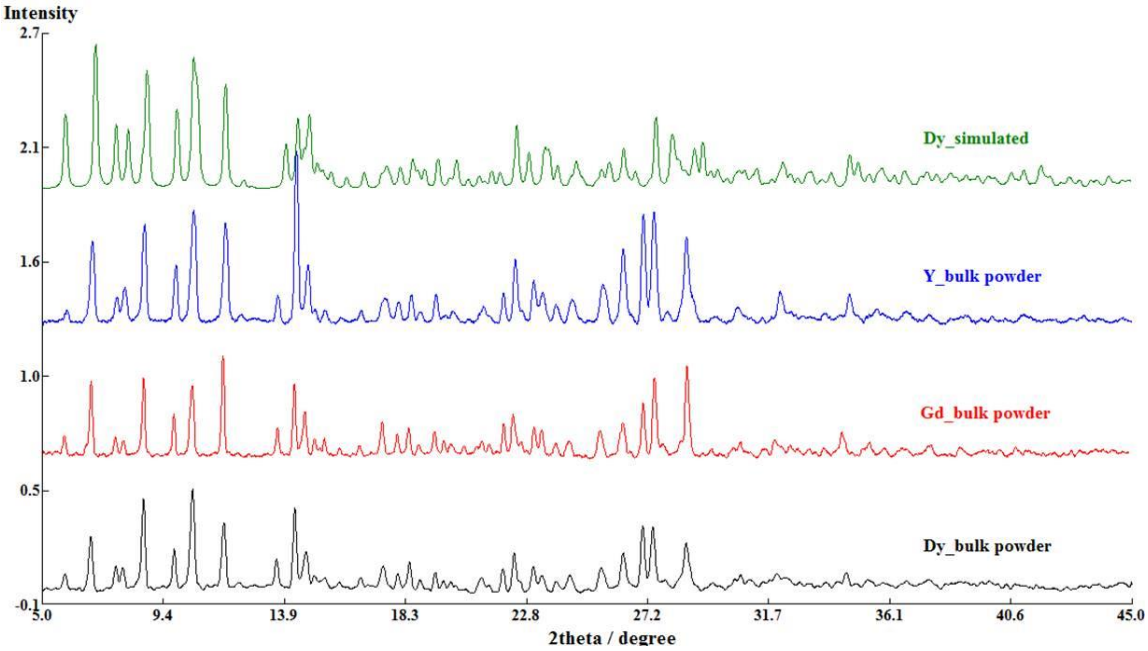

Figure 45. Powder X-ray diffraction patterns of [Ln(TPMA)(μ-TCNQ)(μ-OH)](TCNQ)$_2$ CH_3CN (Ln = Y, Gd, Dy). The green trace is a simulation produced from single-crystal X-ray diffraction data of [Dy(TPMA)(μ-TCNQ)(μ-OH)](TCNQ)$_2$ CH_3CN and the other three are from bulk polycrystalline samples.

Table 10. Summary of crystallographic parameters for **[**Dy(TPMA)(μ-TCNQ)(μ-OH)](TCNQ)$_2$ CH_3CN.

Empirical formula	$C_{56}H_{33}DyN_{17}O$
Formula weight	1122.49
Temperature/K	100
Crystal system	triclinic
Space group	P-1
a/Å	12.0565(11)
b/Å	13.3616(13)
c/Å	15.5728(14)
α/°	98.761(2)
β/°	98.832(2)
γ/°	104.227(2)
Volume/Å^3	2355.1(4)
Z	2
ρ_{calc}g/cm^3	1.583
μ/mm^{-1}	1.650
F(000)	1124.0
Crystal size/mm^3	0.08 × 0.07 × 0.04
Radiation	MoKα (λ = 0.71073)
2Θ range for data collection/°	4.934 to 46.656
Index ranges	$-13 \leq h \leq 13$, $-14 \leq k \leq 14$, $-17 \leq l \leq 17$
Reflections collected	78503
Independent reflections	6800 [R_{int} = 0.1873, R_{sigma} = 0.1056]
Data/restraints/parameters	6800/31/627
Goodness-of-fit on F^2	1.125
Final R indexes [I>=2σ (I)]	R_1 = 0.0661, wR_2 = 0.0958
Final R indexes [all data]	R_1 = 0.1046, wR_2 = 0.1067
Largest diff. peak/hole / e Å^{-3}	1.26/-1.82

$R_1 = \Sigma||F_o|-|F_c||/\Sigma|F_o|$. $wR_2=[\Sigma w(|F_o|-|F_c|)^2/|\Sigma w(F_o)^2]^{1/2}$. $w= 0.75/(\sigma^2(F_o)+0.00010F_o^2)$.

Goodness-of-fit = $\{\sum[w(F_o^2 - F_c^2)^2]/(n-p)\}^{1/2}$, where n is the number of reflections and p is the total number of parameters refined.

Table 11. Bond distances of **[**Dy(TPMA)(μ-TCNQ)(μ-OH)](TCNQ)$_2$ CH_3CN.

Atom	Atom	Length/Å		Atom	Atom	Length/Å
Dy1	Dy1[1]	3.6901(8)		C27	C26	1.370(10)
Dy1	O1	2.208(6)		C13	C14	1.370(11)
Dy1	O1[1]	2.251(6)		C1	C2	1.386(11)
Dy1	N4	2.558(6)		C14	C15	1.368(11)
Dy1	N5	2.550(7)		C4	C3	1.380(11)
Dy1	N1	2.518(6)		C8	C9	1.364(11)
Dy1	N2	2.615(7)		C8	C7	1.367(12)
Dy1	N8[2]	2.525(7)		C3	C2	1.374(10)
Dy1	N3	2.513(6)		C38	C37	1.428(11)
O1	Dy1[1]	2.251(6)		C38	C39	1.336(10)
N4	C6	1.473(9)		C37	C36	1.450(10)
N4	C12	1.478(10)		C37	C40	1.368(11)
N4	C18	1.480(9)		C35	C36	1.329(10)
N5	C19	1.152(9)		C35	C34	1.437(10)
N1	C5	1.345(9)		C41	C40	1.437(12)
N1	C1	1.341(10)		C41	N11	1.146(9)
N2	C11	1.337(9)		C40	C42	1.442(11)
N2	C7	1.345(10)		C52	C54	1.405(11)
N8	Dy1[2]	2.525(7)		C52	C49	1.392(10)
N8	C30	1.152(9)		C52	C53	1.438(12)
N6	C21	1.154(10)		C48	C49	1.435(10)
N3	C17	1.340(9)		C48	C47	1.342(10)
N3	C13	1.349(9)		C54	N16	1.154(9)
C6	C5	1.497(11)		C49	C50	1.423(10)
C28	C30	1.416(11)		C53	N15	1.143(9)
C28	C29	1.423(11)		C51	C46	1.430(10)
C28	C25	1.414(10)		C51	C50	1.341(10)
C11	C12	1.494(11)		N9	C31	1.146(9)
C11	C10	1.372(11)		C46	C47	1.419(10)
N7	C29	1.145(9)		C46	C44	1.416(11)
C19	C20	1.390(11)		C31	C32	1.430(11)
C5	C4	1.363(11)		C32	C34	1.371(10)
C23	C22	1.430(10)		C32	C33	1.430(12)
C23	C24	1.361(10)		C34	C39	1.436(10)
C20	C22	1.407(10)		N12	C42	1.149(10)
C20	C21	1.430(12)		N10	C33	1.144(10)
C22	C27	1.410(10)		C44	C43	1.405(12)
C16	C17	1.373(11)		C44	C45	1.421(12)
C16	C15	1.362(11)		C43	N13	1.135(10)
C10	C9	1.381(11)		C45	N14	1.148(9)
C25	C24	1.427(10)		C56	C55	1.448(12)
C25	C26	1.414(10)		N17	C55	1.124(10)
C18	C17	1.497(10)				

Table 12. Bond angles of **[**Dy(TPMA)(μ-TCNQ)(μ-OH)](TCNQ)$_2$ CH_3CN.

Atom	Atom	Atom	Angle/°		Atom	Atom	Atom	Angle/°
O1	Dy1	Dy1^1	34.53(16)		C22	C20	C21	121.8(7)
O1^1	Dy1	Dy1^1	33.78(16)		C20	C22	C23	120.4(7)
O1	Dy1	O1^1	68.3(3)		C20	C22	C27	123.0(7)
O1	Dy1	N4	82.49(19)		C27	C22	C23	116.5(7)
O1^1	Dy1	N4	130.40(19)		C15	C16	C17	119.7(8)
O1^1	Dy1	N5	74.2(2)		C11	C10	C9	118.8(7)
O1	Dy1	N5	142.1(2)		N7	C29	C28	177.9(8)
O1	Dy1	N1	98.9(2)		C28	C25	C24	120.2(7)
O1^1	Dy1	N1	81.0(2)		C26	C25	C28	122.6(7)
O1	Dy1	N2	79.1(2)		C26	C25	C24	117.1(7)
O1^1	Dy1	N2	138.5(2)		N4	C18	C17	114.5(6)
O1	Dy1	N8^2	104.2(2)		N6	C21	C20	177.5(8)
O1^1	Dy1	N8^2	87.0(2)		C23	C24	C25	121.6(7)
O1	Dy1	N3	143.0(2)		N3	C17	C16	122.8(7)
O1^1	Dy1	N3	148.4(2)		N3	C17	C18	115.5(7)
N4	Dy1	Dy1^1	108.49(13)		C16	C17	C18	121.5(7)
N4	Dy1	N2	66.2(2)		C26	C27	C22	122.3(7)
N5	Dy1	Dy1^1	107.83(14)		N3	C13	C14	123.7(7)
N5	Dy1	N4	128.2(2)		N1	C1	C2	122.8(7)
N5	Dy1	N2	130.05(19)		C27	C26	C25	121.0(7)
N1	Dy1	Dy1^1	89.88(14)		C15	C14	C13	118.6(7)
N1	Dy1	N4	64.5(2)		C5	C4	C3	119.7(7)
N1	Dy1	N5	80.1(2)		C9	C8	C7	118.4(8)
N1	Dy1	N2	130.4(2)		C8	C9	C10	119.3(8)
N1	Dy1	N8^2	147.8(2)		C2	C3	C4	118.2(7)
N2	Dy1	Dy1^1	110.09(14)		C3	C2	C1	119.1(8)
N8^2	Dy1	Dy1^1	96.58(15)		N2	C7	C8	123.5(8)
N8^2	Dy1	N4	140.2(2)		C16	C15	C14	118.9(8)
N8^2	Dy1	N5	67.9(2)		C39	C38	C37	121.8(7)
N8^2	Dy1	N2	76.5(2)		C38	C37	C36	116.8(7)
N3	Dy1	Dy1^1	175.95(14)		C40	C37	C38	120.7(7)
N3	Dy1	N4	67.54(19)		C40	C37	C36	122.5(7)
N3	Dy1	N5	74.8(2)		C36	C35	C34	121.4(7)
N3	Dy1	N1	87.6(2)		C35	C36	C37	121.4(7)
N3	Dy1	N2	69.4(2)		N11	C41	C40	179.0(9)
N3	Dy1	N8^2	87.2(2)		C37	C40	C41	122.6(7)
Dy1	O1	Dy1^1	111.7(3)		C37	C40	C42	120.6(7)
C6	N4	Dy1	107.1(4)		C41	C40	C42	116.9(7)

Table 12. Continued.

Atom	Atom	Atom	Angle/°		Atom	Atom	Atom	Angle/°
C12	N4	Dy1	109.7(4)		C49	C52	C53	123.1(7)
C6	N4	C18	108.9(6)		C49	C52	C54	122.6(7)
C12	N4	C18	109.5(6)		C47	C48	C49	121.4(7)
C18	N4	Dy1	111.6(4)		N16	C54	C52	178.0(9)
C19	N5	Dy1	142.6(6)		C52	C49	C48	121.5(7)
C5	N1	Dy1	119.4(5)		C52	C49	C50	121.9(7)
C1	N1	Dy1	123.6(5)		C50	C49	C48	116.6(7)
C1	N1	C5	117.0(7)		N15	C53	C52	177.3(8)
C11	N2	Dy1	116.4(5)		C50	C51	C46	121.6(7)
C11	N2	C7	117.1(7)		C47	C46	C51	116.7(7)
C7	N2	Dy1	125.3(5)		C44	C46	C51	121.6(7)
C30	N8	Dy1[2]	158.4(6)		C44	C46	C47	121.7(7)
C17	N3	Dy1	119.6(5)		N9	C31	C32	179.0(9)
C17	N3	C13	116.3(6)		C31	C32	C33	117.1(7)
C13	N3	Dy1	122.2(5)		C34	C32	C31	122.7(7)
N4	C6	C5	109.8(6)		C34	C32	C33	120.3(7)
C30	C28	C29	114.5(6)		C32	C34	C35	122.0(7)
C25	C28	C30	123.4(7)		C32	C34	C39	120.6(7)
C25	C28	C29	122.1(7)		C39	C34	C35	117.4(7)
N2	C11	C12	116.2(7)		C48	C47	C46	121.9(7)
N2	C11	C10	122.7(7)		N12	C42	C40	177.7(9)
C10	C11	C12	121.1(7)		C51	C50	C49	121.7(7)
N4	C12	C11	112.2(6)		C38	C39	C34	121.2(7)
N5	C19	C20	176.1(8)		C46	C44	C45	121.9(7)
N1	C5	C6	114.4(7)		C43	C44	C46	122.0(7)
N1	C5	C4	123.1(7)		C43	C44	C45	116.1(7)
C4	C5	C6	122.4(7)		N13	C43	C44	179.1(10)
C24	C23	C22	121.4(7)		N14	C45	C44	178.5(9)
N8	C30	C28	176.5(9)		N10	C33	C32	176.2(9)
C19	C20	C22	122.2(7)		N17	C55	C56	178.1(10)
C19	C20	C21	115.9(7)					

[1]1-X,1-Y,1-Z; [2]1-X,1-Y,-Z

Magnetic properties. Temperature dependent magnetic susceptibility studies of [Dy(TPMA)(μ-TCNQ)(μ-OH)](TCNQ)$_2$·CH$_3$CN were carried out at under a static DC field of 1000 Oe over the temperature range of 300-1.8 K (Figure 46). The χT value remains nearly constant at 14.6 emu·K·mol^{-1} (per formula unit) as the temperature is lowered to ~100 K, with the χT value of 14.6 emu·K·mol^{-1} at 300 K matching well with contributions from one Dy(III) ion and one TCNQ$^{\bullet-}$ (Dy(III), $4f^9$, $^6H_{15/2}$, J = 15/2, L = 5, S = 5/2, g = 1.33; TCNQ$^{\bullet-}$, S = 1/2, g = 2.0). Below 100 K, the χT value gradually decreases to a minimum value of 13.2 emu·K·mol^{-1} at ~6 K, which is possibly due to the antiferromagnetic coupling between the spin centers and/or the thermal depopulation of the excited Stark sublevels of Dy(III) ions as the temperature decreases. As the temperature is further lowered, the χT value exhibits an increase to a maximum of 13.5 emu·K·mol^{-1} at 2 K, indicating the presence weak ferromagnetic interactions between the spin centers (*vide infra*). Below 2 K, the χT value drops to 13.4 emu·K·mol^{-1}.

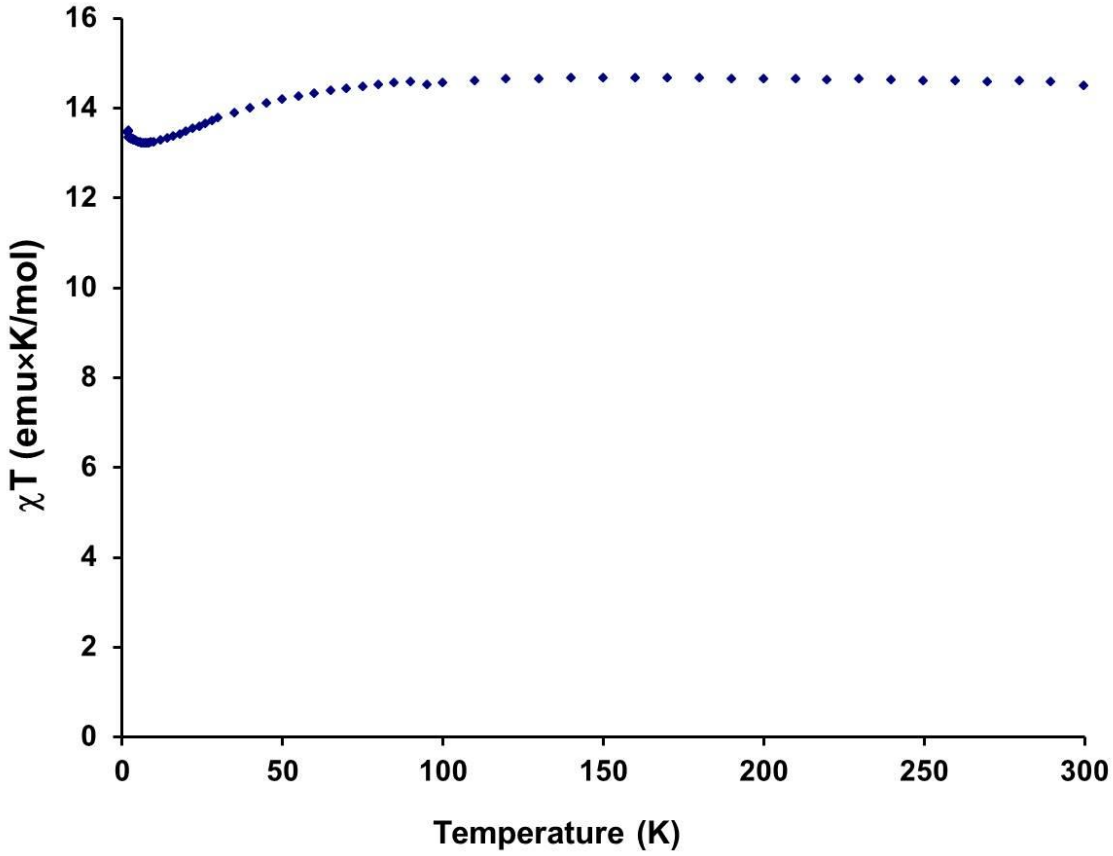

Figure 46. Temperature dependence of χT of [Dy(TPMA)(μ-TCNQ)(μ-OH)](TCNQ)$_2$ CH_3CN under a 1000 Oe applied magnetic field.

The expected magnetic moment for one Dy(III) and one $TCNQ^{\bullet-}$ radical is ~12.4 Bohr magnetons but the observed magnetic moment of [Dy(TPMA)(μ-TCNQ)(μ-OH)](TCNQ)$_2$ CH_3CN is ~5.8 Bohr magnetons at 1.8 K and 7 T (Figure 47). The lack of magnetization saturation even at 7 T in the field-dependent magnetization at 1.8 K supports the presence of significant magnetic anisotropy as expected for Dy(III) compounds.

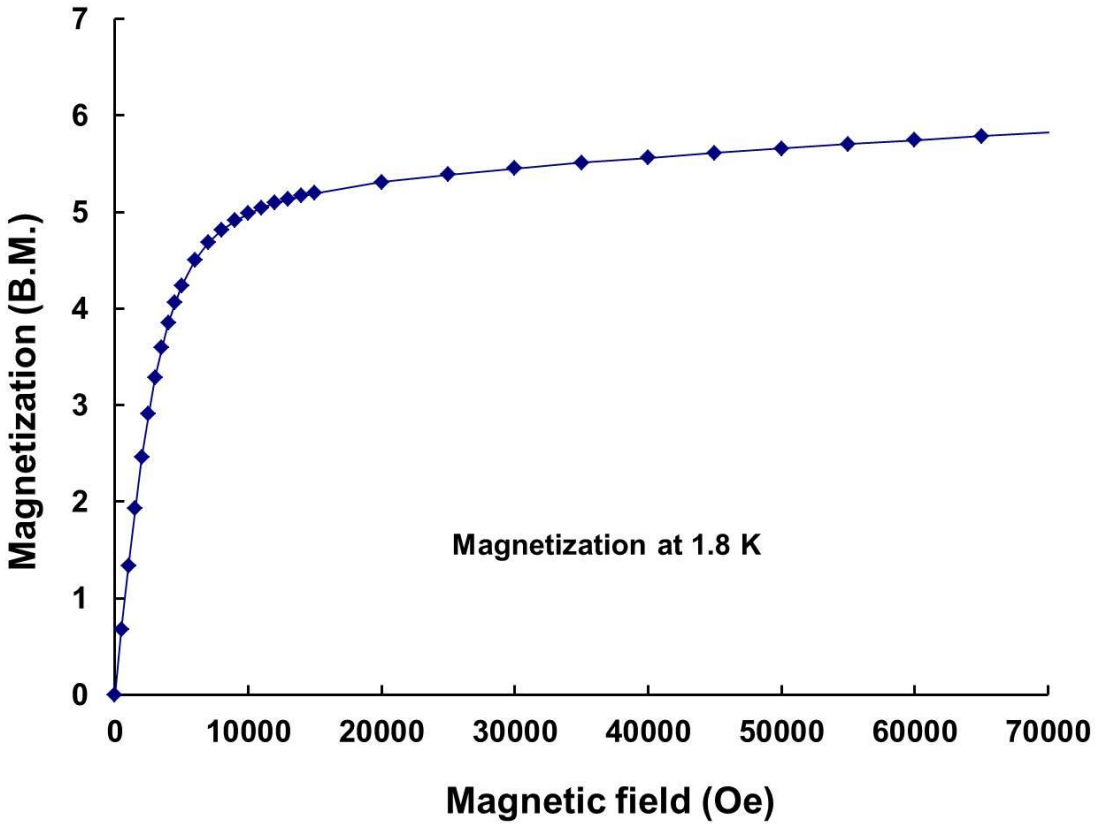

Figure 47. Field dependence of the magnetization of [Dy(TPMA)(μ-TCNQ)(μ-OH)](TCNQ)$_2$ $\cdot$CH$_3$CN at 1.8 K.

AC magnetic susceptibility measurements were preformed to probe the dynamic properties of [Dy(TPMA)(μ-TCNQ)(μ-OH)](TCNQ)$_2$ $\cdot$CH$_3$CN. Under a zero applied DC field, only a beginning in the out-of-phase (χ") AC signals was observed down to 1.8 K (Figure 48). This result is indicative of slow relaxation of the magnetization but it is possible that due fast quantum tunneling of the magnetization, no peaks in the out-of-phase signal can be observed above 1.8 K, which is the lower limit of the instrument.

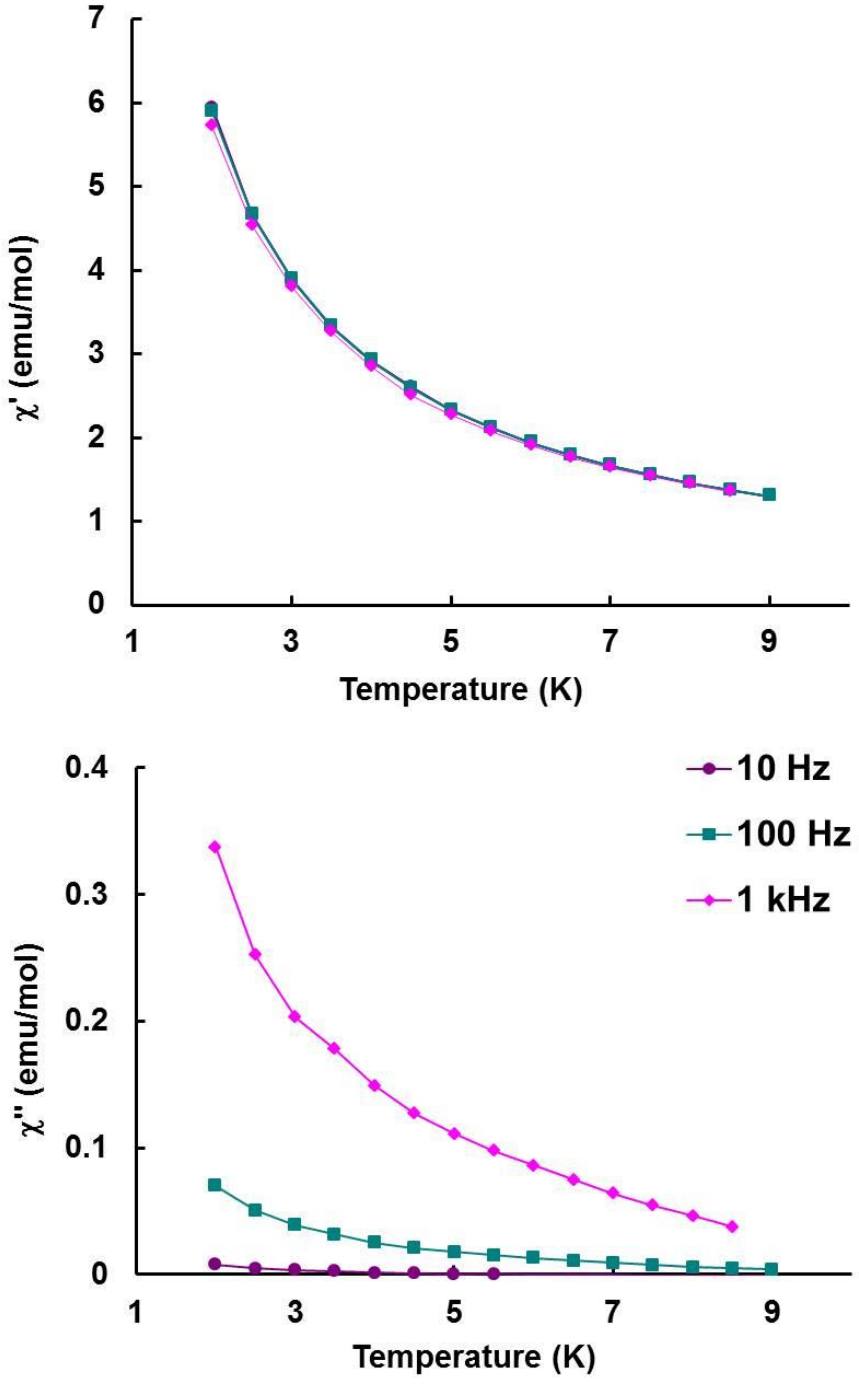

Figure 48. Temperature dependence of the in-phase (top) and out-of-phase (bottom) AC magnetic susceptibilities of [Dy(TPMA)(μ-TCNQ)(μ-OH)](TCNQ)$_2$ CH_3CN under a zero applied DC magnetic field.

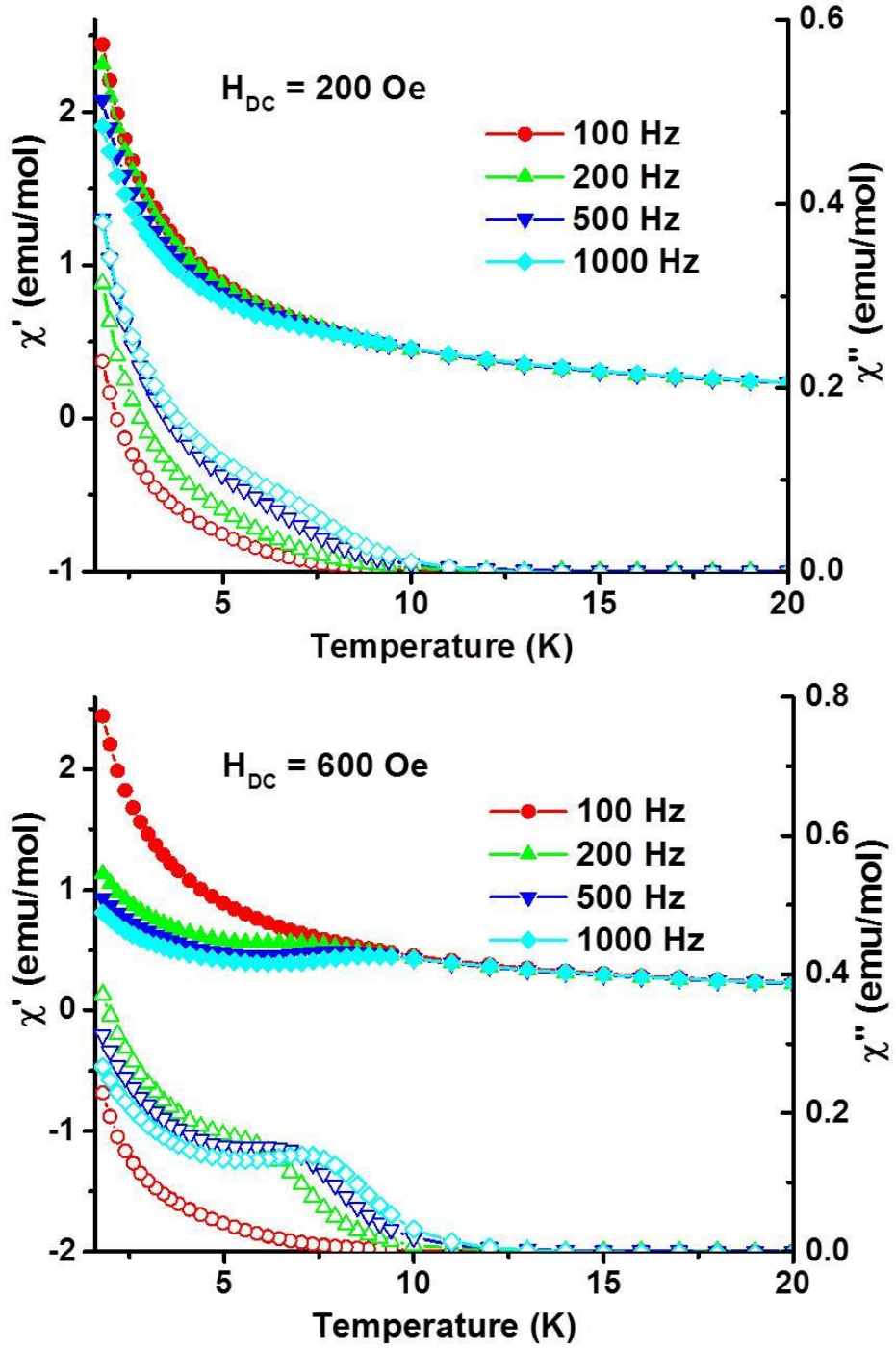

Figure 49. Temperature dependence of the in-phase (solid symbols) and out-of-phase AC magnetic susceptibilities of [Dy(TPMA)(μ-TCNQ)(μ-OH)](TCNQ)$_2$ CH_3CN under applied DC magnetic fields of 200 Oe (top) and 600 Oe (bottom).

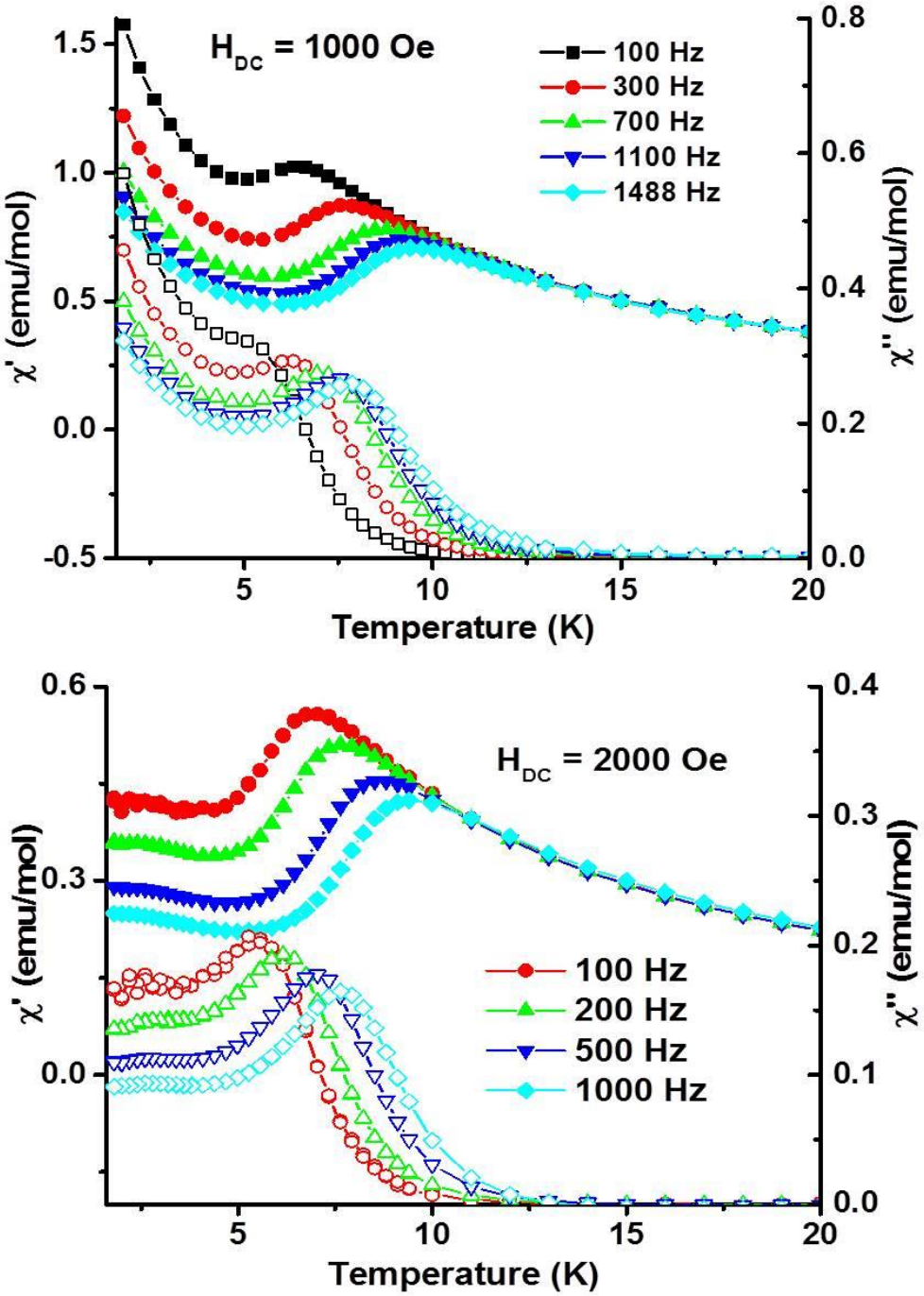

Figure 50. Temperature dependence of the in-phase (solid symbols) and out-of-phase AC magnetic susceptibilities of [Dy(TPMA)(μ-TCNQ)(μ-OH)](TCNQ)$_2$ CH_3CN under applied DC magnetic fields of 1000 Oe (top) and 2000 Oe (bottom).

Given this result, DC magnetic fields of different magnitudes were applied for the AC magnetic measurement to probe the slow relaxation of the magnetization. As the DC field is increased from 200 to 1000 Oe, a series of frequency-dependent peaks in the out-of-phase (χ") signals appear over the temperature range of 5-8 K (Figure 49 and Figure 50). At 2000 Oe, quantum tunneling has been minimized and a field-induced slow relaxation of the magnetization behavior is observed. This is solely a thermally activated relaxation process as the relaxation time can be fitted well to an Arrhenius law to yield an effective energy barrier for the reversal of magnetization of 43.4 K with a pre-exponential factor of $\tau_0 = 7.8 \times 10^{-7}$ s (Figure 51).

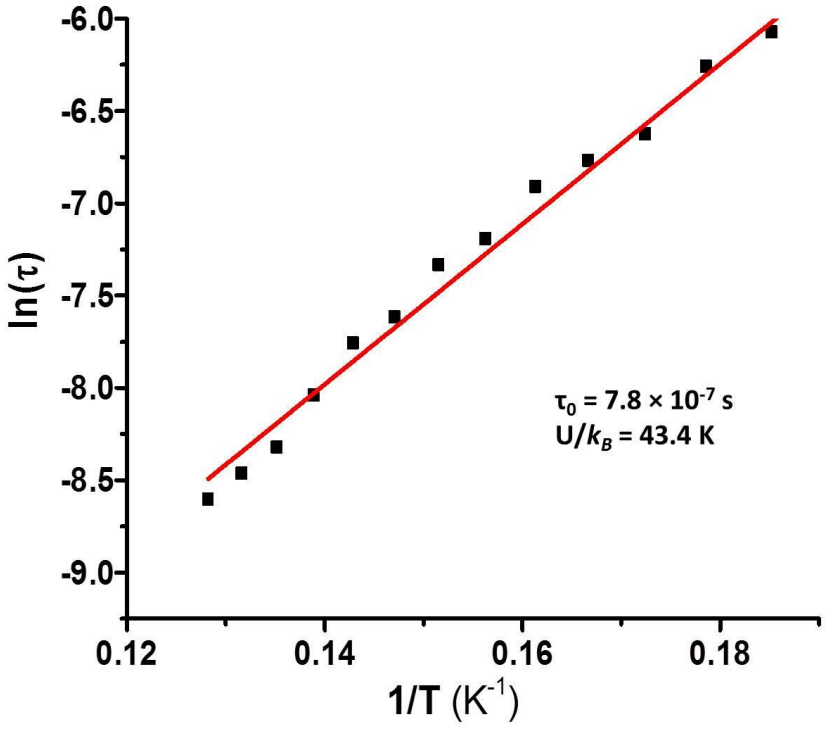

Figure 51. Arrhenius plot of the relaxation time, as determined from variable-temperature AC susceptibilities of [Dy(TPMA)(μ-TCNQ)(μ-OH)](TCNQ)$_2$ CH_3CN at temperatures between 5 and 11 K and under a 1000 Oe DC magnetic field.

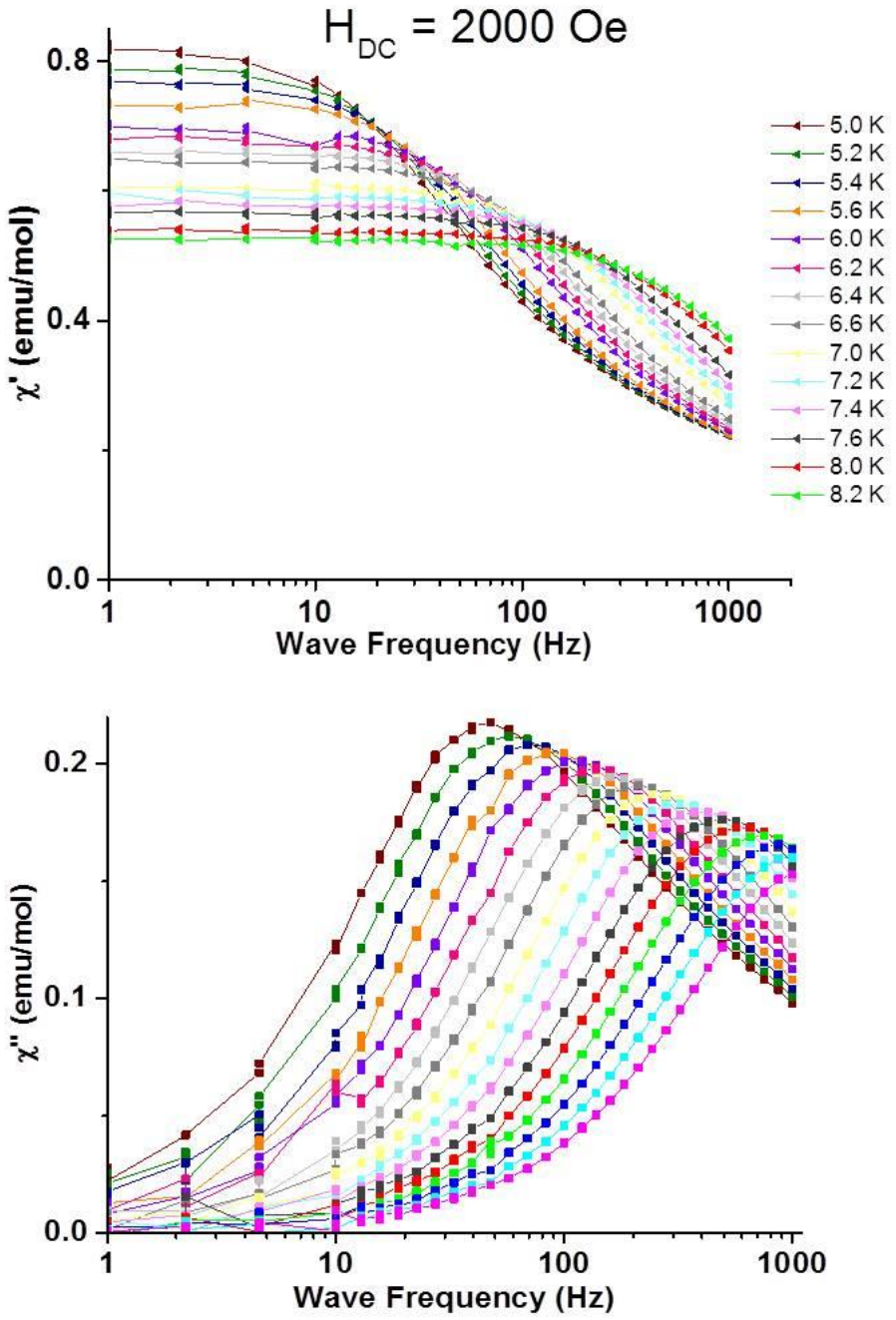

Figure 52. Frequency dependence of in-phase (top) and out-of-phase (bottom) AC magnetic susceptibilities of [Dy(TPMA)(μ-TCNQ)(μ-OH)](TCNQ)$_2$ CH_3CN at different temperatures under an applied DC magnetic field of 2000 Oe.

As the dynamic magnetic properties of [Dy(TPMA)(μ-TCNQ)(μ-OH)](TCNQ)$_2$·CH$_3$CN show a dependence on the applied DC magnetic field, its temperature dependent magnetic susceptibilities were also investigated under various DC magnetic fields in order to probe the effect of external DC fields on the magnetic interactions in [Dy(TPMA)(μ-TCNQ)(μ-OH)](TCNQ)$_2$·CH$_3$CN. Below 2000 Oe the χT values showed pronounced increases at ~2 K, indicating the presence of weak ferromagnetic interactions at low fields (Figure 53). Another feature that is worth noting is that the peaks in the χT plots at 2 K diminish as the fields are increased and disappear when the fields are above 3000 Oe, indicating that these weak ferromagnetic interactions are suppressed by the application of external DC magnetic fields. These observations taken together with the AC studies suggest that the application of DC magnetic fields in this case not only suppresses the quantum tunneling of the magnetization, but also tunes the magnetic interactions in [Dy(TPMA)(μ-TCNQ)(μ-OH)](TCNQ)$_2$·CH$_3$CN. However, due to the possible complications of the system involving magnetic anisotropy of Dy(III) ions, the super-exchange interactions between the Dy(III) ions through both the TCNQ radicals and hydroxide groups, as well as the inter-chain interactions through the π-π stacking interactions between the TCNQ species, makes it highly challenging to decipher the magnetic properties.

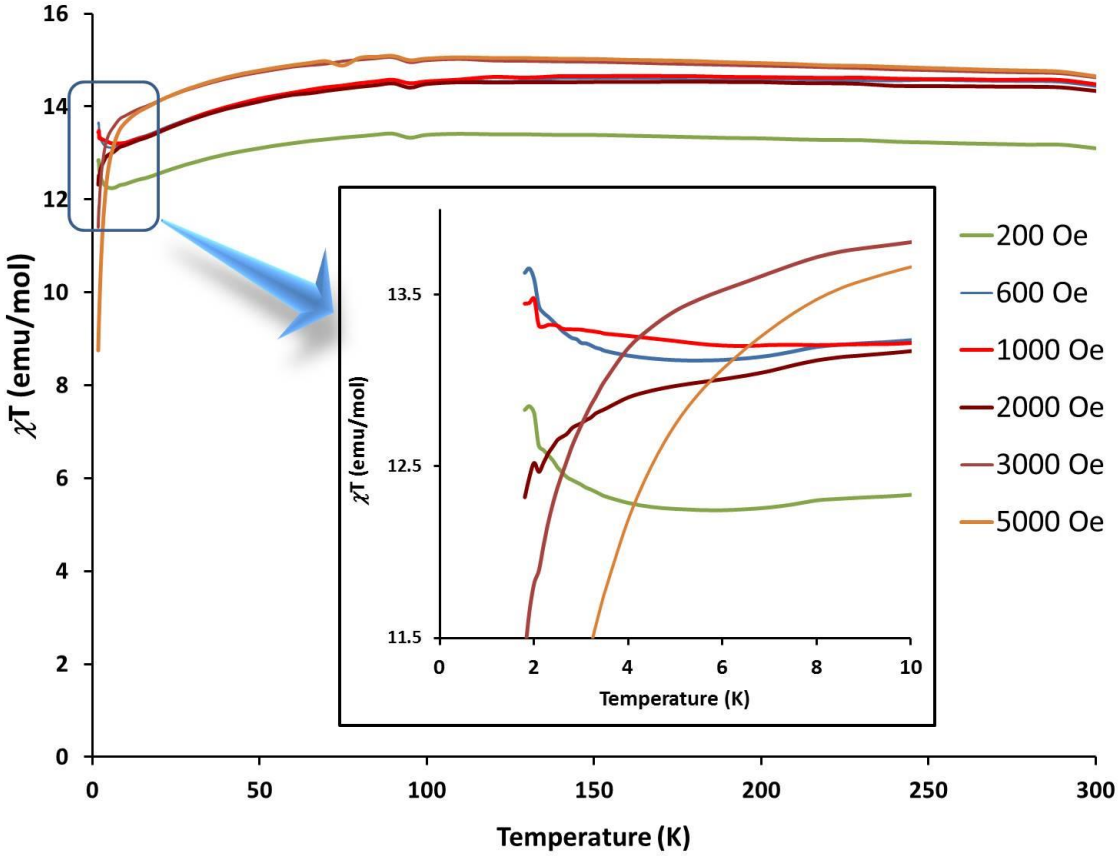

Figure 53. Temperature dependence of χT for [Dy(TPMA)(μ-TCNQ)(μ-OH)](TCNQ)$_2$·CH$_3$CN under different applied DC magnetic fields. The inset shows the low temperature region as indicated.

In order to simplify the system by eliminating some of the factors mentioned above, the isostructural compound, [Gd(TPMA)(μ-TCNQ)(μ-OH)](TCNQ)$_2$·CH$_3$CN was synthesized. Because Gd(III) ions are isotropic (S = 7/2, g = 2.0), the compound will serve as a model for the study of the magnetic interactions between the lanthanide ions through TCNQ radicals and hydroxide bridges without the complication of magnetic anisotropy. Variable temperature magnetic susceptibility studies were first carried out under a DC magnetic field of 1000 Oe. The χT values remain almost unchanged from 300 down to 100 K, below which temperature they decrease gradually at first then abruptly as the temperature reaches 1.8 K (Figure 54, top). The χT value of 8.3 emu·K·mol^{-1} at 300 K matches well with the presence of one Gd(III) ion and one TCNQ radical (Gd(III), S = 7/2, g = 2.0; TCNQ radical, S = 1/2, g = 2.0). Fitting of the experimental data to a Curie-Weiss law $\chi = C/(T-\theta)$ results in a Curie constant C of 8.3 emu·K·mol^{-1} and a Weiss constant θ of -2.5 K. The negative Weiss constant is a characteristic of antiferromagnetic interactions in this compound. The temperature dependence of the magnetic susceptibilities were also measured at different DC magnetic fields in which the iso-field lines overlapped quite well (Figure 54, bottom), suggesting that the magnitude of the DC magnetic field has no discernable effect on the magnetic interactions.

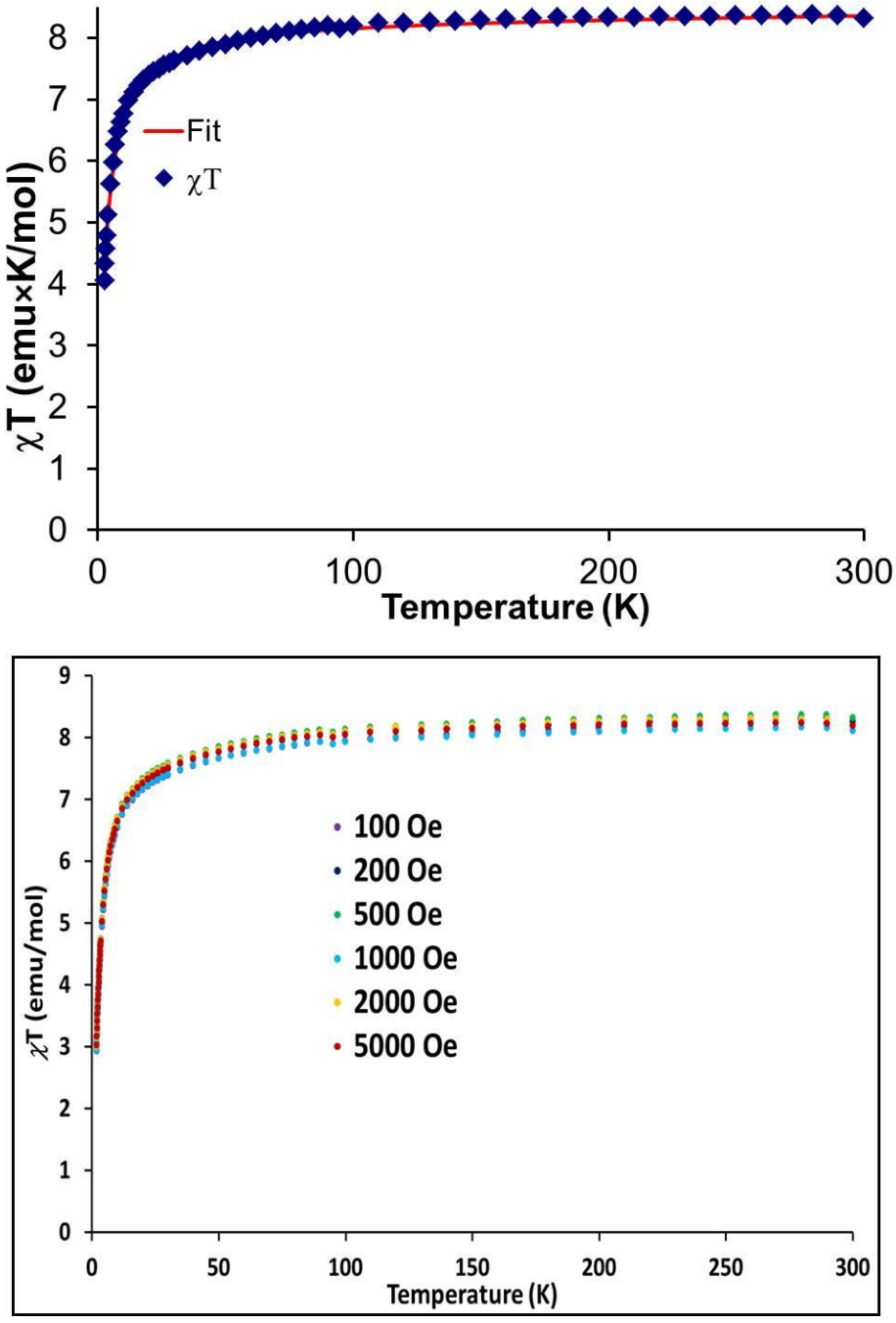

Figure 54. Top: Experimental data and fitted line of the temperature dependence of χT for [Gd(TPMA)(μ-TCNQ)(μ-OH)](TCNQ)$_2$ CH_3CN under a 1000 Oe applied magnetic field. Bottom: the temperature dependence of the χT product of [Gd(TPMA)(μ-TCNQ)(μ-OH)](TCNQ)$_2$ CH_3CN under different applied DC magnetic fields.

Two facts are established by the comparison of the isostructural Gd(III) and Dy(III) compounds, namely that the magnetic field dependent responses in the magnetic interactions in the Dy(III) compound is due to the contribution of magnetic anisotropy and that antiferromagnetic interactions are dominant in the system. As a result, the increase of χT at low temperatures at low magnetic fields is likely due to spin-canting of the anisotropic Dy(III) centers, which are coupled by antiferromagnetic interactions through the TCNQ radical and hydroxide bridges.

Other possible contributors to the magnetic interactions of the spin centers are the inter-chain interactions through the π-π stacking of the TCNQ species, although it may be quite small compared to the super-exchange interactions through the TCNQ radical and hydroxide bridges. In order to investigate the magnetic interactions of the π-π stacked TCNQ species, another isostructural Y(III) compound, [Y(TPMA)(μ-TCNQ)(μ-OH)](TCNQ)$_2$·CH_3CN was prepared. As Y(III) is diamagnetic, the only magnetic contribution of the magnetic moment is from the paramagnetic TCNQ radicals. Fitting of the experimental data in the high temperature region of 20-300 K to a Curie-Weiss law with a correction for temperature-independent paramagnetism (TIP), $\chi = C/(T-\theta) + TIP$, results in a Curie constant C = 0.33 emu·K·mol^{-1}, a Weiss constant θ = -42 K and a TIP of 6.8×10^{-4} emu·mol^{-1}. The large negative Weiss constant indicates strong antiferromagnetic interactions between the stacked TCNQ radicals. The presence of a significant TIP is attributed to Pauli paramagnetism due to the delocalized electrons in the stacked TCNQ species.[160] The temperature-dependent magnetic susceptibilities measured at different DC magnetic fields revealed that iso-field lines overlapped DC

magnetic field affects the delocalization of the electrons on the stacked TCNQ species. The fitting of experimental data collected at 100 Oe of applied DC magnetic field results in a Curie constant C = 0.2 emu·K·mol^{-1}, a Weiss constant θ = -42 K and a TIP of 2.1 × 10^{-3} emu·mol^{-1}. The fitting of experimental data collected at a 5000 Oe applied DC magnetic field results in a Curie constant C = 0.34 emu·K·mol^{-1}, a Weiss constant θ = -42 K and a TIP of 5.0 × 10^{-5} emu·mol^{-1}. Therefore, the increased DC magnetic field diminishes the TIP and the delocalization of electrons in the TCNQ stacks in addition to the magnetic anisotropy in the Dy(III) compound. In addition, the antiferromagnetic inter-chain interactions through the stacked TCNQ species contribute to the spin-canted states of [Dy(TPMA)(μ-TCNQ)(μ-OH)](TCNQ)$_2$·CH$_3$CN. However, due to the fact that the magnetic contributions from the TCNQ radicals are very small as compared to those of Dy(III), the anisotropy of Dy(III) plays a more important role for the magnetic behavior of [Dy(TPMA)(μ-TCNQ)(μ-OH)](TCNQ)$_2$·CH$_3$CN.

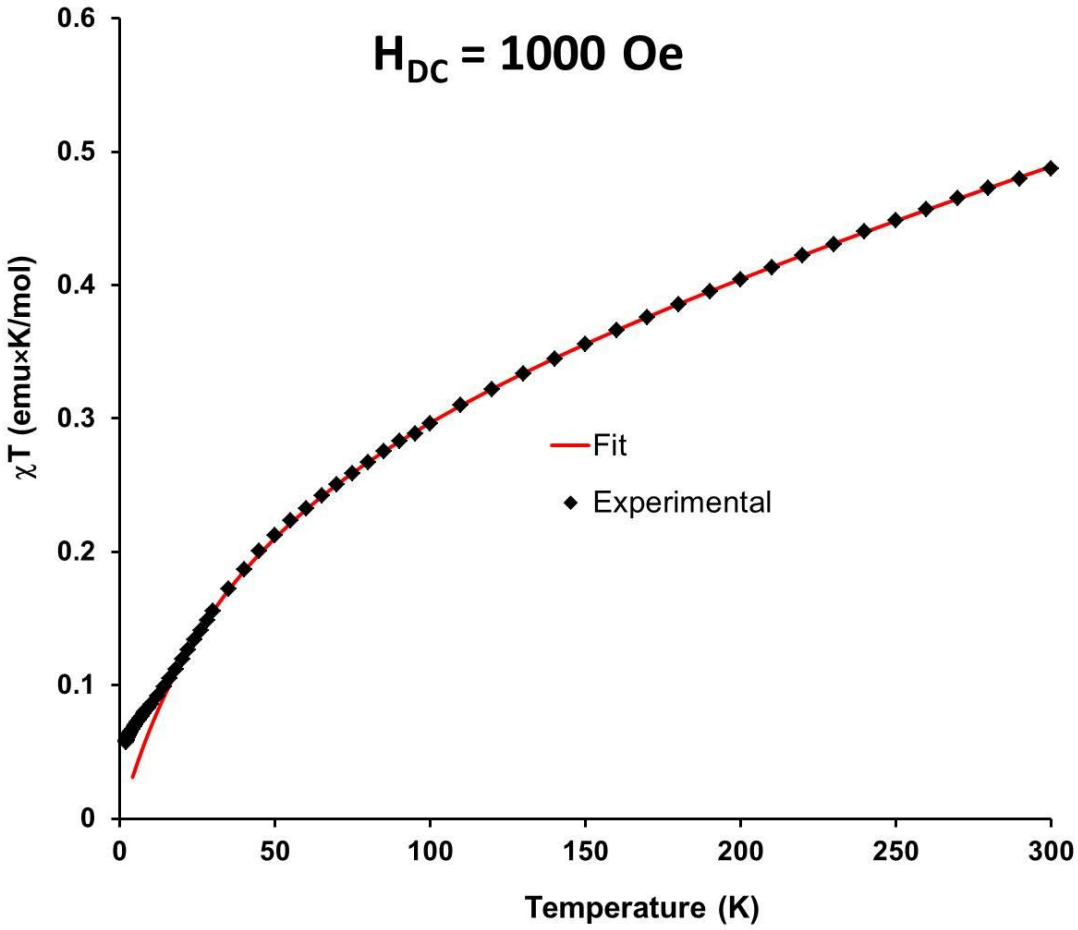

Figure 55. Experimental data and fitted line of the temperature dependence of χT for [Y(TPMA)(μ-TCNQ)(μ-OH)](TCNQ)$_2$ CH_3CN under a 1000 Oe applied magnetic field.

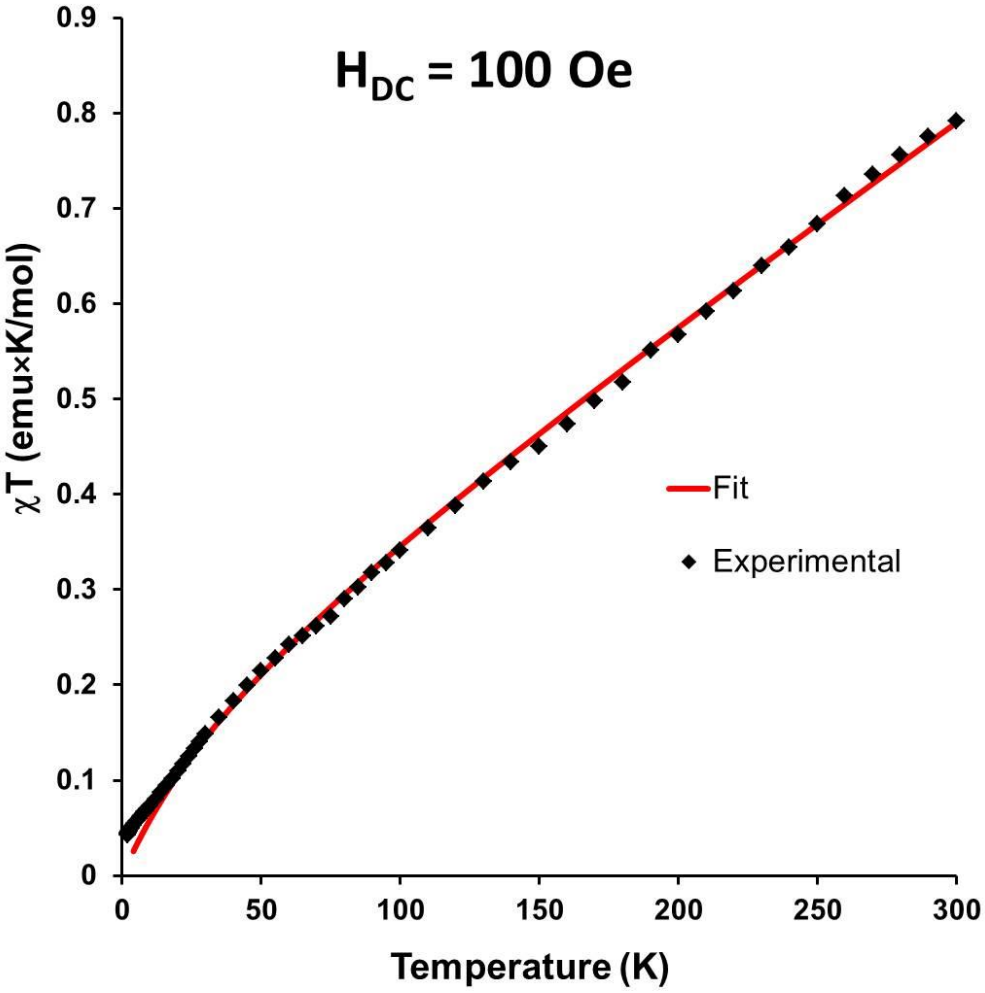

Figure 56. Experimental data and fitted line of the temperature dependence of χT for [Y(TPMA)(μ-TCNQ)(μ-OH)](TCNQ)$_2$ CH_3CN under a 100 Oe applied magnetic field.

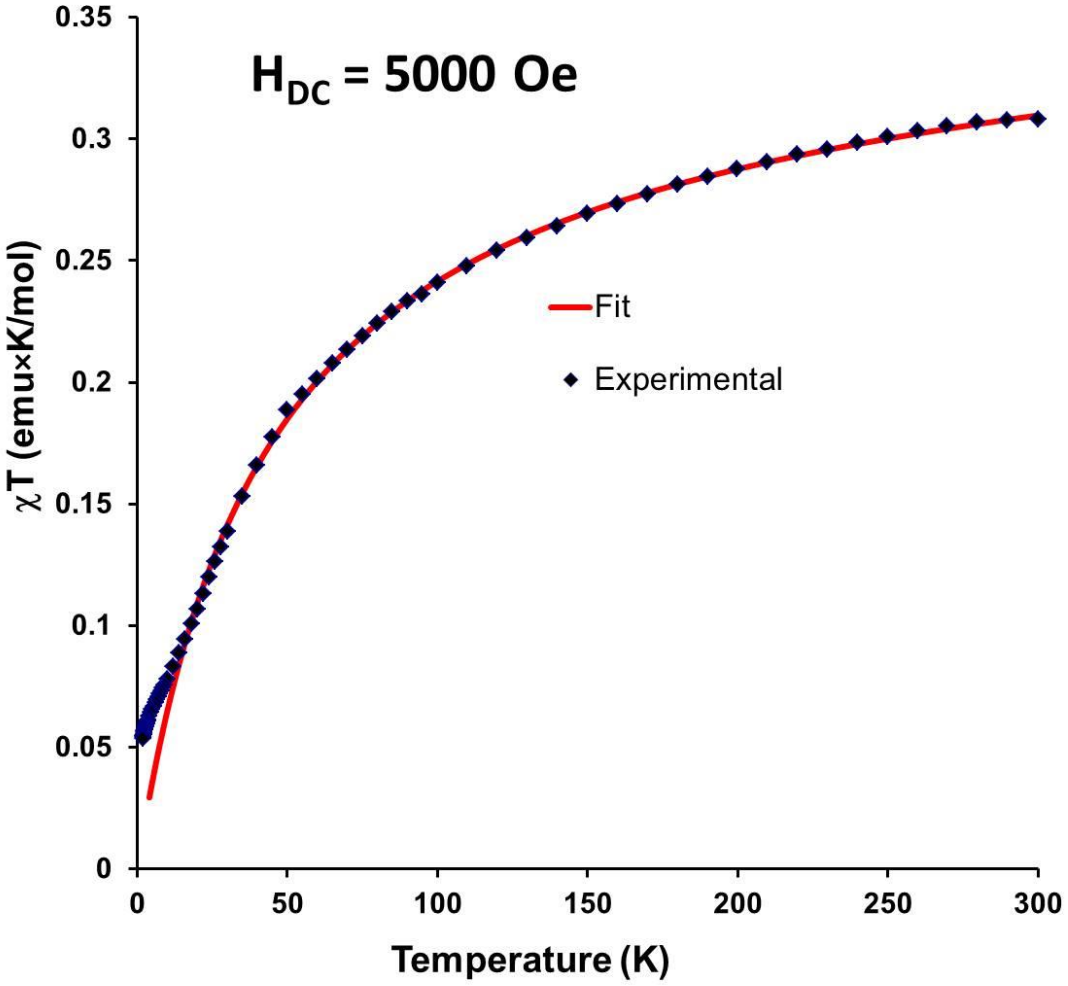

Figure 57. Experimental data and fitted line of the temperature dependence of χT for [Y(TPMA)(μ-TCNQ)(μ-OH)](TCNQ)$_2$ CH_3CN under a 5000 Oe applied magnetic field.

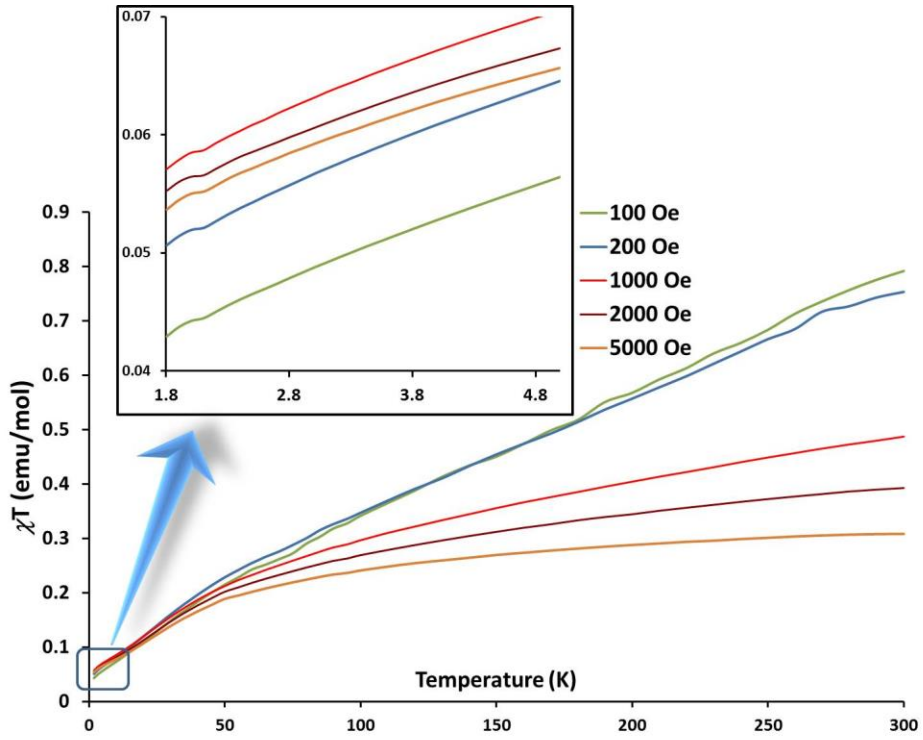

Figure 58. The temperature dependence of χT for [Y(TPMA)(μ-TCNQ)(μ-OH)](TCNQ)$_2$·CH$_3$CN under different applied DC magnetic fields. The inset shows the low temperature region as indicated.

Electrical conducting properties. Conductivity measurements were carried out on pressed pellets of polycrystalline samples of [Dy(TPMA)(μ-TCNQ)(μ-OH)](TCNQ)$_2$·CH$_3$CN by the four-probe method. The compound behaves as a semiconductor in the temperature range of 180-350 K with a small activation energy of 0.43 eV (Figure 59). The conductivity at room temperature is 5.0×10^{-4} S·cm^{-1}.

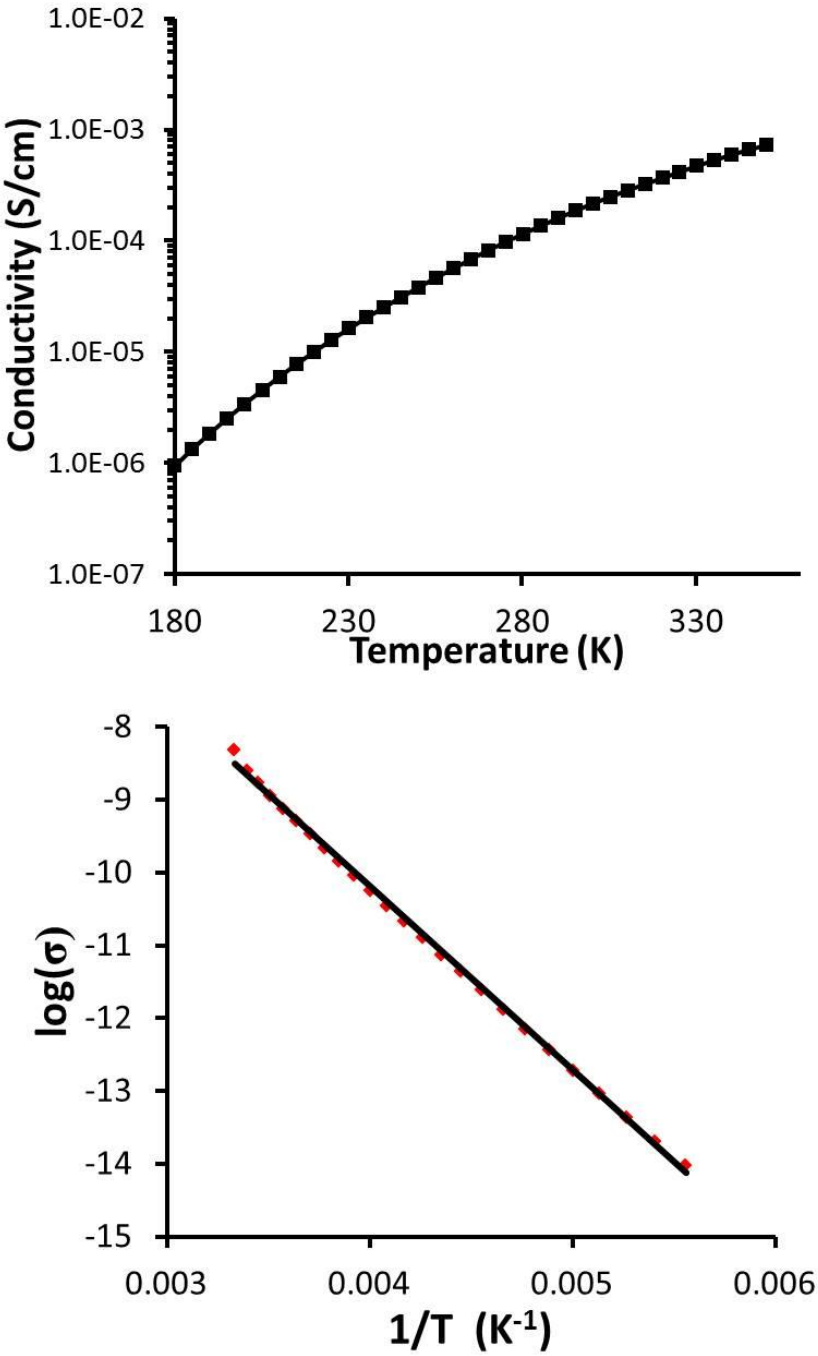

Figure 59. Top: temperature dependence of the electrical conductivity. Bottom: Arrhenius plot of electrical conductivity of [Dy(TPMA)(μ-TCNQ)(μ-OH)](TCNQ)$_2$ CH_3CN. The red symbols are experimental data and the black line is the linear fit with an activation energy of 0.43 eV.

Cobalt-TCNQ-based electrically conducting SMM

It was discovered recently in the Dunbar group that the $[Co(Tpm)_2][ClO_4]_2$ (Tpm = tris(pyrazol-1-yl)methane) and $[Co(Tpm)_2][BPh_4]_2 \cdot 2MeCN$ behave as field induced SMMs with large uniaxial anisotropy (D values around -100 cm^{-1}). The effective energy barriers under optimized DC fields for the former and the latter are 30.6 and 44.7 cm^{-1}, respectively.[161] The Co(II) ion is in a trigonal antiprismatic geometry, which forces the trigonal distortion and results in the large single-ion anisotropy. The cationic part of these two complexes are responsible for the SMM behaviors and, fortunately, they are stable in air. Therefore, it occurred to us that the $[Co(Tpm)_2]^{2+}$ cation would be a good candidate for the incorporation of SMMs into into electrical conducting materials with anionic TCNQ radicals.

Reaction of $[Co(Tpm)_2]Cl_2$ with $(Et_3NH)(TCNQ)_2$ in a mixture of methanol and acetonitrile resulted in the formation of dark purple crystals of $[Co(Tpm)_2](TCNQ)_3$ after a few minutes. The salt crystallizes in the triclinic space group P-1 with the asymmetric unit consisting of one-half of a $[Co(Tpm)_2]^{2+}$ cation and one and one-half of TCNQ species (Figure 60 and Table 13).

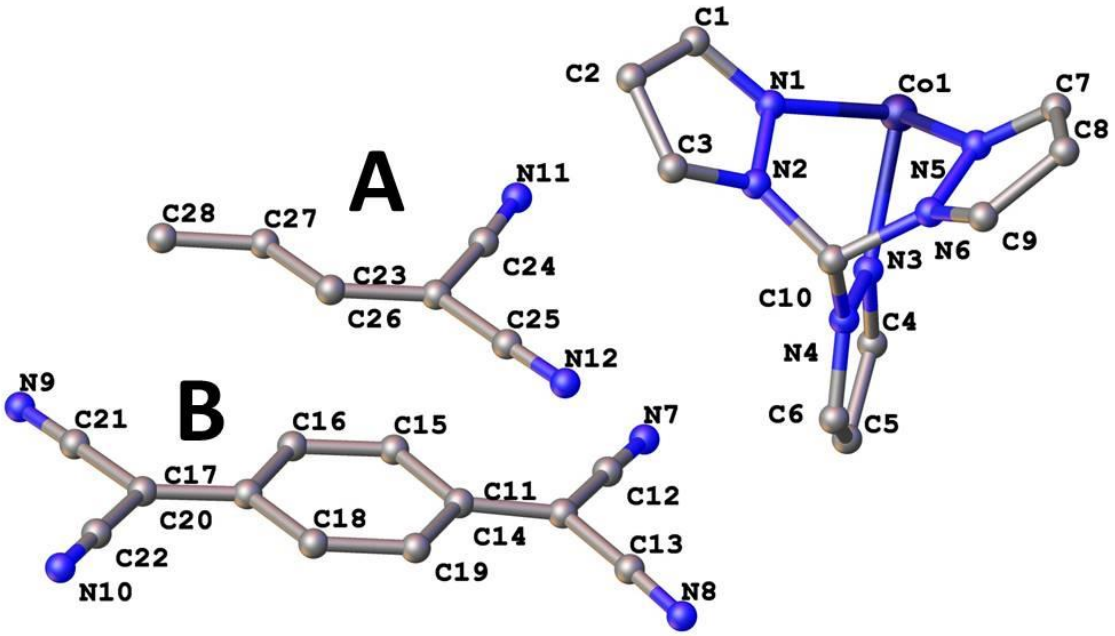

Figure 60. Asymmetric unit of $[Co(Tpm)_2](TCNQ)_3$. Hydrogen atoms have been omitted for the sake of clarity.

Table 13. Summary of crystallographic parameters for $[Co(Tpm)_2](TCNQ)_3$ and $[Fe(Tpm)_2](TCNQ)_3$.

Empirical formula	$C_{56}H_{32}CoN_{24}$	$C_{56}FeN_{24}H_{32}$
Formula weight	1099.98	1096.90
Temperature/K	110.15	150.15
Crystal system	triclinic	triclinic
Space group	P-1	P-1
a/Å	8.026(4)	8.122(3)
b/Å	10.025(5)	10.034(3)
c/Å	16.873(9)	16.752(5)
α/°	101.751(6)	101.121(4)
β/°	92.267(7)	91.063(4)
γ/°	110.553(6)	111.195(4)
Volume/$Å^3$	1235.5(11)	1243.1(7)
Z	1	1
$\rho_{calc}g/cm^3$	1.478	1.465
μ/mm^{-1}	0.416	0.372
F(000)	563.0	562.0
Crystal size/mm^3	0.08 × 0.06 × 0.01	0.21 × 0.18 × 0.016
Radiation	MoKα (λ = 0.71073)	MoKα (λ = 0.71073)
2Θ range for data collection/ °	2.484 to 52.952	4.458 to 50.056
Index ranges	$-10 \le h \le 10$, $-12 \le k \le 12$, $-21 \le l \le 21$	$-9 \le h \le 9$, $-11 \le k \le 11$, $-19 \le l \le 19$
Reflections collected	13261	11906
Independent reflections	5047 [R_{int} = 0.2536, R_{sigma} = 0.3876]	4387 [R_{int} = 0.0698, R_{sigma} = 0.0589]
Data/restraints/parameters	5047/0/367	4387/0/367
Goodness-of-fit on F^2	0.926	1.074
Final R indexes [I>=2σ (I)]	R_1 = 0.0946, wR_2 = 0.1660	R_1 = 0.0372, wR_2 = 0.0948
Final R indexes [all data]	R_1 = 0.2954, wR_2 = 0.2608	R_1 = 0.0449, wR_2 = 0.0991
Largest diff. peak/hole / e $Å^{-3}$	0.40/-0.45	0.29/-0.53

$R_1 = \Sigma||F_o|-|F_c||/\Sigma|F_o|$. $wR_2=[\Sigma w(|F_o|-|F_c|)^2/|\Sigma w(F_o)^2]^{1/2}$. $w = 0.75/(\sigma^2(F_o)+0.00010F_o^2)$.

Goodness-of-fit = $\{\sum[w(F_o^2 - F_c^2)^2]/(n-p)\}^{1/2}$, where n is the number of reflections and p is the total number of parameters refined.

Three of the TCNQ molecules stack into one triad with no long-range stacking with each other being evident; instead, the TCNQ triads are staggered with respect to each other (Figure 61). The TCNQ molecules are partially charged with estimated charges from the structural parameters listed in Table 14.

Table 14. The charges (ρ) of different TCNQ species in $[Co(Tpm)_2](TCNQ)_3$ at 110 K as estimated from the Kistenmacher's formula (A, B as denoted in Figure 60; b, c and d are average C-C bond distances as depicted below).

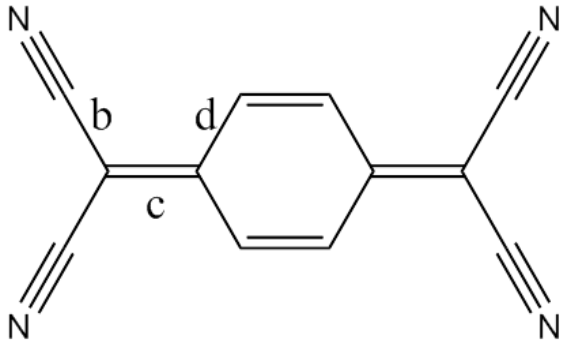

TCNQ	b /Å	c /Å	d /Å	ρ
A	1.423	1.399	1.410	-0.74
B	1.425	1.385	1.426	-0.40

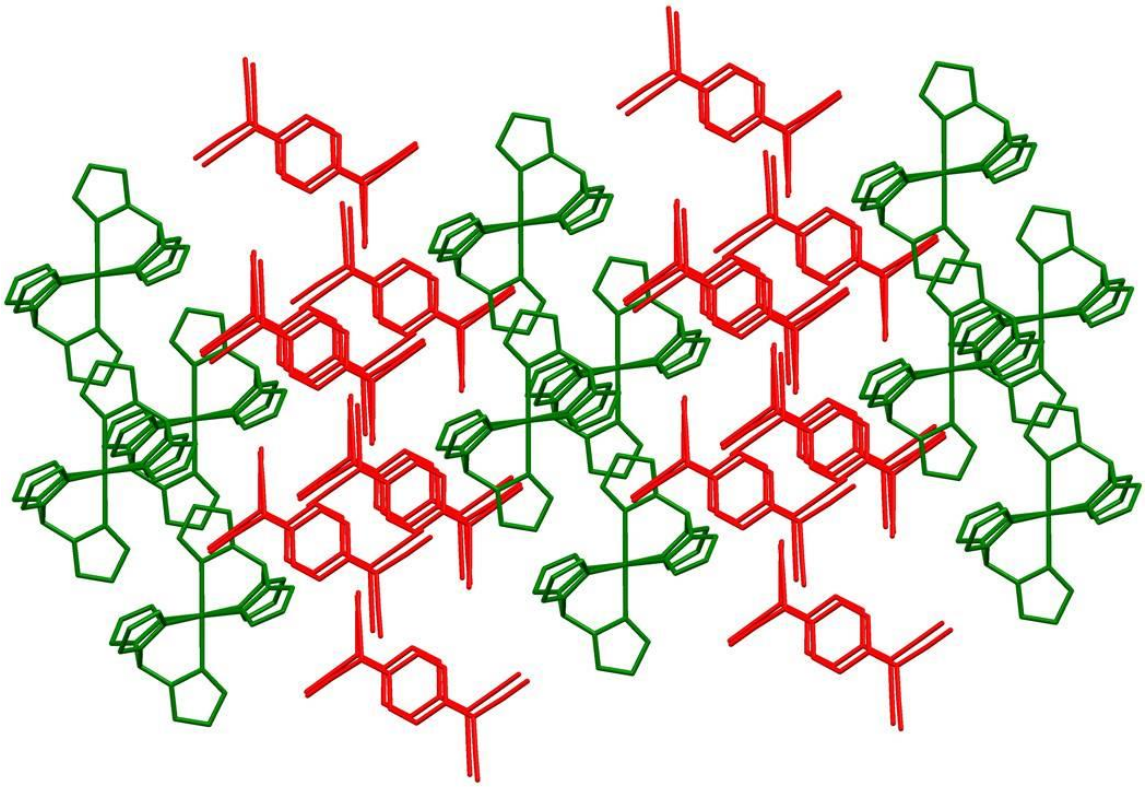

Figure 61. Packing diagram of the crystal structure of $[Co(Tpm)_2](TCNQ)_3$. The $[Co(Tpm)_2]^{2+}$ cations are in green and the TCNQ species are in red.

The magnetic properties of $[Co(Tpm)_2](TCNQ)_3$ are similar to the single-ion behavior of the $[Co(Tpm)_2]^{2+}$ cation. The temperature dependence of the magnetic susceptibility measurements were carried out under a DC magnetic field of 1000 Oe in the temperature range of 2-300 K (Figure 62). The χT value of 2.7 emu·K·mol^{-1} at 300 K is much higher than the spin-only contributions from a Co(II) ion (S = 3/2), which is attributed to spin-orbit coupling. The χT value remians essentially constant at 2.7 emu K mol^{-1} (per formula unit) as the temperature is lowered to 120 K, below which temperature it gradually decreases to ~2.0 emu K mol^{-1} at 2.0 K. An isostructural compound was obtained with Fe(II) instead of Co(II) but this compound is diamagnetic.

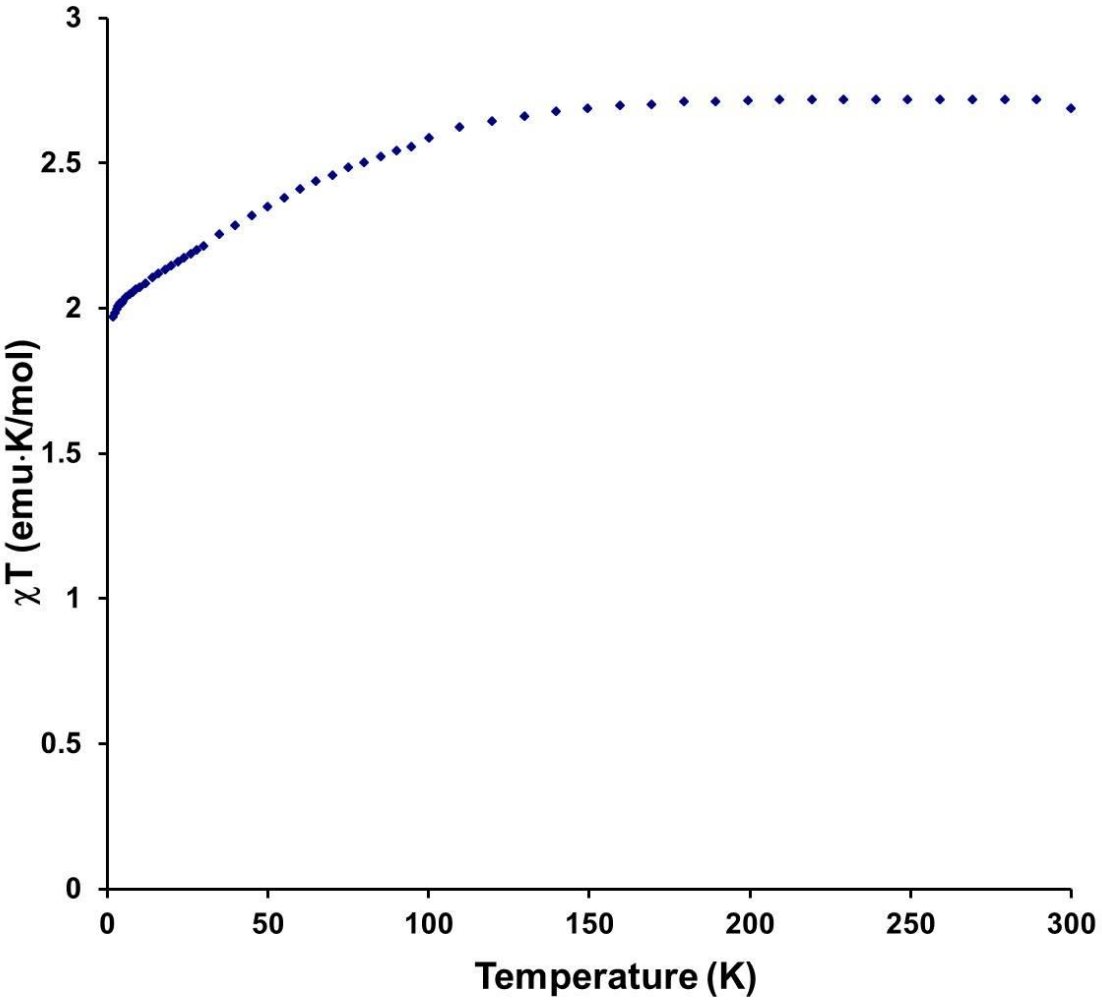

Figure 62. The temperature dependence of χT for $[Co(Tpm)_2](TCNQ)_3$ under a 1000 Oe DC magnetic field.

Frequency-dependent AC magnetic studies were conducted under an optimized DC magnetic field of 1200 Oe. Frequency-dependent peaks in the out-of-phase signals were observed in the temperature range of 5-11 K (Figure 63 and Figure 64). Fitting of the relaxation time to the Arrhenius law yielded an effective energy barrier of 37.8 K and a pre-exponential factor of 3.2×10^{-6} s (Figure 65).

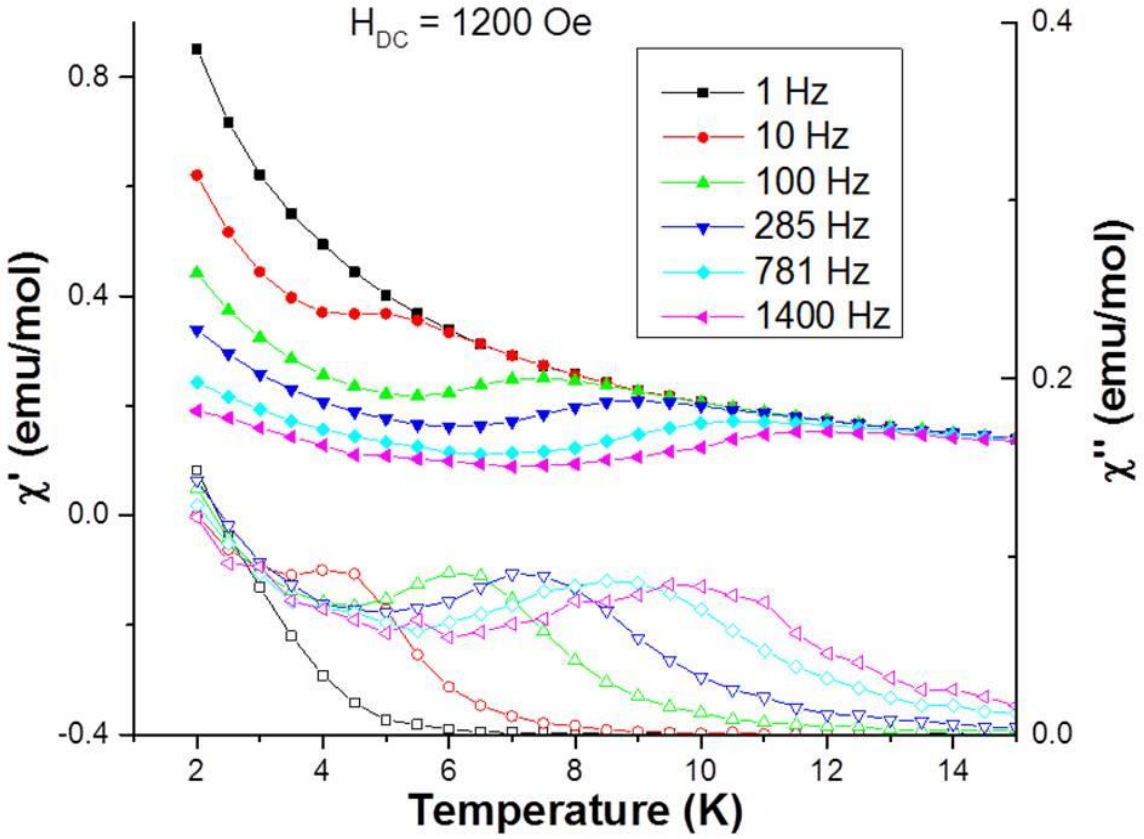

Figure 63. Temperature dependence of the in-phase (solid symbols) and out-of-phase AC magnetic susceptibilities of $[Co(Tpm)_2](TCNQ)_3$ under an applied DC magnetic field of 1200 Oe.

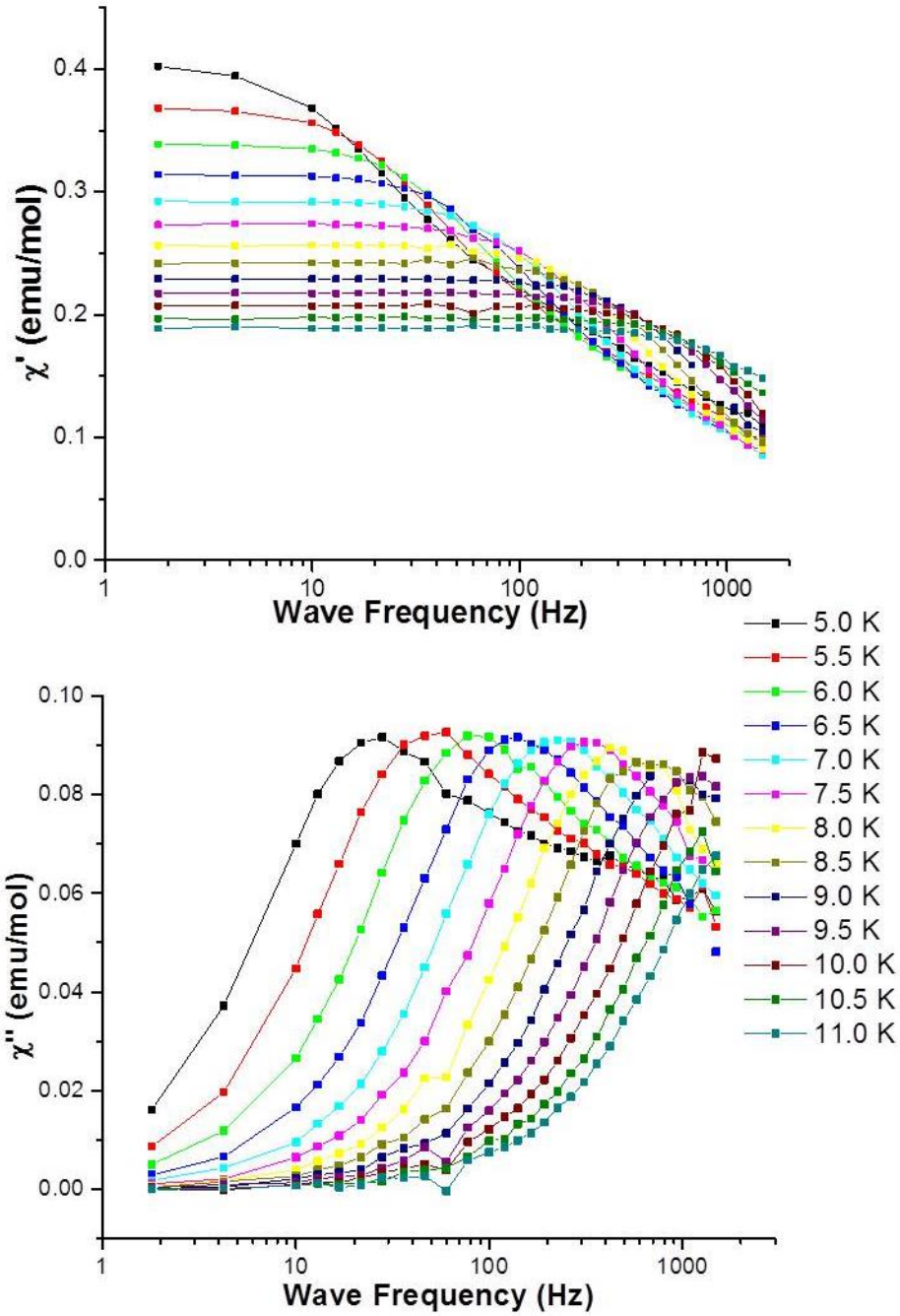

Figure 64. Frequency dependence of in-phase (top) and out-of-phase (bottom) AC magnetic susceptibilities of $[Co(Tpm)_2](TCNQ)_3$ at different temperatures under an applied DC magnetic field of 1200 Oe.

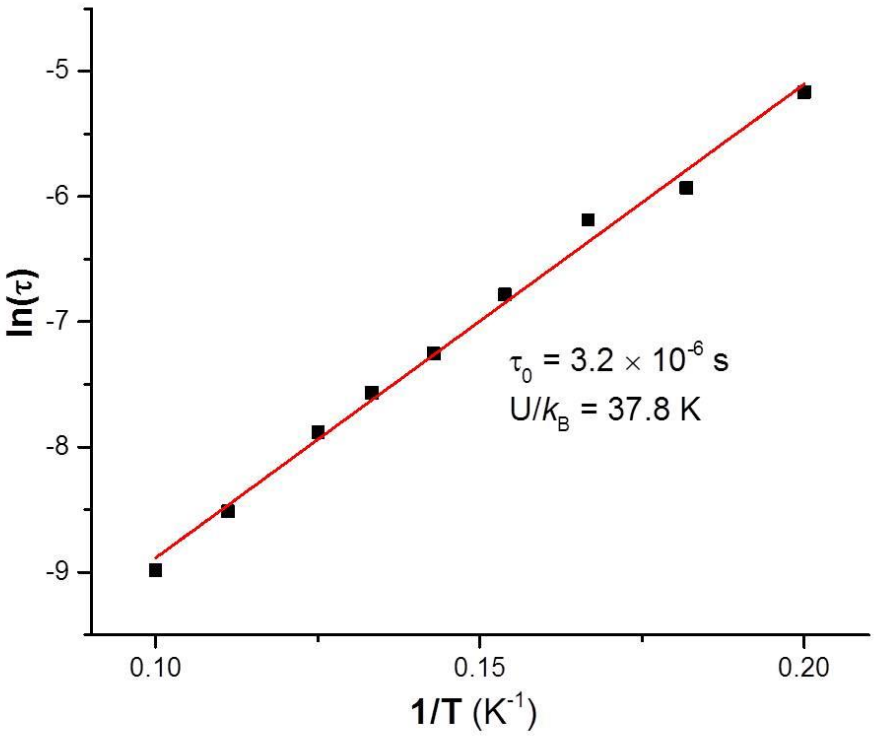

Figure 65. Arrhenius plot of the relaxation time, as determined from variable-temperature AC susceptibilities of $[Co(Tpm)_2](TCNQ)_3$ at temperatures between 5 and 11 K under a DC magnetic field of 1200 Oe.

Conductivity measurements were carried out on pressed pellets of polycrystalline samples of $[Co(Tpm)_2](TCNQ)_3$ by the two-probe method. It behaves as a semiconductor over the temperature range of 125-300 K with a small activation energy of 0.33 eV (Figure 59). The conductivity at room temperature is 1.3×10^{-3} S cm^{-1}.

Table 15. Bond distances for $[Co(Tpm)_2](TCNQ)_3$.

Atom	Atom	Length/Å		Atom	Atom	Length/Å
Co1	N1[1]	2.132(8)		N8	C13	1.145(11)
Co1	N1	2.132(8)		N9	C21	1.141(11)
Co1	N3[1]	2.091(7)		N10	C22	1.146(10)
Co1	N3	2.091(7)		C11	C12	1.417(13)
Co1	N5[1]	2.122(7)		C11	C13	1.431(13)
Co1	N5	2.122(7)		C11	C14	1.382(11)
N1	N2	1.370(9)		C14	C15	1.433(11)
N1	C1	1.321(11)		C14	C19	1.413(11)
N2	C3	1.356(10)		C15	C16	1.341(11)
N2	C10	1.418(10)		C16	C17	1.425(11)
N3	N4	1.370(9)		C17	C18	1.434(11)
N3	C4	1.340(10)		C17	C20	1.385(11)
N4	C6	1.325(11)		C18	C19	1.353(11)
N4	C10	1.455(10)		C20	C21	1.430(13)
N5	N6	1.360(9)		C20	C22	1.421(11)
N5	C7	1.314(10)		N11	C24	1.153(10)
N6	C9	1.367(10)		N12	C25	1.148(11)
N6	C10	1.449(10)		C23	C24	1.416(12)
C1	C2	1.383(12)		C23	C25	1.432(12)
C2	C3	1.354(12)		C23	C26	1.399(11)
C4	C5	1.415(12)		C26	C27	1.411(11)
C5	C6	1.350(11)		C26	C28[2]	1.422(11)
C7	C8	1.395(12)		C27	C28	1.344(11)
C8	C9	1.368(12)		C28	C26[2]	1.421(11)
N7	C12	1.162(11)				

[1]1-X,1-Y,2-Z; [2]-X,1-Y,1-Z

Table 16. Bond angles for $[Co(Tpm)_2](TCNQ)_3$.

Atom	Atom	Atom	Angle/°		Atom	Atom	Atom	Angle/°
N1	Co1	N1[1]	180.0		N4	C6	C5	109.0(8)
N3	Co1	N1	85.3(3)		N5	C7	C8	110.7(8)
N3[1]	Co1	N1[1]	85.3(3)		C9	C8	C7	105.6(9)
N3[1]	Co1	N1	94.7(3)		N6	C9	C8	107.2(8)
N3	Co1	N1[1]	94.7(3)		N2	C10	N4	111.6(7)
N3[1]	Co1	N3	180.0		N2	C10	N6	109.9(7)
N3	Co1	N5	85.3(3)		N6	C10	N4	109.1(7)
N3	Co1	N5[1]	94.7(3)		C12	C11	C13	116.3(9)
N3[1]	Co1	N5	94.7(3)		C14	C11	C12	121.5(9)
N3[1]	Co1	N5[1]	85.3(3)		C14	C11	C13	122.2(8)
N5[1]	Co1	N1[1]	81.7(3)		N7	C12	C11	178.7(12)
N5[1]	Co1	N1	98.2(3)		N8	C13	C11	178.2(10)
N5	Co1	N1[1]	98.3(3)		C11	C14	C15	120.6(8)
N5	Co1	N1	81.7(3)		C11	C14	C19	120.5(8)
N5[1]	Co1	N5	180.00(15)		C19	C14	C15	118.9(8)
N2	N1	Co1	118.0(6)		C16	C15	C14	120.6(8)
C1	N1	Co1	138.0(7)		C15	C16	C17	121.0(8)
C1	N1	N2	104.0(7)		C16	C17	C18	118.2(8)
N1	N2	C10	119.3(7)		C20	C17	C16	121.2(8)
C3	N2	N1	111.5(7)		C20	C17	C18	120.6(8)
C3	N2	C10	128.4(7)		C19	C18	C17	120.6(8)
N4	N3	Co1	119.0(5)		C18	C19	C14	120.6(9)
C4	N3	Co1	135.8(6)		C17	C20	C21	121.7(8)
C4	N3	N4	105.1(7)		C17	C20	C22	122.1(8)
N3	N4	C10	119.0(7)		C22	C20	C21	116.2(8)
C6	N4	N3	111.0(7)		N9	C21	C20	179.4(11)
C6	N4	C10	130.0(7)		N10	C22	C20	179.3(10)
N6	N5	Co1	116.3(5)		C24	C23	C25	113.8(8)
C7	N5	Co1	136.3(7)		C26	C23	C24	122.1(8)
C7	N5	N6	106.9(7)		C26	C23	C25	123.9(8)
N5	N6	C9	109.6(7)		N11	C24	C23	176.2(10)
N5	N6	C10	122.0(7)		N12	C25	C23	178.6(10)
C9	N6	C10	128.0(7)		C23	C26	C27	121.2(8)
N1	C1	C2	112.0(9)		C23	C26	C28[2]	121.4(8)
C3	C2	C1	106.0(9)		C27	C26	C28[2]	117.3(8)
C2	C3	N2	106.5(8)		C28	C27	C26	122.6(9)
N3	C4	C5	109.9(8)		C27	C28	C26[2]	120.1(9)
C6	C5	C4	105.0(8)					

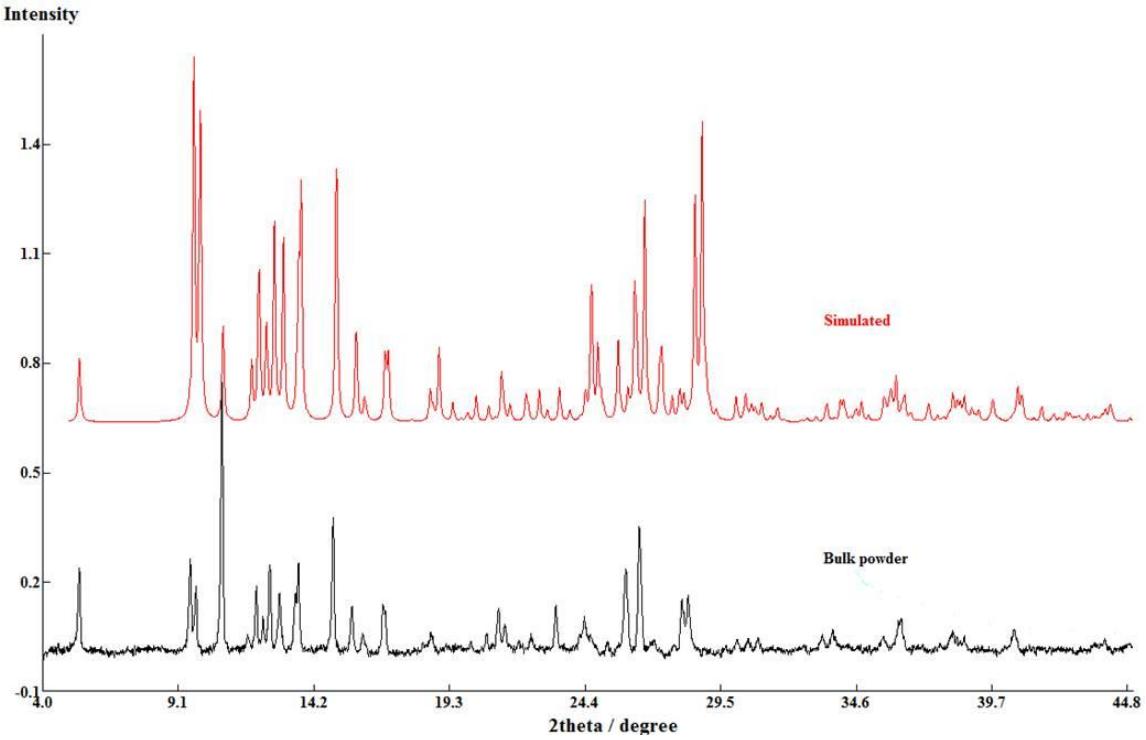

Figure 66. Powder X-ray diffraction patterns of $[Co(Tpm)_2](TCNQ)_3$. The red trace (top) is a simulated pattern from single-crystal X-ray diffraction data of $[Co(Tpm)_2](TCNQ)_3$ and the black trace (bottom) is from a bulk polycrystalline sample.

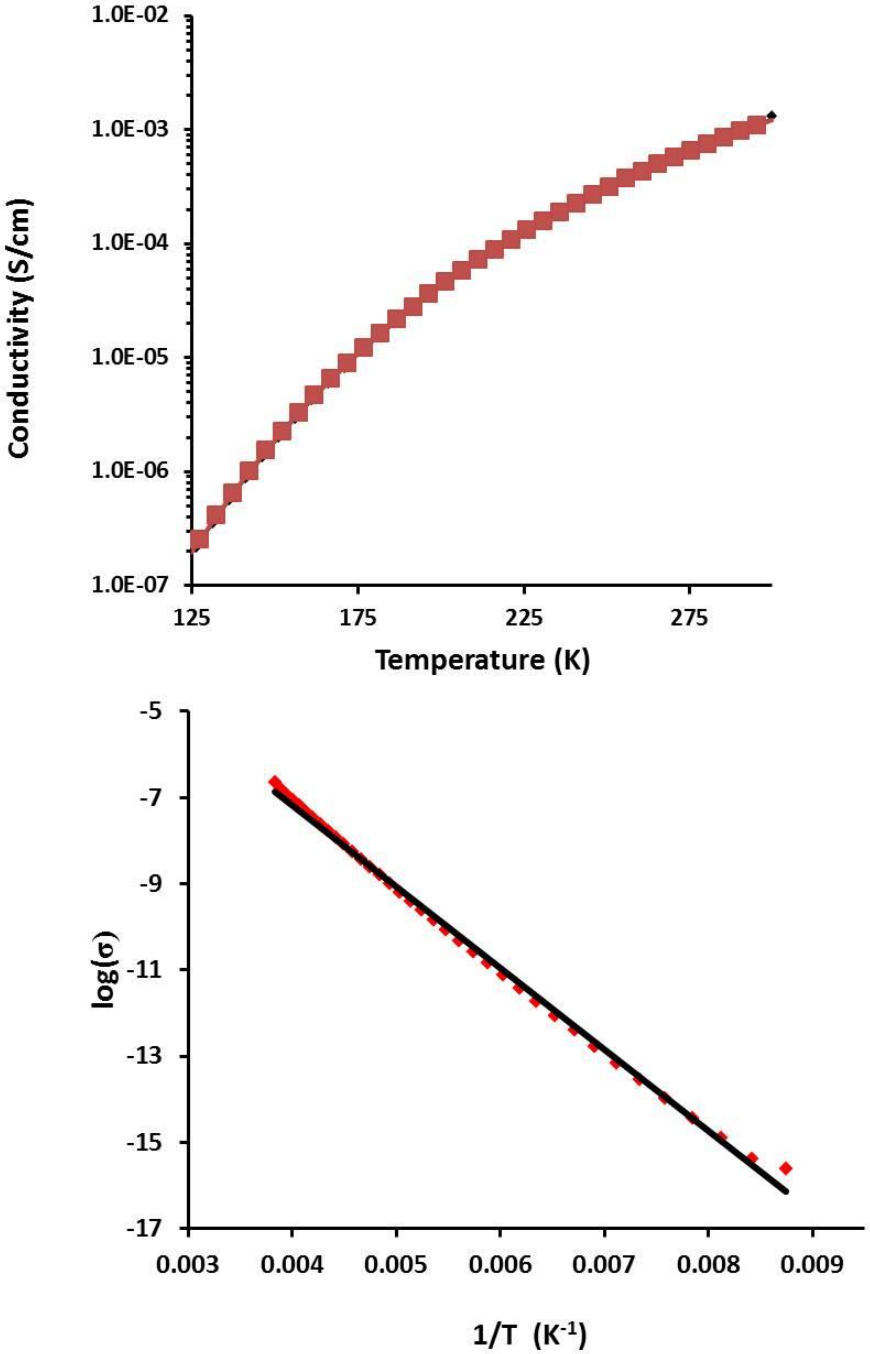

Figure 67. Top: temperature dependence of the electrical conductivity. Bottom: Arrhenius plot of electrical conductivity of $[Co(Tpm)_2](TCNQ)_3$. The red symbols are experimental data and the black line is the linear fit with an activation energy of 0.33 eV.

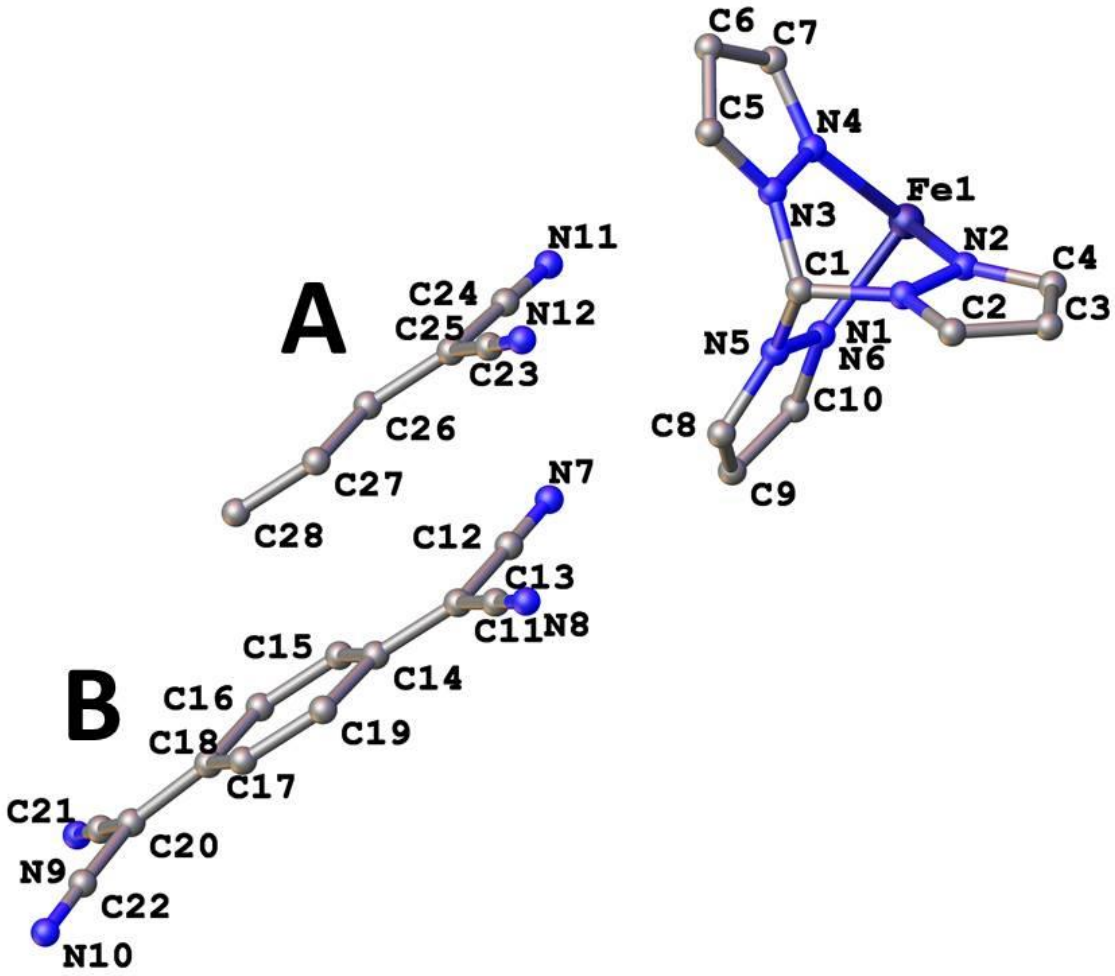

Figure 68. Asymmetric unit of $[Fe(Tpm)_2](TCNQ)_3$. Hydrogen atoms have been omitted for the sake of clarity.

Table 17. Bond distances for $[Fe(Tpm)_2](TCNQ)_3$.

Atom	Atom	Length/Å		Atom	Atom	Length/Å
Fe1	N2[1]	1.9642(17)		N8	C13	1.152(3)
Fe1	N2	1.9642(17)		N9	C21	1.150(3)
Fe1	N4	1.9610(17)		N10	C22	1.144(3)
Fe1	N4[1]	1.9610(17)		C11	C12	1.432(3)
Fe1	N6[1]	1.9683(17)		C11	C13	1.427(3)
Fe1	N6	1.9683(17)		C11	C14	1.396(3)
N1	N2	1.368(2)		C14	C15	1.436(3)
N1	C1	1.447(3)		C14	C19	1.435(3)
N1	C2	1.347(2)		C15	C16	1.351(3)
N2	C4	1.326(3)		C16	C17	1.441(3)
N3	N4	1.369(2)		C17	C18	1.430(3)
N3	C1	1.447(2)		C17	C20	1.395(3)
N3	C5	1.349(3)		C18	C19	1.354(3)
N4	C7	1.331(3)		C20	C21	1.425(3)
N5	N6	1.370(2)		C20	C22	1.428(3)
N5	C1	1.437(3)		N11	C24	1.153(3)
N5	C8	1.356(2)		N12	C25	1.154(3)
N6	C10	1.324(3)		C23	C24	1.420(3)
C2	C3	1.369(3)		C23	C25	1.427(3)
C3	C4	1.404(3)		C23	C26	1.414(3)
C5	C6	1.368(3)		C26	C27	1.427(3)
C6	C7	1.395(3)		C26	C28[2]	1.431(3)
C8	C9	1.361(3)		C27	C28	1.360(3)
C9	C10	1.393(3)		C28	C26[2]	1.431(3)
N7	C12	1.148(2)				

[1]-X,1-Y,-Z; [2]1-X,1-Y,1-Z

Table 18. Bond angles for $[Fe(Tpm)_2](TCNQ)_3$.

Atom	Atom	Atom	Angle/°		Atom	Atom	Atom	Angle/°
$N2^1$	Fe1	N2	180.0		N2	C4	C3	111.05(18)
N2	Fe1	$N6^1$	94.42(7)		N3	C5	C6	106.43(18)
$N2^1$	Fe1	$N6^1$	85.58(7)		C5	C6	C7	106.40(19)
$N2^1$	Fe1	N6	94.42(7)		N4	C7	C6	110.48(18)
N2	Fe1	N6	85.58(7)		N5	C8	C9	106.47(18)
$N4^1$	Fe1	N2	91.88(7)		C8	C9	C10	105.87(18)
N4	Fe1	$N2^1$	91.88(7)		N6	C10	C9	111.70(18)
$N4^1$	Fe1	$N2^1$	88.12(7)		C13	C11	C12	116.39(17)
N4	Fe1	N2	88.12(7)		C14	C11	C12	121.44(18)
N4	Fe1	$N4^1$	180.00(8)		C14	C11	C13	122.16(17)
$N4^1$	Fe1	$N6^1$	88.33(7)		N7	C12	C11	179.3(2)
N4	Fe1	N6	88.33(7)		N8	C13	C11	179.6(2)
$N4^1$	Fe1	N6	91.67(7)		C11	C14	C15	121.22(17)
N4	Fe1	$N6^1$	91.67(7)		C11	C14	C19	121.00(18)
N6	Fe1	$N6^1$	180.0		C19	C14	C15	117.78(17)
N2	N1	C1	118.73(15)		C16	C15	C14	121.16(18)
C2	N1	N2	111.56(16)		C15	C16	C17	121.08(18)
C2	N1	C1	129.50(17)		C18	C17	C16	117.55(17)
N1	N2	Fe1	117.90(12)		C20	C17	C16	120.71(18)
C4	N2	Fe1	136.86(14)		C20	C17	C18	121.67(17)
C4	N2	N1	104.95(16)		C19	C18	C17	121.41(17)
N4	N3	C1	118.08(15)		C18	C19	C14	120.96(18)
C5	N3	N4	111.59(16)		C17	C20	C21	121.52(18)
C5	N3	C1	130.30(17)		C17	C20	C22	121.57(18)
N3	N4	Fe1	118.51(12)		C21	C20	C22	116.83(18)
C7	N4	Fe1	136.39(14)		N9	C21	C20	179.0(2)
C7	N4	N3	105.10(16)		N10	C22	C20	178.8(3)
N6	N5	C1	117.43(15)		C24	C23	C25	115.86(17)
C8	N5	N6	111.71(16)		C26	C23	C24	120.80(18)
C8	N5	C1	130.19(17)		C26	C23	C25	123.23(17)
N5	N6	Fe1	118.85(12)		N11	C24	C23	178.2(2)
C10	N6	Fe1	136.87(14)		N12	C25	C23	177.6(2)
C10	N6	N5	104.24(16)		C23	C26	C27	121.87(18)
N3	C1	N1	109.48(16)		C23	C26	$C28^2$	121.01(17)
N5	C1	N1	109.16(16)		C27	C26	$C28^2$	117.12(17)
N5	C1	N3	109.72(15)		C28	C27	C26	121.33(18)
N1	C2	C3	107.03(17)		C27	C28	$C26^2$	121.55(17)
C2	C3	C4	105.40(18)					

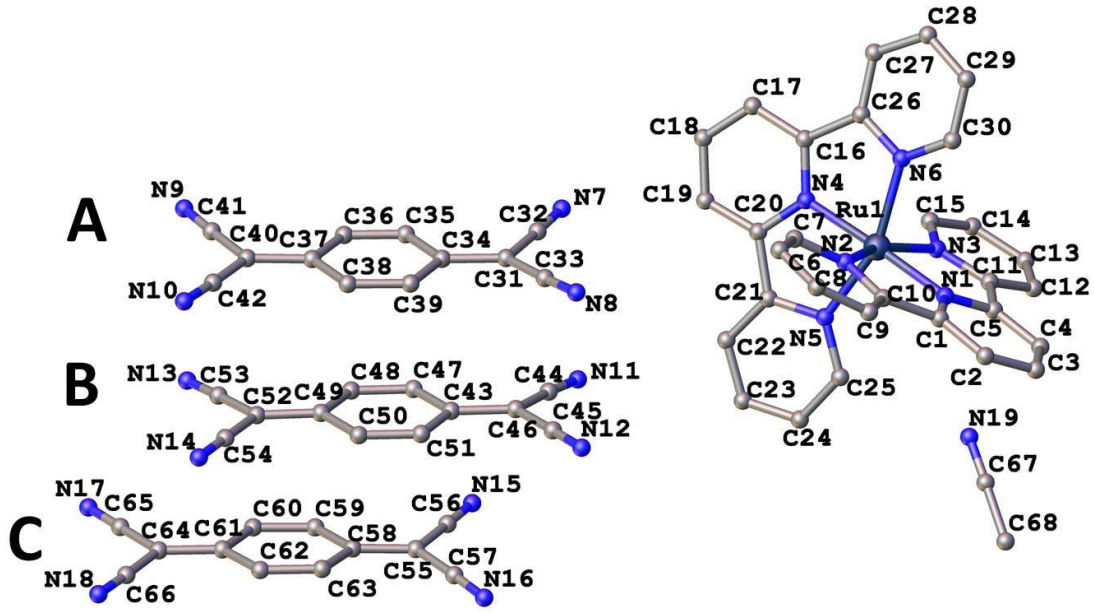

Figure 69. Asymmetric unit of $[Ru(terpy)_2](TCNQ)_3 \cdot CH_3CN$. Hydrogen atoms have been omitted for the sake of clarity.

Table 19. Summary of the crystallographic parameters for $[Ru(terpy)_2](TCNQ)_3\ CH_3CN$ and $[Ru(bpy)_3](TCNQ)_4$.

Compound	**[**$Ru(terpy)_2](TCNQ)_3\ CH_3CN$	$[Ru(bpy)_3](TCNQ)_4$
Empirical formula	$C_{68}H_{37}N_{19}Ru$	$C_{78}N_{22}RuH_{40}$
Formula weight	1221.23	1386.39
Temperature/K	110.15	110.15
Crystal system	orthorhombic	triclinic
Space group	$Pna2_1$	P-1
a/Å	18.9142(17)	13.4651(13)
b/Å	8.6872(8)	15.6768(15)
c/Å	33.690(3)	16.2631(16)
α/°	90	98.7730(10)
β/°	90	95.4600(10)
γ/°	90	94.1520(10)
Volume/$Å^3$	5535.7(9)	3364.2(6)
Z	4	2
$\rho_{calc}g/cm^3$	1.465	1.369
μ/mm^{-1}	0.348	0.297
F(000)	2488.0	1412.0
Crystal size/mm^3	0.27 ×0.05 ×0.03	0.2 ×0.11 ×0.04
Radiation	MoKα (λ = 0.71073)	MoKα (λ = 0.71073)
2Θ range for data collection/ °	4.306 to 53.462	3.362 to 48.814
Index ranges	-23 ≤ h ≤ 23, -10 ≤ k ≤ 10, -42 ≤ l ≤ 42	-15 ≤ h ≤ 15, -18 ≤ k ≤ 18, -18 ≤ l ≤ 18
Reflections collected	58686	30695
Independent reflections	11714 [R_{int} = 0.0780, R_{sigma} = 0.0737]	11052 [R_{int} = 0.0383, R_{sigma} = 0.0450]
Data/restraints/parameters	11714/1/795	11052/0/910
Goodness-of-fit on F^2	0.922	1.047
Final R indexes [I>=2σ (I)]	R_1 = 0.0345, wR_2 = 0.0553	R_1 = 0.0344, wR_2 = 0.0848
Final R indexes [all data]	R_1 = 0.0494, wR_2 = 0.0587	R_1 = 0.0434, wR_2 = 0.0880
Largest diff. peak/hole / e $Å^{-3}$	0.57/-0.88	0.59/-0.56
Flack parameter	-0.03(2)	N/A

$R_1 = \Sigma||F_o|-|F_c||/\Sigma|F_o|$. $wR_2=[\Sigma w(|F_o|-|F_c|)^2/|\Sigma w(F_o)^2]^{1/2}$. $w= 0.75/(\sigma^2(F_o)+0.00010F_o^2)$.

Goodness-of-fit = $\{\sum[w(F_o^2 - F_c^2)^2]/(n-p)\}^{1/2}$, where n is the number of reflections and p is the total number of parameters refined.

Table 20. Bond distances for $[Ru(terpy)_2](TCNQ)_3\ CH_3CN$.

Atom	Atom	Length/Å		Atom	Atom	Length/Å
Ru1	N2	2.050(3)		C34	C35	1.431(6)
Ru1	N4	1.971(4)		C34	C39	1.417(6)
Ru1	N6	2.064(3)		C26	C16	1.472(6)
Ru1	N1	1.971(4)		C26	C27	1.384(6)
Ru1	N3	2.077(3)		C47	C48	1.361(5)
Ru1	N5	2.068(3)		C47	C46	1.422(6)
N2	C10	1.373(5)		C5	C4	1.378(5)
N2	C6	1.346(5)		C10	C1	1.477(6)
N15	C56	1.142(5)		C10	C9	1.376(5)
N4	C16	1.341(5)		C61	C62	1.435(5)
N4	C20	1.343(5)		C61	C60	1.435(6)
N6	C30	1.346(6)		C31	C33	1.425(6)
N6	C26	1.376(6)		C37	C38	1.421(6)
N1	C5	1.352(5)		C37	C40	1.419(6)
N1	C1	1.354(5)		C59	C60	1.354(7)
N14	C54	1.146(5)		C7	C6	1.386(5)
N3	C15	1.347(5)		C7	C8	1.377(7)
N3	C11	1.372(5)		C2	C1	1.388(6)
N5	C21	1.370(5)		C2	C3	1.387(6)
N5	C25	1.352(5)		C25	C24	1.390(6)
N11	C44	1.159(6)		C38	C39	1.365(6)
N10	C42	1.145(6)		C29	C28	1.378(6)
N17	C65	1.148(5)		C16	C17	1.388(5)
C30	C29	1.377(6)		C57	C55	1.440(6)
N16	C57	1.144(5)		N18	C66	1.129(5)
C12	C11	1.380(6)		C27	C28	1.386(6)
C12	C13	1.381(6)		C49	C48	1.426(6)
C52	C54	1.425(6)		C49	C50	1.422(5)
C52	C53	1.418(6)		C62	C63	1.345(5)
C52	C49	1.405(5)		C55	C56	1.438(6)
C15	C14	1.370(5)		C20	C19	1.390(6)
N12	C45	1.154(5)		C43	C45	1.422(6)
N7	C32	1.153(5)		C43	C46	1.415(6)
N13	C53	1.145(5)		C43	C44	1.427(6)
C64	C65	1.433(6)		C40	C42	1.430(6)
C64	C61	1.392(6)		C40	C41	1.415(6)
C64	C66	1.438(6)		N9	C41	1.148(6)
C11	C5	1.476(6)		C24	C23	1.369(6)
C58	C59	1.430(6)		C14	C13	1.388(6)

Table 20. Continued.

Atom	Atom	Length/Å		Atom	Atom	Length/Å
C58	C63	1.442(6)		C3	C4	1.388(6)
N8	C33	1.155(5)		C51	C50	1.362(5)
C21	C20	1.470(6)		C8	C9	1.387(6)
C21	C22	1.390(6)		C22	C23	1.372(7)
C36	C37	1.417(6)		C17	C18	1.383(6)
C36	C35	1.346(6)		N19	C67	1.141(7)
C32	C31	1.434(6)		C68	C67	1.461(7)
C34	C31	1.398(6)		C18	C19	1.372(7)

Table 21. Bond angles for $[Ru(terpy)_2](TCNQ)_3 \cdot CH_3CN$.

Atom	Atom	Atom	Angle/°		Atom	Atom	Atom	Angle/°
N2	Ru1	N6	90.27(12)		C62	C61	C60	117.1(4)
N2	Ru1	N3	158.43(12)		C34	C31	C32	120.8(4)
N2	Ru1	N5	92.95(13)		C34	C31	C33	124.1(4)
N4	Ru1	N2	97.76(13)		C33	C31	C32	114.9(4)
N4	Ru1	N6	78.94(17)		C36	C37	C38	117.2(4)
N4	Ru1	N1	176.98(14)		C36	C37	C40	121.3(4)
N4	Ru1	N3	103.79(14)		C40	C37	C38	121.5(4)
N4	Ru1	N5	79.49(15)		C60	C59	C58	120.9(5)
N6	Ru1	N3	93.06(12)		C8	C7	C6	119.5(4)
N6	Ru1	N5	158.43(16)		N13	C53	C52	178.9(5)
N1	Ru1	N2	79.69(14)		C3	C2	C1	118.7(4)
N1	Ru1	N6	102.60(17)		N5	C25	C24	121.4(5)
N1	Ru1	N3	78.79(14)		C39	C38	C37	120.6(4)
N1	Ru1	N5	98.96(14)		C30	C29	C28	119.3(5)
N5	Ru1	N3	91.73(13)		N4	C16	C26	112.7(4)
C10	N2	Ru1	114.1(3)		N4	C16	C17	120.4(4)
C6	N2	Ru1	127.9(3)		C17	C16	C26	126.8(4)
C6	N2	C10	117.8(3)		N16	C57	C55	177.8(5)
C16	N4	Ru1	119.6(3)		C26	C27	C28	119.6(5)
C16	N4	C20	122.1(4)		C52	C49	C48	121.2(4)
C20	N4	Ru1	118.1(3)		C52	C49	C50	121.6(4)
C30	N6	Ru1	127.6(4)		C50	C49	C48	117.2(4)
C30	N6	C26	118.5(4)		C63	C62	C61	121.5(4)
C26	N6	Ru1	113.8(3)		N1	C1	C10	112.9(4)
C5	N1	Ru1	119.9(3)		N1	C1	C2	120.0(4)
C5	N1	C1	121.5(4)		C2	C1	C10	127.1(4)
C1	N1	Ru1	118.5(3)		C58	C55	C57	122.1(4)
C15	N3	Ru1	127.4(3)		C58	C55	C56	121.9(4)
C15	N3	C11	118.6(4)		C56	C55	C57	115.9(4)
C11	N3	Ru1	113.9(3)		C47	C48	C49	121.6(4)
C21	N5	Ru1	113.5(3)		N4	C20	C21	114.0(4)
C25	N5	Ru1	127.9(3)		N4	C20	C19	119.5(4)
C25	N5	C21	118.6(4)		C19	C20	C21	126.4(4)
N6	C30	C29	122.4(5)		C36	C35	C34	120.3(4)
C11	C12	C13	120.0(4)		C38	C39	C34	121.7(4)
C53	C52	C54	115.4(4)		C45	C43	C44	115.1(4)
C49	C52	C54	122.3(4)		C46	C43	C45	120.9(4)
C49	C52	C53	122.3(4)		C46	C43	C44	123.8(4)
N3	C15	C14	122.3(4)		N12	C45	C43	178.4(5)

Table 21. Continued.

Atom	Atom	Atom	Angle/°		Atom	Atom	Atom	Angle/°
C61	C64	C65	121.9(4)		C41	C40	C37	121.1(4)
C61	C64	C66	123.2(4)		C41	C40	C42	115.9(4)
N3	C11	C12	120.9(4)		N15	C56	C55	179.0(5)
N3	C11	C5	115.0(4)		N2	C6	C7	122.4(4)
C12	C11	C5	124.1(4)		C62	C63	C58	121.3(4)
C59	C58	C63	117.4(4)		C23	C24	C25	119.6(5)
C55	C58	C59	121.3(4)		N10	C42	C40	177.6(5)
C55	C58	C63	121.3(4)		C15	C14	C13	119.5(4)
N5	C21	C20	114.4(4)		C59	C60	C61	121.7(4)
N5	C21	C22	121.2(4)		C12	C13	C14	118.7(4)
C22	C21	C20	124.4(4)		C43	C46	C47	121.4(4)
C35	C36	C37	122.6(4)		C43	C46	C51	121.0(4)
N7	C32	C31	178.1(5)		C51	C46	C47	117.6(4)
C31	C34	C35	121.3(4)		N9	C41	C40	178.4(6)
C31	C34	C39	121.3(4)		N11	C44	C43	176.5(5)
C39	C34	C35	117.5(4)		N18	C66	C64	176.8(5)
N14	C54	C52	177.6(5)		C2	C3	C4	120.6(4)
N17	C65	C64	178.0(5)		C5	C4	C3	118.7(4)
N6	C26	C16	114.6(4)		C50	C51	C46	121.5(4)
N6	C26	C27	120.8(4)		C51	C50	C49	121.2(4)
C27	C26	C16	124.7(4)		C29	C28	C27	119.2(5)
C48	C47	C46	120.9(4)		C7	C8	C9	118.7(4)
N1	C5	C11	112.3(4)		N8	C33	C31	177.7(5)
N1	C5	C4	120.5(4)		C23	C22	C21	119.3(5)
C4	C5	C11	127.2(4)		C18	C17	C16	118.0(4)
N2	C10	C1	114.6(4)		C24	C23	C22	119.8(5)
N2	C10	C9	121.7(4)		C10	C9	C8	119.7(4)
C9	C10	C1	123.6(4)		C19	C18	C17	121.0(4)
C64	C61	C62	121.2(4)		N19	C67	C68	179.2(7)
C64	C61	C60	121.8(4)		C18	C19	C20	119.0(5)

Table 22. The charges (ρ) of different TCNQ species in $[Ru(terpy)_2](TCNQ)_3 \cdot CH_3CN$ at 110 K as estimated from the Kistenmacher's formula (A, B, C as denoted in Figure 69; b, c and d are average C-C bond distances as depicted below).

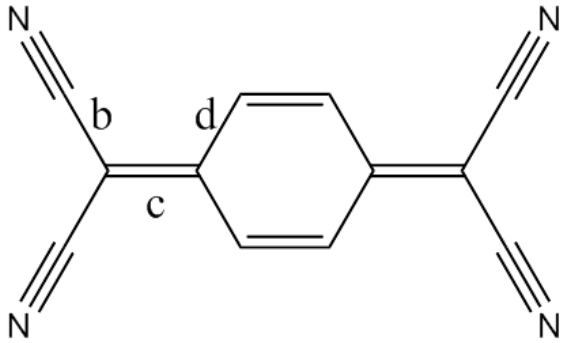

TCNQ	b /Å	c /Å	d /Å	ρ
A	1.426	1.409	1.422	-0.79
B	1.384	1.410	1.4238	-1.09
C	1.437	1.388	1.436	-0.29

Extension of the synthetic methodology to other functional systems with partially charged TCNQ species

From the aforementioned results, it can be ascertained $[Et_3NH](TCNQ)_2$ is a very good starting material for the preparation of bifunctional materials with electrical conducting properties and, as such, is also of interest for the design of other functional cationic species such as photosensitizers.

Three compounds have been obtained with cationic species of $[Ru(terpy)_2]^{2+}$, $[Ru(bpy)_3]^{2+}$ and $[Zn(terpy)_2]^{2+}$, respectively. It is interesting to note that the products $[Ru(terpy)_2](TCNQ)_3 \cdot CH_3CN$ and $[Zn(terpy)_2](TCNQ)_{2.5} \cdot 3CH_3CN$ give rise to different structures. $[Ru(terpy)_2](TCNQ)_3 \cdot CH_3CN$ is isostructural with $[Co(terpy)_2](TCNQ)_3 \cdot CH_3CN$ as discussed in Chapter II, whereas

$[Zn(terpy)_2](TCNQ)_{2.5}$ $3CH_3CN$ crystallizes in triclinic P-1 with two and one-half TCNQ species per formula unit (Table 19, Figure 69 and Figure 70).

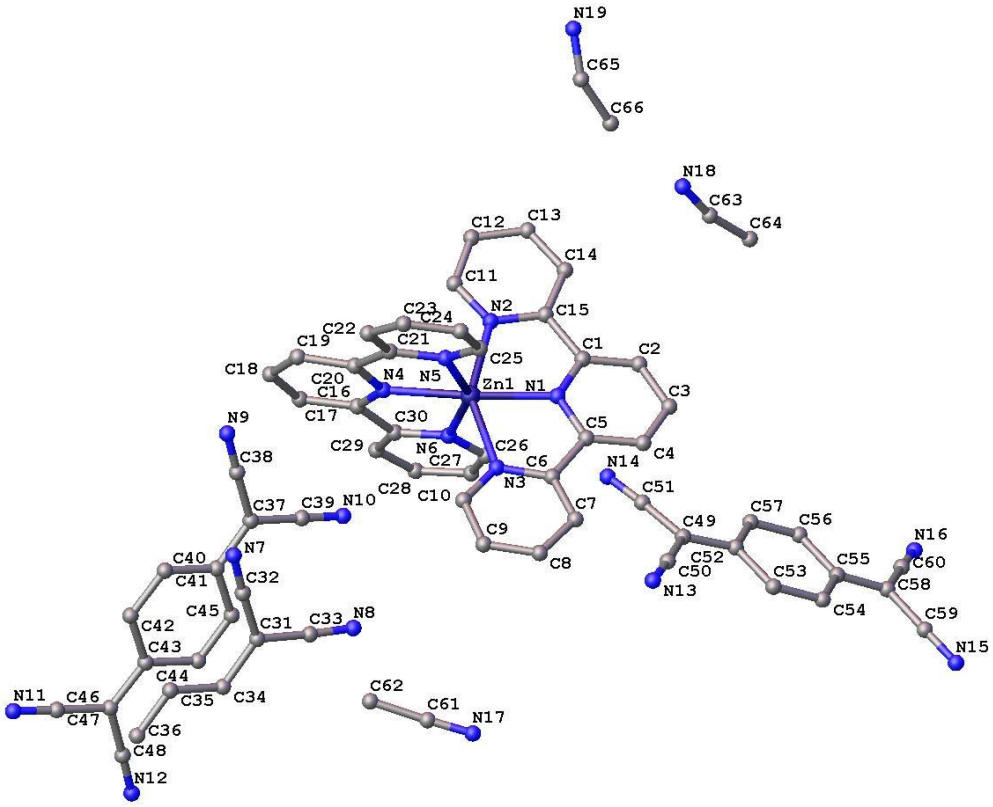

Figure 70. Asymmetric unit of $[Zn(terpy)_2](TCNQ)_{2.5}$ $3CH_3CN$. Hydrogen atoms have been omitted for the sake of clarity.

Table 23. Summary of crystallographic parameters for $[Zn(terpy)_2](TCNQ)_{2.5} \cdot 3CH_3CN$.

Empirical formula	$C_{66}H_{41}N_{19}Zn$
Formula weight	1165.55
Temperature/K	110.15
Crystal system	triclinic
Space group	P-1
a/Å	8.163(3)
b/Å	9.859(3)
c/Å	35.001(11)
α/°	89.943(3)
β/°	87.170(3)
γ/°	86.208(3)
Volume/Å^3	2807.3(15)
Z	2
ρ_{calc}g/cm^3	1.379
μ/mm^{-1}	0.500
F(000)	1200.0
Crystal size/mm^3	0.17 × 0.11 × 0.07
Radiation	MoKα (λ = 0.71073)
2Θ range for data collection/°	3.496 to 48.814
Index ranges	$-9 \leq h \leq 9$, $-11 \leq k \leq 11$, $-40 \leq l \leq 40$
Reflections collected	20580
Independent reflections	8999 [R_{int} = 0.0691, R_{sigma} = 0.1102]
Data/restraints/parameters	8999/0/748
Goodness-of-fit on F^2	1.076
Final R indexes [I>=2σ (I)]	R_1 = 0.0766, wR_2 = 0.1768
Final R indexes [all data]	R_1 = 0.1132, wR_2 = 0.1899
Largest diff. peak/hole / e Å^{-3}	0.75/-0.67

$R_1 = \Sigma||F_o|-|F_c||/\Sigma|F_o|$. $wR_2=[\Sigma w(|F_o|-|F_c|)^2/\Sigma w(F_o)^2]^{1/2}$. $w = 0.75/(\sigma^2(F_o)+0.00010F_o^2)$.

Goodness-of-fit = $\{\sum[w(F_o^2 - F_c^2)^2]/(n-p)\}^{1/2}$, where n is the number of reflections and p is the total number of parameters refined.

Table 24. Bond lengths for $[Zn(terpy)_2](TCNQ)_{2.5} \cdot 3CH_3CN$.

Atom	Atom	Length/Å		Atom	Atom	Length/Å
Zn1	N1	2.090(5)		N10	C39	1.156(7)
Zn1	N2	2.193(5)		N11	C47	1.157(7)
Zn1	N3	2.194(5)		N12	C48	1.147(7)
Zn1	N4	2.091(4)		C37	C38	1.436(8)
Zn1	N5	2.164(5)		C37	C39	1.430(8)
Zn1	N6	2.183(4)		C37	C40	1.401(7)
N1	C1	1.348(7)		C40	C41	1.429(7)
N1	C5	1.346(7)		C40	C45	1.437(7)
N2	C11	1.344(7)		C41	C42	1.359(7)
N2	C15	1.348(7)		C42	C43	1.435(7)
N3	C6	1.347(7)		C43	C44	1.432(7)
N3	C10	1.336(7)		C43	C46	1.381(7)
N4	C16	1.338(7)		C44	C45	1.356(7)
N4	C20	1.347(7)		C46	C47	1.435(8)
N5	C21	1.359(7)		C46	C48	1.440(8)
N5	C25	1.345(7)		N13	C50	1.147(8)
N6	C26	1.333(7)		N14	C51	1.146(8)
N6	C30	1.341(7)		N15	C59	1.157(8)
C1	C2	1.382(8)		N16	C60	1.145(8)
C1	C15	1.471(9)		C49	C50	1.407(10)
C2	C3	1.389(10)		C49	C51	1.421(10)
C3	C4	1.353(9)		C49	C52	1.427(8)
C4	C5	1.384(8)		C52	C53	1.416(8)
C5	C6	1.478(8)		C52	C57	1.421(8)
C6	C7	1.393(8)		C53	C54	1.375(8)
C7	C8	1.393(9)		C54	C55	1.418(8)
C8	C9	1.358(9)		C55	C56	1.428(8)
C9	C10	1.389(8)		C55	C58	1.415(8)
C11	C12	1.378(9)		C56	C57	1.366(8)
C12	C13	1.373(10)		C58	C59	1.423(9)
C13	C14	1.381(11)		C58	C60	1.429(10)
C14	C15	1.385(9)		N7	C32	1.149(7)
C16	C17	1.396(7)		N8	C33	1.155(7)
C16	C30	1.480(7)		C31	C32	1.422(8)
C17	C18	1.388(8)		C31	C33	1.417(8)
C18	C19	1.383(8)		C31	C34	1.416(7)
C19	C20	1.388(7)		C34	C35	1.433(7)
C20	C21	1.484(8)		C34	$C36^1$	1.437(7)
C21	C22	1.385(8)		C35	C36	1.346(7)

Table 24. Continued.

Atom	Atom	Length/Å		Atom	Atom	Length/Å
C23	C24	1.381(8)		N19	C65	1.251(18)
C24	C25	1.374(8)		C65	C66	1.493(19)
C26	C27	1.387(8)		N18	C63	1.226(15)
C27	C28	1.380(8)		C63	C64	1.444(16)
C28	C29	1.398(7)		N17	C61	1.130(9)
C29	C30	1.389(7)		C61	C62	1.445(10)
N9	C38	1.139(7)				

[1]1-X,2-Y,1-Z

Table 25. Bond angles for $[Zn(terpy)_2](TCNQ)_{2.5}$ $3CH_3CN$.

Atom	Atom	Atom	Angle/°		Atom	Atom	Atom	Angle/°
N1	Zn1	N2	75.45(19)		N5	C21	C22	121.2(5)
N1	Zn1	N3	75.22(18)		C22	C21	C20	123.7(5)
N1	Zn1	N4	172.03(18)		C23	C22	C21	119.1(5)
N1	Zn1	N5	109.68(17)		C22	C23	C24	120.0(5)
N1	Zn1	N6	100.18(17)		C25	C24	C23	118.6(5)
N2	Zn1	N3	150.55(18)		N5	C25	C24	122.3(5)
N4	Zn1	N2	97.84(18)		N6	C26	C27	122.9(5)
N4	Zn1	N3	111.60(16)		C28	C27	C26	118.0(5)
N4	Zn1	N5	75.55(17)		C27	C28	C29	119.7(5)
N4	Zn1	N6	74.84(16)		C30	C29	C28	118.5(5)
N5	Zn1	N2	101.22(16)		N6	C30	C16	115.4(5)
N5	Zn1	N3	86.25(17)		N6	C30	C29	121.6(5)
N5	Zn1	N6	150.13(17)		C29	C30	C16	122.8(5)
N6	Zn1	N2	86.66(16)		C39	C37	C38	115.8(5)
N6	Zn1	N3	101.02(16)		C40	C37	C38	123.0(5)
C1	N1	Zn1	119.0(4)		C40	C37	C39	121.3(5)
C5	N1	Zn1	119.4(4)		N9	C38	C37	178.8(6)
C5	N1	C1	120.8(5)		N10	C39	C37	179.6(6)
C11	N2	Zn1	127.1(4)		C37	C40	C41	121.5(5)
C11	N2	C15	118.5(5)		C37	C40	C45	120.8(5)
C15	N2	Zn1	114.3(4)		C41	C40	C45	117.7(5)
C6	N3	Zn1	115.1(4)		C42	C41	C40	121.1(5)
C10	N3	Zn1	126.0(4)		C41	C42	C43	121.2(5)
C10	N3	C6	118.7(5)		C44	C43	C42	117.8(4)
C16	N4	Zn1	119.7(4)		C46	C43	C42	120.7(5)
C16	N4	C20	120.5(5)		C46	C43	C44	121.6(5)
C20	N4	Zn1	119.5(4)		C45	C44	C43	121.0(5)
C21	N5	Zn1	115.7(3)		C44	C45	C40	121.3(5)
C25	N5	Zn1	124.9(4)		C43	C46	C47	122.5(5)
C25	N5	C21	118.8(5)		C43	C46	C48	123.0(5)
C26	N6	Zn1	124.5(4)		C47	C46	C48	114.4(5)
C26	N6	C30	119.4(5)		N11	C47	C46	178.8(6)
C30	N6	Zn1	115.6(3)		N12	C48	C46	178.8(6)
N1	C1	C2	120.0(6)		C50	C49	C51	116.0(6)
N1	C1	C15	113.8(5)		C50	C49	C52	122.7(6)
C2	C1	C15	126.2(6)		C51	C49	C52	121.3(6)
C1	C2	C3	119.2(6)		N13	C50	C49	177.2(7)
C4	C3	C2	119.8(6)		N14	C51	C49	177.3(8)
C3	C4	C5	119.7(6)		C53	C52	C49	121.0(6)

Table 25. Continued.

Atom	Atom	Atom	Angle/°		Atom	Atom	Atom	Angle/°
N1	C5	C6	114.3(5)		C57	C52	C49	121.8(6)
C4	C5	C6	125.4(6)		C54	C53	C52	121.4(6)
N3	C6	C5	115.6(5)		C53	C54	C55	121.6(6)
N3	C6	C7	121.7(6)		C54	C55	C56	116.9(5)
C7	C6	C5	122.7(5)		C58	C55	C54	121.7(6)
C8	C7	C6	118.4(6)		C58	C55	C56	121.4(6)
C9	C8	C7	119.7(6)		C57	C56	C55	121.2(6)
C8	C9	C10	119.0(6)		C56	C57	C52	121.9(6)
N3	C10	C9	122.4(6)		C55	C58	C59	121.7(6)
N2	C11	C12	122.7(6)		C55	C58	C60	122.9(6)
C13	C12	C11	118.5(7)		C59	C58	C60	115.2(6)
C12	C13	C14	119.7(7)		N15	C59	C58	177.5(8)
C13	C14	C15	119.0(7)		N16	C60	C58	178.2(8)
N2	C15	C1	116.4(5)		C33	C31	C32	114.5(5)
N2	C15	C14	121.5(6)		C34	C31	C32	122.6(5)
C14	C15	C1	122.0(6)		C34	C31	C33	122.8(5)
N4	C16	C17	121.4(5)		N7	C32	C31	177.3(6)
N4	C16	C30	113.9(5)		N8	C33	C31	176.7(6)
C17	C16	C30	124.6(5)		C31	C34	C35	121.2(5)
C18	C17	C16	118.1(5)		C31	C34	C36[1]	122.0(5)
C19	C18	C17	120.2(5)		C35	C34	C36[1]	116.7(5)
C18	C19	C20	118.8(5)		C36	C35	C34	121.8(5)
N4	C20	C19	120.9(5)		C35	C36	C34[1]	121.4(5)
N4	C20	C21	113.6(5)		N19	C65	C66	149.6(17)
C19	C20	C21	125.4(5)		N18	C63	C64	167.2(15)
N5	C21	C20	115.1(5)		N17	C61	C62	177.8(8)

[1]1-X,2-Y,1-Z

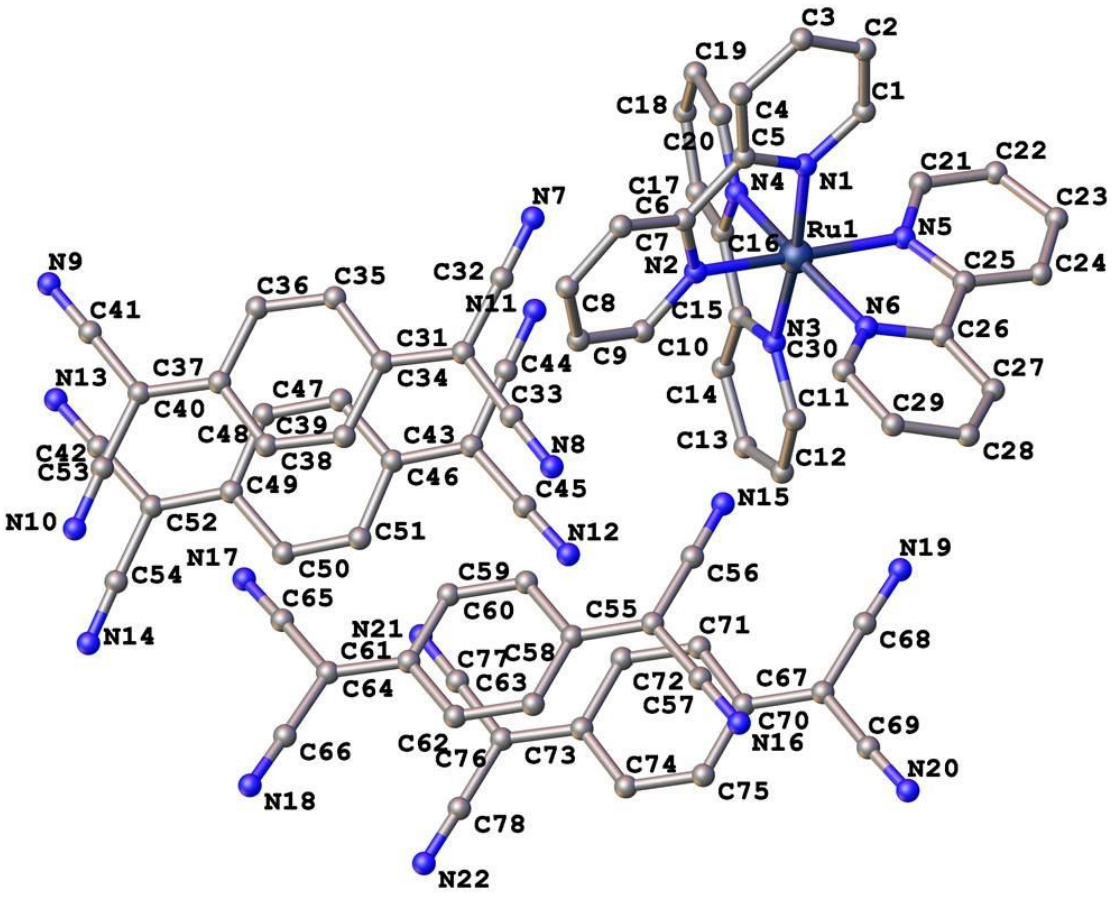

Figure 71. Asymmetric unit of $[Ru(bpy)_3](TCNQ)_4$. Hydrogen atoms have been omitted for the sake of clarity.

Table 26. Bond distances for $[Ru(bpy)_3](TCNQ)_4$.

Atom	Atom	Length/Å		Atom	Atom	Length/Å
Ru1	N1	2.0456(19)		C48	C49	1.427(4)
Ru1	N2	2.0471(18)		C49	C50	1.445(4)
Ru1	N3	2.0677(19)		C49	C52	1.393(4)
Ru1	N4	2.0593(18)		C50	C51	1.334(4)
Ru1	N5	2.0501(19)		C52	C53	1.438(4)
Ru1	N6	2.0581(18)		C52	C54	1.417(5)
N1	C1	1.354(3)		N15	C56	1.146(3)
N1	C5	1.366(3)		N16	C57	1.151(3)
N2	C6	1.355(3)		N17	C65	1.151(3)
N2	C10	1.355(3)		N18	C66	1.146(3)
N3	C11	1.353(3)		C55	C56	1.428(3)
N3	C15	1.356(3)		C55	C57	1.430(3)
N4	C16	1.353(3)		C55	C58	1.394(3)
N4	C20	1.349(3)		C58	C59	1.435(3)
N5	C21	1.345(3)		C58	C63	1.423(3)
N5	C25	1.360(3)		C59	C60	1.349(3)
N6	C26	1.365(3)		C60	C61	1.426(3)
N6	C30	1.343(3)		C61	C62	1.436(3)
C1	C2	1.368(3)		C61	C64	1.398(3)
C2	C3	1.373(4)		C62	C63	1.352(3)
C3	C4	1.386(3)		C64	C65	1.427(3)
C4	C5	1.388(3)		C64	C66	1.427(3)
C5	C6	1.469(3)		N7	C32	1.149(3)
C6	C7	1.387(3)		N8	C33	1.152(3)
C7	C8	1.384(3)		N9	C41	1.152(3)
C8	C9	1.375(3)		N10	C42	1.147(3)
C9	C10	1.371(3)		C31	C32	1.426(3)
C11	C12	1.373(3)		C31	C33	1.428(3)
C12	C13	1.377(4)		C31	C34	1.401(3)
C13	C14	1.392(3)		C34	C35	1.437(3)
C14	C15	1.388(3)		C34	C39	1.428(3)
C15	C16	1.474(3)		C35	C36	1.350(3)
C16	C17	1.384(3)		C36	C37	1.428(3)
C17	C18	1.377(3)		C37	C38	1.426(3)
C18	C19	1.369(4)		C37	C40	1.397(3)
C19	C20	1.373(3)		C38	C39	1.349(3)
C21	C22	1.373(4)		C40	C41	1.425(3)
C22	C23	1.372(4)		C40	C42	1.430(3)
C23	C24	1.365(4)		N19	C68	1.144(3)

Table 26. Continued.

Atom	Atom	Length/Å		Atom	Atom	Length/Å
C25	C26	1.470(3)		N21	C77	1.147(3)
C26	C27	1.383(3)		N22	C78	1.148(3)
C27	C28	1.367(4)		C67	C68	1.429(3)
C28	C29	1.378(4)		C67	C69	1.429(3)
C29	C30	1.378(3)		C67	C70	1.395(3)
N11	C44	1.145(4)		C70	C71	1.433(3)
N12	C45	1.147(3)		C70	C75	1.431(3)
N13	C53	1.150(3)		C71	C72	1.351(3)
N14	C54	1.153(4)		C72	C73	1.433(3)
C43	C44	1.423(5)		C73	C74	1.431(3)
C43	C45	1.436(4)		C73	C76	1.394(3)
C43	C46	1.383(4)		C74	C75	1.353(3)
C46	C47	1.436(4)		C76	C77	1.431(3)
C46	C51	1.429(4)		C76	C78	1.431(3)
C47	C48	1.341(4)				

Table 27. Bond angles for $[Ru(bpy)_3](TCNQ)_4$.

Atom	Atom	Atom	Angle/°		Atom	Atom	Atom	Angle/°
N1	Ru1	N2	78.82(7)		N11	C44	C43	179.0(4)
N1	Ru1	N3	173.43(7)		N12	C45	C43	178.8(4)
N1	Ru1	N4	95.90(7)		C43	C46	C47	120.8(3)
N1	Ru1	N5	95.33(7)		C43	C46	C51	121.8(3)
N1	Ru1	N6	91.63(7)		C51	C46	C47	117.4(3)
N2	Ru1	N3	97.73(7)		C48	C47	C46	121.3(3)
N2	Ru1	N4	92.61(7)		C47	C48	C49	121.4(3)
N2	Ru1	N5	172.10(7)		C48	C49	C50	117.2(3)
N2	Ru1	N6	95.65(7)		C52	C49	C48	121.3(3)
N4	Ru1	N3	78.59(7)		C52	C49	C50	121.5(3)
N5	Ru1	N3	88.60(7)		C51	C50	C49	121.3(3)
N5	Ru1	N4	93.26(7)		C50	C51	C46	121.5(3)
N5	Ru1	N6	79.10(7)		C49	C52	C53	122.6(3)
N6	Ru1	N3	94.29(7)		C49	C52	C54	123.5(3)
N6	Ru1	N4	169.76(8)		C54	C52	C53	113.9(3)
C1	N1	Ru1	126.52(17)		N13	C53	C52	179.3(4)
C1	N1	C5	117.5(2)		N14	C54	C52	178.9(4)
C5	N1	Ru1	115.92(14)		C56	C55	C57	116.4(2)
C6	N2	Ru1	116.14(14)		C58	C55	C56	121.7(2)
C6	N2	C10	118.1(2)		C58	C55	C57	121.8(2)
C10	N2	Ru1	125.68(16)		N15	C56	C55	177.8(3)
C11	N3	Ru1	126.45(16)		N16	C57	C55	178.9(3)
C11	N3	C15	118.0(2)		C55	C58	C59	120.7(2)
C15	N3	Ru1	115.41(15)		C55	C58	C63	121.7(2)
C16	N4	Ru1	115.58(14)		C63	C58	C59	117.5(2)
C20	N4	Ru1	125.80(17)		C60	C59	C58	120.9(2)
C20	N4	C16	118.0(2)		C59	C60	C61	121.7(2)
C21	N5	Ru1	126.25(16)		C60	C61	C62	117.3(2)
C21	N5	C25	118.0(2)		C64	C61	C60	121.4(2)
C25	N5	Ru1	115.67(15)		C64	C61	C62	121.3(2)
C26	N6	Ru1	114.83(15)		C63	C62	C61	121.0(2)
C30	N6	Ru1	126.70(16)		C62	C63	C58	121.5(2)
C30	N6	C26	118.22(19)		C61	C64	C65	121.5(2)
N1	C1	C2	123.3(2)		C61	C64	C66	122.9(2)
C1	C2	C3	119.5(2)		C66	C64	C65	115.6(2)
C2	C3	C4	118.5(2)		N17	C65	C64	178.5(2)
C3	C4	C5	120.1(2)		N18	C66	C64	178.2(3)
N1	C5	C4	121.1(2)		C32	C31	C33	116.0(2)
N1	C5	C6	114.2(2)		C34	C31	C32	122.3(2)

Table 27. Continued.

Atom	Atom	Atom	Angle/°		Atom	Atom	Atom	Angle/°
N2	C6	C5	114.7(2)		N7	C32	C31	179.0(3)
N2	C6	C7	121.7(2)		N8	C33	C31	178.5(2)
C7	C6	C5	123.6(2)		C31	C34	C35	121.3(2)
C8	C7	C6	119.0(2)		C31	C34	C39	121.2(2)
C9	C8	C7	119.4(2)		C39	C34	C35	117.50(19)
C10	C9	C8	119.2(2)		C36	C35	C34	121.2(2)
N2	C10	C9	122.5(2)		C35	C36	C37	121.0(2)
N3	C11	C12	122.6(2)		C38	C37	C36	117.7(2)
C11	C12	C13	119.7(2)		C40	C37	C36	121.5(2)
C12	C13	C14	118.6(2)		C40	C37	C38	120.7(2)
C15	C14	C13	119.3(2)		C39	C38	C37	121.5(2)
N3	C15	C14	121.7(2)		C38	C39	C34	121.0(2)
N3	C15	C16	114.9(2)		C37	C40	C41	123.0(2)
C14	C15	C16	123.4(2)		C37	C40	C42	120.9(2)
N4	C16	C15	114.8(2)		C41	C40	C42	116.1(2)
N4	C16	C17	121.6(2)		N9	C41	C40	178.7(2)
C17	C16	C15	123.6(2)		N10	C42	C40	178.1(2)
C18	C17	C16	119.2(2)		C69	C67	C68	114.9(2)
C19	C18	C17	119.3(2)		C70	C67	C68	122.5(2)
C18	C19	C20	119.2(2)		C70	C67	C69	122.6(2)
N4	C20	C19	122.5(2)		N19	C68	C67	178.1(3)
N5	C21	C22	122.0(3)		N20	C69	C67	177.1(3)
C23	C22	C21	120.0(3)		C67	C70	C71	121.0(2)
C24	C23	C22	118.7(3)		C67	C70	C75	121.5(2)
C23	C24	C25	119.7(2)		C75	C70	C71	117.50(19)
N5	C25	C24	121.5(2)		C72	C71	C70	121.4(2)
N5	C25	C26	114.7(2)		C71	C72	C73	120.9(2)
C24	C25	C26	123.7(2)		C74	C73	C72	117.9(2)
N6	C26	C25	114.89(19)		C76	C73	C72	120.5(2)
N6	C26	C27	121.3(2)		C76	C73	C74	121.6(2)
C27	C26	C25	123.8(2)		C75	C74	C73	121.0(2)
C28	C27	C26	119.4(2)		C74	C75	C70	121.3(2)
C27	C28	C29	119.7(2)		C73	C76	C77	121.8(2)
C28	C29	C30	118.8(2)		C73	C76	C78	122.4(2)
N6	C30	C29	122.5(2)		C78	C76	C77	115.82(19)
C44	C43	C45	116.0(3)		N21	C77	C76	178.7(2)
C46	C43	C44	122.3(3)		N22	C78	C76	178.7(2)
C46	C43	C45	121.6(3)					

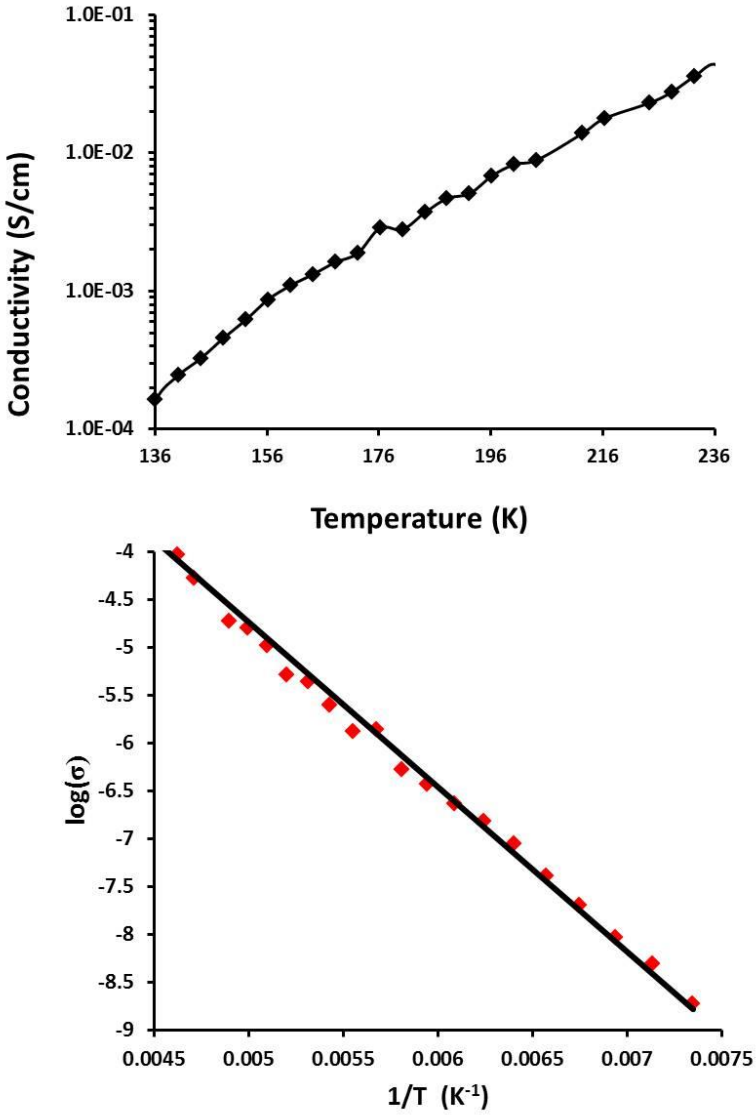

Figure 72. Top: temperature dependence of the electrical conductivity. Bottom: Arrhenius plot of electrical conductivity of $[Ru(terpy)_2](TCNQ)_3\ CH_3CN$. The red symbols are experimental data and the black line is the linear fit with an activation energy of 0.30 eV.

The product $[Ru(bpy)_3](TCNQ)_4$ contains four TCNQ species in the formula unit which leads to an average charge of -0.5. Conductivity measurements were carried out on single crystals of these three samples. The four-probe method was used on single crystal samples of $[Ru(bpy)_3](TCNQ)_4$ and $[Ru(terpy)_2](TCNQ)_3\ CH_3CN$.

$[Ru(terpy)_2](TCNQ)_3 \cdot CH_3CN$ behaves as a semiconductor over the temperature range of 136-236 K with a small activation energy of 0.30 eV (Figure 72). At temperatures new to room temperature the conductivity was unstable. $[Ru(bpy)_3](TCNQ)_4$ behaves as a semiconductor in the temperature range of 120-300 K with a small activation energy of 0.29 eV (Figure 73). It exhibits a good conductivity of 2.7×10^{-2} S/cm and it is noted that it also shows instability of the conductivity around room temperature.

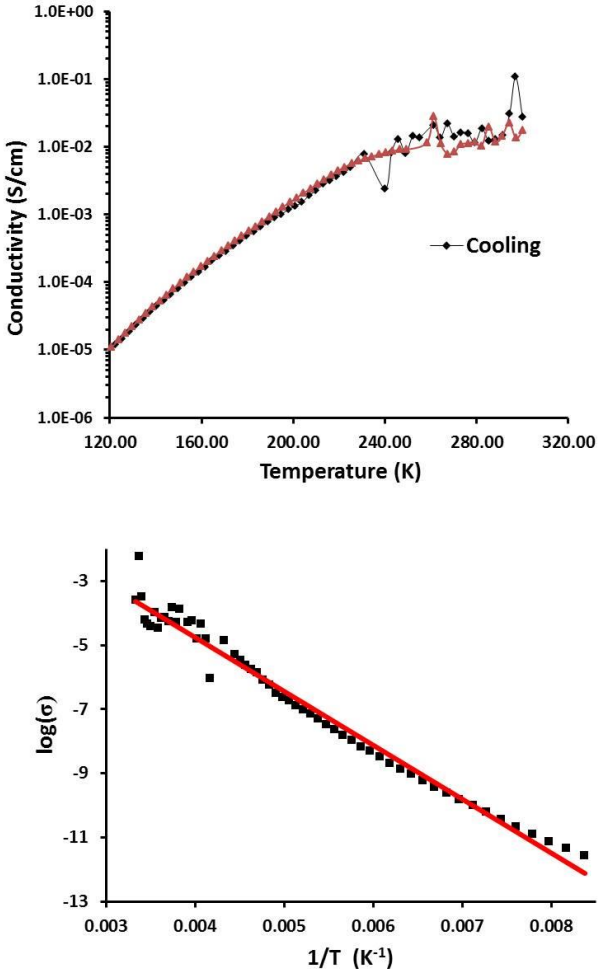

Figure 73. Top: temperature dependence of the electrical conductivity of $[Ru(bpy)_3](TCNQ)_4$. Bottom: Arrhenius plot of electrical conductivity of $[Ru(bpy)_3](TCNQ)_4$. The black symbols are experimental data and the red line is the linear fit with an activation energy of 0.29 eV.

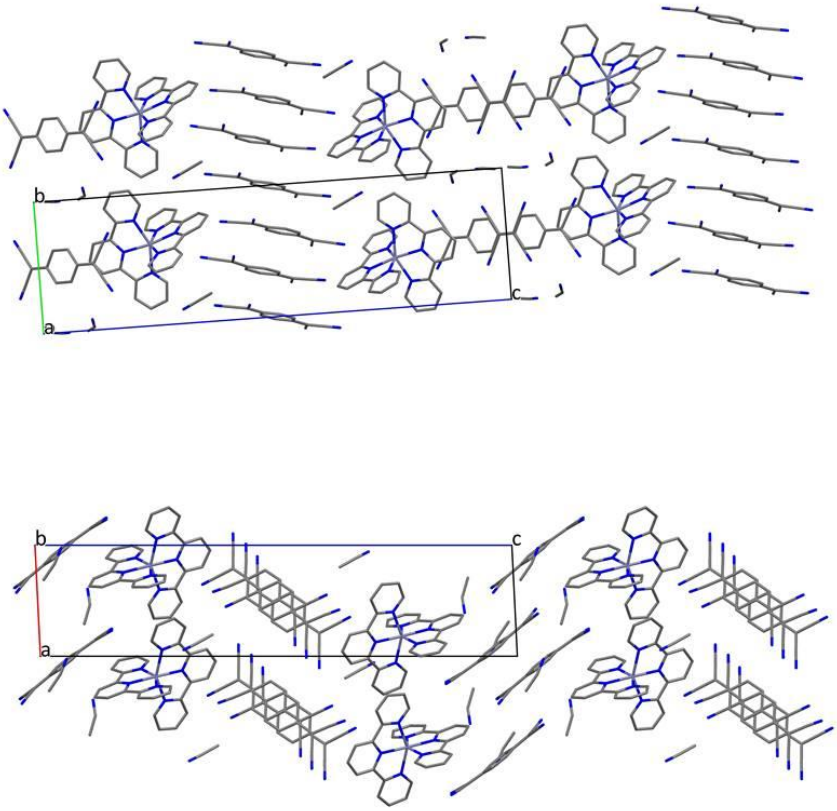

Figure 74. Packing diagrams for $[Zn(terpy)_2](TCNQ)_{2.5}$ $3CH_3CN$ viewed along the *a* (top) and *b* (bottom) axes.

For $[Zn(terpy)_2](TCNQ)_{2.5}$ $3CH_3CN$, single crystal conductivity measurements were performed by the two-probe method. The compound behaves as a semiconductor over the temperature range of 120-300 K with a small activation energy of 0.19 eV (Figure 75). It exhibits a lower conductivity of 3.9×10^{-6} S/cm at room temperature, which is likely due to the poor packing of TCNQ species in the structure, as one of the TCNQ species does not participate in long-range interactions which interrupts the charge carrier pathway (Figure 74).

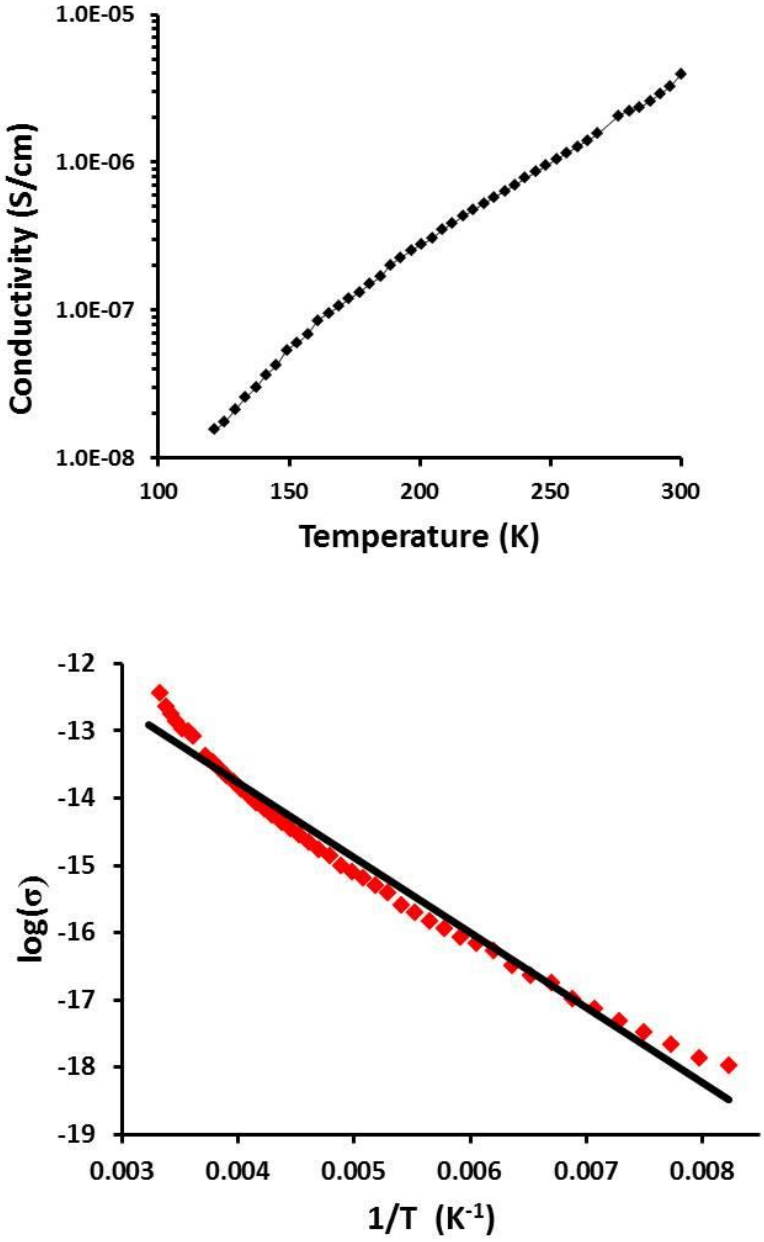

Figure 75. Top: temperature dependence of the electrical conductivity. Bottom: Arrhenius plot of electrical conductivity of $[Zn(terpy)_2](TCNQ)_{2.5} \cdot 3CH_3CN$. The red symbols are experimental data and the black line is the linear fit with an activation energy of 0.19 eV.

Conclusions

A series of isostructural chain-like compounds [Ln(TPMA)(μ-TCNQ)(μ-OH)](TCNQ)$_2$·CH$_3$CN (Ln = Dy, Gd, Y) have been synthesized. Magnetic and electrical conductivity studies revealed that the Dy(III) compound exhibited slow relaxation of the magnetization at 5.0-8.2 K and semiconductivity at 180-350 K. DC magnetic fields have been found to not only suppress the quantum tunneling of the magnetization, but also affect the spin-canted antiferromagnetic interactions in [Dy(TPMA)(μ-TCNQ)(μ-OH)](TCNQ)$_2$·CH$_3$CN. In addition, the increased DC magnetic field diminishes the TIP and the delocalization of electrons in the TCNQ stacks in the compounds.

It has also been demonstrated that other functional species like SMMs and photosensitizers such as $[Co(Tpm)_2]^{2+}$, $[Ru(terpy)_2]^{2+}$, $[Ru(bpy)_3]^{2+}$ and $[Zn(terpy)_2]^{2+}$can also be incorporated into electrically conducting bifunctional materials through a generalized modular synthetic approach by using the easily accessible TCNQ radical source of $[Et_3NH](TCNQ)_2$. The hybrid conducting SMM $[Co(Tpm)_2](TCNQ)_3$ retained the slow relaxation of the magnetization of the cationic unit and constitutes a good example for the study of interactions between SMM units and conducting frameworks in future work. The hybrid conducting photosensitizers will be good examples for the study of the effect of photoirradiation on the electrically conducting properties.

CHAPTER IV

MAGNETIC ORDERING IN TCNQ-BASED METAL-ORGANIC FRAMEWORKS WITH HOST-GUEST INTERACTIONS*

Introduction

Metal-organic frameworks (MOFs), also known as porous coordination polymers (PCPs), have attracted enormous attention over the past two decades because of their potential applications in gas separation/storage, catalysis and sensing.[162-165] These versatile crystalline materials exhibit rich structural variability and porosity and are ideal platforms for introducing multi-functionality. The topic of MOF materials has primarily focused on increasing porosity for gas storage but recent exciting advances are being made in relatively underexplored areas of catalytic reactivity,[166,167] electrical conductivity[71,168-172] and magnetic properties.[173,174] Ligand design is extremely important in MOF research due to the plethora of choices these organic linkers offer for the variation of MOF topologies and functionalities. Long rigid anionic carboxylate and phosphonate, and/or neutral N-donor ligands have been commonly used as MOF linkers in order to ensure both large void spaces and thermodynamic stability of the framework.

Recently, the use of redox active organic linkers or those equipped with functional groups has been on the upsurge as part of the current trend to design MOF's

---

* Part of this chapter is reprinted with permission from "Magnetic ordering in TCNQ-based metal–organic frameworks with host–guest interactions", by Xuan Zhang, Mohamed R. Saber, Andrey P. Prosvirin, Joseph H. Reibenspies, Lei Sun, Maria Ballesteros-Rivas, Hanhua Zhao and Kim R. Dunbar, *Inorganic Chemistry Frontiers*, **2015**, 2, 904-911, DOI: 10.1039/C5QI00128E, Copyright 2015 by Chinese Chemical Society (CCS), Peking University (PKU), and the Royal Society of Chemistry.

that display special properties such as selective gas/guest adsorption, catalytic reactivity, charge mobility and conductivity.[175,176] The use of redox-active linkers as alternatives to carboxylic acid ligands in MOFs is exemplified by the implementation of ligands such as TTF derivatives, NDIs, $TCNQ^{\bullet-}$, $TCNQ^{2-}$ and $(TCNQ\text{-}TCNQ)^{2-}$ (TTF = tetrathiafulvalene, NDI = naphthalenediimide, TCNQ = 7,7,8,8-tetracyanoquino-dimethane) in the formation of MOFs.[49,99,168,177-184]

The investigation of MOF materials for different applications in magnetism, such as data storage and quantum computing,[185-187] is hindered by the fact that the long linkers typically employed in the syntheses of MOF materials are not effective at mediating magnetic interactions. To tackle this problem, we have been studying metal-organocyanide linkers that are known to engender conducting and magnetic properties in extended architectures and have potential applications in non-volatile switching and memory devices.[46,49,60-64,66,74,188] The tunability of the redox activity of the organocyanide ligands make them very promising for accessing materials that combine semiconducting properties and magnetic ordering. Both theoretical and experimental studies have demonstrated that doubly reduced diamagnetic organocyanide ligands are capable of engendering effective magnetic coupling between metal spins, results that are attributed to an energetically favorable match between the ligand pπ orbitals and the metals dπ orbitals.[189-191] In this vein, we recently studied the magnetic properties of a series of anionic frameworks of the type $[M_2(TCNQ)_3]^{2-}$ (M= Mn, Fe, Co, Ni) and it was found that the $TCNQ^{2-}$ ligand promotes long range magnetic ordering despite the long coupling pathway.[68] The lack of accessible cavities in these three-dimensional materials,

however, precluded the possibility of enhancing magnetic and electronic properties via post-synthetic modifications or interactions with small guest molecules.

With the backdrop of previous work as a source of inspiration, we turned our attention to guest responsive magnetic MOFs as interesting targets because of their potential applications in molecular recognition and sensing in addition to the possibility for fine-tuning the magnetic properties by absorption/release of small guest molecules.[192-195] Previously, we had found that $[Mn_2(TCNQF_4)(CH_3OH)_{7.5}(H_2O)_{0.5}](TCNQF_4)_2 \bullet 7.5CH_3OH$ acts as a "magnetic sponge" and can reversibly switch between a glassy magnetic and a paramagnetic state triggered by de-solvation and solvation effects.[196] Of interest in the context of this work is the existence of TCNQ dianionic-based MOFs, $M(TCNQ)(4,4'\text{-bpy}) \supset CH_3OH$ (M = Zn, Cd, Mn, Fe, Co; 4,4'-bpy = 4,4'-bipyridine),[54,67,70,88,181,197] which exhibit 3D structures composed of 2D M^{II}-$TCNQ^{2-}$ neutral networks pillared by 4,4'-bpy (4,4'-bipyridine) linkers. It has been shown that these redox active MOF materials preferentially absorb aromatic solvent molecules such as benzene, nitrobenzene and anisole, leading to distinct color changes owing to variable degrees of charge-transfer between the host frameworks and the guest molecules (Figure 76).[67] We postulated that host-guest charge-transfer interactions could lead to guest-induced magnetic responses of the M-TCNQ grids of the MOFs based on changes in the electron density on the TCNQ dianion.

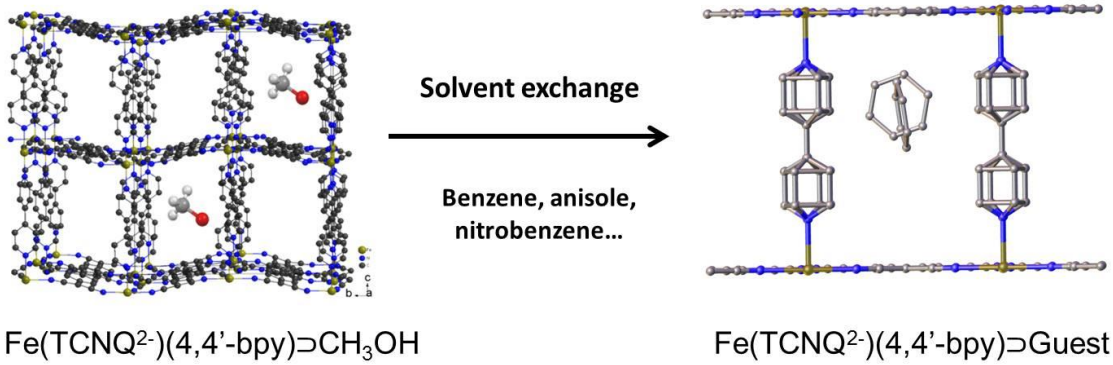

Figure 76. Scheme of the solvent exchange process in Fe(TCNQ)(4,4'-bpy) where the methanol molecules in the as-synthesized MOF can be exchanged by aromatic guest molecules such as benzene, anisole and nitrobenzene.

Herein, we report the guest modulated magnetic properties of the MOFs, M(TCNQ)(4,4'-bpy)⊃solvent (M = Fe (**1**), Mn(**2**)), with the inclusion of different aromatic solvent molecules as well as two new 2-D network compounds, $Fe(TCNQ)(DMF)_2 \cdot 2DMF$ (**3,** DMF = N,N-dimethylformamide) and $Fe(TCNQ)(CH_3CN)_2 \cdot 2\ CH_3CN$. The $TCNQ^{2-}$ anions were found to promote cooperative interactions between the high-spin Fe^{II} ions modulated by the aromatic guest molecules. This case study of solvent mediated magnetic behavior of redox-active MOFs resulting from electrostatic and steric interactions between the framework and the guest molecules serves as a proof of concept for the realization of guest controlled magnetic MOFs.[107]

Experimental Section

Syntheses and characterization

The synthetic procedures were carried out under a nitrogen atmosphere using standard Schlenk-line techniques. The H_2TCNQ molecule was prepared according to the literature by the reduction of TCNQ with mercaptoacetic acid.[198] The compound

Fe(TCNQ)(4,4'-bpy)•6CH_3OH was prepared by a slight modification of the reported procedures.[54,88]

Soaking of the Fe(TCNQ)(4,4'-bpy) MOFs in benzene, toluene, aniline, nitrobenzene was carried out with degassed solvents under a nitrogen atmosphere. Powder X-ray diffraction measurements were performed with a BRUKER D8-Focus Bragg-Brentano X-ray Powder Diffractometer equipped with an CuKα radiation source (λ = 1.5406 Å, 40 kV and 40 mA). The samples for magnetic measurements were prepared by sealing crushed crystals with a minimum volume of the corresponding solvents in quartz NMR tubes.

Fe(TCNQ)(DMF)$_2$ 2DMF. A solution of 0.2 mmol of $Fe(SO_4)_2$•7H_2O, 0.5 mmol of Li(OAc)•2H_2O and 20 mg of ascorbic acid in methanol was layered on a solution of 0.2 mmol of H_2TCNQ in (N, N-dimethylformamide (DMF). Yellowish green crystals formed in two days. IR: ν(CN) 2196.7, 2134.5 cm^{-1}; ν(CO) 1639.7 cm^{-1}.

Results and Discussions

Syntheses and structures

The formation of $TCNQ^{2-}$ containing coordination networks has been achieved by disproportionation of $TCNQ^{\bullet-}$, the deprotonation of H_2TCNQ by lithium acetate and the direct reduction of neutral TCNQ by metal complexes.[54,88,190] The synthetic method employed in this work is slightly modified from reported procedures and was carried out using 4,4'-bpy/DMF in the absence of LiOAc to deprotonate H_2TCNQ in order to generate $TCNQ^{2-}$ *in situ*. Under anaerobic conditions, layering of a solution of $FeSO_4$•7H_2O in CH_3OH onto a mixture of H_2TCNQ and 4,4'-bpy in DMF results in the

formation of red-orange crystals of the product $Fe^{II}(TCNQ)(4,4'\text{-bpy})\supset CH_3OH$ (**1**$\supset CH_3OH$) in three days. The reaction is considerably slower than the reported procedures with either LiOAc as the deprotonation reagent for H_2TCNQ or the disproportionation reactions TCNQ radicals to produce $TCNQ^{2-}$, a favorable situation which leads to the formation of larger single crystals.

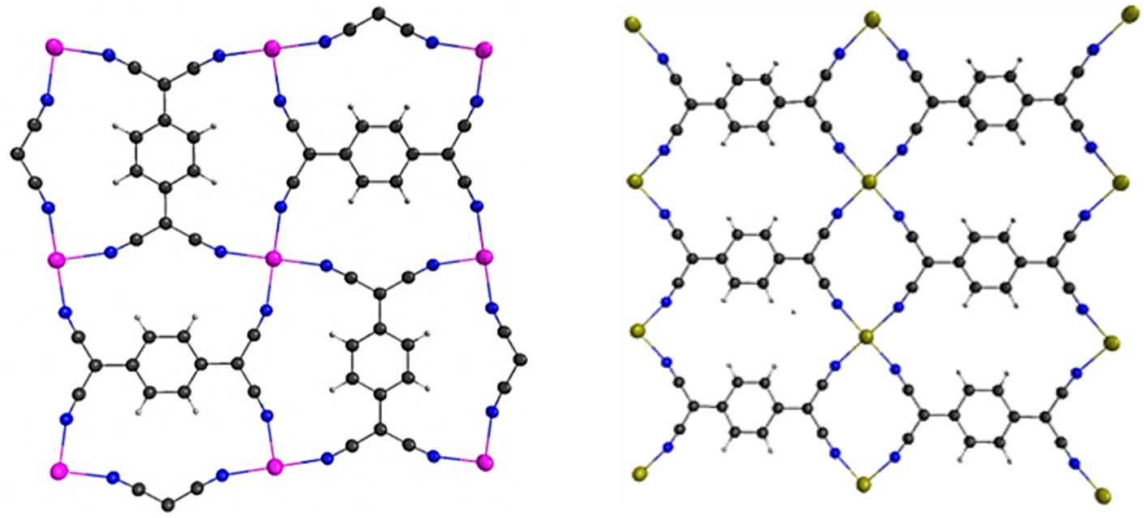

Figure 77. Two of the most common coordination modes of TCNQ dianions, with adjacent TCNQ species being perpendicular (left) and parallel (right) to each other.

The structure of the compound (**1**$\supset CH_3OH$) was confirmed to be the same as previously reported by Kitagawa and coworkers.[88] As they reported, data collected at 133 K reveal that the (Fe^{II}-$TCNQ^{2-}$) units form corrugated sheets with adjacent μ_4-$TCNQ^{2-}$ bridges being arranged perpendicular to each other (Figure 77, left); these sheets become more flattened as the temperature increases from 133 to 243 K. The 2-D networks are pillared by 4,4'-bipyridine to form the 3-D frameworks (Figure 78) and the cavities are filled with methanol molecules that can be replaced with aromatic guest molecules by soaking the crystals in neat aromatic solvents. Single crystals are preserved

during these experiments bu,t only in the case of Zn(TCNQ)(4,4'-bpy)⊃C_6H_6 compound, were the benzene molecules crystallographically located.[67] For the reported nitrobenzene and anisole soaked crystals of compound **1**, the framework structures were solved with the Fe-TCNQ network being disordered between the corrugated sheets and the planar sheets; weak peaks of electron density were observed in the cavity and are ascribed to disordered guest molecules. Charge-transfer between the $TCNQ^{2-}$ in the host framework and the guest aromatic molecules was reported previously on the basis of diffuse reflectance UV-Vis spectra but no additional properties were reported.[88]

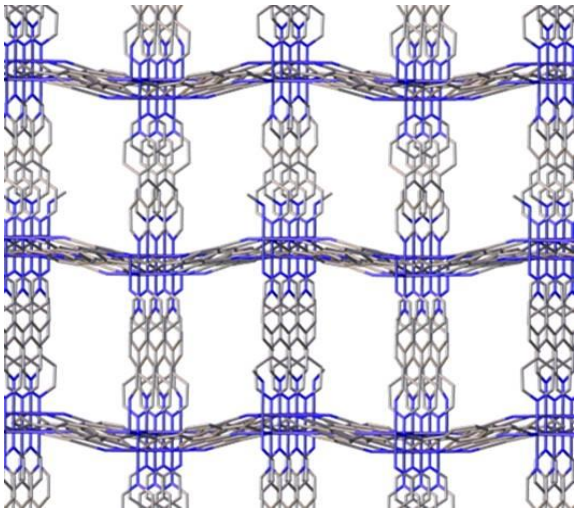

Figure 78. Structure of the metal-organic frameworks Fe(TCNQ)(4,4'-bpy)⊃CH_3OH. Solvent molecules are omitted for the sake of clarity.

Single crystal X-ray structures of compound **1** with different interstitial aromatic solvents were colllectes in order to probe structure-property relationships (Table 1). For benzene, toluene and aniline, low electron densities of the disordered solvent molecules were observed in the frameworks. The structures were solved in the tetragonal space group I4/mcm, which is consistent with reported structures of these frameworks.[88]

Refinement of the guest molecules in the pores of the framework was carried out by using models of the corresponding aromatic molecules to fit the residual electron densities. The positioning of the guest molecules from refinement of **2**⊃C_6H_6 is consistent with the structure of Zn(TCNQ)(4,4'-bpy)⊃C_6H_6 as previously reported (Figure 3, right), where no intimate interaction between the aromatic guest molecules and the host framework is observed and the planes of the aromatic molecule are vertical to the M-TCNQ 2-D planes. Unfortunately, the crystal structure of compound **1**⊃$C_6H_5NO_2$ exhibited severe twinning and disorder problems and was not refined satisfactorily.[‡] A possible lower symmetry space group was found, as compared to benzene, toluene and aniline containing frameworks of **1**, which is consistent with the observation of extra peaks for **1**⊃$C_6H_5NO_2$ in the powder X-ray diffraction patterns (*vide infra*).

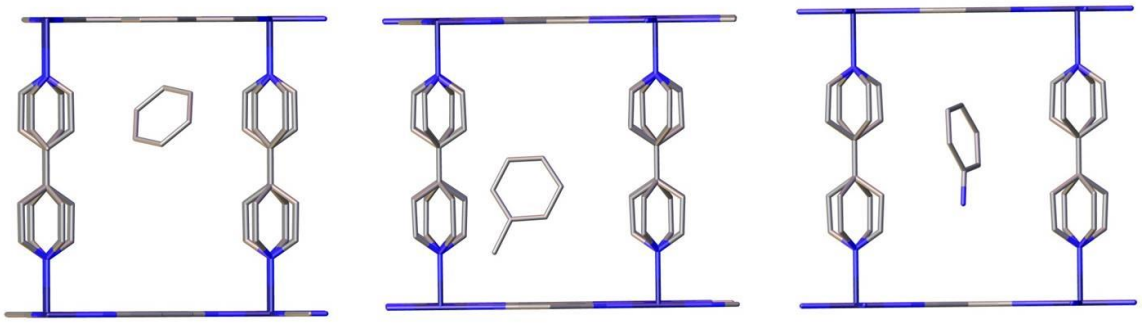

Figure 79. Fragments of the crystal structure of 1⊃guest (benzene (left), toluene (middle) and aniline (right)) showing the relative positions of the different guest molecules in the MOF. The pyridyl and benzene rings are disordered, and only one of the disordered guest molecules are shown for the sake of clarity.

In addition to the relative positions of the guest molecules in the framework, structural distortions were also observed with the inclusion of different guest molecules as reflected in the bond distances and angles listed in Table 1. The Fe-TCNQ 2-D sheets

of the benzene, toluene and aniline- containing MOFs are essentially planar with respect to the $TCNQ^{2-}$ bridges, whereas those of $1\supset CH_3OH$ and $1\supset C_6H_5NO_2$ are clearly corrugated with larger TCNQ dihedral angles. Presumably the observed structural distortions reflect both steric and electrostatic effects of the guest molecules and are expected to exert different effects on the magnetic coupling through the $TCNQ^{2-}$ bridges as well as the canting angles of the Fe(II) centers.

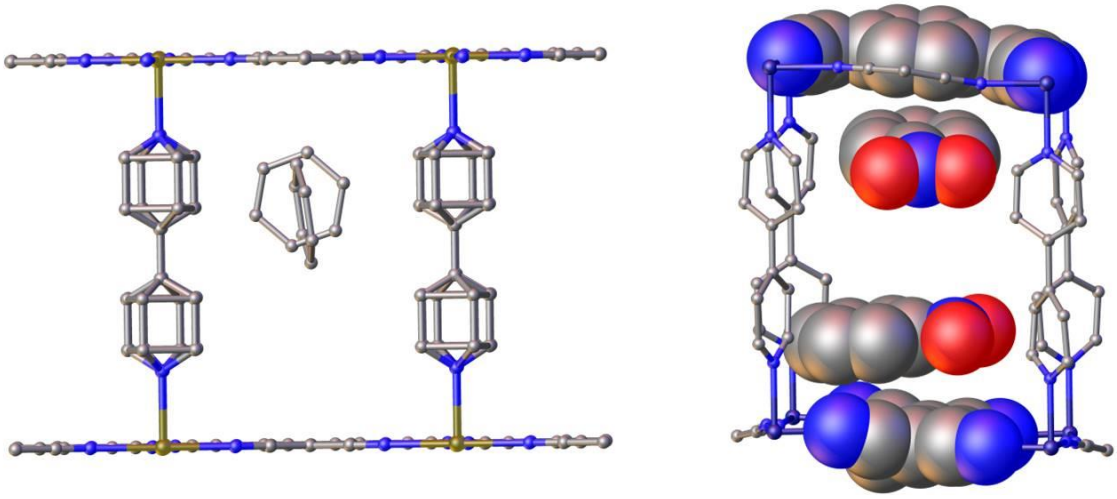

Figure 80. Left: Ball and stick model of the crystal structure of Mn(TCNQ)(4,4'-bpy)$\supset C_6H_6$ with the pyridyl and benzene rings disordered. Right: A fragment of the structure of Fe(TCNQ)(4,4'-bpy)$\supset C_6H_5NO_2$ with the TCNQ and nitrobenzene species highlighted in a space-filling model.

In order to further investigate the effects of structural distortions as well as the single-ion magnetic anisotropy of the metal center, two additional model compounds were prepared, *viz.*, Mn(TCNQ)(4,4'-bpy) (**2**)[54] with the isotropic Mn^{II} ions and the new 2D compound $Fe(TCNQ)(DMF)_2$•2DMF (**3**•2DMF) with planar Fe-TCNQ networks. In this case, DMF molecules occupy the axial positions of the Fe(II) coordination sites due to the absence of the pillaring ligand 4,4'-bipyridine. As in the case of the Fe^{II}

analogues, crystallographic studies of **2**⊃CH_3OH revealed corrugated 2-D Mn-TCNQ networks whereas a new structure for **2**⊃C_6H_6 was found to contain planar Mn-TCNQ networks with disordered benzene molecules situated vertical to the Mn-TCNQ planes (Figure 3,right). These results further support the electrostatic nature of the interactions. Single crystal X-ray studies of compound **3**•2DMF revealed a 2D structure with flat Fe-TCNQ sheets (the $TCNQ^{2-}$ units are parallel to each other as shown in Figure 1b, Fe-N(cyano) bond lengths are 2.124(5) and 2.113(6) Å), with two DMF molecules occupying the axial positions (Figure 4).

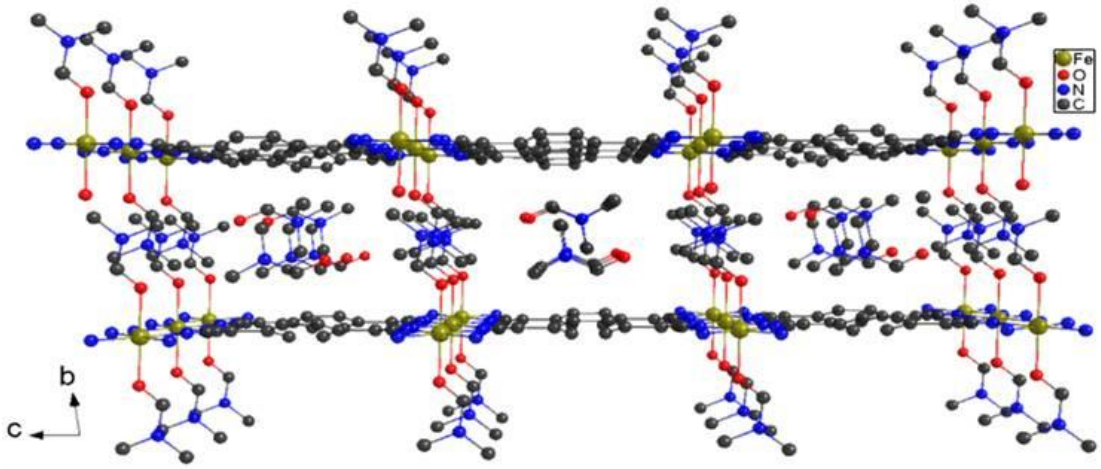

Figure 81. Packing diagram of 3 showing the flat planes of Fe^{II}-$TCNQ^{2-}$.

Single crystal X-ray crystallography

Single-crystal X-ray data were collected at 110 or 100 K on a Bruker APEX CCD diffractometer equipped with a graphite monochormated MoKα radiation source (λ=0.71073 Å) or a Synchrotron source (λ=0.41328 Å), respectively. Suitable crystals were affixed to a nylon loop with Paratone oil and place in a cold steam of N_2(g). The data sets were recorded by the ω-scan method and integrated followed by an absorption correction in the Bruker APEX II software package. Solution and refinement of the crystal structures were carried out using the SHELXT[139] and SHELXL[140] programs and the graphical interface Olex2.[141] Hydrogen atoms were placed at calculated positions. A summary of pertinent information relating to unit cell parameters are provided in Tables S1. CCDC 1414461-1414463, 1414477 contain the supplementary crystallographic data for this paper. These data can be obtained free of charge from the Cambridge Crystallographic Data Centre via www.ccdc.cam.ac.uk/data_request/cif.

Table 28. Pertinent crystallographic data for **1**⊃solvent and **3**.

Compound	**1**⊃C_6H_6	**1**⊃$C_6H_5NH_2$	**1**⊃$C_6H_5CH_3$	**3**
Empirical formula	$C_{42}FeN_6H_{32}$	$C_{34}H_{26}FeN_8$	$C_{36}H_{28}FeN_6$	$C_{24}H_{32}FeN_8O_4$
Formula weight	676.58	602.48	600.49	552.42
Temperature/K	100	110	100	110.15
Crystal system	tetragonal	tetragonal	tetragonal	triclinic
Space group	I4/mcm	I4/mcm	I4/mcm	P-1
a/Å	12.3580(6)	12.340(2)	12.3673(3)	7.3351(15)
b/Å	12.3580(6)	12.340(2)	12.3673(3)	8.8483(18)
c/Å	22.9288(15)	22.852(4)	22.9031(6)	11.466(2)
α/°	90	90	90	82.20(3)
β/°	90	90	90	89.30(3)
γ/°	90	90	90	68.41(3)
Volume/$Å^3$	3501.7(4)	3480.0(13)	3503.03(19)	685.0(3)
Z	4	4	4	1
$\rho_{calc}g/cm^3$	1.283	1.150	1.139	1.3391
μ/mm^{-1}	0.470	0.466	0.090	0.594
F(000)	1408.0	1248.0	1248.0	290.5
Crystal size/mm^3	0.08 × 0.04 × 0.04	0.1 × 0.08 × 0.04	0.04 × 0.04 × 0.04	0.15 × 0.12 × 0.1
Radiation	synchrotron (λ = 0.41328)	MoKα (λ = 0.71073)	synchrotron(λ = 0.41328)	Mo Kα (λ = 0.71073)
2Θ range for data collection/ °	7.584 to 49.836	3.564 to 49.986	3.408 to 26.536	5 to 50.16

Table 28. Continued.

Compound	**1**⊃C_6H_6	**1**⊃$C_6H_5NH_2$	**1**⊃$C_6H_5CH_3$	**3**
Index ranges	-14 ≤ h ≤ 14, -14 ≤ k ≤ 14, -27 ≤ l ≤ 27	-14 ≤ h ≤ 14, -14 ≤ k ≤ 14, -27 ≤ l ≤ 27	-13 ≤ h ≤ 13, -13 ≤ k ≤ 13, -25 ≤ l ≤ 25	-8 ≤ h ≤ 8, -10 ≤ k ≤ 10, -13 ≤ l ≤ 13
Reflections collected	38815	15663	39663	6240
Independent reflections	835 [R_{int} = 0.0635, R_{sigma} = 0.0152]	838 [R_{int} = 0.0343, R_{sigma} = 0.0112]	689 [R_{int} = 0.0352, R_{sigma} = 0.0078]	2396 [R_{int} = 0.0546, R_{sigma} = 0.0745]
Data/restraints/parameters	835/0/60	838/59/60	689/101/66	2396/0/172
Goodness-of-fit on F^2	1.182	1.335	1.122	1.052
Final R indexes [I>=2σ (I)]	R_1 = 0.0598, wR_2 = 0.1639	R_1 = 0.0774, wR_2 = 0.2042	R_1 = 0.0592, wR_2 = 0.1632	R_1 = 0.0887, wR_2 = 0.2517
Final R indexes [all data]	R_1 = 0.0638, wR_2 = 0.1781	R_1 = 0.0884, wR_2 = 0.2294	R_1 = 0.0609, wR_2 = 0.1676	R_1 = 0.1059, wR_2 = 0.2680
Largest diff. peak/hole / e $Å^{-3}$	0.65/-0.47	1.29/-0.52	0.56/-0.38	2.05/-1.50

$R_1 = \Sigma||F_o| - |F_c||/ \Sigma|F_o|$. $wR_2 = [\Sigma w(|F_o| - |F_c|)^2/|\Sigma w(F_o)^2]^{1/2}$. $w = 0.75/(\sigma^2(F_o)+0.00010F_o^2)$.

The structure of **1**⊃$C_6H_5NO_2$ was determined with a similar unit cell (tetragonal, a = 17.375, c = 22.963) to the reported one at room temperature,[88] but was best refined in a different tetragonal space group namely $P42_12$. However, it should be noted that this space group is still somewhat ambiguous and the structure could only be refined isotropically due to twinning and disorder. Several data sets were collected on single crystals of **1**⊃$C_6H_5NO_2$ from different batches of reactions but the same problem persisted. It is interesting to note from the electron density difference maps that, unlike the cases of benzene, toluene and aniline containing frameworks of **1** and **2**⊃C_6H_6 where the plane of the aromatic molecules are situated vertical to the M-TCNQ plane (Figure 3, left), the nitrobenzene molecule exhibits a face-to-face contact with the TCNQ moiety of the Fe-TCNQ network (Figure 3). Such a positioning indicates the presence of π-π stacking/electrostatic interactions between the $TCNQ^{2-}$ anions and the polar nitrobenzene molecules. The perpendicular orientation of the nitrobenzene dipole moment to the $TCNQ^{2-}$ molecule suggests an electrostatic interaction.

Powder X-ray diffraction

Room temperature powder X-ray diffraction methods were employed to monitor the structures of bulk samples containing different aromatic solvent molecules. The match of the patterns indicates that the frameworks of the structures are preserved in all cases (Figure 5). Several new peaks arising from the inclusion of different solvent molecules may be attributed to the ordered arrangement of the corresponding solvent molecules and the small distortions of the host frameworks resulting from the included guest molecules.

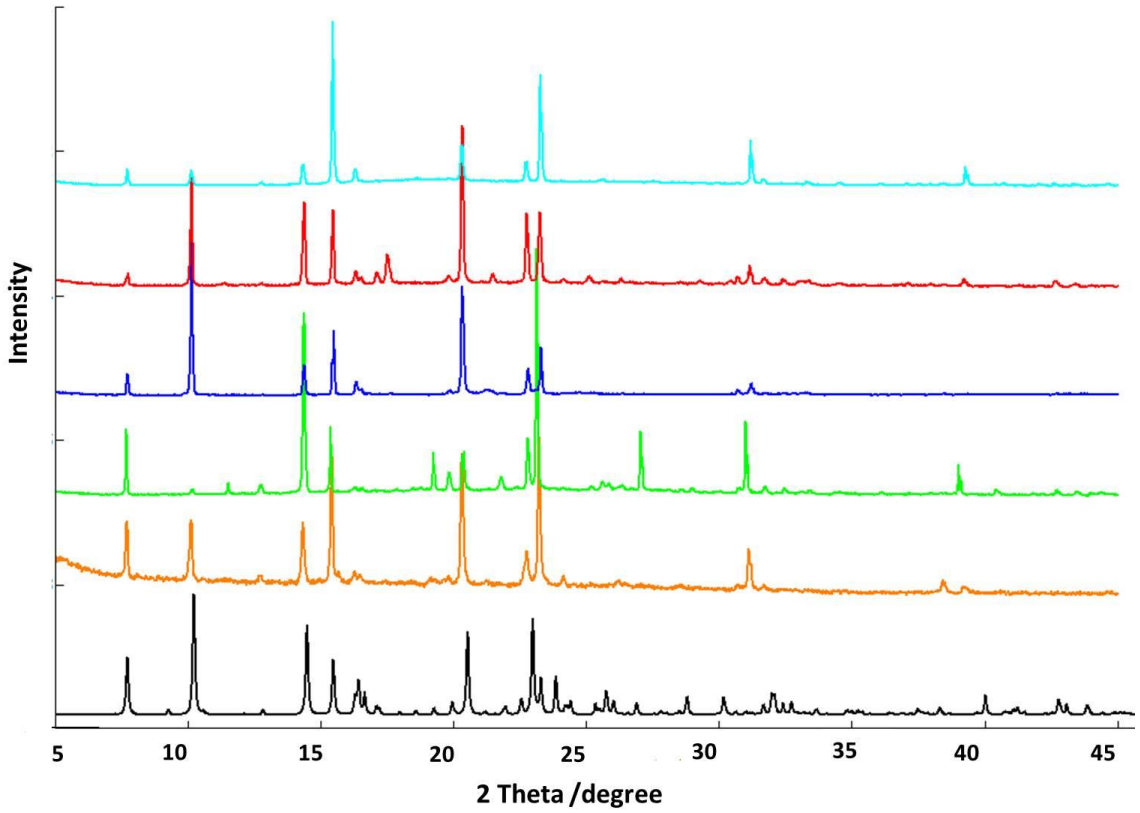

Figure 82. Powder X-ray diffraction patterns of Fe(TCNQ)(4,4'-bpy) with the inclusion of different solvent molecules: methanol (black, simulated), methanol (orange, experimental), benzene (blue), toluene (red), nitrobenzene (green) and aniline (turquoise).

Infrared spectroscopy

Infrared spectral data, summarized in Table 2, indicate the presence of ν(C≡N) stretching modes characteristic of $TCNQ^{2-}$.[68] The lower energies of these bands as compared to previously reported compounds indicate a slightly higher negative charge on the $TCNQ^{2-}$ units, consistent with charge-transfer from aromatic guest molecules to the $TCNQ^{2-}$ units.

Table 29. IR stretching frequencies of the –CN groups in different $TCNQ^{2-}$ species.

Compound	ν(CN)/cm^{-1}
H_2TCNQ	2257, 2204
1⊃CH_3OH	2181, 2112
1⊃C_6H_6	2185, 2059
1⊃$C_6H_5NO_2$	2183, 2114
1⊃C_7H_8	2183, 2116, 2055
1⊃$C_6H_5NH_2$	2182, 2116
3	2197, 2134

Magnetic properties

The tendency of the compounds in this study to lose interstitial solvents renders it difficult to accurately characterize them in the dry state. Owing to this situation, samples for magnetic measurements were conducted on crushed crystals covered in a minimum volume of the solvent in sealed quartz tubes to avoid interstitial solvent loss. The magnetic measurements of these compounds were carried out using a SQUID MPMS instrument over the temperature range 1.8-300 K. Diamagnetic contributions of the intercalated and excess solvent were accounted for during the subsequent data analysis process.

The temperature dependence of χT data are shown in figure 6. The room temperature χT values (**1**⊃CH_3OH, 3.32 emu K mol^{-1}; **1**⊃C_6H_6, 3.41 emu K mol^{-1}; **1**⊃C_7H_8, 3.33 emu K mol^{-1}; **1**⊃$C_6H_5NO_2$, 3.48 emu K mol^{-1}; **1**⊃$C_6H_5NH_2$, 3.41 emu K mol^{-1}) correspond to the expected value for an isolated high spin iron(II) center (S=2, g

= 2.12). Upon lowering the temperature, the χT values decrease monotonically down to ~ 5 K (Figure 6) indicative of antiferromagnetic interactions. The small fluctuations in the χT values above 50 K are attributed to freezing of the solvents. The temperature dependence of the magnetic susceptibilities between 300-5K were fit to a Curie-Weiss law with Weiss constant values of θ = -9.4 K for **1**⊃CH_3OH, -11.1 K for **1**⊃$C_6H_5NO_2$ and -11.2 K for all three of **1**⊃C_6H_6, **1**⊃C_7H_8 and **1**⊃$C_6H_5NH_2$ (Table 1), data that support the presence of antiferromagnetic interactions within the MOF framework (Table 3), in addition to other possible contributing factors such as spin-orbit coupling at high temperatures and zero-field splitting at low temperatures.

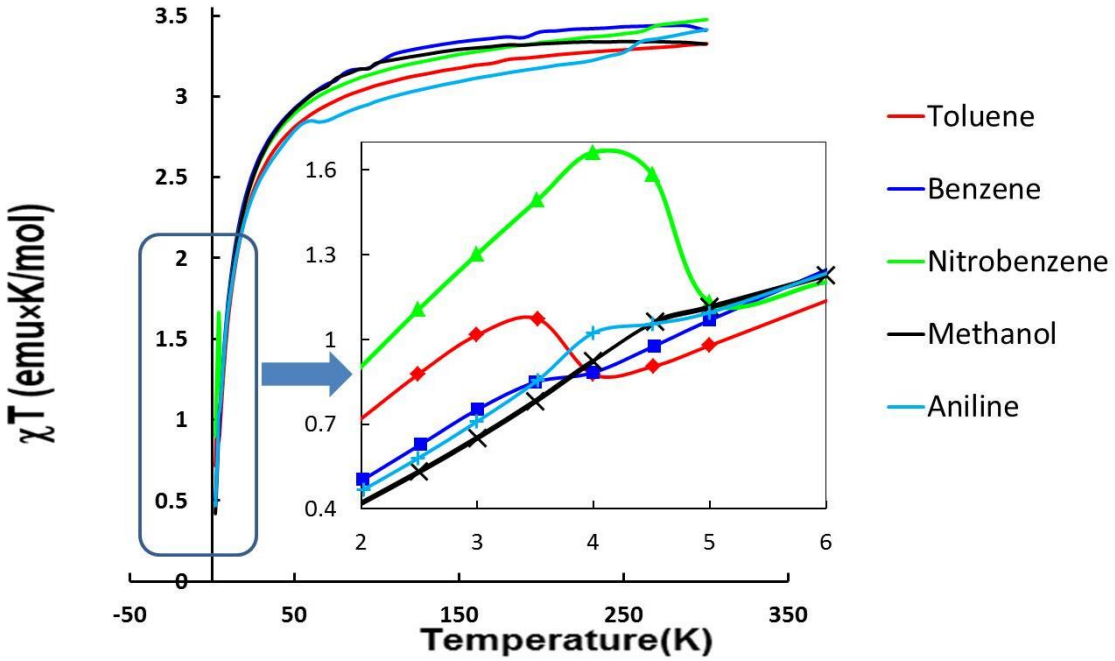

Figure 83. Temperature dependence of the χT plot of the MOF Fe(TCNQ)(4,4'-bpy) in different solvents.

For estimation of the magnetic exchange parameter the mean field approximation formula[199] can be used:

$J = 3\theta kB/(2zS(S+1))$. Eq. 1

where z is the number of neighbor ions. Keeping in mind a layered motif of the compounds in our case $z = 4$. The obtained values are in the Table 30.

Given the crystal structure, the magnetic susceptibility data can be alternatively interpreted using eq. 2, describing the χT of a 2D Heisenberg quadratic-layer antiferromagnet. This formula, based on the isotropic Heisenberg Hamiltonian $H = -2J\Sigma_{ij}S_iS_j$ is as follows:[200]

$$Ng^2\beta^2/\,2\chi T = 3x + \sum C_n/x^{n-1}$$ Eq. 2

where $x = kT/JS(S+1)$, N is Avogadro's number, β – Bohr magneton and k – Boltzmann constant and C_n are tabulated constants. The results of fitting the data to Eq. 2 (Figure 84-Figure 88) are summarized in Table 3.

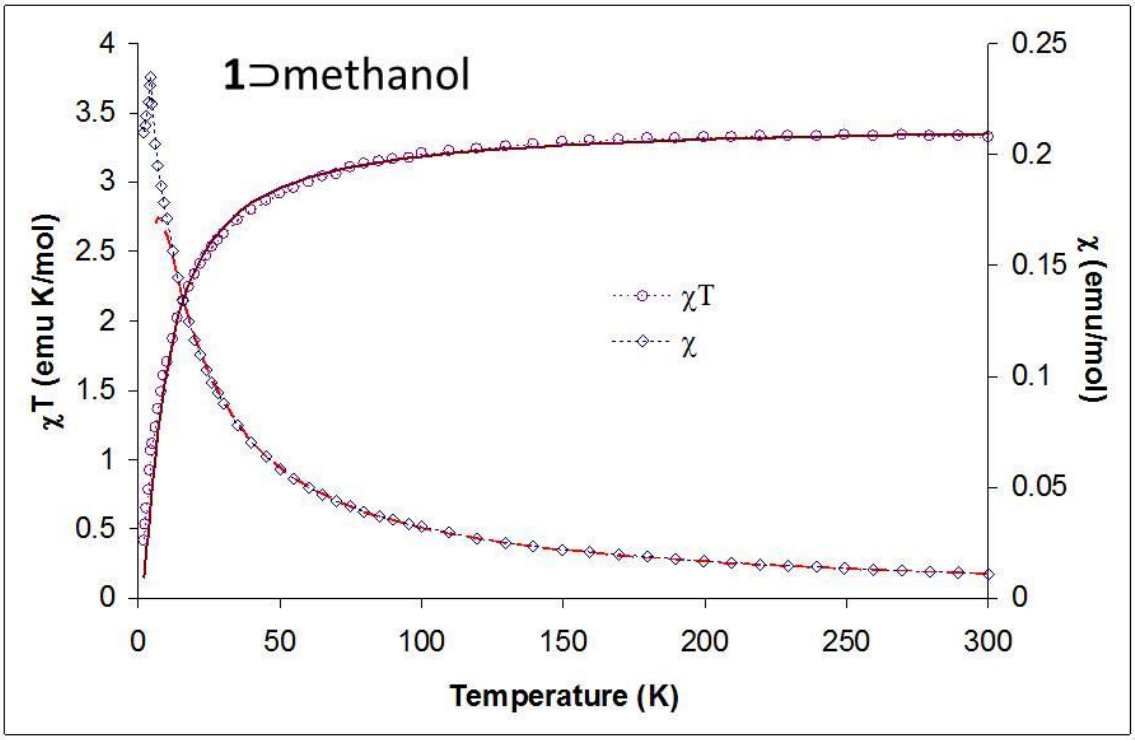

Figure 84. The fitting of temperature dependent molar magnetic susceptibility of $1\supset CH_3OH$ to Eq. 2. The symbols are the experimental data and the dotted lines are the fitted data.

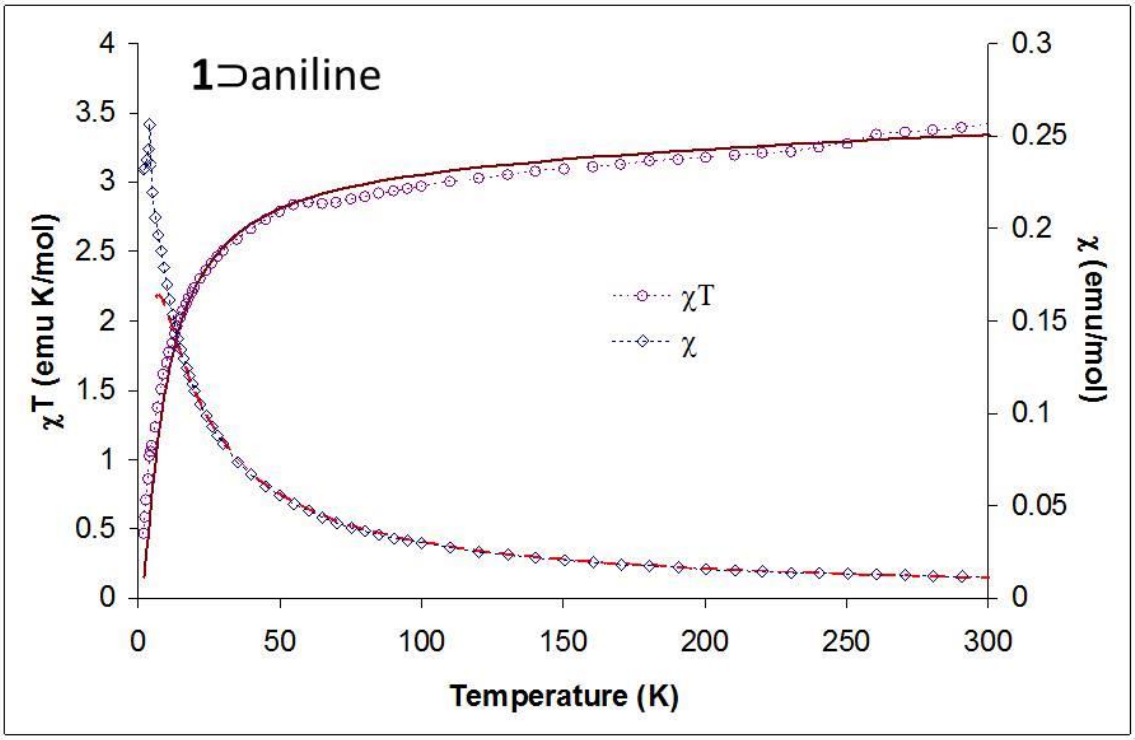

Figure 85. The fitting of temperature dependent molar magnetic susceptibility of $1 \supset C_6H_5NH_2$ to Eq. 2. The symbols are the experimental data and the dotted lines are the fitted data.

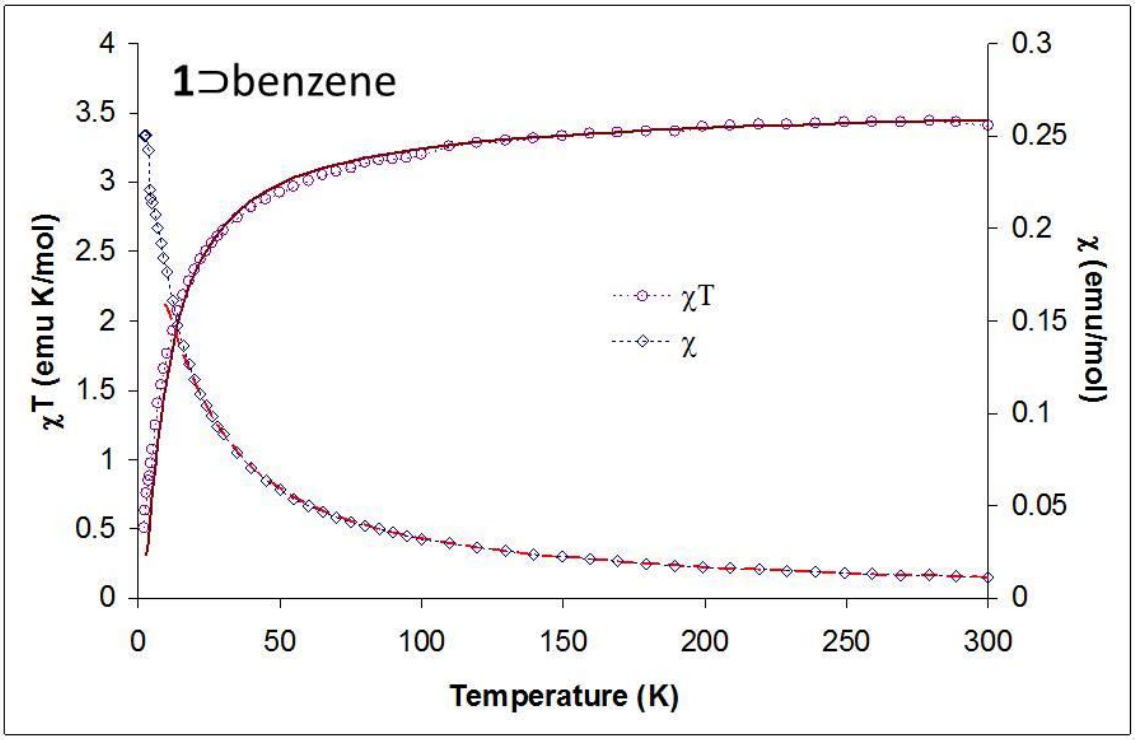

Figure 86. The fitting of temperature dependent molar magnetic susceptibility of $1\supset C_6H_6$ to Eq. 2. The symbols are the experimental data and the dotted lines are the fitted data.

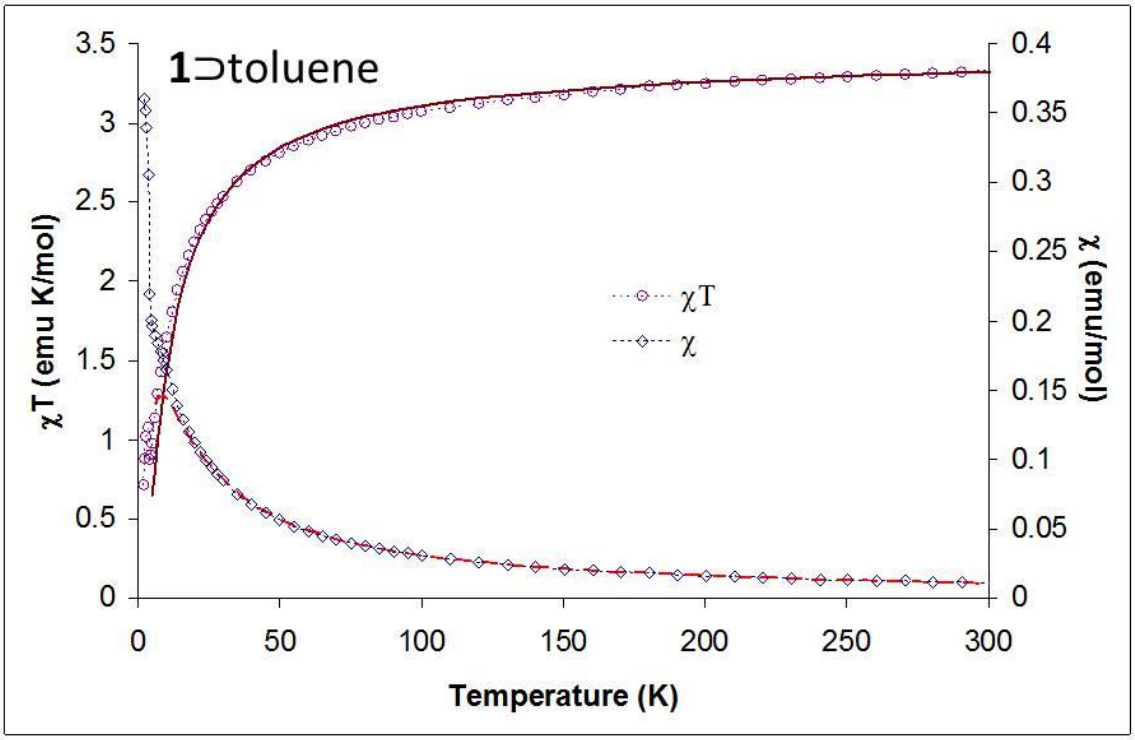

Figure 87. The fitting of temperature dependent molar magnetic susceptibility of $1\supset C_6H_5CH_3$ to Eq. 2. The symbols are the experimental data and the dotted lines are the fitted data.

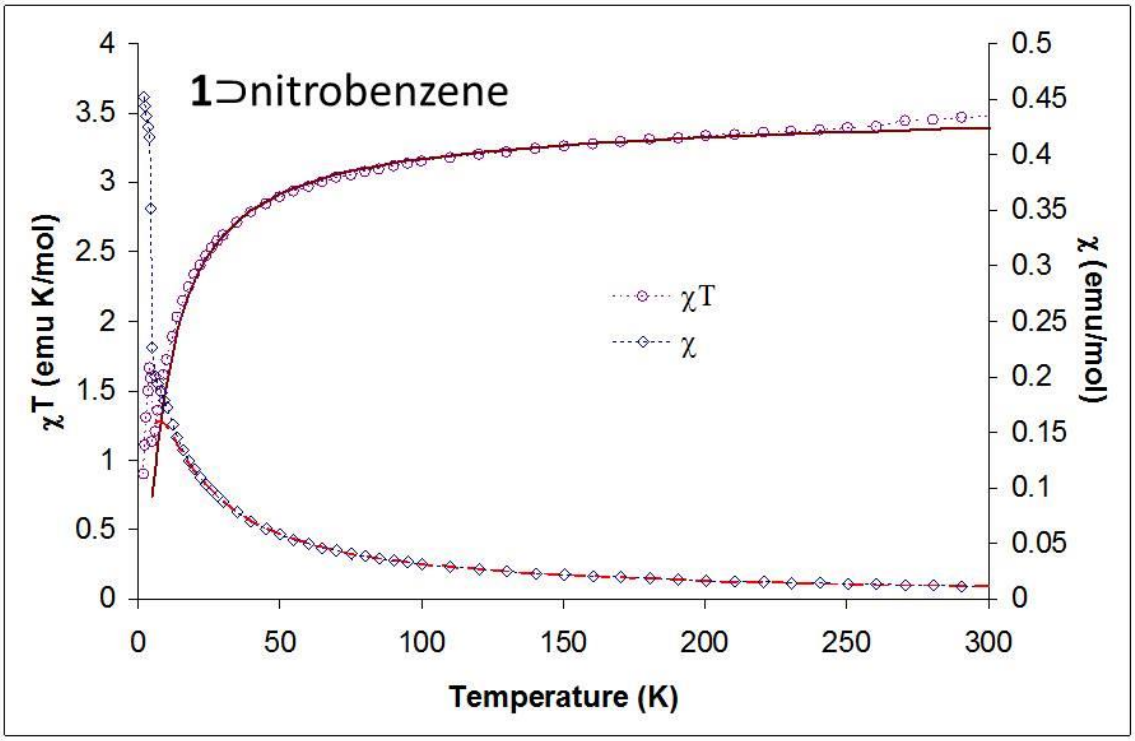

Figure 88. The fitting of temperature dependent molar magnetic susceptibility of $1\supset C_6H_5NO_2$ to Eq. 2. The symbols are the experimental data and the dotted lines are the fitted data.

Table 30. Summary of the magnetic parameters in 1⊃guest.

Guest	T_c /K	θ /K	J/cm^{-1} (estimated)	J/cm^{-1} (calculated)	Canting angle /degree
Methanol	4.5(2)	-9.4	-0.41	-0.32	0.02
Aniline	4.9(5)	-11.2	-0.49	-0.32	0.19
Benzene	3.9(2)	-11.2	-0.49	-0.35	0.42
Toluene	3.7(2)	-11.2	-0.49	-0.37	0.49
Nitrobenzene	4.7(2)	-11.1	-0.48	-0.34	0.84

Similar behavior was observed in our recently reported $[Ph_3PMe]_2[Fe_2(TCNQ)_3]$ magnetic MOF,[68] but it is worth noting that the estimated coupling constants using the same equation for the current series is more than double of that in the former case. This finding is presumably due to the higher degree of planarity of the bridging TCNQ units which allows for better dπ-pπ overlap between the metal centers and TCNQ dianions. In the case of $[Ph_3PMe]_2[Fe_2(TCNQ)_3]$, the planarity of the $TCNQ^{2-}$ moiety has been significantly disrupted (the dicyanomethyl and the phenyl fragments of $TCNQ^{2-}$ have an average dihedral angle of 28.05 °), whereas in compound **1,** the $TCNQ^{2-}$ moiety remains planar with only a little distortion in the case of methanol and nitrobenzene (see dihedral angles in Table 31). Therefore, two additional magnetic superexchange coupling pathways (through trans-7,8- and cis-7,8-cyano groups) may be contributing to the dominate antiferromagnetic interactions in the temperature range of 300-5 K in addition to the 7,7-cyano coupling pathway through the short end of $TCNQ^{2-}$ as found in the case of $[Ph_3PMe]_2[Fe_2(TCNQ)_3]$. The presence of additional coupling pathways helps to explain the increased coupling in the current series. Given the structural similarity of the dicyanomethyl fragment of the $TCNQ^{2-}$ bridge and dicyanamide anion, it is noted that they exhibit comparable magnetic coupling strength between Fe(II) centers.[201,202]

Table 31. Summary of the structural parameters of 1⊃guest from single crystal X-ray studies.

Guest	Space group	Fe-N(cyano) /Å	Fe-N(pyridyl) /Å	Fe-N-C(cyano) / °	TCNQ dihedral angle / °
Methanol	P-42_1c	2.144(2)	2.184(2)	160.01	3.84
Benzene	I4/mcm	2.138(3)	2.187(5)	165.83	0
Aniline	I4/mcm	2.127(4)	2.196(7)	164.62	0
Toluene	I4/mcm	2.139(3)	2.196(4)	165.07	0
Nitrobenzene	P42_12	2.125	2.180	161.31	9.92

Below 5 K, maxima in χT begin to appear for all samples indicating the onset of weak ferromagnetic interactions. Taking into account that the magnetic interactions of the metal ions through 4,4'-bpy are usually weakly antiferromagnetic,[74,203-205] the magnetic behavior is essentially 2-D between the Fe^{II} centers in the frameworks bridged by μ_4-$TCNQ^{2-}$ linkers; the increase in χT at low temperatures can be ascribed to canted spin states from the interlayer interactions. Structural distortions in the 2-D sheets of Fe(TCNQ) and/or electronic interactions between $TCNQ^{2-}$ and the aromatic solvent molecules are the plausible reasons for the uncompensated magnetic moments and therefore "weak ferromagnetic" (canted antiferromagnetic) responses at 3-5 K.

Zero-field-cooled (ZFC) and field-cooled (FC) magnetization data at 10 Oe exhibit bifurcations in all cases (Figure S1), implying that long-range ordering of the magnetic moments is occurring. This conclusion is also supported by the appearance of

frequency independent peaks in both the in-phase and out-of-phase AC magnetic susceptibilities at low temperatures which suggests a magnetic transition is occurring from a paramagnetic state with antiferromagnetic interactions to a canted antiferromagnetic state (Figure 7). In addition, field dependent magnetization hysteresis loops were observed for all samples at 1.8 K (Figure 91), which signifies the presence of spontaneous magnetization below their corresponding T_c values.

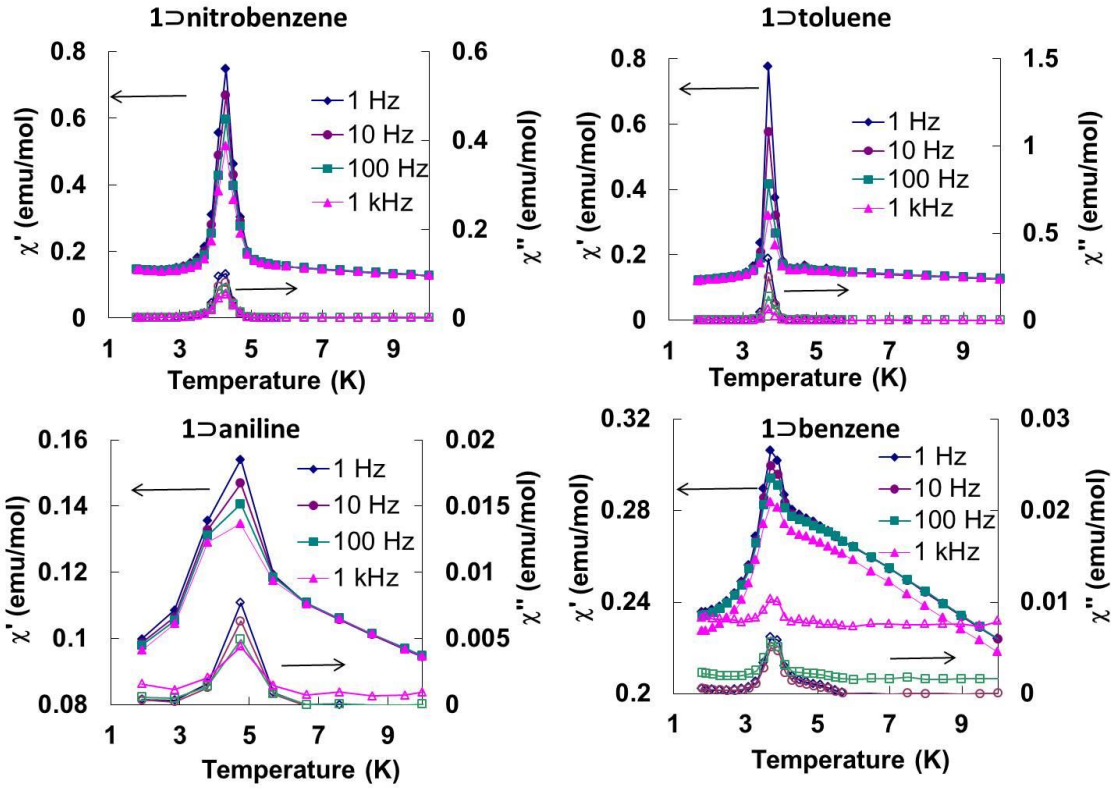

Figure 89. Variable temperature in-phase and out-of-phase AC magnetic susceptibility data for the Fe(TCNQ)(4,4'-bpy) MOFs in four aromatic solvents at different AC frequencies.

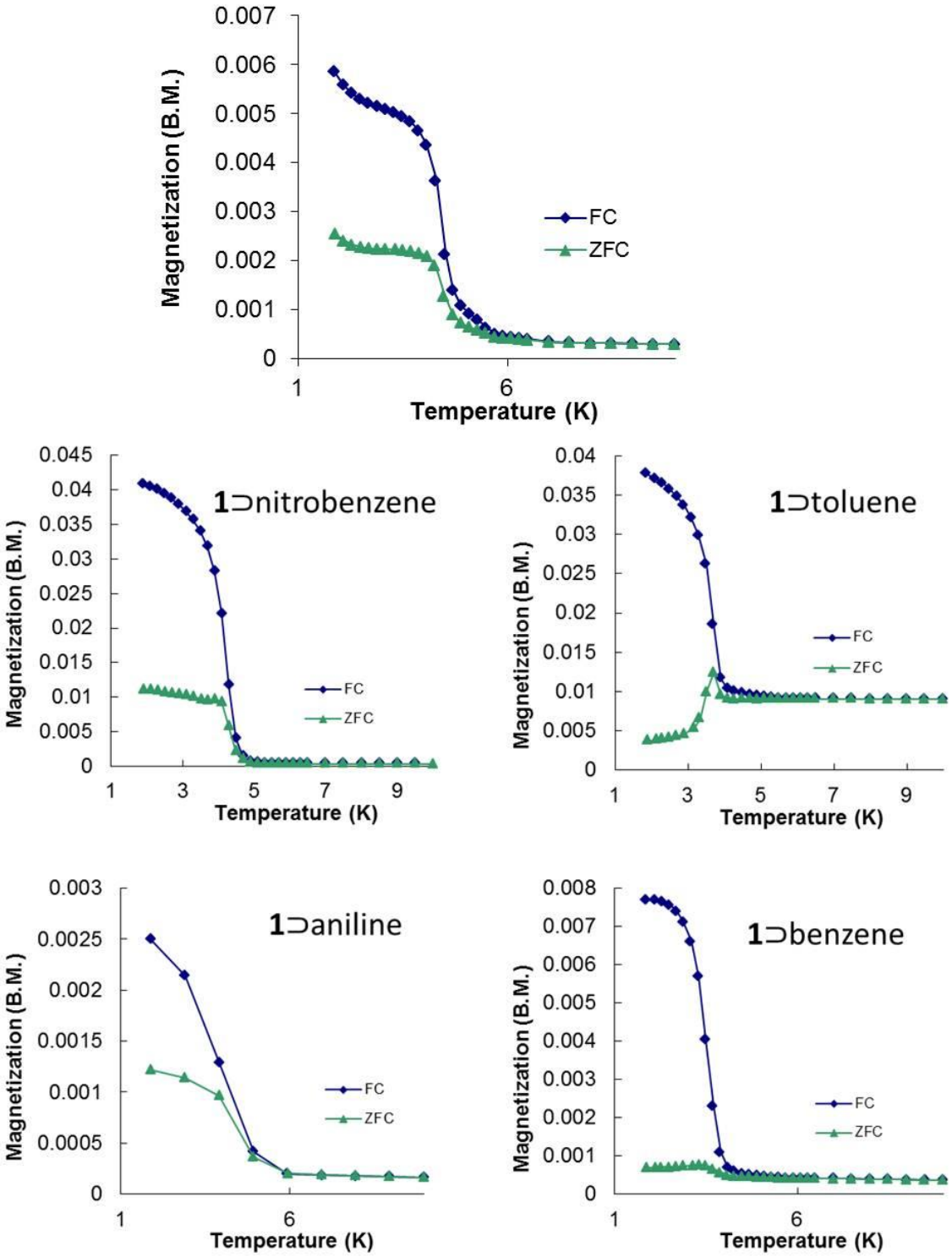

Figure 90. ZFC and FC of the "as-synthesized" Fe(TCNQ)(4,4'-bpy) ⊃guest.

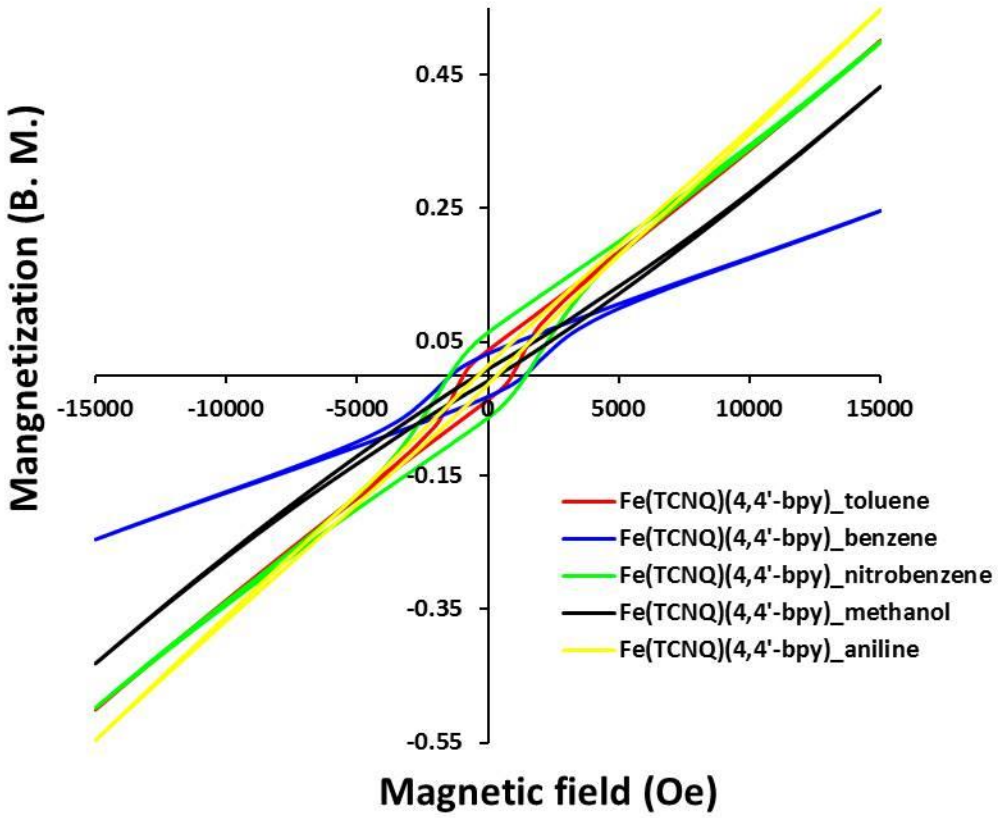

Figure 91. Hysteresis of the Fe(TCNQ)(4,4'-bpy) MOFs at 1.8 K in different aromatic solvents.

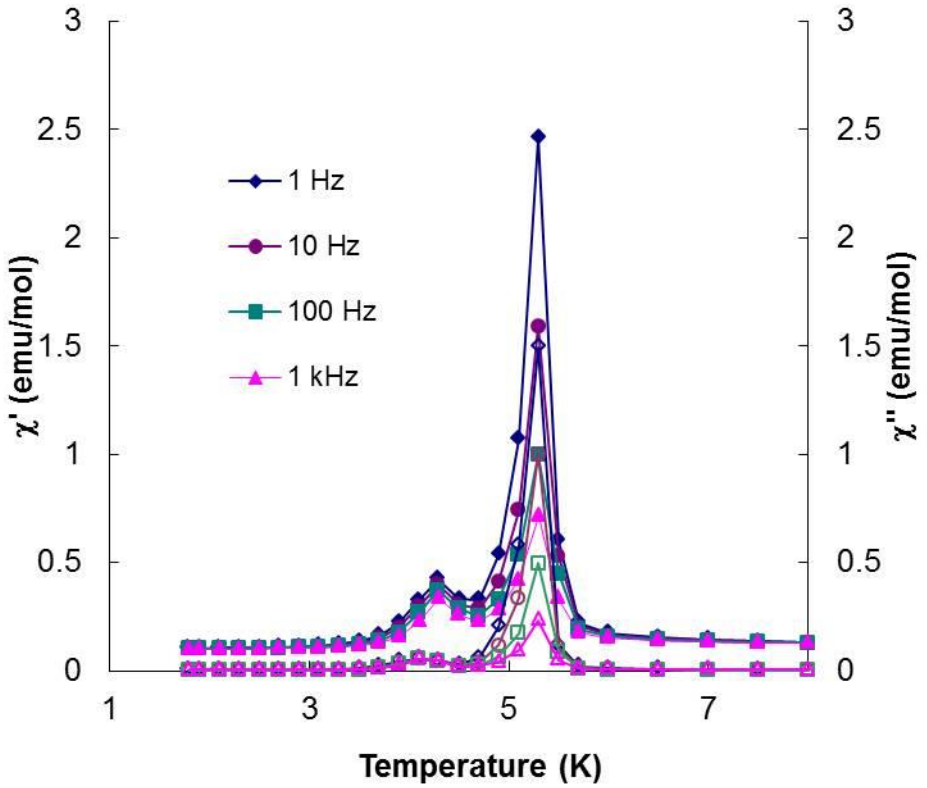

Figure 92. Temperature dependence of the AC magnetic susceptibility of Fe(TCNQ)(4,4'-bpy) after being dried under vacuum.

The field dependent magnetization curves at 1.8 K (Figure S4) did not reach saturation even under a field of 7 T which is another piece of evidence for uncompensated moments from the spin-canted states. The canting angles (Table 1) were estimated from the equation $\psi = \tan^{-1}(M_r/M_s)$, where $M_s = gS$ is the saturation magnetization when all the moments are aligned in a parallel manner in the structure and M_r is the remnant magnetization (intercept of the linear part of magnetization curve).[206] The largest canting angles of the **1**⊃nitrobenzene and

1⊃toluene are consistent with the most prominent weak ferromagnetic responses at low temperatures.

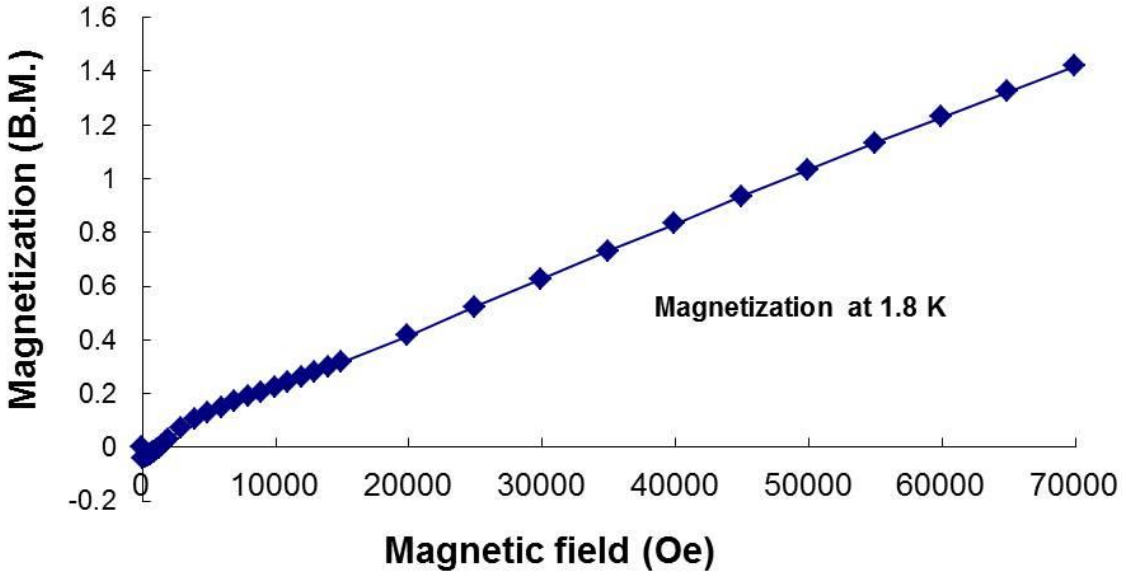

Figure 93. The magnetization of the Fe(TCNQ)(4,4'-bpy)⊃$C_5H_5NO_2$ at 1.8 K This is shown as an example; other samples of Fe(TCNQ)(4,4'-bpy)⊃guest showed similar behavior.

The trend of ordering temperatures in the present series is affected by the structural distortions of the Fe(TCNQ) planes which are the main source of spin canting. The effect of structural distortions is evident in **1**⊃CH_3OH and **1**⊃$C_6H_5NO_2$ which exhibit corrugated Fe(TCNQ) sheets unlike the planar sheets in the structures containing benzene, toluene and aniline. It is worth noting that the three polar solvents, CH_3OH, $C_6H_5NO_2$ and $C_6H_5NH_2$ induce higher T_c values (4.5, 4.7 and 4.9 K respectively) as compared to the less polar benzene and toluene guest molecules (T_c = 3.9 and 3.7 K, respectively). Such an observation suggests an effect of guest polarity (Table 32) on the ordering temperature which is consistent with the orientation of the guest molecules

observed in the crystal structures. Another possible factor is charge-transfer between the host frameworks and the guest molecules which was previously reported.[88] Such interactions should affect the spin density on the $TCNQ^{2-}$ units hence the magnetic coupling through it, but the observed T_c values do not simply follow the order of π-accepting strength of the guest molecules. It is also possible that the electrostatic interaction between the framework and guest molecules results in changes of the electron density on the $TCNQ^{2-}$, and, in turn, affects magnetic coupling.

Table 32. A summary of pertinent polarity,[207] IR and magnetic data for **1**⊃guest.

Guest	**Snyder polarity index**	**ν(C≡N) /cm^{-1}**	T_c
Methanol	6.6	2181.1, 2111.7	4.5
Aniline	6.2	2182.2, 2115.8	4.9
Nitrobenzene	4.5	2182.6, 2113.7	4.7
Benzene	3.0	2185.0, 2059.1	3.9
Toluene	2.3	2183.0, 2116.3, 2055.3	3.7

The relationship between the distortion of the structures and the magnetic properties can be further modeled for the 2-D network compound **3** which exhibits flat rather than corrugated planes of Fe-TCNQ units (Figure 4). The hypothesis that structural distortion leads to the spin-canted states in the magnetically coupled 2-D network is further supported by this model compound. Temperature dependent magnetic measurements performed on **3** revealed that it is a paramagnet with antiferromagnetic interactions with no spin-canted states at low temperatures. However, the χT value of a dry sample (**3a**) exhibits an increase at low temperatures (Figure 8a), indicating the onset

of a spin-canted antiferromagnetic state, which is most likely due to the distortion of the flat plane to a corrugated plane upon the loss of DMF molecules. The lack of saturation of the magnetization for both samples indicates that the net magnetic moments stem from uncompensated canted spin states. The observation of a hysteresis loop and bifurcation in ZFC-FC curve (Figure 8b and Figure 95) for the dry sample **3a** also underscores the importance of structural distortion for the canted spin states in the present series.

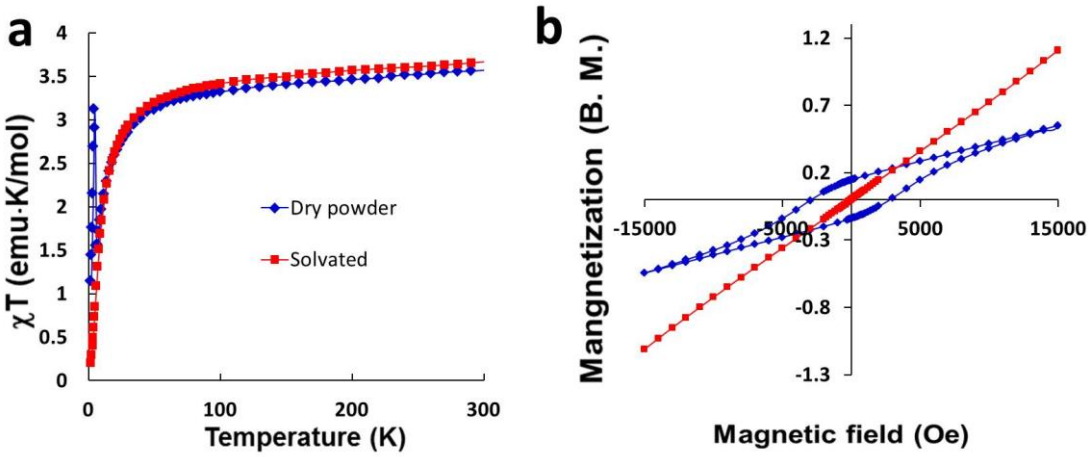

Figure 94. Temperature dependence of the χT product (left) and hysteresis of the magnetization (right) for $Fe(TCNQ)(DMF)_2$•2DMF.

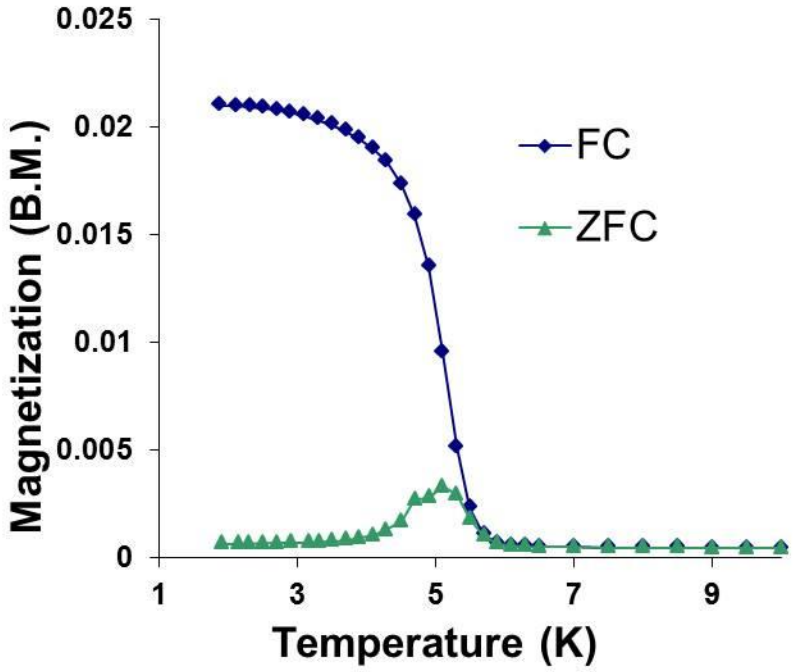

Figure 95. ZFC and FC magnetization data for **3.**

Single-ion magnetic anisotropy was also found to play a role in the canted states in the Fe(TCNQ)(bpy) MOFs. When the isotropic Mn^{II} analog was used, **2**⊃CH_3OH exhibits only antiferromagnetic ordering at low temperatures without the presence of the canted spin states although the 2-D networks of Mn-TCNQ are substantially corrugated (Figure 96).

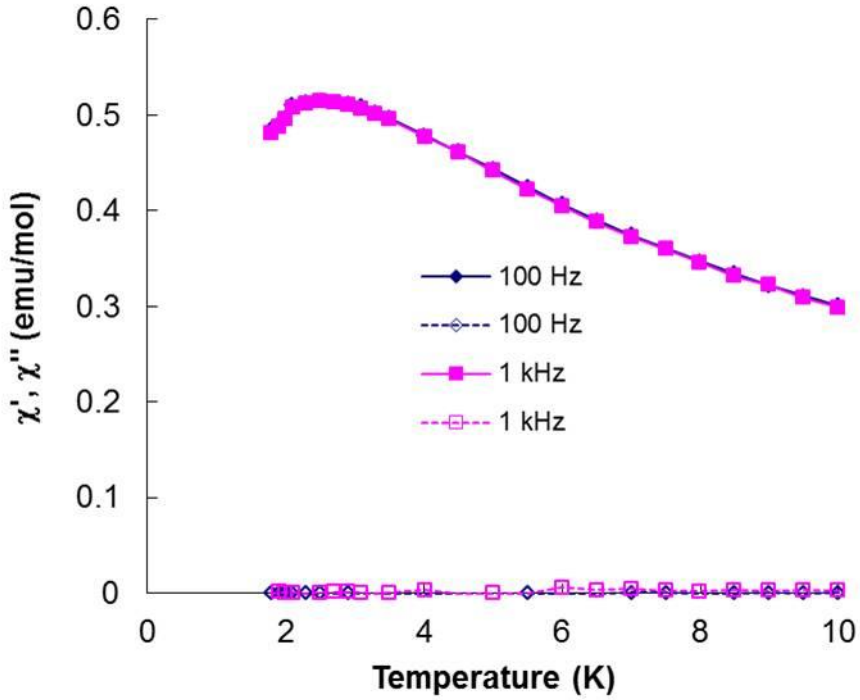

Figure 96. The in-phase (solid symbols) and out-of-phase (hollow symbols) AC susceptibilities of $2 \supset CH_3OH$.

Conclusions

The properties of TCNQ-based magnetic MOF materials were investigated by magnetic, structural and infrared studies. The magnetic behavior of Fe(TCNQ)(4,4'-bpy) MOFs can be modulated by altering the polarity and the size of the aromatic guest molecules. In addition, an investigation of the magnetic properties of this series of MOFs revealed that the TCNQ-dianion bridge is a promising candidate for incorporation into magnetic MOF materials. Structural evidence was obtained to support the conclusion that significant steric and electrostatic interactions between the polar nitrobenzene and the negatively charged $TCNQ^{2-}$ species occurs in the frameworks. The 2-D model compound $Fe(TCNQ)(DMF)_2 \bullet 2DMF$ was synthesized and magnetic studies suggest that

structural distortion is responsible for the transition to canted spin states. A comparison to the isostructural Mn(II) analogs of the MOFs indicate that single-ion magnetic anisotropy is crucial for the presence of canted spin states in the Fe-TCNQ-based MOFs. The magnetic phase transitions are due to the electrostatic and steric interactions between the guest molecules and the host frameworks. The opportunity to modulate magnetic properties by the interaction of TCNQ dianions in framework solids with aromatic small molecules of different polarity and steric hindrance make them promising for applications in molecule recognition and sensors.

CHAPTER V

METAL-ORGANIC MACROCYCLES WITH BRIDGING ORGANOCYANIDE DIANIONS: DINUCLEAR COMPLEXES AND POLYMERIC ARCHITECTURES INCLUDING AN UNPRECEDENTED QUADRUPLE HELICAL APERIODIC STRUCTURE*

Introduction

Molecule-based magnetic materials are of high interest due to their potential applications in data storage and quantum computing.[208,209] One of the most fundamental subjects in molecular magnetism is the superexchange interactions between spin carriers through atomic/molecular bridging ligands and, in this vein, efforts to achieve strong coupling through relatively long organic linkers is a subject of great importance for the synthesis of magnetic metal-organic frameworks (MOFs) and multifunctional molecular materials.[174,192,210]

The organocyanide acceptors TCNQ and DCNQI (Figure 1, TCNQ = 7,7,8,8-tetracyanoquinodimethane, DCNQI = dicyanoquinodiimine) have been widely studied as organic components in charge-transfer complexes that exhibit interesting magnetic and electrically conducting properties.[61,62,99,100,107,122,211] The dianionic forms of DCNQI are useful bridging ligands in charge-transfer and mixed-valence molecules as reported

---

* Part of this chapter is reprinted with permission from "Self-Assembly of Organocyanide Dianions and Metal-Organic Macrocycles into Polymeric Architectures Including an Unprecedented Quadruple Helical Aperiodic Structure", by Xuan Zhang, Hanhua Zhao, Lukas Palatinus, Kevin Gagnon, John Bacsa, Kim R. Dunbar, *Crystal Growth & Design*, **2016**, 16, 1805-1811, DOI: 10.1021/acs.cgd.6b00112, Copyright 2016 by American Chemical Society.

before by Crutchley and coworkers for the meta- and para-dicyanamidobenzene dianions and their derivatives.[212-214] Recently, Robson and Abrahams demonstrated that the doubly reduced forms are also convenient ligands for metal-organic frameworks.[215] As an example of the remarkable properties imparted by these reduced organocyanide molecules, we noted that strong antiferromagnetic coupling of $J \geq -400$ cm^{-1} ($H = -2JS_1S_2$) between trivalent ruthenium ions in dinuclear complexes through the para-dicyanamidobenzene dianion ($DCNQI^{2-}$) and a J value of ~ -100 cm^{-1} for the mixed valence analogues have been observed.[216] In the context of this research, we became intrigued by chemistry of the *meta*-dicyanamidobenzene dianion ($DCNB^{2-}$) which was predicted by Ruiz and coworkers to facilitate ferromagnetic interactions between specific paramagnetic metal ions.[191]

In addition, organocyanide dianions have been widely used as linkers in the synthesis of metal-organic frameworks that show interesting properties of host-guest charge-transfer interactions.[55,67,88,183,215,217,218] Miyasaka and coworkers have also reported interesting magnetic superexchange interactions between paddlewheel diruthenium complexes through $TCNQ^{2-}$ dianions. Our group has been interested in the superexchange interactions through TCNQ dianions in MOFs for their potential to produce magnetic MOFs for small molecule sensing applications.[68,196]

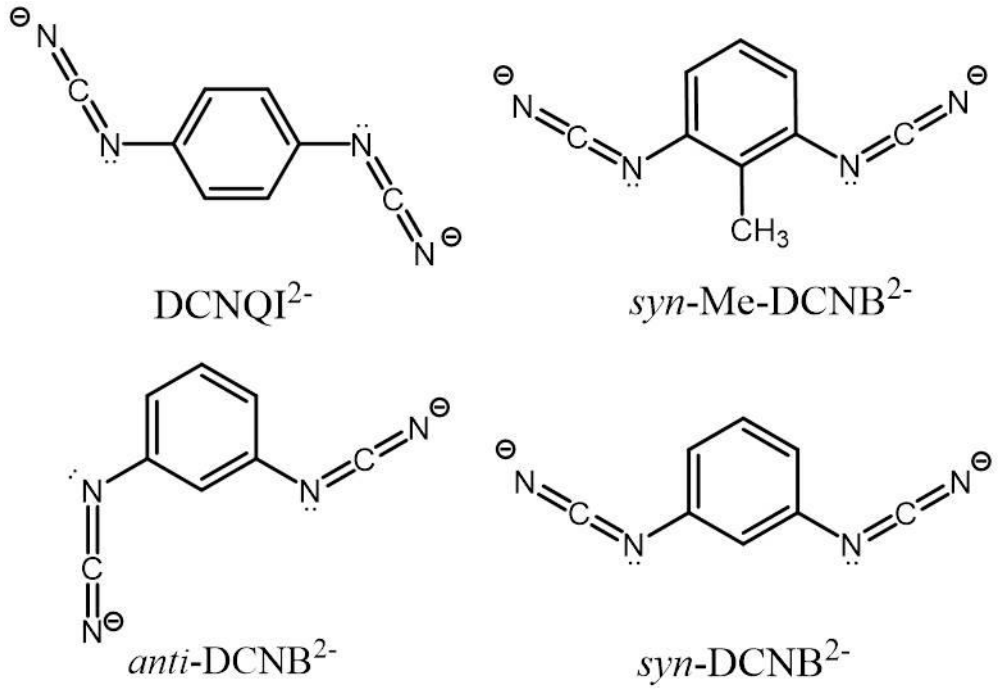

Figure 97. Molecular structures of the organocyanide dianions $DCNQI^{2-}$, *syn*-Me-$DCNB^{2-}$ and the *syn*- and *anti*- conformers of $DCNB^{2-}$.

Dinuclear models are the simplest ones for the study of superexchange interactions. In our pursuit of organocyanide dianions as bridging ligands in the formation of magnetic MOFs, we targeted model complexes to study the magnetic superexchange intereactions through organocyanide dianions in order to learn whether they would be suitable candidates for the synthesis of magnetic MOFs. It has been predicted from computational studies of organocyanide dianions that Kahn-Sham orbital symmetry matching of the ortho- and para-dicyanamidobenzene dianions can mediate strong ferro- and antiferro- magnetic coupling between paramagnetic trivalent metal centers, respectively, despite the diamagnetic nature of these dianions.

In addition to the stronger covalent and coordination bonds in common organic and inorganic compounds, supramolecular interactions play a central role in the self-

assembly of functional molecular materials.[219] The elaboration of supramolecular architectures using building block approaches has been widely employed for the synthesis of electrical conducting and magnetic materials.[46,135,220,221] Interactions such as weak covalent bonding, hydrogen bonding, anion-π, cation-π and π-π interactions are all of interest in this chemistry due to the crucial roles that they play in dictating the structures and properties of the resulting materials.[222,223]

Macrocyclic metal-organic complexes such as $[M(dpop)(H_2O)_2]Cl_2 \cdot 4H_2O$ (M = Mn, Fe, Co, dpop=2,13-dimethyl-3,6,9,12,18-pentaazabicyclo-[12.3.1]octadeca-1(18),2,12,14,16-pentaene) (Figure 2) have been used as precursors for the formation of cyanide bridged molecular magnets with versatile architectures including polynuclear complexes, molecular wheels and one-dimensional coordination polymers.[224-229] The equatorial plane of these cationic building blocks consists of five neutral nitrogen donors from the dpop ligand with the axial positions being occupied by two water molecules that serve as potential labile coordination sites for bridging ligands that can lead to one-dimensional coordination polymers.

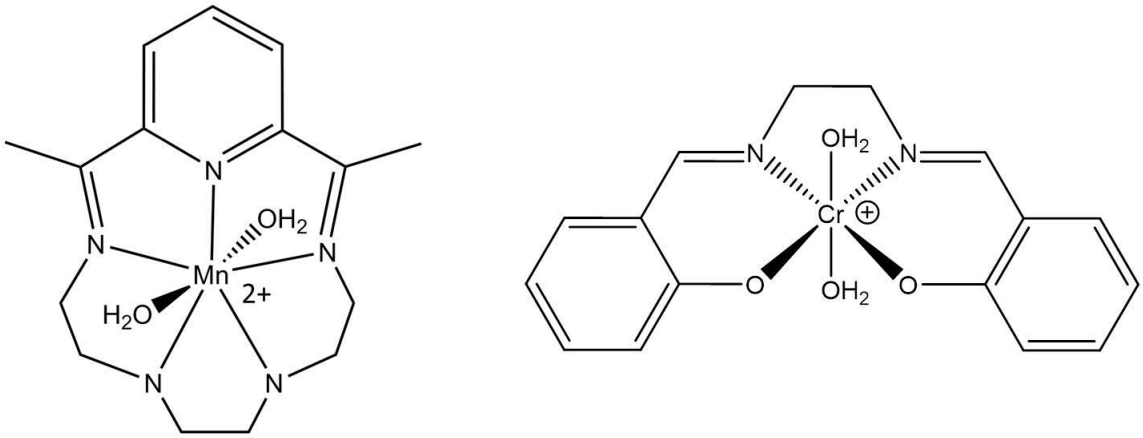

Figure 98. Molecular structure of the cationic metal-organic macrocycle building block $[Mn(dpop)(H_2O)_2]^{2+}$ and $[Cr(salen)(H_2O)_2]^{2+}$.

Herein, we report a series of para- and meta-dicyanamidobenzene dianion bridged Mn(III) complexes as model compounds to study their ability to mediate magnetic superexchange coupling between Mn(III) ions. The organocyanide dianions employed are para-dicyanamidobenzene ($DCNQI^{2-}$), 2,5-dimethyl-para-dicyanamidobenzene ($DM\text{-}DCNQI^{2-}$), meta-dicyanamidobenzene ($DCNB^{2-}$) and 2-methyl- meta-dicyanamidobenzene ($Me\text{-}DCNB^{2-}$). We investigated the electronic and steric effects of the methyl groups on the structures and magnetic properties of the resulting dinuclear complexes.

In another effort, self-assembly reactions of the metal-organic macrocyclic complex $[Mn(dpop)(H_2O)_2]Cl_2 \cdot 4H_2O$ with the organocyanide dianions $(TCNQ)^{2-}$, $(DCNQI)^{2-}$ and $(DCNB)^{2-}$ have been investigated. Four new coordination polymers and one mononuclear compound, $Mn(dpop)(\mu\text{-}anti\text{-}TCNQ) \cdot n$ Sol (**1**), $Mn(dpop)(\mu\text{-}DCNQI) \cdot n$Sol (**2**), $\{Mn(dpop)\}_5(\mu\text{-}syn\text{-}DCNB)_3(\mu\text{-}anti\text{-}DCNB)_2 \cdot n$Sol (**3**), $Mn(dpop)(\mu\text{-}anti\text{-}DCNB) \cdot (H_2O)(CH_3CN)$ (**4**) and $Mn(dpop)(\mu_1\text{-}DCNB)(H_2O)$ (**5**) have been

synthesized and structurally characterized. Compound **3** represents a rare coordination polymer composed of quadruple helices. It was found that the $(DCNB)^{2-}$ anion self-assembles with metal-organic building blocks to afford a variety of chain-like structures depending on the variable crystallization conditions. The differences in the structures of the reported compounds are discussed in the context of the conformations of the organocyanide ligands and the role of supramolecular interactions such as π-stacking and hydrogen bonding interactions.[230,231]

Experimental Section

Syntheses and crystallography

The reactions were carried out under a nitrogen atmosphere using standard Schlenk-line techniques unless otherwise stated. The starting materials were used as received without further purification. The starting materials $[Mn(salen)]ClO_4•2H_2O$ and $[Cr(salen)(H_2O)_2]Cl$ were prepared according to reported procedures.[232-234] CAUTION! Perchlorates are potentially explosive and should be handled with great care in small quantities. Avoid drying, heating and grinding.

$[Mn(dpop)(H_2O)_2]Cl_2·4H_2O$, H_2DCNQI, H_2DCNB, H_2(Me-DCNB), $[Ph_4As]_2$(DCNB) and $[Ph_4As]_2$(Me-DCNB) were prepared according to literature methods.[216,235] The precursor $[Ph_4As]_2$(DCNB) was prepared as reported in the literature by a metathesis reaction of H_2DCNB with tetraphenylarsonium chloride hydrate in a 2 M NaOH solution.[234]

Synthesis of Mn(dpop)(*μ*-TCNQ)$_n$ Sol (1). A solution of 55.3 mg (0.1 mmol) of $[Mn(dpop)(H_2O)_2]Cl_2•4H_2O$ in 5 mL of methanol was added to a solution of 20.7 mg

(0.1 mmol) of H_2TCNQ and 20.2 mg (0.4 mmol) of lithium acetate dihydrate in 15 mL of methanol. After standing undisturbed overnight, the orange solution was filtered and the filtrate was layered with diethyl ether. Orange crystals were harvested after three days (yield: 22.5 mg, 42%). IR: ν(CN) 2162 cm^{-1}, 2098 cm^{-1}.

Synthesis of Mn(dpop)(μ-DCNQI)$_2$·2CH$_3$OH·H$_2$O (2). A 110.5 mg (0.2 mmol) sample of [Mn(dpop)(H_2O)$_2$]Cl_2·4H_2O, 31.5 mg (0.2 mmol) of H_2DCNQI and 40.6 mg (0.4 mmol) of lithium acetate dihydrate were dissolved in 10 mL of methanol and stirred for 1 hour after which time a mixture of diethyl ether and hexanes (1:2.5) was layered on top of the solution. Brown crystals were harvested after four days (yield: 32 mg, 28%). IR: ν(CN) 2143 cm^{-1}.

Synthesis of {Mn(dpop)}$_5$(μ-*syn*-DCNB)$_3$(μ-*anti*-DCNB)$_2$·n Sol (3). A 50.8 mg (0.1 mmol) sample of [Mn(dpop)(H_2O)$_2$]Cl_2·4H_2O and 92.1 mg (0.1 mmol) of [Ph_4As]$_2$(DCNB) were dissolved in 5 mL of methanol and 20 mL of acetonitrile was added. Orange needles of the product formed over the course of 3 hours (yield: 36 mg, 71%). IR: ν(CN) 2091 cm^{-1}.

Synthesis of Mn(dpop)(μ-*anti*-DCNB)·H$_2$O·CH$_3$CN (4). A 50.8 mg (0.1 mmol) sample of [Mn(dpop)(H_2O)$_2$]Cl_2·4H_2O and 92.1 mg (0.1 mmol) of [Ph_4As]$_2$(DCNB) were dissolved in 5 mL of methanol and 15 mL acetonitrile. The solution was then layered on top of 5 mL of water. Orange platelet crystals of the product formed over the course of 3 days (yield: 4 mg, 7%). IR: ν(CN) 2191 cm^{-1}.

Synthesis of Mn(dpop)(μ_1-DCNB)(H_2O) (5). Needle-like crystals of {Mn(dpop)}$_5$(μ-*syn*-DCNB)$_3$(μ-*anti*-DCNB)$_2$ in Sol were soaked in water for three days in air and pale orange block crystals of **5** were obtained. IR: ν(CN) 2193 cm^{-1}.

{Mn(salen)(CH_3OH)}$_2$(μ-DCNQI)·CH_3CN (6). A solution of 88 mg (0.2 mmol) [Mn(salen)(H_2O)]ClO_4 in 10 mL of acetonitrile was added to a solution of H_2DCNQI (0.2 mmol, 31 mg) and 1,8-Bis(dimethylamino)naphthalene (0.4 mmol, 86 mg) in 10 mL of methanol. The mixture was stirred for 30 min and filtered before being concentrated to ~2/3 of the volume. This solution was stored at 4 ℃ overnight which led to the formation of dark brown crystals (49 mg, 26% yield based on Mn). IR: Nujol mulls on KBr plates: ν(CN) 2092.2 cm^{-1}.

{Mn(salen)(CH_3OH)}$_2$(μ-DM-DCNQI) (7). A solution of 88 mg (0.2 mmol) of [Mn(salen)(H_2O)]ClO_4 in 10 mL of methanol was added to a solution of [Ph_4As]$_2$(DM-DCNQI) (0.1 mmol, 95 mg) in 5 mL of methanol. The mixture was stirred for 30 min and filtered before being concentrated to ~one-half of the original volume. This solution was stored at 4 ℃ for four days which led to the formation of brown crystals (49 mg, 26% yield based on Mn)

{Mn(salen)(CH_3OH)}$_2$(μ-*anti*-N(cyano),N(amido)-DCNB)·CH_3CN (8). A solution of 44 mg (0.1 mmol) [Mn(salen)(H_2O)]ClO_4 in 5 mL of methanol was added to a solution of [Ph_4As]$_2$(DCNB) (0.1 mmol, 92 mg) in 10 mL of methanol. The mixture was stirred for 30 min and kept at 4 ℃ for two days which led to the formation of red crystals.

{Cr(salen)(CH_3OH)}$_2$(μ-Me-DCNB) ·CH_3CN ·CH_3OH (9). A solution of 47 mg of $[Ph_4As]_2$(Me-DCNB) in 14 mL of methanol was layered on a solution of 44 mg (0.1 mmol) $[Cr(salen)(H_2O)_2]ClO_4$ in 14 mL of acetonitrile. Yellow brown crystals were harvested after four days.

Crystallography details

General data collection and structural refinement procedures. Single crystal X-ray diffraction data of compound 1 were collected on a Bruker D8 Venture X-ray (CuKα, λ = 1.54178) diffractometer. Single crystal X-ray diffraction data of compounds 2, 4, and 5 were collected on a Bruker APEX 2 X-ray (Mo-Kα, λ = 0.71073) diffractometer. Single crystal X-ray diffraction data of compound 3 were collected on a Bruker D8 diffractometer equipped with an ApexII CCD detector on beamline 11.3.1 (Synchrotron, λ = 0.7749) at the Advanced Light Source in Berkeley, CA. Solution and refinement of the crystal structures of compounds 1, 2, 4, and 5 were carried out using the SHELX[140] suite of programs by direct methods and least squares minimization, respectively, using the graphical interface Olex2.[141]

Solution and refinement details of compound 3. The analysis of the diffraction patterns revealed an incommensurately modulated structure with highly visible first order satellites and very faint second order satellites. Structure solution was therefore performed directly in (3+1)-dimensional superspace by the program Superflip.[236] The analysis of the solution[237] confirmed the superspace group symbol *P*4/*nnc*(00γ)0000 estimated from the symmetry of the diffraction pattern and systematic absences.

The interpretation of the superspace electron density yielded the positions and modulation functions of all atoms of the organometallic moieties, and revealed an intricate structure formed by columns of interpenetrating helices that form large channels. The contents of the channels were, however, uninterpretable in terms of solvent molecules. The 3:2 ratio of the *syn* and *anti* forms is approximate, valid only in the supercell description. In the actual incommensurate structure there is a (very slight) excess of the *anti* form.

The structural refinement was performed also using the superspace formalism with the program Jana2006.[238] The refinement was complicated. The modulation is very strong and involves switching of the DCNB molecule between *syn* and *anti* conformations (Figure 5). It is likely that the modulation involves a certain degree of disorder, but it was impossible to model such disorder in such a complex structure with a manageable number of parameters. Moreover, the channels contain disordered solvent molecules which form continuous electron density in the channels. This density is also modulated. It was impossible to locate individual solvent molecules in the channels, with the exception of two methanol molecules and one group in the axis of the channel, which was interpreted as an acetonitrile molecule. The density in the channels was modelled with partially occupied carbon atoms modulated with harmonic occupational modulation functions. All these limitations in the completeness of the structure model combined with only a moderate quality of the diffraction data led to the refinement with a R-value R1(obs) = 13.03%. Despite this relatively high R-value, the basic features of the structure – the positions and connectivity of the $[Mn(dpop)]^{2-}$ building blocks and

$DCNB^{2-}$ anions are undoubtedly correct and the higher-than-usual R-value is attributed to the difficulties in accounting accurately for the residual disorder and in describing the channel contents. During the refinement, distance only restraints on the C-O distance of one methanol molecules and acetonitrile were used. No restraints were applied to the DCNB or dpop moieties.

Two CIFs of this structure were deposited in CCDC. The file named helical_superspace.cif is the CIF of the full modulated structure in the the superspace formalism. This file can be used to analyze the modulated structure, but its use requires sufficient knowledge of the superspace description of the modulated structures. The file named helical_supercell.cif contains an approximation to the true modulated structure in a five-fold supercell. This approximation is relatively good, because the length of the modulation vector is 0.411c*, which is close to the commensurate value 0.4c* used for the supercell approximation. This approximation thus captures most of the features of the real structure and is easily tractable because it has a high symmetry (*P*4/*nnc*) and relatively few independent atoms. It is still an approximation, however, and it does not capture all the features of the model, especially not the non-periodic sequence of the *syn* and *anti* conformations of the $DCNB^{2-}$ moiety along the helix as well as the arrangement of the disordered Mn(dpop) groups. An anaIysis of the modulated structure revealed that the model contains ~ 2% of disordered $[Mn(dpop)]^{2+}$ groups.

A summary of pertinent crystallographic information is provided in Table **1**. CCDC 1448303-1448308 contains the supplementary crystallographic data for this

work. These data can be obtained free of charge from the Cambridge Crystallographic Data Centre via www.ccdc.cam.ac.uk/data_request/cif.

X-ray structural determination of 9. A pale yellow-brown plate of dimensions 0.03 × 0.02 × 0.005 mm^3 was mounted on a MiTeGen kapton loop in a 100(2) K nitrogen cold stream provided by an Oxford Cryosystems Cryostream 700 Plus low temperature apparatus on the goniometer head of a Bruker D8 diffractometer equipped with an ApexII CCD detector on beamline 11.3.1 at the Advanced Light Source in Berkeley, CA. Diffraction data were collected using synchrotron radiation monochromated using silicon(111) to a wavelength of 0.7749(1) Å. A two-shell data collection was performed to optimize dynamic range, an approximate full sphere was collected with 2θ = 0.0 ° at 2 second exposure and an additional hemisphere was collected with 2θ = -48 ° at 7 second exposure. A total of 42052 reflections were collected of which 8150 were unique [R(int) = 0.0550] and 5873 were observed [I>2σ (I)]. The structure was solved by direct methods (SHELXT) and refined by full-matrix least-squares on F^2 (SHELXL-2013) using 581 parameters and 14 restraints.

Table 33. Pertinent crystallographic data for compounds 1-5.

Compound	**1**	**2**	**3**	**4**	**5**
Empirical formula	$C_{27}H_{26}MnN_9$	$C_{23}H_{27}MnN_9O$	$C_{125}H_{125}Mn_5N_{45}$	$C_{25}H_{32}N_{10}OMn$	$C_{23}H_{33}N_9O_3Mn$
Formula weight	530.52	484.47	2532.3	543.54	538.52
Temperature/K	100	110	100	110	110
Crystal system	triclinic	monoclinic	tetragonal	monoclinic	triclinic
Space group	P-1	P21/c	P4/nnc(00γ)0000	$P2_1/c$	P-1
a/Å	7.9873(5)	8.2615(17)	28.9206(16)	17.284(4)	7.6509(15)
b/Å	13.7930(9)	27.899(6)	28.9206(16)	7.6577(15)	11.237(2)
c/Å	15.8770(10)	11.966(2)	37.7665(8)	19.598(4)	15.457(3)
α/°	71.108(3)	90	90	90	105.76(3)
β/°	77.419(3)	96.19(3)	90	93.58(3)	95.39(3)
γ/°	74.256(3)	90	90	90	99.92(3)
Modulation vector	-	-	0.41065(6)**c***	-	-
Volume	1576.53(18)	2742.0(10)	6317.6(6)	2588.8(9)	1245.8(5)
Z	2	4	8	4	2
ρ_{calc} / g/cm^3	1.064	1.174	1.190	1.395	1.436
μ/mm^{-1}	3.626	0.507	0.564	0.549	0.575
F(000)	500.0	1012.0	2332.6	1140.0	566.0
Crystal size/mm^3	0.15 × 0.11 × 0.08	0.110 × 0.080 × 0.020	0.10× 0.08 × 0.06	0.23 × 0.21 × 0.04	0.27 × 0.14 × 0.11
Radiation	CuKα (λ = 1.54178)	MoKα (λ = 0.71073)	Synchrotron (λ = 0.7749)	MoKα (λ = 0.71073)	MoKα (λ = 0.71073)
2Θ range for data collection/°	7.764 to 109.612	2.92 to 42.506	5.42 to 59.36	4.164 to 56.79	3.85 to 52.694
Index ranges	-8 ≤ h ≤ 8, -14 ≤ k ≤ 14, -16 ≤ l ≤ 16	-8 ≤ h ≤ 8, -28 ≤ k ≤ 28, -12 ≤ l ≤ 12	-36 ≤ h ≤ 36, -36 ≤ k ≤ 36, -10 ≤ l ≤ 10, -1 ≤ m ≤ 1	-22 ≤ h ≤ 23, -10 ≤ k ≤ 10, -26 ≤ l ≤ 26	-9 ≤ h ≤ 9, -14 ≤ k ≤ 14, -19 ≤ l ≤ 19
Reflections collected	20035	19638	152130	29688	13546
Independent reflections	3864 [R_{int} = 0.0356, $R_σ$ = 0.0255]	3046 [R_{int} = 0.1100, $R_σ$ = 0.0672]	10321 [R_{int} = 0.1588, $R_σ$ = 0.0482]	6439 [R_{int} = 0.1274, $R_σ$ = 0.1244]	5063 [R_{int} = 0.0236, $R_σ$ = 0.0301]
Data/restraints/parameters	3864/1030/538	3046/0/300	10321/4/461	6439/0/346	5063/0/334
Goodness-of-fit on F^2	1.082	1.038	3.76	1.023	1.027
Final R indexes [I>=2σ (I)]	R_1 = 0.0480, wR_2 = 0.1255	R_1 = 0.0445, wR_2 = 0.0931	R_1 = 0.1395, wR_2 = 0.2331	R_1 = 0.0668, wR_2 = 0.1488	R_1 = 0.0667, wR_2 = 0.1609
Final R indexes [all data]	R_1 = 0.0540, wR_2 = 0.1327	R_1 = 0.0763, wR_2 = 0.1048	R_1 = 0.1675, wR_2 = 0.2364	R_1 = 0.1426, wR_2 = 0.1821	R_1 = 0.0762, wR_2 = 0.1674
Largest diff. peak/hole / e Å^{-3}	0.65/-0.33	0.23/-0.30	1.07/-0.90	1.04/-0.53	1.39/-0.65

$R_1 = \Sigma||F_o| - |F_c||/ \Sigma|F_o|$. $wR_2 = [\Sigma w(|F_o| - |F_c|)^2/|\Sigma w(F_o)^2]^{1/2}$. $w = 0.75/(\sigma^2(F_o)+0.00010F_o^2)$.

Table 34. Pertinent crystallographic data for compounds **6-9**.

Identification code	**6**	**7**	**8**	**9**
Empirical formula	$C_{44.66}H_{40}Mn_2N_{9.34}O_{6.67}$	$C_{46}H_{52}Mn_2N_8O_8$	$C_{42}H_{40}Mn_2N_8O_6$	$C_{46}H_{49}Cr_2N_9O_7$
Formula weight	924.05	954.83	862.70	943.94
Temperature/K	110(2)	110(2)	110(2)	100(2)
Crystal system	monoclinic	triclinic	monoclinic	orthorhombic
Space group	$P2_1/c$	P-1	$P2_1/n$	Pbca
a/Å	9.5987(17)	8.0954(10)	12.6060(16)	17.2983(6)
b/Å	18.583(3)	11.7929(14)	15.677(2)	21.2906(8)
c/Å	12.656(2)	12.8286(15)	19.331(3)	24.3309(8)
α/°	90	68.0550(10)	90	90
β/°	107.687(2)	83.802(2)	92.416(2)	90
γ/°	90	81.431(2)	90	90
Volume/$Å^3$	2150.7(7)	1121.5(2)	3817.0(8)	8960.9(5)
Z	2	1	4	8
$\rho_{calc}g/cm^3$	1.427	1.414	1.501	1.399
μ/mm^{-1}	0.649	0.626	0.723	0.689
F(000)	953.0	498.0	1784.0	3936.0
Crystal size/mm^3	0.14 × 0.05 × 0.02	0.19 × 0.11 × 0.08	0.18 × 0.08 × 0.04	0.030 × 0.020 × 0.005
Radiation	MoKα (λ = 0.71073)	MoKα (λ = 0.71073)	MoKα (λ = 0.71073)	synchrotron (λ = 0.7749)
2Θ range for data collection/ °	5.536 to 53.446	3.428 to 52.744	3.346 to 54.206	5.836 to 55.65
Index ranges	$-12 \le h \le 12$, $-23 \le k \le 23$, $-16 \le l \le 15$	$-10 \le h \le 10$, $-14 \le k \le 14$, $-16 \le l \le 16$	$-16 \le h \le 16$, $-20 \le k \le 20$, $-24 \le l \le 24$	$-20 \le h \le 10$, $-25 \le k \le 24$, $-28 \le l \le 29$
Reflections collected	22828	12310	43535	42052
Independent reflections	4548 [R_{int} = 0.0678, R_{sigma} = 0.0555]	4555 [R_{int} = 0.0242, R_{sigma} = 0.0303]	8420 [R_{int} = 0.0637, R_{sigma} = 0.0486]	8150 [R_{int} = 0.0550, R_{sigma} = 0.0550]
Data/restraints/parameters	4548/3/302	4555/3/296	8420/6/531	8150/14/581
Goodness-of-fit on F^2	1.038	1.051	1.031	1.032
Final R indexes [I>=2σ (I)]	R_1 = 0.0486, wR_2 = 0.1145	R_1 = 0.0318, wR_2 = 0.0742	R_1 = 0.0389, wR_2 = 0.0850	R_1 = 0.0612, wR_2 = 0.1574
Final R indexes [all data]	R_1 = 0.0797, wR_2 = 0.1306	R_1 = 0.0396, wR_2 = 0.0780	R_1 = 0.0600, wR_2 = 0.0946	R_1 = 0.0879, wR_2 = 0.1724
Largest diff. peak/hole / e $Å^{-3}$	0.92/-0.35	0.34/-0.23	0.54/-0.43	1.22/-0.53

$R_1 = \Sigma||F_o| - |F_c||/ \Sigma|F_o|$. $wR_2 = [\Sigma w(|F_o| - |F_c|)^2/|\Sigma w(F_o)^2]^{1/2}$. $w = 0.75/(\sigma^2(F_o)+0.00010F_o^2)$.

There are two solvent sites, one acetonitrile and the other methanol. The second site has a residual difference peak of 1.215 $eÅ^{-3}$ which does not correspond to any logical modeling. The restraints were used to fix the distance and displacement of the hydrogen atoms on the coordinated methanol molecules as well as to constrain the displacement parameters of the solvent molecules. The hydrogen atoms on carbon atoms were generated geometrically and refined as riding atoms with C-H = 0.95- 0.99 Å and Uiso(H) =1.2 times Ueq(C) for CH and CH2 groups and Uiso(H) =1.5 times Ueq(C) for CH3 groups.

Results and Discussions

Dinuclear complexes

The series of compounds are all neutral dinuclear $[M(salen)(CH_3OH)]^+$ complexes bridged by dicyanamidobenzene dianions. 1,4-dicyananamidobenzene dianion ($DCNQI^{2-}$) exhibited only one conformation while the flexibility of 1,3-dicyananamidobenzene dianion ($DCNB^{2-}$) allows itself to exist in *syn* or *anti* conformations.

It has been predicted by Ruiz and coworkers that *para*-dicyanamidobenzene (DCNQI) and *meta*-dicyanamidobenzene (DCNB) bridging dianions should result in strong coupling (antiferromagnetic and ferromagnetic, respectively) between trivalent transition metals based on the model compound $(NH_3)_5M$-(μ-DCNQI)-$M(NH_3)_5$ (M=Cr, Mn, Fe).[191] Therefore, in this work, trivalent metal-salen compounds were prepared and the reactions between $[M(salen)(H_2O)_2]ClO_4$ (salen=N,N'-ethylenebis(salicylimine), M=Cr, Mn and para- and meta- dicyanamidobenzene dianions were planned.

The di-protonated forms the bridging ligands (H_2DCNQI and H_2DCNB) were prepared by using literature methods[216,234,234] and they were found to be quite stable in the solid state. The dianion forms of the ligands were obtained by the de-protonation of H_2DCNQI and H_2DCNB using bases such as lithium acetate, triethylamine, sodium hydroxide and proton sponge (1,8-bis(dimethylamino)naphthalene). These dianions were introduced into the reactions by either using the preformed tetraphenylarsonium salts or via *in situ* de-protonation of the di-protonated forms.

Table 35. Calculated exchange coupling constants (in cm^{-1}) between select metal ions through $DCNQI^{2-}$ and $DCNB^{2-}$ bridging ligands based on the Hamiltonian $\hat{H} = -J\hat{S}_1\hat{S}_2$.

	electron configuration	**J($DCNQI^{2-}$) /cm^{-1}**	**J($DCNB^{2-}$) /cm^{-1}**
Cr(III)	t_{2g}^3	−161.3	+62.1
Mn(III)	$t_{2g}^3 e_g^1$	−177.9	+116.6
Fe(III)	$t_{2g}^3 e_g^2$	−289.2	+86.5
Mn(II)	$t_{2g}^3 e_g^2$	−0.8	-0.001
Ni(II)	$t_{2g}^6 e_g^2$	+0.1	+0.14

The low dimensional compounds based on trivalent metal ions bridged by $DCNQI^{2-}$ will serve as models for fundamental studies of the efficacy of these bridges to mediate exchange couplings. A dinuclear complex of {Mn(salen)(CH_3OH)}$_2$(μ-DCNQI) was obtained by the reaction of $[Ph_4As]_2$[DCNQI] and Mn(salen)$(H_2O)_2]ClO_4$ in a mixture of CH_3CN and CH_3OH as dark brown crystals. The product {Mn(salen)(CH_3OH)}$_2$(μ-DCNQI) crystallizes in the monoclinic $P2_1/c$ space group with the asymmetric unit being composed of one-half of a $DCNQI^{2-}$ anion and one

$[Mn(salen)(CH_3OH)]^+$ cation. Magnetic measurements conducted on crushed crystals of the product showed only weak antiferromagnetic interactions between the Mn(III) centers. A dinuclear Heisenberg-Dirac-Van Vleck (HDVV) Hamiltonian ($\widehat{H} = -2J\widehat{S_1}\widehat{S_2}$) superexchange model was employed to fit the experimental data.

$$\chi T=\frac{3g^2}{8}\cdot\frac{60e^{\frac{20J}{T}}+28e^{\frac{12J}{T}}+10e^{\frac{6J}{T}}+2e^{\frac{2J}{T}}}{9e^{\frac{20J}{T}}+7e^{\frac{12J}{T}}+5e^{\frac{6J}{T}}+3e^{\frac{2J}{T}}+1} \qquad \text{(equation 3)}$$

For an S=2 system, the χT value was obtained from the Van Vleck equation as shown in Equation 3, and the best fitting resulted in a coupling constant of J = -0.28 cm^{-1} and g = 1.97 (Figure 100). These results indicate that very weak antiferromagnetic interactions through the $DCNQI^{2-}$ bridging ligand are occurring in this case. This situation is quite different from the claims of Ruiz and coworkers, who predicted the coupling of Mn(III) through $DCNQI^{2-}$ would be strongly antiferromagnetic with J= -89 cm^{-1}.[191] This discrepancy could be explained by the strong Jahn-Teller distortion along the axial direction (perpendicular to the Mn-salen plane) of the Mn(III) coordination sphere, which causes an elongation of Mn1-N3 distance (2.243(3) Å) and a bending of the Mn1-N3-C17 angle (157.2(3)˚). In their calculations, the molecular parameters were adopted from a compound reported by Crutchley and coworkers, $(NH_3)_5Ru$-(μ-DCNQI)-$Ru(NH_3)_5$, and a metal-nitrogen (M-N) bond distance of 1.938 Å and a metal-nitrogen-carbon (M-N-C) bond angle of 175˚ were used.[216] The longer Mn-N distance and smaller Mn-N-C angle caused by Jahn-Teller distortion in $\{Mn(salen)(CH_3OH)\}_2$(μ-DCNQI) of this study will cause diminished dπ-pπ overlap between the metal and the bridging $DCNQI^{2-}$. As a result, the ability of $DCNQI^{2-}$ to mediate antiferromagnetic interactions

in {Mn(salen)(CH_3OH)}$_2$(μ-DCNQI) is much weaker than the theoretical prediction and that found for $(NH_3)_5$Ru-(μ-DCNQI)-Ru$(NH_3)_5$. In another compound, DM-DCNQI with two electron-donating methyl groups was employed instead of DCNQI but the product {Mn(salen)(CH_3OH)}$_2$(μ-DM-DCNQI) **(7)** showed weak antiferromagnetic interactions as well. The dinuclear complex of {Mn(salen)(CH_3OH)}$_2$(μ-DM-DCNQI) was obtained as dark brown crystals by the reaction of $[Ph_4As]_2$[DM-DCNQI] and Mn(salen)$(H_2O)_2]ClO_4$ in CH_3OH. Different from {Mn(salen)(CH_3OH)}$_2$(μ-DCNQI), the product {Mn(salen)(CH_3OH)}$_2$(μ-DM-DCNQI) crystalizes in the triclinic P-1 space group with the asymmetric unit being composed of one-half of a DM-DCNQI^{2-} anion and one [Mn(salen)(CH_3OH)]$^+$ cation. The Mn-N3 bond distance (2.179(2) Å) of {Mn(salen)(CH_3OH)}$_2$(μ-DM-DCNQI) **(7)** is shorter than that in {Mn(salen)(CH_3OH)}$_2$(μ-DCNQI) (2.243(3) Å) but the Mn1-N3-C1 bond angle (135.5(1)˚) of the former is more bent than the latter (157.2(3)˚). Hydrogen bonding interactions between the cyano-N atom and hydroxyl group of the methanol molecule also contributes to the distortion of Mn1-N3-C1 bond (Figure 102). It is possible that the bent Mn1-N3-C1 bond angle weakens the dπ-pπ overlap between the metal and the bridging DM-DCNQI^{2-} ligand.

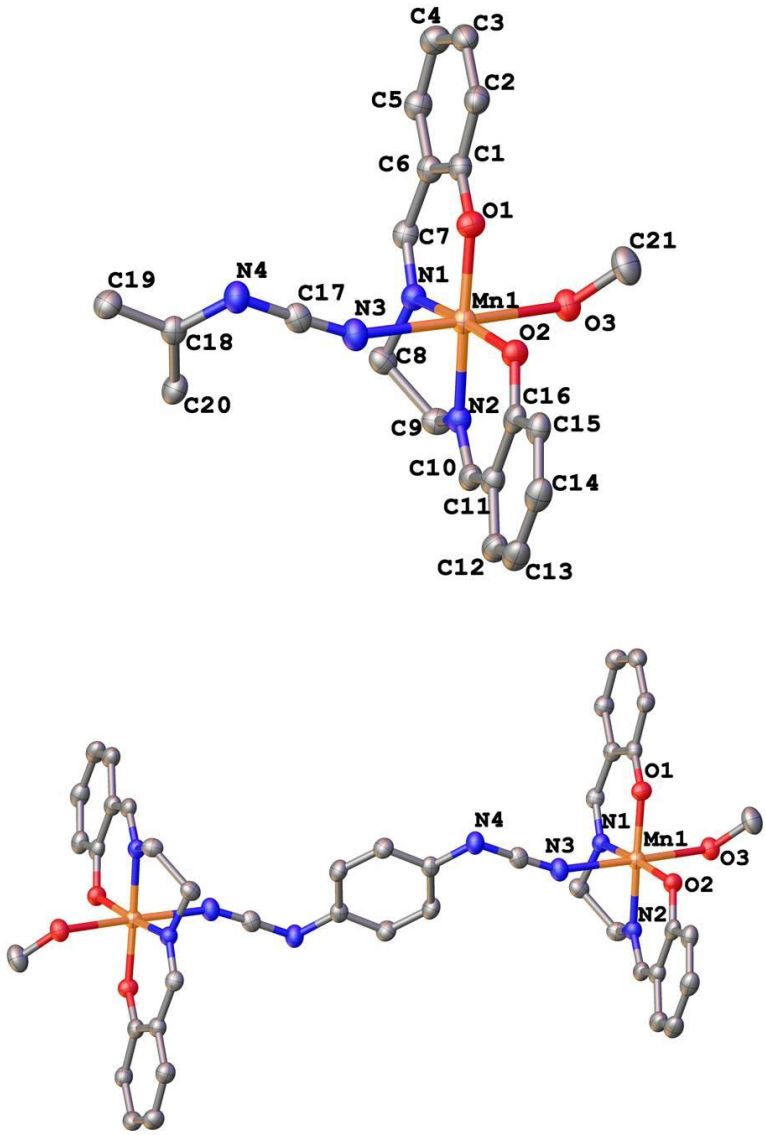

Figure 99. Asymmetric unit (top) and molecular structure (bottom) of the crystal structure of $\{Mn(salen)(CH_3OH)\}_2(\mu\text{-DCNQI})$ (**6**). Thermal ellipsoids are drawn at the 50% probability level. Hydrogen atoms and disordered free solvent molecules are omitted for the sake of clarity.

Table 36. Bond distances of {Mn(salen)(CH_3OH)}$_2$(μ-DCNQI) (**6**).

Atom	Atom	Length/Å		Atom	Atom	Length/Å
Mn1	O2	1.884(2)		C10	C11	1.444(4)
Mn1	O1	1.877(2)		C16	C11	1.415(4)
Mn1	O3	2.315(2)		C16	C15	1.412(4)
Mn1	N1	1.979(2)		C6	C5	1.406(4)
Mn1	N2	1.989(3)		C11	C12	1.412(4)
Mn1	N3	2.243(3)		C9	C8	1.523(4)
O2	C16	1.322(4)		C2	C3	1.375(4)
O1	C1	1.317(3)		C18	C19	1.385(4)
O3	C21	1.426(4)		C18	C20	1.391(4)
N1	C7	1.279(4)		C14	C15	1.372(4)
N1	C8	1.477(4)		C14	C13	1.384(5)
N2	C10	1.281(4)		C5	C4	1.367(4)
N2	C9	1.473(4)		C12	C13	1.377(4)
N3	C17	1.166(4)		C19	C20[1]	1.389(4)
N4	C17	1.294(4)		C20	C19[1]	1.389(4)
N4	C18	1.422(4)		C4	C3	1.411(4)
C7	C6	1.434(4)		C22	N5	1.186(10)
C1	C6	1.425(4)		C22	C23	1.315(9)
C1	C2	1.400(4)				

[1]2-X,1-Y,1-Z

Table 37. Bond angles of {Mn(salen)(CH_3OH)}$_2$(μ-DCNQI) (**6**).

Atom	Atom	Atom	Angle/°		Atom	Atom	Atom	Angle/°
O2	Mn1	O3	92.63(8)		O1	C1	C2	118.7(3)
O2	Mn1	N1	173.23(10)		C2	C1	C6	117.6(3)
O2	Mn1	N2	91.31(9)		N2	C10	C11	124.7(3)
O2	Mn1	N3	95.35(9)		O2	C16	C11	123.9(3)
O1	Mn1	O2	93.65(9)		O2	C16	C15	118.4(3)
O1	Mn1	O3	87.82(9)		C15	C16	C11	117.7(3)
O1	Mn1	N1	92.51(9)		C1	C6	C7	122.9(3)
O1	Mn1	N2	173.25(9)		C5	C6	C7	117.2(3)
O1	Mn1	N3	93.72(9)		C5	C6	C1	119.8(3)
N1	Mn1	O3	84.81(9)		C16	C11	C10	122.5(3)
N1	Mn1	N2	82.33(10)		C12	C11	C10	118.0(3)
N1	Mn1	N3	87.04(10)		C12	C11	C16	119.4(3)
N2	Mn1	O3	87.39(9)		N2	C9	C8	106.9(2)
N2	Mn1	N3	90.35(10)		C3	C2	C1	121.3(3)
N3	Mn1	O3	171.76(8)		C19	C18	N4	118.4(3)
C16	O2	Mn1	127.02(19)		C19	C18	C20	117.9(3)
C1	O1	Mn1	128.43(18)		C20	C18	N4	123.6(3)
C21	O3	Mn1	120.65(18)		C15	C14	C13	121.6(3)
C7	N1	Mn1	125.5(2)		N1	C8	C9	106.6(2)
C7	N1	C8	121.6(3)		C14	C15	C16	121.1(3)
C8	N1	Mn1	112.85(18)		C4	C5	C6	121.6(3)
C10	N2	Mn1	125.6(2)		C13	C12	C11	121.5(3)
C10	N2	C9	121.1(3)		C12	C13	C14	118.7(3)
C9	N2	Mn1	113.22(18)		C18	C19	C20[1]	120.9(3)
C17	N3	Mn1	157.2(3)		C19[1]	C20	C18	121.1(3)
C17	N4	C18	117.9(3)		C5	C4	C3	118.5(3)
N1	C7	C6	125.5(3)		C2	C3	C4	121.1(3)
N3	C17	N4	175.7(3)		N5	C22	C23	167.5(8)
O1	C1	C6	123.6(3)					

[1]2-X,1-Y,1-Z

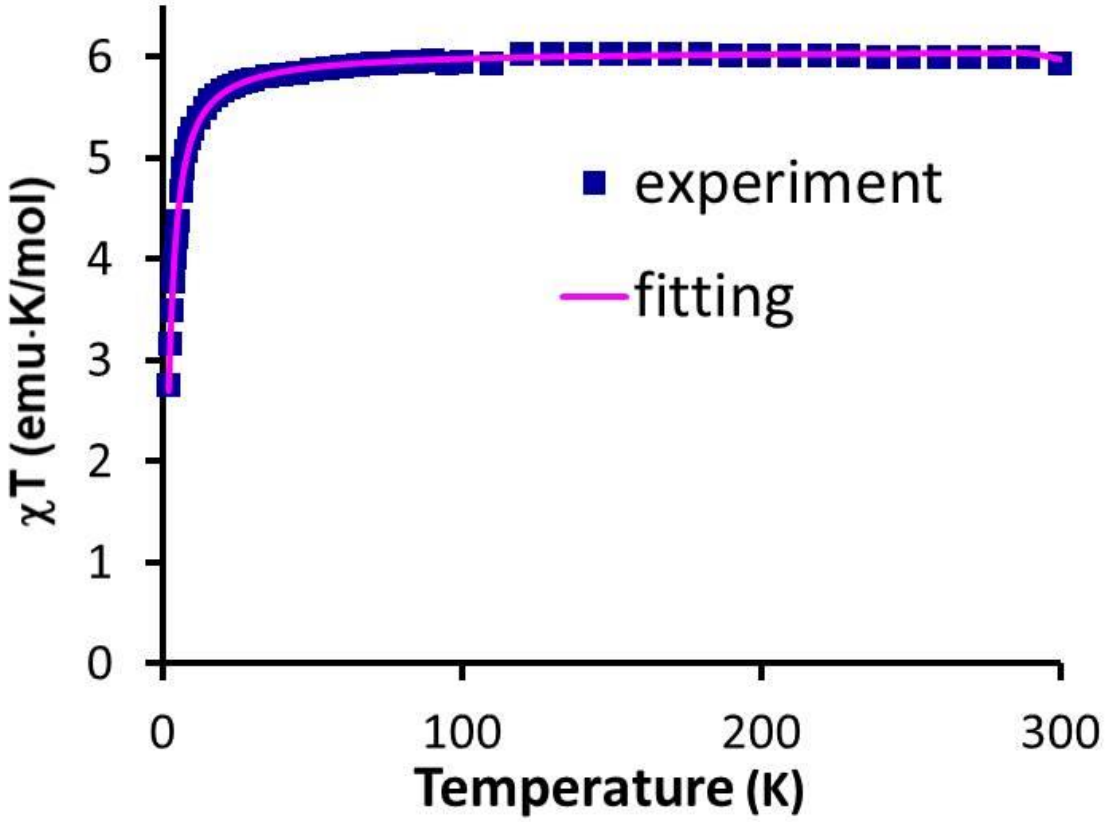

Figure 100. Temperature dependence of the χT of $\{Mn(salen)(CH_3OH)\}_2(\mu\text{-DCNQI})$ (**6**) showing both the experimental data (solid square) and fitting result (solid line).

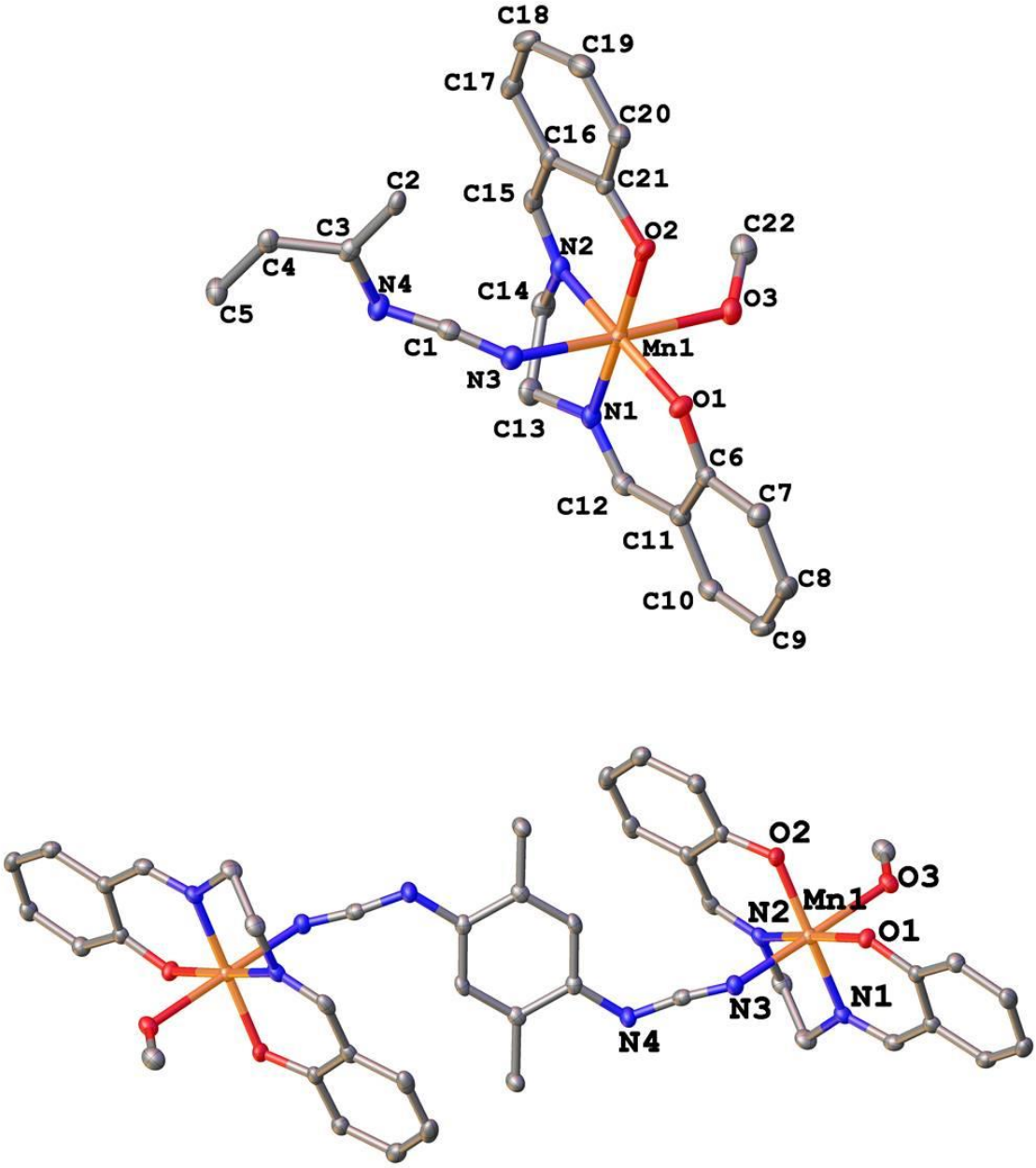

Figure 101. Asymmetric unit (top) and molecular structure (bottom) of the crystal structure of {Mn(salen)(CH_3OH)}$_2$(μ-DM-DCNQI) (**7**). Thermal ellipsoids are drawn at the 50% level- these are not thermal ellipsoids. Hydrogen atoms and free solvent molecules are omitted for the sake of clarity.

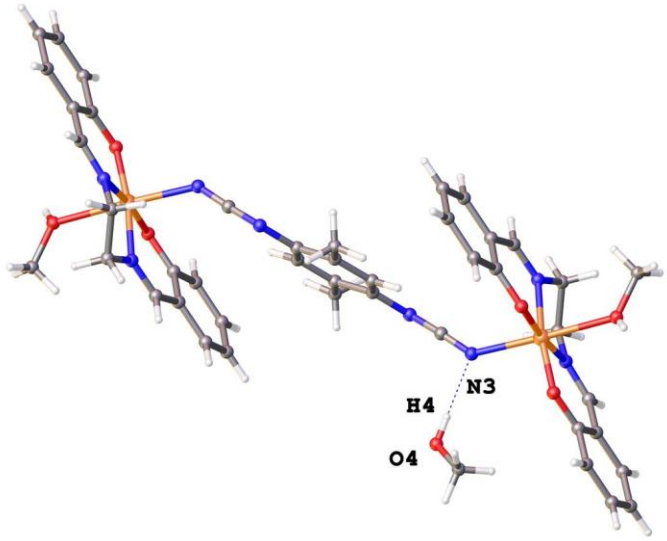

Figure 102. Crystal structure of {Mn(salen)(CH_3OH)}$_2$(μ-DM-DCNQI) (**7**) showing the hydrogen bonding interactions between the cyano-nitrogen and hydroxyl group of the methanol molecule.

Table 38. Bond distances of {Mn(salen)(CH_3OH)}$_2$(μ-DM-DCNQI) (**7**).

Atom	Atom	Length/Å		Atom	Atom	Length/Å
Mn1	O1	1.8778(12)		C4	C2[1]	1.391(2)
Mn1	O2	1.9067(12)		C4	C5	1.508(2)
Mn1	O3	2.3428(13)		C6	C7	1.408(2)
Mn1	N1	1.9815(15)		C6	C11	1.420(2)
Mn1	N2	1.9954(14)		C7	C8	1.379(2)
Mn1	N3	2.1786(15)		C8	C9	1.399(3)
O1	C6	1.324(2)		C9	C10	1.371(3)
O2	C21	1.332(2)		C10	C11	1.414(2)
O3	C22	1.435(2)		C11	C12	1.439(2)
N1	C12	1.291(2)		C13	C14	1.521(3)
N1	C13	1.475(2)		C15	C16	1.438(3)
N2	C14	1.472(2)		C16	C17	1.416(2)
N2	C15	1.288(2)		C16	C21	1.424(2)
N3	C1	1.189(2)		C17	C18	1.368(3)
N4	C1	1.267(2)		C18	C19	1.399(3)
N4	C3	1.413(2)		C19	C20	1.382(3)
C2	C3	1.398(2)		C20	C21	1.400(3)
C2	C4[1]	1.391(2)		O4	C23	1.409(3)
C3	C4	1.405(2)				

[1]-X,1-Y,-Z

Table 39. Bond angles of {Mn(salen)(CH_3OH)}$_2$(μ-DM-DCNQI) (7).

Atom	Atom	Atom	Angle/°		Atom	Atom	Atom	Angle/°
O1	Mn1	O2	94.25(5)		C2	C3	C4	119.27(16)
O1	Mn1	O3	85.51(5)		C4	C3	N4	117.07(15)
O1	Mn1	N1	92.13(6)		C2[1]	C4	C3	118.58(16)
O1	Mn1	N2	171.41(6)		C2[1]	C4	C5	121.50(16)
O1	Mn1	N3	96.67(5)		C3	C4	C5	119.92(16)
O2	Mn1	O3	87.89(5)		O1	C6	C7	118.51(15)
O2	Mn1	N1	172.18(6)		O1	C6	C11	123.57(15)
O2	Mn1	N2	91.37(6)		C7	C6	C11	117.91(16)
O2	Mn1	N3	92.01(6)		C8	C7	C6	121.19(17)
N1	Mn1	O3	88.11(5)		C7	C8	C9	121.07(17)
N1	Mn1	N2	81.79(6)		C10	C9	C8	118.84(17)
N1	Mn1	N3	91.73(6)		C9	C10	C11	121.67(17)
N2	Mn1	O3	88.22(5)		C6	C11	C12	123.26(16)
N2	Mn1	N3	89.61(6)		C10	C11	C6	119.30(16)
N3	Mn1	O3	177.82(5)		C10	C11	C12	117.43(16)
C6	O1	Mn1	128.96(11)		N1	C12	C11	124.75(16)
C21	O2	Mn1	126.41(11)		N1	C13	C14	107.02(14)
C22	O3	Mn1	127.84(11)		N2	C14	C13	107.16(14)
C12	N1	Mn1	126.00(12)		N2	C15	C16	125.26(16)
C12	N1	C13	120.23(15)		C17	C16	C15	117.63(16)
C13	N1	Mn1	113.71(11)		C17	C16	C21	118.97(17)
C14	N2	Mn1	113.77(11)		C21	C16	C15	123.31(16)
C15	N2	Mn1	124.63(13)		C18	C17	C16	121.56(17)
C15	N2	C14	121.36(15)		C17	C18	C19	119.33(17)
C1	N3	Mn1	135.46(13)		C20	C19	C18	120.54(18)
C1	N4	C3	121.30(15)		C19	C20	C21	121.45(17)
N3	C1	N4	173.22(19)		O2	C21	C16	123.22(16)
C4[1]	C2	C3	122.14(16)		O2	C21	C20	118.60(16)
C2	C3	N4	123.66(15)		C20	C21	C16	118.16(16)

[1]-X,1-Y,-Z

As the para-dicyanamidobenzene dianions (DCNQI) did not give rise to strong antiferromagnetic coupling between Mn(III) centers as expected, the meta-dicyanamidobenzene dianions were also employed as bridging ligands to test if this ligand would mediate ferromagnetic coupling between trivalent metal ions. In order to obtain the dinuclear complex of $[Mn(salen)(CH_3OH)]^+$ bridged by $DCNB^{2-}$ in a similar fashion to the ones bridged by $DCNQI^{2-}$ and $DM\text{-}DCNQI^{2-}$, the reaction between $[Ph_4As]_2[DCNB]$ and $Mn(salen)(H_2O)_2]ClO_4$ was carried out in a mixture of CH_3OH which led to dark brown crystals. Surprisingly, the crystals turned out to be $\{Mn(salen)(CH_3OH)\}_2$(μ-anti-N(cyano),N(amido)-DCNB)•CH_3CN which is different from the terminal nitrogen bridged dinuclear complexes of $\{Mn(salen)(CH_3OH)\}_2$(μ-DCNQI) and $\{Mn(salen)(CH_3OH)\}_2$(μ-DM-DCNQI). $\{Mn(salen)(CH_3OH)\}_2$(μ-anti-N(cyano),N(amido)-DCNB)•CH_3CN crystalizes in the monoclinic $P2_1/c$ space group with the asymmetric unit being composed of one $DCNB^{2-}$ anion and one $[Mn(salen)(CH_3OH)]^+$ cation. It is worth noting that the two Mn-N bond distances are quite different with Mn1-N3(cyano) and Mn2-N5(imido) being 2.175 (2) and 2.260(2) Å, respectively. The former is similar to the Mn1-N3 bond distance in $\{Mn(salen)(CH_3OH)\}_2$(μ-DM-DCNQI) (2.179(2) Å) while the latter is close to the Mn1-N3 bond distance in $\{Mn(salen)(CH_3OH)\}_2$(μ-DCNQI) (2.243(3) Å). The $DCNB^{2-}$ bridged dinuclear molecules are engaged in hydrogen bonding interactions with each other through the methanol oxygen and salen oxygen atoms of the adjacent molecules (Figure 104). Phenyl rings of the salen ligands also engage in π-π stacking interactions (Figure 105). As a result, only weak antiferromagnetic interactions have been observed

in {Mn(salen)(CH_3OH)}$_2$(μ-anti-N(cyano),N(amido)-DCNB)•CH_3CN. Fitting of the experimental temperature dependent χT data to a Curie-Weiss law revealed a Weiss constant of -1.0 cm^{-1} and a g value of 1.95 (Figure 106).

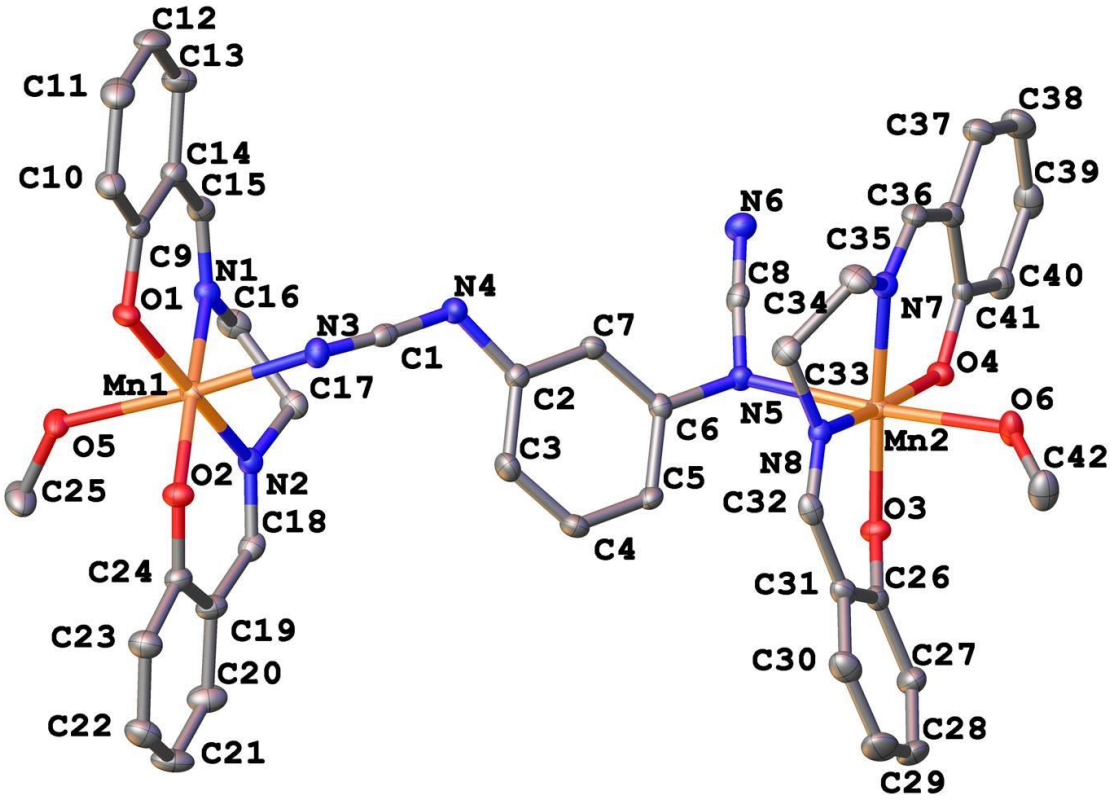

Figure 103. Asymmetric unit of the crystal structure of {Mn(salen)(CH_3OH)}$_2$(μ-anti-N(cyano),N(amido)-DCNB)•CH_3CN (**8**). Thermal ellipsoids are drawn at the 50% probability level. Hydrogen atoms are omitted for the sake of clarity.

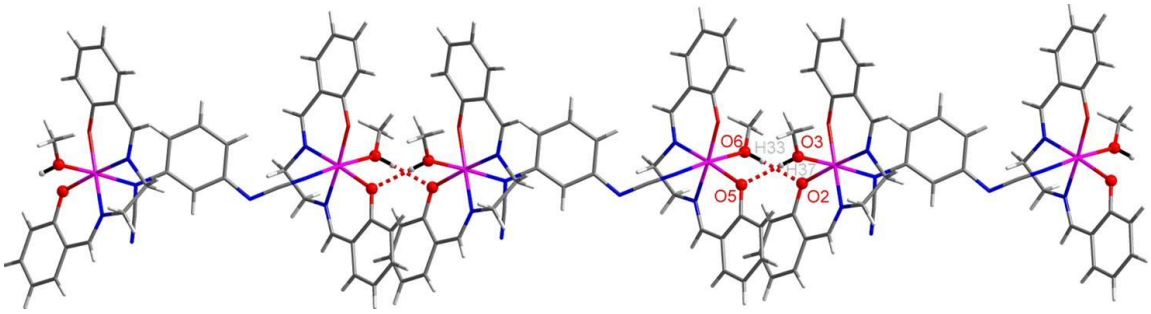

Figure 104. Crystal structure of {Mn(salen)(CH_3OH)}$_2$(μ-anti-N(cyano),N(amido)-DCNB)•CH_3CN **(8)** showing the hydrogen bonding interactions between the methanol and salen oxygen atoms of the adjacent molecules.

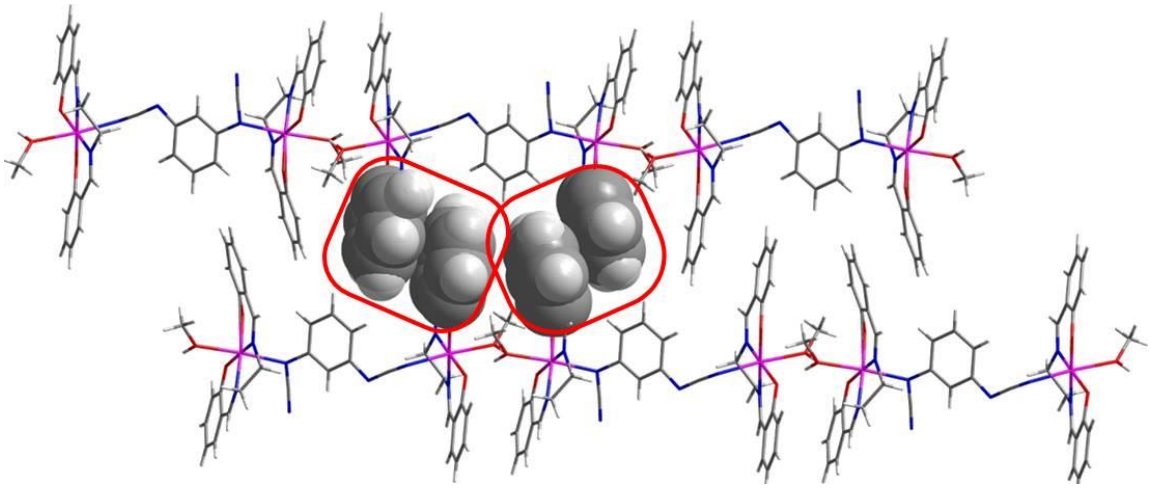

Figure 105. Crystal structure of {Mn(salen)(CH_3OH)}$_2$(μ-anti-N(cyano),N(amido)-DCNB)•CH_3CN **(8)** showing the π-π stacking interactions between the phenyl rings of the salen ligands.

Table 40. Bond distances of {Mn(salen)(CH_3OH)}$_2$(μ-anti-N(cyano),N(amido)-DCNB)•CH_3CN **(8)**.

Atom	Atom	Length/Å		Atom	Atom	Length/Å
Mn1	O2	1.8777(16)		C26	C31	1.419(3)
Mn1	O1	1.9111(16)		C26	C27	1.400(3)
Mn1	O5	2.3110(16)		C17	C16	1.517(3)
Mn1	N2	1.9823(19)		C5	C6	1.401(3)
Mn1	N3	2.1753(19)		C5	C4	1.384(3)
Mn1	N1	1.9988(19)		C18	C19	1.439(3)
Mn2	O4	1.9055(16)		C24	C19	1.412(3)
Mn2	O3	1.8759(16)		C24	C23	1.404(3)
Mn2	O6	2.3278(17)		C33	C34	1.519(3)
Mn2	N8	1.9755(19)		C32	C31	1.436(3)
Mn2	N5	2.2602(19)		C6	C7	1.392(3)
Mn2	N7	2.0011(19)		C31	C30	1.409(3)
O4	C41	1.342(3)		C15	C14	1.440(3)
O3	C26	1.332(3)		C7	C2	1.385(3)
O2	C24	1.323(3)		C36	C35	1.441(3)
O1	C9	1.337(3)		C36	C37	1.404(3)
O5	C25	1.418(3)		C14	C9	1.409(3)
O6	C42	1.422(3)		C14	C13	1.412(3)
N8	C33	1.473(3)		C9	C10	1.407(3)
N8	C32	1.286(3)		C19	C20	1.413(3)
N2	C17	1.476(3)		C10	C11	1.384(3)
N2	C18	1.288(3)		C4	C3	1.381(3)
N5	C8	1.319(3)		C13	C12	1.375(4)
N5	C6	1.417(3)		C30	C29	1.371(4)
N4	C1	1.281(3)		C23	C22	1.384(3)
N4	C2	1.408(3)		C40	C39	1.381(3)
N7	C35	1.281(3)		C2	C3	1.401(3)
N7	C34	1.477(3)		C39	C38	1.387(4)
N3	C1	1.178(3)		C37	C38	1.375(4)
N1	C15	1.285(3)		C11	C12	1.389(4)
N1	C16	1.472(3)		C20	C21	1.363(4)
N6	C8	1.166(3)		C22	C21	1.398(4)
C41	C36	1.410(3)		C28	C27	1.375(3)
C41	C40	1.402(3)		C28	C29	1.390(4)

Table 41. Bond angles of $\{Mn(salen)(CH_3OH)\}_2$(μ-anti-N(cyano),N(amido)-DCNB)•CH_3CN **(8)**.

Atom	Atom	Atom	Angle/°		Atom	Atom	Atom	Angle/°
O2	Mn1	O1	95.76(7)		O3	C26	C31	122.8(2)
O2	Mn1	O5	89.18(7)		O3	C26	C27	118.7(2)
O2	Mn1	N2	91.68(7)		C27	C26	C31	118.4(2)
O2	Mn1	N3	94.41(7)		N2	C17	C16	106.57(18)
O2	Mn1	N1	173.06(7)		C4	C5	C6	119.3(2)
O1	Mn1	O5	86.70(6)		N2	C18	C19	124.7(2)
O1	Mn1	N2	170.78(7)		O2	C24	C19	123.6(2)
O1	Mn1	N3	91.06(7)		O2	C24	C23	118.3(2)
O1	Mn1	N1	90.43(7)		C23	C24	C19	118.1(2)
N2	Mn1	O5	87.97(7)		N8	C33	C34	106.17(18)
N2	Mn1	N3	93.80(7)		N6	C8	N5	176.0(2)
N2	Mn1	N1	81.87(8)		N8	C32	C31	124.4(2)
N3	Mn1	O5	175.94(7)		C5	C6	N5	118.6(2)
N1	Mn1	O5	88.03(7)		C7	C6	N5	122.6(2)
N1	Mn1	N3	88.60(7)		C7	C6	C5	118.8(2)
O4	Mn2	O6	90.08(6)		C26	C31	C32	123.0(2)
O4	Mn2	N8	172.30(7)		C30	C31	C26	119.2(2)
O4	Mn2	N5	95.07(7)		C30	C31	C32	117.7(2)
O4	Mn2	N7	90.99(7)		N1	C15	C14	125.5(2)
O3	Mn2	O4	94.46(7)		C2	C7	C6	121.9(2)
O3	Mn2	O6	90.15(7)		C41	C36	C35	123.6(2)
O3	Mn2	N8	91.84(7)		C37	C36	C41	119.1(2)
O3	Mn2	N5	95.68(7)		C37	C36	C35	117.2(2)
O3	Mn2	N7	171.57(8)		N1	C16	C17	107.33(18)
N8	Mn2	O6	85.49(7)		C9	C14	C15	123.1(2)
N8	Mn2	N5	88.69(7)		C9	C14	C13	119.1(2)
N8	Mn2	N7	82.26(8)		C13	C14	C15	117.8(2)
N5	Mn2	O6	171.89(7)		O1	C9	C14	122.8(2)
N7	Mn2	O6	83.41(7)		O1	C9	C10	118.2(2)
N7	Mn2	N5	90.22(7)		C10	C9	C14	118.9(2)
C41	O4	Mn2	129.49(14)		C24	C19	C18	122.9(2)
C26	O3	Mn2	125.91(14)		C24	C19	C20	119.5(2)
C24	O2	Mn1	127.68(15)		C20	C19	C18	117.6(2)
C9	O1	Mn1	125.90(14)		N7	C35	C36	125.4(2)
C25	O5	Mn1	134.56(15)		C11	C10	C9	120.5(2)
C42	O6	Mn2	134.76(15)		C3	C4	C5	121.8(2)
C33	N8	Mn2	112.96(14)		N7	C34	C33	108.51(18)
C32	N8	Mn2	125.82(16)		C12	C13	C14	121.2(2)
C32	N8	C33	121.21(19)		C29	C30	C31	121.1(2)
C17	N2	Mn1	113.33(14)		C22	C23	C24	121.0(2)
C18	N2	Mn1	125.64(16)		C39	C40	C41	120.3(2)
C18	N2	C17	121.03(19)		C7	C2	N4	117.2(2)
C8	N5	Mn2	111.35(14)		C7	C2	C3	118.8(2)
C8	N5	C6	115.21(18)		C3	C2	N4	123.9(2)
C6	N5	Mn2	122.90(14)		C40	C39	C38	121.5(2)
C1	N4	C2	118.36(19)		C38	C37	C36	121.7(2)
C35	N7	Mn2	126.66(16)		C10	C11	C12	120.9(2)
C35	N7	C34	120.4(2)		C21	C20	C19	121.4(2)
C34	N7	Mn2	112.90(14)		C13	C12	C11	119.5(2)

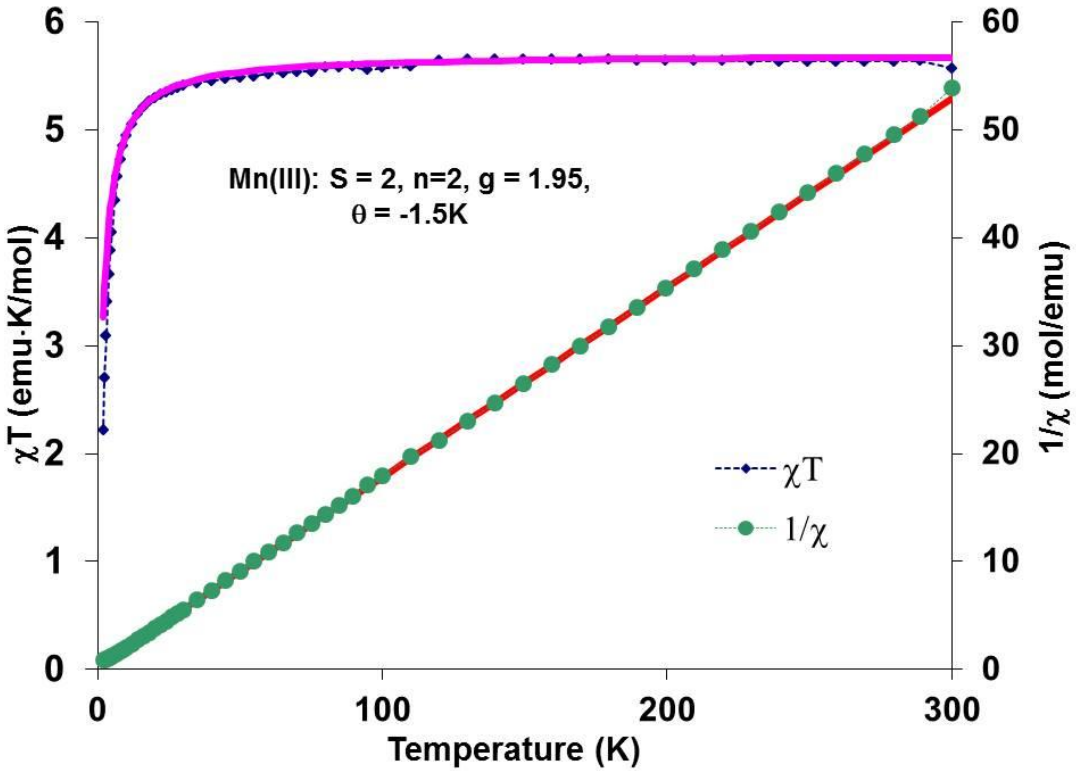

Figure 106. Temperature dependence of the χT and 1/χ data for {Mn(salen)(CH_3OH)}$_2$(μ-anti-N(cyano),N(amido)-DCNB)•CH_3CN **(8)** showing both the experimental data (blue and green dotted lines) and fitting result according to the Curie-Weiss law (pink and red lines).

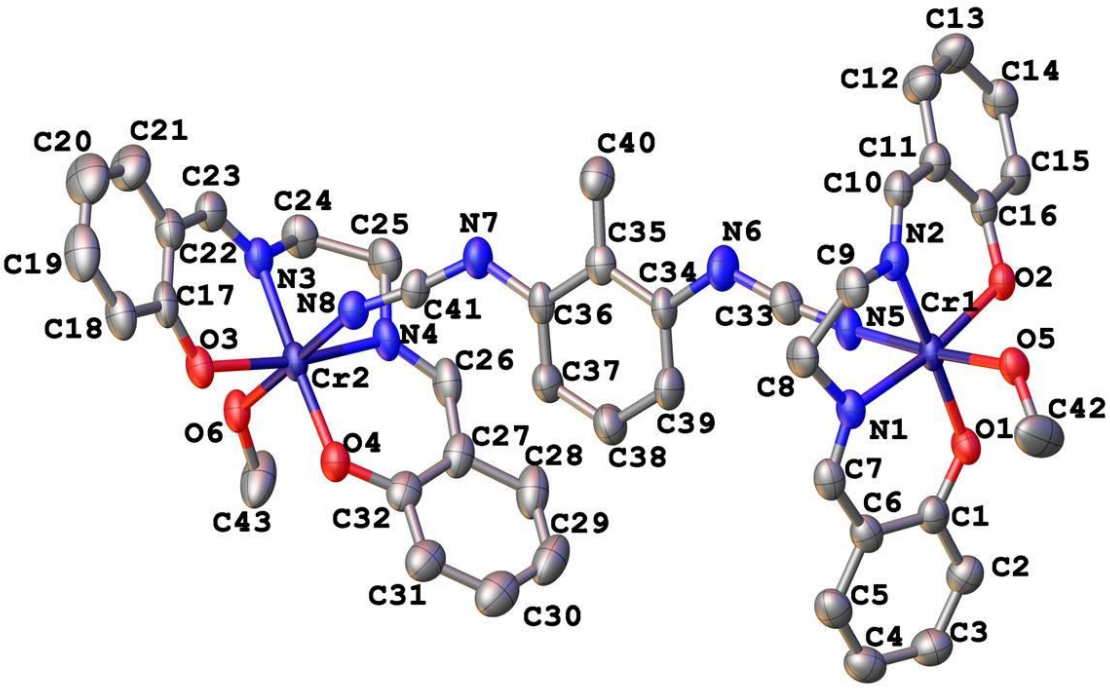

Figure 107. Asymmetric unit of the crystal structure of {Cr(salen)(CH_3OH)}$_2$(μ-Me-DCNB) •CH_3CN•CH_3OH (**9**). Thermal ellipsoids are drawn at the 50% probability level. Hydrogen atoms and free solvent molecules are omitted for the sake of clarity.

Due to the flexibility of the $DCNB^{2-}$ ligand, in order to force of the conformation to syn-$DCNB^{2-}$ (which was used in the theoretical studies) it is necessary to install a substituent group such as methyl group. Another issue that needs to be considered, as mentioned above, is the Jahn-Teller elongation along the axial position of Mn(III). Therefore, in this case, Cr(III) and Me-$DCNB^{2-}$ were prepared to take into account of both the steric and electronic factors. The reaction of $[Cr(salen)(H_2O)_2]ClO_4$ with $[Ph_4As]_2$[Me-DCNB] resulted in yellow brown crystals of $\{Cr(salen)(CH_3OH)\}_2$(μ-Me-DCNB) $\bullet CH_3CN \bullet CH_3OH$ (**9**). The produce crystallizes in the orthorhombic Pbca space group with the asymmetric unit being composed of one Me-$DCNB^{2-}$ anion and one $[Cr(salen)(CH_3OH)]^+$ cation. Although the Cr-N bond distances (Cr1-N5 = 1.974(4) Å and Cr2-N8 = 1.984(4) Å) are significantly shorter than the Mn-N bond distances in compounds **6**-**8** (Mn1-N3 = 2.243(3) Å in compound **6**, Mn1-N3 = 2.1786(15) Å in compound **7**, Mn1-N3 = 2.1753(19) and Mn2-N5 = 2.2602(19) Å in compound **8**), presumably due to the absence of Jahn-Teller elongation of the axial positions, the magnetic coupling did not show a big difference. Only weak antiferromagnetic interactions were observed in $\{Cr(salen)(CH_3OH)\}_2$(μ-Me-DCNB)$\bullet CH_3CN \bullet CH_3OH$ with a Weiss constant of -1.8 cm^{-1} (Figure 108) in contrast to the calculated strong ferromagnetic interactions.

Table 42. Bond distances of {Cr(salen)(CH_3OH)}$_2$(μ-Me-DCNB) •CH_3CN•CH_3OH (**9**).

Atom	Atom	Length/Å		Atom	Atom	Length/Å
Cr1	O1	1.909(3)		C4	C5	1.370(7)
Cr1	O2	1.954(3)		C5	C6	1.415(6)
Cr1	N5	1.974(4)		C6	C7	1.440(6)
Cr1	N1	2.003(3)		C8	C9	1.530(6)
Cr1	N2	2.015(4)		C10	C11	1.439(6)
Cr1	O5	2.024(3)		C11	C12	1.402(6)
Cr2	O4	1.912(3)		C11	C16	1.419(6)
Cr2	O3	1.961(3)		C12	C13	1.381(6)
Cr2	N8	1.984(4)		C13	C14	1.386(7)
Cr2	N4	2.009(3)		C14	C15	1.365(6)
Cr2	N3	2.014(4)		C15	C16	1.396(6)
Cr2	O6	2.025(3)		C17	C22	1.400(7)
N1	C7	1.277(6)		C17	C18	1.412(6)
N1	C8	1.480(5)		C18	C19	1.386(7)
N2	C10	1.272(5)		C19	C20	1.369(9)
N2	C9	1.481(5)		C20	C21	1.375(8)
N3	C23	1.272(6)		C21	C22	1.406(7)
N3	C24	1.480(5)		C22	C23	1.450(6)
N4	C26	1.290(6)		C24	C25	1.519(7)
N4	C25	1.472(6)		C26	C27	1.417(7)
N5	C33	1.182(6)		C27	C28	1.424(6)
N6	C33	1.278(6)		C27	C32	1.431(6)
N6	C34	1.416(5)		C28	C29	1.388(8)
N7	C41	1.268(5)		C29	C30	1.382(8)
N7	C36	1.415(5)		C30	C31	1.369(7)
N8	C41	1.178(5)		C31	C32	1.405(7)
O1	C1	1.308(5)		C34	C39	1.389(6)
O2	C16	1.337(5)		C34	C35	1.402(6)
O3	C17	1.342(5)		C35	C36	1.401(6)
O4	C32	1.310(5)		C35	C40	1.497(6)
O5	C42	1.416(6)		C36	C37	1.392(6)
O6	C43	1.432(6)		C37	C38	1.371(6)
C1	C2	1.413(6)		C38	C39	1.399(6)
C1	C6	1.428(6)		C1S	N1S	1.151(10)
C2	C3	1.371(7)		C1S	C2S	1.445(10)
C3	C4	1.391(7)		O1S	C3S	1.355(12)

Table 43. Bond angles of {Cr(salen)(CH_3OH)}$_2$(μ-Me-DCNB) •CH_3CN•CH_3OH (**9**).

Atom	Atom	Atom	Angle/°		Atom	Atom	Atom	Angle/°
O1	Cr1	O2	97.14(12)		C4	C5	C6	121.3(5)
O1	Cr1	N5	96.04(15)		C5	C6	C1	119.6(4)
O2	Cr1	N5	90.06(13)		C5	C6	C7	117.0(4)
O1	Cr1	N1	91.78(14)		C1	C6	C7	123.4(4)
O2	Cr1	N1	170.84(14)		N1	C7	C6	125.4(4)
N5	Cr1	N1	86.91(14)		N1	C8	C9	108.2(3)
O1	Cr1	N2	172.55(13)		N2	C9	C8	106.5(3)
O2	Cr1	N2	88.82(13)		N2	C10	C11	123.6(4)
N5	Cr1	N2	88.40(15)		C12	C11	C16	118.0(4)
N1	Cr1	N2	82.46(14)		C12	C11	C10	117.7(4)
O1	Cr1	O5	89.33(12)		C16	C11	C10	124.3(4)
O2	Cr1	O5	88.86(11)		C13	C12	C11	121.9(5)
N5	Cr1	O5	174.62(15)		C12	C13	C14	119.1(5)
N1	Cr1	O5	93.36(13)		C15	C14	C13	120.7(4)
N2	Cr1	O5	86.31(13)		C14	C15	C16	121.3(4)
O4	Cr2	O3	97.22(13)		O2	C16	C15	119.2(4)
O4	Cr2	N8	92.44(14)		O2	C16	C11	121.8(4)
O3	Cr2	N8	92.25(13)		C15	C16	C11	119.0(4)
O4	Cr2	N4	91.79(14)		O3	C17	C22	123.7(4)
O3	Cr2	N4	170.97(15)		O3	C17	C18	117.7(5)
N8	Cr2	N4	87.98(14)		C22	C17	C18	118.6(4)
O4	Cr2	N3	172.67(13)		C19	C18	C17	119.6(5)
O3	Cr2	N3	88.74(14)		C20	C19	C18	121.8(5)
N8	Cr2	N3	91.58(15)		C19	C20	C21	119.3(6)
N4	Cr2	N3	82.23(15)		C20	C21	C22	120.8(6)
O4	Cr2	O6	88.85(13)		C17	C22	C21	119.8(5)
O3	Cr2	O6	88.97(11)		C17	C22	C23	124.0(4)
N8	Cr2	O6	178.10(14)		C21	C22	C23	116.2(5)
N4	Cr2	O6	90.58(13)		N3	C23	C22	122.7(5)
N3	Cr2	O6	86.99(14)		N3	C24	C25	106.5(4)
C7	N1	C8	119.8(4)		N4	C25	C24	108.5(4)
C7	N1	Cr1	125.6(3)		N4	C26	C27	125.6(4)
C8	N1	Cr1	113.1(3)		C26	C27	C28	116.8(5)
C10	N2	C9	121.8(4)		C26	C27	C32	124.4(4)
C10	N2	Cr1	126.4(3)		C28	C27	C32	118.6(5)
C9	N2	Cr1	111.5(3)		C29	C28	C27	120.2(5)
C23	N3	C24	120.8(4)		C30	C29	C28	120.5(5)
C23	N3	Cr2	127.2(3)		C31	C30	C29	120.5(6)
C24	N3	Cr2	111.7(3)		C30	C31	C32	121.6(5)

Table 43. Continued.

Atom	Atom	Atom	Angle/°		Atom	Atom	Atom	Angle/°
C26	N4	Cr2	125.3(3)		O4	C32	C27	123.1(4)
C26	N4	C25	121.1(4)		O4	C32	C31	118.5(4)
C25	N4	Cr2	112.7(3)		C31	C32	C27	118.5(4)
C33	N5	Cr1	149.7(3)		N5	C33	N6	173.4(5)
C33	N6	C34	119.0(4)		C39	C34	C35	121.9(4)
C41	N7	C36	121.5(4)		C39	C34	N6	121.2(4)
C41	N8	Cr2	144.0(3)		C35	C34	N6	116.9(4)
C1	O1	Cr1	128.7(3)		C34	C35	C36	118.0(4)
C16	O2	Cr1	123.8(2)		C34	C35	C40	121.2(4)
C17	O3	Cr2	123.0(3)		C36	C35	C40	120.8(4)
C32	O4	Cr2	129.0(3)		C37	C36	C35	120.3(4)
C42	O5	Cr1	128.4(3)		C37	C36	N7	122.9(4)
C43	O6	Cr2	127.5(3)		C35	C36	N7	116.8(4)
O1	C1	C2	119.2(4)		C38	C37	C36	120.7(4)
O1	C1	C6	123.9(4)		C37	C38	C39	120.6(5)
C2	C1	C6	116.9(4)		C34	C39	C38	118.6(4)
C3	C2	C1	121.9(5)		N8	C41	N7	172.7(5)
C2	C3	C4	121.0(5)		N1S	C1S	C2S	174.1(9)
C5	C4	C3	119.2(5)					

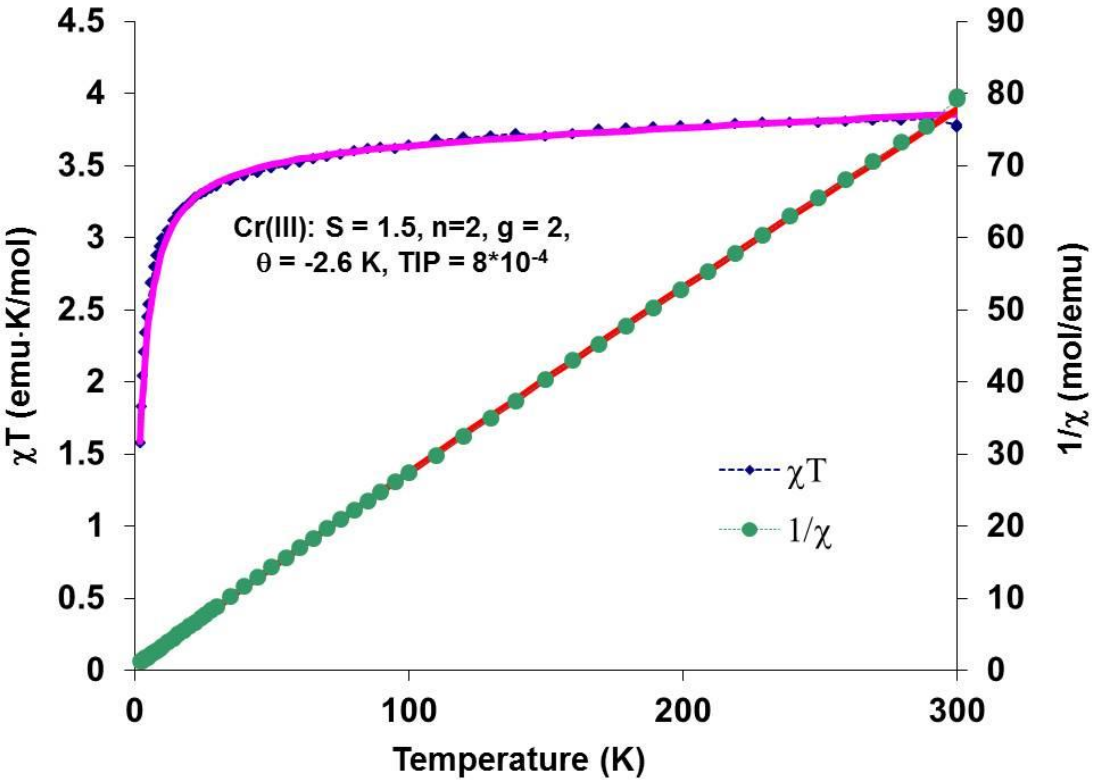

Figure 108. Temperature dependence of the χT and $1/\chi$ of $\{Cr(salen)(CH_3OH)\}_2(\mu\text{-Me-DCNB}) \bullet CH_3CN \bullet CH_3OH$ (**9**) showing both the experimental data (blue and green dotted lines) and fitting result according to the Curie-Weiss law (pink and red lines).

Self-assembled polymeric architectures

One can logically expect that, by substituting the axial water molecules of the metal-organic macrocyclic complex $[Mn(dpop)(H_2O)_2]Cl_2$ with dianionic bridging ligands such as $TCNQ^{2-}$, $DCNQI^{2-}$ and $DCNB^{2-}$, neutral 1-D chain-like coordination polymers can be formed. Indeed, the reaction between $[Mn(dpop)(H_2O)_2]Cl_2 \bullet 4H_2O$ and deprotonated H_2TCNQ produces orange plate-like crystals of compound **1**. A single crystal X-ray crystallographic study revealed that the $TCNQ^{2-}$ ligand serves as a μ_2-bridge in which only two anti-CN groups of the four cyano groups of TCNQ dianions are coordinated to the axial positions of the macrocycles to form a 1-D zigzag chain-like structure (Figure 3 top). These chains pack in the crystal structure by establishing π-π stacking interactions between the pyridyl groups of the dpop ligands (Figure S2) to form one dimensional channels along the crystallographic *a* axis which are occupied by solvent molecules (Figure 3, bottom).

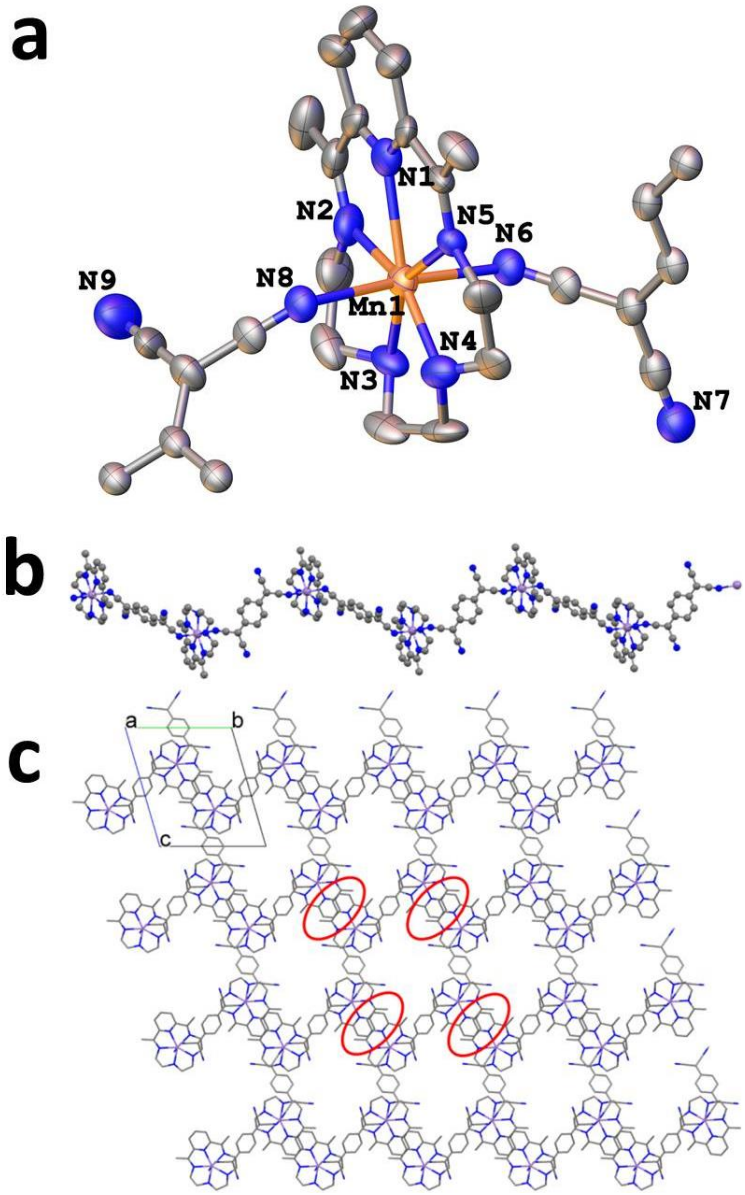

Figure 109. The asymmetric unit of the crystal structure of **1** (a). The zigzag chain-like structure of **1** (b) and the packing diagram viewed along the *a* axis (c). The π-π stacking interactions between the pyridyl groups of the dpop ligands are indicated by the red circles. The disordered species, hydrogen atoms and free solvent molecules are omitted for the sake of clarity.

Table 44. Bond Lengths of compound **1**.

Atom	Atom	Length/Å		Atom	Atom	Length/Å
Mn1	N6	2.276(4)		N8	C22	1.169(16)
Mn1	N5	2.31(3)		C22	C23	1.47(2)
Mn1	N4	2.21(4)		C27	C25	1.38(3)
Mn1	N1	2.30(2)		C27	C25[2]	2.00(3)
Mn1	N3	2.23(2)		C27	C26[2]	0.96(3)
Mn1	N2	2.306(15)		C25	C27[2]	2.00(3)
Mn1	N8	2.331(11)		C25	C23	1.40(2)
Mn1	N8A	2.236(11)		C25	C26	1.46(2)
Mn1	N1A	2.163(17)		C23	C24	1.31(2)
Mn1	N4A	2.39(4)		C26	C27[2]	0.96(3)
Mn1	N5A	2.25(3)		C24	N9	1.23(2)
Mn1	N2A	2.312(14)		N8A	C22A	1.140(15)
N6	C16	1.158(6)		C22A	C23A	1.32(2)
N5	C6	1.27(3)		C23A	C24A	1.46(2)
N5	C8	1.46(2)		C23A	C25A	1.43(2)
N4	C9	1.60(4)		C24A	N9A	1.139(19)
N4	C10	1.50(3)		C26A	C25A	1.41(2)
N7	C18	1.145(6)		C26A	C27A[2]	1.89(3)
C21	C19[1]	1.397(6)		C25A	C27A	1.44(3)
C21	C20	1.378(6)		C27A	C26A[2]	1.89(3)
N1	C5	1.34(2)		N1A	C5A	1.30(2)
N1	C1	1.33(2)		N1A	C1A	1.27(2)
C16	C17	1.384(7)		C5A	C4A	1.45(2)
C17	C19	1.472(6)		C5A	C6A	1.53(3)
C17	C18	1.407(7)		C4A	C3A	1.20(3)
C19	C21[1]	1.396(6)		C3A	C2A	1.40(3)
C19	C20	1.418(6)		C2A	C1A	1.44(2)
N3	C11	1.37(3)		C1A	C14A	1.46(2)
N3	C12	1.50(3)		C14A	C15A	1.56(2)
C6	C5	1.51(2)		C14A	N2A	1.30(2)
C6	C7	1.52(2)		C13A	C12A	1.50(2)
C5	C4	1.460(18)		C13A	N2A	1.44(2)
N2	C13	1.46(2)		C12A	N3A	1.52(2)
N2	C14	1.35(2)		N3A	C11A	1.442(18)
C8	C9	1.569(18)		C11A	C10A	1.51(3)
C10	C11	1.55(3)		C10A	N4A	1.49(3)
C13	C12	1.48(3)		N4A	C9A	1.41(3)
C2	C1	1.52(3)		C9A	C8A	1.58(2)
C2	C3	1.41(3)		C8A	N5A	1.42(3)
C1	C14	1.43(2)		C7A	C6A	1.52(2)
C14	C15	1.49(2)		C6A	N5A	1.28(2)
C4	C3	1.36(2)				

A similar compound, namely Mn(dpop)(μ-DCNQI)•nSol, was obtained by using H_2DCNQI instead of H_2TCNQ. Single crystal X-ray crystallography revealed that the product is composed of zigzag chains of Mn(dpop)(μ-DCNQI) • n Solvent (Figure 4). These chains pack with the aid of hydrogen bonding interactions between the amido-nitrogen atoms of the $DCNQI^{2-}$ ligand and solvent methanol molecules as well as by π-stacking interactions of the pyridyl rings (inter-plane distance of about 3.523(8) Å) of the dpop ligands. The result is the formation of one-dimensional channels along the *a* axis which are occupied by solvent molecules of methanol and water.

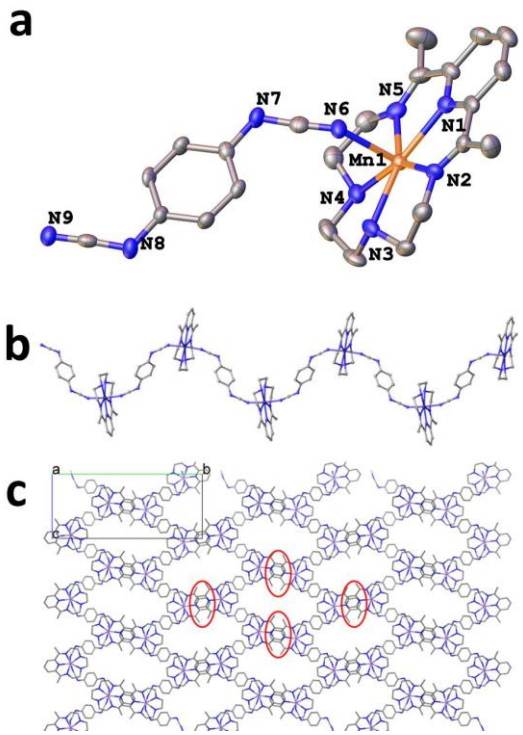

Figure 110. The asymmetric unit of the crystal structure of **2** (a). The zigzag chain structure of **2** (top) and its packing diagram viewed along the *a* axis (bottom). The π-π stacking interactions between the pyridyl groups of the dpop ligands are indicated by red circles. Hydrogen atoms and free solvent molecules are omitted for the sake of clarity.

Table 45. Bond Lengths of **2**.

Atom	Atom	Length/Å		Atom	Atom	Length/Å
Mn1	N1	2.236(3)		N8	C23	1.301(6)
Mn1	N2	2.299(4)		N9	Mn1[2]	2.224(4)
Mn1	N3	2.330(3)		N9	C23	1.176(5)
Mn1	N4	2.319(4)		C1	C2	1.385(6)
Mn1	N5	2.303(4)		C1	C14	1.504(6)
Mn1	N6	2.232(4)		C2	C3	1.373(6)
Mn1	N9[1]	2.224(4)		C3	C4	1.380(6)
N1	C1	1.343(5)		C4	C5	1.389(6)
N1	C5	1.349(5)		C5	C6	1.501(6)
N2	C6	1.263(5)		C6	C7	1.505(6)
N2	C8	1.462(5)		C8	C9	1.514(6)
N3	C9	1.479(5)		C10	C11	1.519(6)
N3	C10	1.475(5)		C12	C13	1.521(6)
N4	C11	1.474(5)		C14	C15	1.498(6)
N4	C12	1.464(5)		C17	C18	1.389(5)
N5	C13	1.467(5)		C17	C22	1.397(5)
N5	C14	1.268(5)		C18	C19	1.387(6)
N6	C16	1.190(5)		C19	C20	1.387(5)
N7	C16	1.295(6)		C20	C21	1.391(5)
N7	C17	1.417(5)		C21	C22	1.386(6)
N8	C20	1.410(5)				

[1]1+X,3/2-Y,-1/2+Z; [2]-1+X,3/2-Y,1/2+Z

The $DCNB^{2-}$ anions assemble with the Mn(II) macrocyclic building blocks to yield $\{Mn(dpop)\}_5(\mu\text{-}syn\text{-}DCNB)_{3-\delta}(\mu\text{-}anti\text{-}DCNB)_{2+\delta}\cdot n$ Solvent ($\delta \approx 0.1$), an unprecedented example of an inorganic quadruple helix with an incommensurately modulated structure (Figure 5). In this reaction, $[Mn(dpop)(H_2O)_2]Cl_2\bullet 4H_2O$ and $[Ph_4As]_2(DCNB)$ were combined in a mixture of acetonitrile and methanol to produce orange needle-like crystals of compound **3**. The flexibility of the $DCNB^{2-}$ anion allows it to exist in *anti* or *syn* conformations which leads to the formation of a helical chain-like structure as evidenced by single crystal X-ray diffraction studies (Figure 5). Five of the

bridging $DCNB^{2-}$ ligands serve as a repeat unit which then follows a pattern of *SASSA-SASSA (A = anti*-$DCNB^{2-}$, *S = syn*-$DCNB^{2-}$*).* Four of the symmetry-related helical chains further organize into a quadruple helix, which is then tethered into a three-dimensional structure by π-stacking interactions between the pyridyl groups of the dpop ligands (Figure 6). Two types of 1-D channels are formed along the *c* axis, with the smaller one formed inside the quadruple helix and the larger one formed by the packing of these quadruple helical tubes through the π-stacking interaction of the pyridyl groups of the dpop ligands. It is also noted that the adjacent quadruple helices possess opposite chirality due to the symmetry (Figure 5, bottom right). The packing of helical chains through π-stacking of pyridyl groups leads to 1-D nanochannels that are filled with solvent molecules which occupy approximately 38.6% of the unit cell volume (calculated using the SQUEEZE option in PLATON).[239]

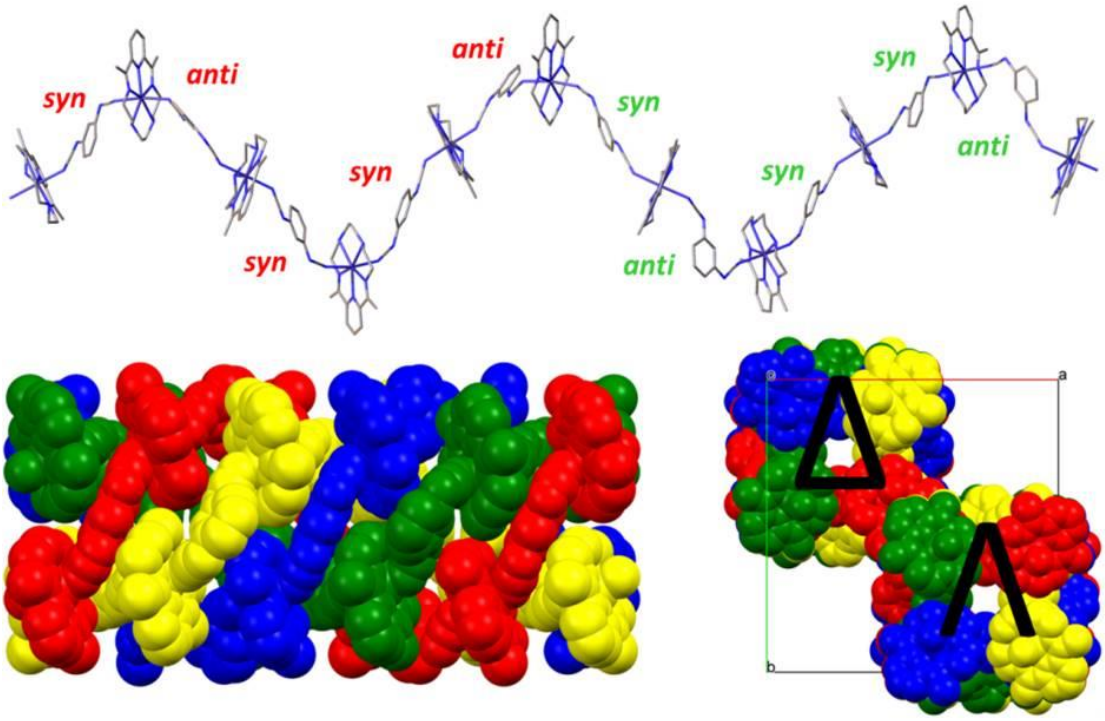

Figure 111. Top: 1-D neutral chain of [{Mn(dpop)}$_5$(μ-syn-DCNB)$_3$(μ-anti-DCNB)$_2$]n showing the repeat units for different conformers of $(DCNB)^{2-}$ in the chain with a pattern of SASSA-SASSA (S = *syn*, A = *anti*). Bottom left: four chains forming a quadruple helical tube with each color corresponding to one chain. Bottom right: two tubes connected by π-stacking of the pyridyl rings of the dpop ligands.

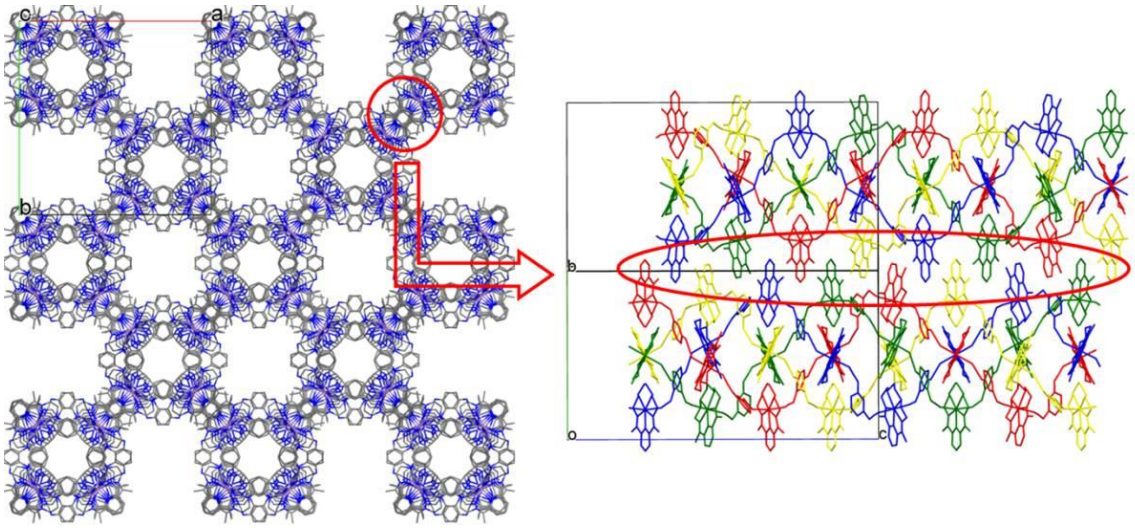

Figure 112. Packing diagram of **3** illustrating the alternating large and small channels viewed along the *c* axis (left) and side view of the channels highlighting the π-stacking interactions between the pyridyl groups of the dpop ligands (right).

The structure of compound **3** is incommensurately modulated, but the modulation vector q = 0.41065(6)**c*** is close to a commensurate value of 2/5c*. Therefore, a supercell approximate to the incommensurate structure may be constructed which has a high symmetry space group *P4/nnc* with a *c* parameter five times that of the basic structure. One of the five positions of $Mn(dpop)^{2+}$ is disordered in the supercell due to the high symmetry of the approximation in the supercell. Apart from this artifact, the supercell model captures most of the important features of the structure.

It is interesting to note that, in the presence of water, 1-D zigzag chains of compound **4** instead of the helical chains in compound **3** is produced from the same starting materials. Compound **4** crystallizes in the monoclinic space group $P2_1/c$ with the asymmetric unit consisting of one $[Mn(dpop)]^{2+}$ macrocycle, one *anti*-$DCNB^{2-}$ bridging ligand and one uncoordinated water molecule (Figure 7). Only the *anti*- conformation of $DCNB^{2-}$ is present in the structure of **4**, while both the *anti*- and *syn*- conformations are

present in compound **3** when the quadruple helical tubes are formed. This structural difference is ascribed to the role that the water molecules play, because the hydrogen bonding interactions between the water molecules and the cyano-N atoms dominate which leads to the stabilization of zigzag chains with only one conformation of the $DCNB^{2-}$ bridging ligand (Figure 8). The distances between the donor and acceptor atoms of the hydrogen bonds are 2.937(5) and 2.972(5) Å for O1-H1···N1 and O1-H2···N2 with corresponding angles of 171(4) and 174(4)˚, respectively (Figure 8). These results indicate that the self-assembly of the flexible chain Mn(dpop)(μ-DCNB) can be controlled by using different crystallizing solvents. Also, by installing different substituents on the phenyl ring of $DCNB^{2-}$, it is possible to force the bridging ligands into specific conformations. A view of the packing of these zigzag chains along the *b* axis in the structure revealed that they form 2-D layers which are separated by layers of acetonitrile solvent molecules (Figure 9).

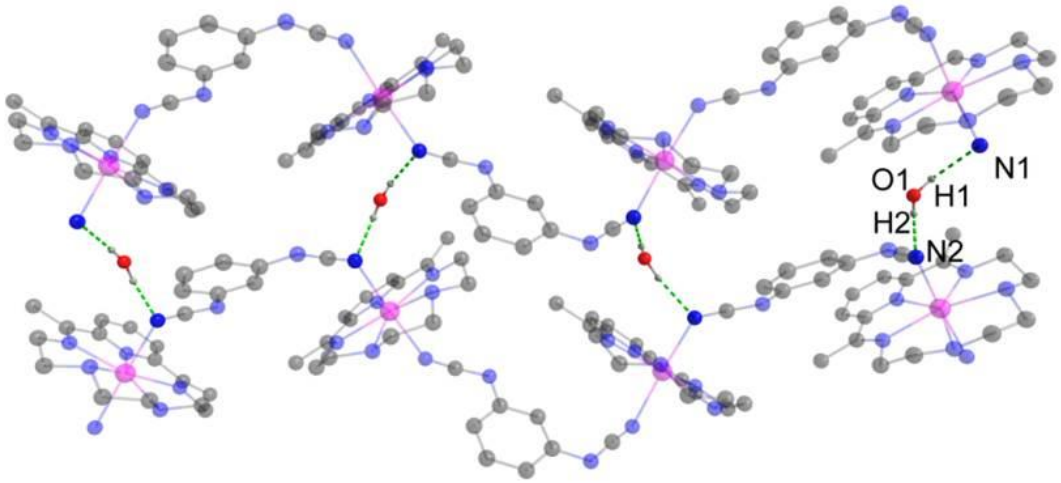

Figure 113. Zig-zag chains of Mn(dpop)(μ-*anti*-DCNB)•(H_2O)(CH_3CN) stitched together by water molecules through hydrogen bonding. The hydrogen bonds are depicted by green dotted lines.

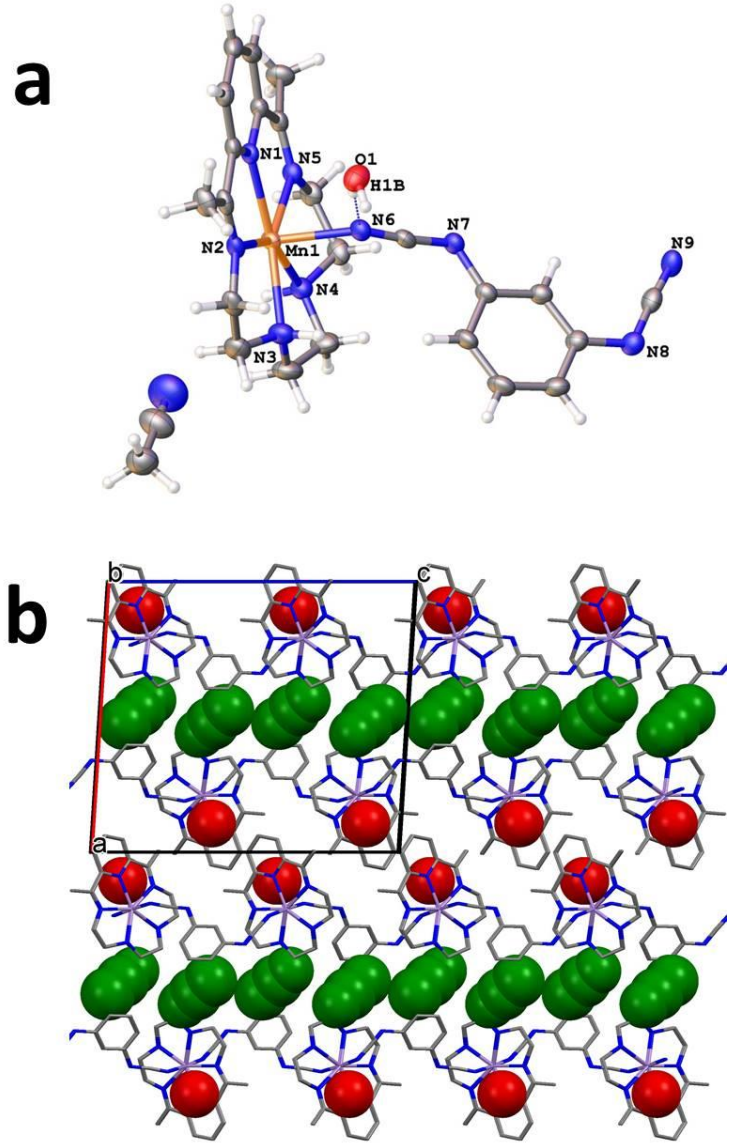

Figure 114. (a). Asymmetric unit of compound 4. Thermal ellipsoids are drawn at the 50% probability level. (b). Stacking diagram of compound **4** viewed along the *b* axis showing the layers of the chains of Mn(dpop)(μ-*anti*-DCNB)•(H_2O) segregated by acetonitrile molecules (green spheres in the space-filling model). Water molecules are represented by the red spheres in the space-filling model. Hydrogen atoms are omitted for the sake of clarity.

Table 46. Bond Lengths of **4**.

Atom	Atom	Length/Å		Atom	Atom	Length/Å
Mn1	N1	2.253(3)		N9	$Mn1^2$	2.275(3)
Mn1	N2	2.288(3)		N9	C23	1.168(5)
Mn1	N3	2.317(3)		C1	C2	1.390(5)
Mn1	N4	2.327(3)		C1	C14	1.501(5)
Mn1	N5	2.289(3)		C2	C3	1.393(5)
Mn1	N6	2.259(3)		C3	C4	1.382(6)
Mn1	$N9^1$	2.275(3)		C4	C5	1.393(5)
N1	C1	1.343(5)		C5	C6	1.495(5)
N1	C5	1.339(5)		C6	C7	1.498(5)
N2	C6	1.278(5)		C8	C9	1.513(6)
N2	C8	1.467(5)		C10	C11	1.501(6)
N3	C9	1.455(5)		C12	C13	1.525(6)
N3	C10	1.464(6)		C14	C15	1.495(5)
N4	C11	1.461(5)		C17	C18	1.393(5)
N4	C12	1.454(5)		C17	C22	1.387(5)
N5	C13	1.461(5)		C18	C19	1.384(6)
N5	C14	1.274(5)		C19	C20	1.392(6)
N6	C16	1.174(5)		C20	C21	1.396(5)
N7	C16	1.284(5)		C21	C22	1.401(5)
N7	C17	1.408(5)		N10	C24	1.165(7)
N8	C21	1.402(5)		C24	C25	1.401(7)
N8	C23	1.295(5)				

[1]+X,1/2-Y,-1/2+Z; [2]+X,1/2-Y,1/2+Z

The versatility in the bridging modes of $DCNB^{2-}$ for the formation of coordination polymers has been reported before in a series of chain-like compounds composed of cationic chains of $[\{Cu^{II}(tpy)\}_2(\mu\text{-DCNB})]^{2+}$ (tpy = 2,2';6',2''-terpyridine) with different counterions.[234,240] Each of the $Cu(tpy)^{2+}$ building units is connected to a cyano nitrogen atom from one $DCNB^{2-}$ and an imide nitrogen atom from another $(DCNB)^{2-}$ ligand, with all four nitrogen atoms of each $DCNB^{2-}$ shared by four different Cu(II) ions. This structure involves a square pyramidal Cu coordination geometry and a shortened pathway of -N-C-N- instead of the length of the entire anion for magnetic

superexchange between the paramagnetic Cu(II) centers. In the presence of small anions such as chloride, inter-chain interactions dominate and only antiferromagnetic interactions were observed. However, when larger anions were employed, inter-chain interactions are minimized and weak ferromagnetic behavior results. It is noted that, in the reported structures, only the *syn*- conformer of $DCNB^{-2}$ ligand is present.

The crystals of compound **3** transformed into crystals of a new mononuclear compound **5** when soaked in water for several days. The asymmetric unit of **5** consists of one $[Mn(dpop)(H_2O)]^{2+}$ cation, one $DCNB^{2-}$ as a monodentate ligand and two water molecules. Only one of the axial positions of the Mn(II) coordination sphere is occupied by the $DCNB^{2-}$ anion, with the other one being coordinated to a water molecule. The distances between the donor and acceptor atoms of the hydrogen bonds are 2.781(5) and 2.814(4) Å for O1-H1B···O2 and O3-H3C···N8 with corresponding angles of 144(5) and 170.9(3)˚, respectively.

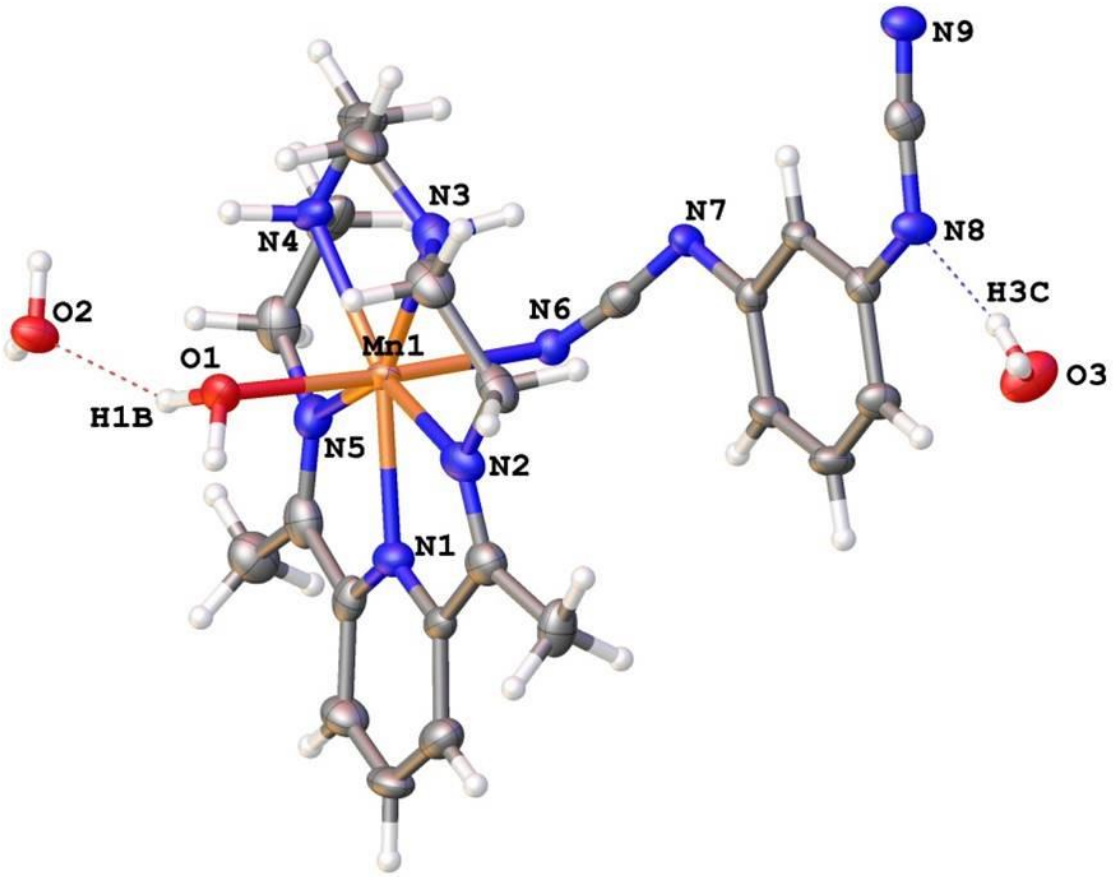

Figure 115. Asymmetric unit of compound **5**. Thermal ellipsoids are drawn at the 50% probability level. The aliphatic and aromatic hydrogen atoms have been omitted for the sake of clarity.

Table 47. Bond Lengths of **5**.

Atom	Atom	Length/Å		Atom	Atom	Length/Å
Mn1	O1	2.241(3)		N8	C21	1.395(4)
Mn1	N1	2.234(3)		N8	C23	1.311(5)
Mn1	N2	2.350(4)		N9	C23	1.189(5)
Mn1	N3	2.372(4)		C1	C2	1.429(6)
Mn1	N4	2.305(3)		C1	C14	1.489(6)
Mn1	N5	2.265(3)		C2	C3	1.352(6)
Mn1	N6	2.292(3)		C3	C4	1.400(6)
N1	C1	1.291(5)		C4	C5	1.397(5)
N1	C5	1.366(5)		C5	C6	1.476(5)
N2	C6	1.259(5)		C6	C7	1.515(6)
N2	C8	1.451(5)		C8	C9	1.494(6)
N3	C9	1.469(6)		C10	C11	1.502(7)
N3	C10	1.449(6)		C12	C13	1.529(6)
N4	C11	1.459(5)		C14	C15	1.474(6)
N4	C12	1.480(5)		C17	C18	1.401(5)
N5	C13	1.444(6)		C17	C22	1.391(5)
N5	C14	1.312(5)		C18	C19	1.386(5)
N6	C16	1.200(5)		C19	C20	1.381(5)
N7	C16	1.288(5)		C20	C21	1.409(5)
N7	C17	1.417(4)		C21	C22	1.402(5)

In conclusion, it has been found that a series of one-dimensional coordination polymers adopt distinct structures depending on the conformations of the bridging ligands, crystallization conditions and dominate weak supramolecular interactions. The flexible nature of the dianionic bridging ligand which can adopt a *syn*- or *anti*-conformation, led to the formation of supramolecular nano-tubular quadruple helices composed of helical chains of inorganic macrocycle building blocks through a self-assembly process. Further research efforts will be directed towards more fine control of the conformations of the *para*- and *meta*-dicyanamidobenzene dianions by introducing substituents on the phenyl rings and by using small chiral molecules to induce homo-chirality in the coordination polymers.

CHAPTER VI

SUMMARY AND OUTLOOK

Multifunctional molecular materials are of high interest because of the coexistence of two or more functionalities such as magnetism, electrical conductivity, ferroelectric and optical properties. In particular, organocyanides such as the prototypical tetracyanoquinodimethane (TCNQ) molecule have played an important role in the development of magnetic and conducting molecular materials. The radical anion form of TCNQ can serve as spin-carrying bridges to enhance magnetic exchange interactions between paramagnetic metal ions and/or form electrical conducting columnar stacks that allow for conduction electrons to travel over long distances. Therefore, coordination compounds with metal complexes and TCNQ are excellent candidates for combining magnetic properties with electrical conductivity. The goal of the research represented in this dissertation has been to synthesize new materials based on organocyanides and to study their structure-property relationships. These findings serve as yseful guidelines for the synthesis of molecular materials with enhanced properties that are promising for applications in electronic devices.

The overarching goal of pushing the frontier of multifunctional materials further towards the realization of synergistic interactions between different functionalities was approached by employing a modular synthetic approach to obtain hybrid inorganic-organic multifunctional materials. One of the well-studied systems is electrically conducting spin-crossover (SCO) complexes, most of which consist of Fe(II) SCO units

and metal dithiolate conducting units. In the current work, we chose a Co(II) SCO unit, which has a much less abrupt spin transition than the Fe(II) analogues, in order to minimize disruption to the stacking interactions of the TCNQ radicals. A facile modular synthetic approach was developed that does not require the previously reported electrochemical or self-redox reactions to realize partially reduced radicals. By taking advantage of the structural breathing features of the metal-organic cations in conjunction with the supramolecular π-stacking interactions of partially charged TCNQ radicals, an anomalous conducting behavior was achieved in the compound $[Co(terpy)_2](TCNQ)_3 \bullet CH_3CN$ which is composed of alternating semiconducting and spin-crossover layers. An anomalous conducting behavior occurs at 180-190 K that is directly correlated with the structural variation arising from the HS to LS transition of Co(II) followed by Jahn-Teller distortion of LS Co(II) and concomitant charge fluctuations of the partially charged TCNQ radicals. This modular synthetic procedure for the introduction of partially charged TCNQ radicals is highly promising for the synthesis of other bifunctional materials with electrical conducting properties.

In addition to the SCO units, other functional species such SMMs and photosensitizers such as $[Co(Tpm)_2]^{2+}$, $[Ru(terpy)_2]^{2+}$, $[Ru(bpy)_3]^{2+}$ and $[Zn(terpy)_2]^{2+}$can also be incorporated into electrically conducting bifunctional materials through a generalized approach by using the easily accessible TCNQ radical source of $[Et_3NH](TCNQ)_2$. The hybrid conducting SMM $[Co(Tpm)_2](TCNQ)_3$ retains slow relaxation of the magnetization of the cationic unit and represents a good start for the study of interactions between the SMM units and conducting units in future work. The

hybrid conducting photosensitizers will be nice examples for the study of the effect of photoirradiation on the electrical conducting properties.

By using a similar method, a series of isostructural chai-like compounds [Ln(TPMA)(μ-TCNQ)(μ-OH)](TCNQ)$_2$ CH_3CN (Ln = Dy, Gd, Y) with mixed-valence TCNQ species have been synthesized. Magnetic and electrical conductivity studies revealed that the Dy(III) compound exhibited slow relaxation of the magnetization at 5.0-8.2 K and semiconductivity at 180-350 K. DC magnetic fields have been found to not only suppress the quantum tunneling of the magnetization, but also affect the spin-canted antiferromagnetic interactions in [Dy(TPMA)(μ-TCNQ)(μ-OH)](TCNQ)$_2$ CH_3CN. In addition, the increased DC magnetic field has been found to diminish the TIP and the delocalization of electrons in the TCNQ stacks. Future work will concentrate on employing other TCNQ derivatives in order to get higher electrical conductivity in the TCNQ radical stacks and studying the effect of electric field on the magnetic properties of these bifunctional materials.

Magnetic metal-organic frameworks (MOFs) are promising for applications in low density data storage, small molecule recognition and sensors. The redox-active TCNQ dianion can be employed as a substitute for carboxylate anions in MOF frameworks that may exhibit interesting interactions between the host framework and guest molecules. It has been found that aromatic guest molecules such as benzene, toluene, aniline and nitrobenzene can induce distinct magnetic ordering in the family of magnetic MOFs Fe(TCNQ)(4,4'-bpy)⊃guest which were structurally characterized by single crystal X-ray studies. In the case of nitrobenzene, close contacts between the

electron accepting nitrobenzene and the electron donating TCNQ dianion in the frameworks constitute structural evidence for charge-transfer interactions. Other aromatic guests did not show such a close contact but the Fe-TCNQ network was found to be more planar, with the phenyl rings of the guests situated vertical to the Fe-TCNQ 2-D networks. Magnetic characterization revealed magnetic phase transitions from a paramagnetic state with antiferromagnetic interactions to a spin-canted state at 3-5 K. In addition, the guest-dependent long-range magnetic ordering through the TCNQ dianions at low temperatures was correlated with the electron accepting ability and sterics of the included aromatic guests. Further oxidation of this series of metal-organic frameworks through post-synthetic modification is underway to prepare materials with stronger magnetic interactions mediated by the radical TCNQ spin-carrier as a bridge for the metal centers in the MOFs.

It has been found that a series of one-dimensional coordination polymers adopt distinct packing structures depending on the conformations of the bridging ligands, crystallization conditions and dominating weak supramolecular interactions. By taking advantage of the flexible nature of the dianionic bridging ligand which can adopt a *syn*- or *anti*- conformation in the structure, supramolecular nano-tubular quadruple helices composed of helical chains of inorganic macrocycle building blocks were achieved through a self-assembly process. Further research efforts will be directed towards the rational control of the conformations of the *para*- and *meta*-dicyanamidobenzene dianions by the choice of substituents on the phenyl rings and the use of small chiral molecules to induce homo-chirality in the coordination polymers.

Apart from the synthetic efforts to obtain SMMs with higher blocking temperatures by design strategies that consider both the spin and anisotropy contributions, the nanostructuring of SMMs and their interactions with other functional properties are of equal importance for the practicle applications of SMMs in spin valves, transistors, quantum information storage and quantum computing. Therefore, as a direction for future work, the organization of SMMs into ordered arrays of 1-D chains, 2-D sheets with layered structures, and the well-defined 3-D porous frameworks of MOFs will be of great interest, especially considering that one may take advantage of the interactions between the SMMs with other functionalities for the control of slow relaxation of the magnetization.[45,46] For example, in a synergistic system with alternating layers of SMMs and electrical conducting materials, it may be possible to address the SMM behaviors by measuring the electrical conductivity responses of the bifunctional material. By the incorporation of SMMs into a porous magnetic matrix, one may be able to control the SMM responses as the intrinsic magnetic field imparted by the magnetic matrix can induce exchange bias which is similar to what has been used in traditional magnetic data storage devices.

REFERENCES

1. Coronado, E.; Giménez-Saiz, C.; Martí-Gastaldo, C. In *Engineering of Crystalline Materials Properties*; Novoa, J., Braga, D., Addadi, L., Eds.; Springer Netherlands: 2008, p 173-191.
2. In *Multifunctional Conducting Molecular Materials*; saito, G., Wudl, F., Haddon, R. C., Tanigaki, K., Enoki, T., Katz, H. E., Maesato, M., Eds.; The Royal Society of Chemistry: 2006, p 105-150.
3. Coronado, E.; Forment-Aliaga, A.; Galán-Mascarós, J. R.; Giménez-Saiz, C.; Gómez-García, C. J.; Martinéz-Ferrero, E.; Nuez, A.; Romero, F. M. *Solid State Sci.* **2003**, *5*, 917-924.
4. Miller, J. S. *Adv. Mater.* **1990**, *2*, 98-99.
5. Coronado, E.; Galan-Mascaros, J. R.; Gomez-Garcia, C. J.; Laukhin, V. *Nature* **2000**, *408*, 447-449.
6. Vincent, R.; Klyatskaya, S.; Ruben, M.; Wernsdorfer, W.; Balestro, F. *Nature* **2012**, *488*, 357-360.
7. Sessoli, R.; Gatteschi, D.; Caneschi, A.; Novak, M. A. *Nature* **1993**, *365*, 141-143.
8. Sessoli, R. *Angew. Chem., Int. Ed.* **2012**, *51*, 43-45.
9. Weber, B. In *Spin-Crossover Materials*; John Wiley & Sons Ltd: 2013, p 55-76.
10. Prins, F.; Monrabal-Capilla, M.; Osorio, E. A.; Coronado, E.; van der Zant, H. S. J. *Adv. Mater.* **2011**, *23*, 1545-1549.

11. Létard, J.-F.; Guionneau, P.; Goux-Capes, L. In *Spin Crossover in Transition Metal Compounds III*; Springer Berlin Heidelberg: 2004; Vol. 235, p 221-249.

12. Garcia, Y.; Ksenofontov, V.; Mentior, S.; Dîrtu, M. M.; Gieck, C.; Bhatthacharjee, A.; Gütlich, P. *Chem.Eur. J.* **2008**, *14*, 3745-3758.

13. Létard, J.-F.; Guionneau, P.; Codjovi, E.; Lavastre, O.; Bravic, G.; Chasseau, D.; Kahn, O. *J. Am. Chem. Soc.* **1997**, *119*, 10861-10862.

14. Cotton, F. A.; Wilkinson, G.; Gaus, P. L. *Basic inorganic chemistry*; J. Wiley, 1995.

15. Real, J. A.; Gaspar, A. B.; Munoz, M. C. *Dalton Trans.* **2005**, 2062-2079.

16. Cambi, L.; Szegö, L. *Berichte der deutschen chemischen Gesellschaft (A and B Series)* **1931**, *64*, 2591-2598.

17. Halcrow, M. A. *Coord. Chem. Rev.* **2009**, *253*, 2493-2514.

18. Santoro, A.; Kershaw Cook, L. J.; Kulmaczewski, R.; Barrett, S. A.; Cespedes, O.; Halcrow, M. A. *Inorg Chem* **2015**, *54*, 682-693.

19. Hauser, A.; Jeftić, J.; Romstedt, H.; Hinek, R.; Spiering, H. *Coord. Chem. Rev.* **1999**, *190–192*, 471-491.

20. Gütlich, P.; Gaspar, A. B.; Garcia, Y. *Beilstein J. Org. Chem.* **2013**, *9*, 342-391.

21. Krivokapic, I.; Zerara, M.; Daku, M. L.; Vargas, A.; Enachescu, C.; Ambrus, C.; Tregenna-Piggott, P.; Amstutz, N.; Krausz, E.; Hauser, A. *Coord. Chem. Rev.* **2007**, *251*, 364-378.

22. Cowan, M. G.; Olguín, J.; Narayanaswamy, S.; Tallon, J. L.; Brooker, S. *J. Am. Chem. Soc.* **2012**, *134*, 2892-2894.

23. Goodwin, H. In *Spin Crossover in Transition Metal Compounds II*; Springer Berlin Heidelberg: 2004; Vol. 234, p 23-47.

24. Hogg, R.; Wilkins, R. G. *J. Chem. Soc.* **1962**, 341-350.

25. Kremer, S.; Henke, W.; Reinen, D. *Inorg. Chem.* **1982**, *21*, 3013-3022.

26. Oshio, H.; Spiering, H.; Ksenofontov, V.; Renz, F.; Gütlich, P. *Inorg. Chem.* **2001**, *40*, 1143-1150.

27. Judge, J. S.; Baker Jr, W. A. *Inorg. Chim. Acta* **1967**, *1*, 68-72.

28. Enachescu, C.; Krivokapic, I.; Zerara, M.; Real, J. A.; Amstutz, N.; Hauser, A. *Inorg. Chim. Acta* **2007**, *360*, 3945-3950.

29. Kilner, C. A.; Halcrow, M. A. *Dalton Trans.* **2010**, *39*, 9008-9012.

30. Gaspar, A. B.; Muñoz, M. C.; Niel, V.; Real, J. A. *Inorg. Chem.* **2001**, *40*, 9-10.

31. Galet, A.; Gaspar, A. B.; Muñoz, M. C.; Real, J. A. *Inorg. Chem.* **2006**, *45*, 4413-4422.

32. Hayami, S.; Shigeyoshi, Y.; Akita, M.; Inoue, K.; Kato, K.; Osaka, K.; Takata, M.; Kawajiri, R.; Mitani, T.; Maeda, Y. *Angew. Chem., Int. Ed.* **2005**, *44*, 4899-4903.

33. Nielsen, P.; Toftlund, H.; Bond, A. D.; Boas, J. F.; Pilbrow, J. R.; Hanson, G. R.; Noble, C.; Riley, M. J.; Neville, S. M.; Moubaraki, B.; Murray, K. S. *Inorg. Chem.* **2009**, *48*, 7033-7047.

34. Hayami, S.; Murata, K.; Urakami, D.; Kojima, Y.; Akita, M.; Inoue, K. *Chem Commun (Camb)* **2008**, 6510-6512.

35. Agusti, G.; Bartual, C.; Martinez, V.; Munoz-Lara, F. J.; Gaspar, A. B.; Munoz, M. C.; Real, J. A. *New J. Chem.* **2009**, *33*, 1262-1267.

36. Hayami, S. In *Spin-Crossover Materials*; John Wiley & Sons Ltd: 2013, p 321-345.

37. Bogani, L.; Wernsdorfer, W. *Nat Mater* **2008**, *7*, 179-186.

38. Barbara, B. *Philos. Trans. R. Soc., A* **2012**, *370*, 4487-4516.

39. Kent, A. D.; Yicheng, Z.; Bokacheva, L.; Ruiz, D.; Hendrickson, D. N.; Sarachik, M. P. *EPL (Europhysics Letters)* **2000**, *49*, 521.

40. Christou, G.; Gatteschi, D.; Hendrickson, D. N.; Sessoli, R. *MRS Bulletin* **2000**, *25*, 66-71.

41. Friedman, J. R.; Sarachik, M. P.; Tejada, J.; Ziolo, R. *Phys. Rev. Lett.* **1996**, *76*, 3830-3833.

42. Goswami, S.; Mondal, A. K.; Konar, S. *Inorg. Chem. Front.* **2015**, *2*, 687-712.

43. Pedersen, K. S.; Dreiser, J.; Weihe, H.; Sibille, R.; Johannesen, H. V.; Sørensen, M. A.; Nielsen, B. E.; Sigrist, M.; Mutka, H.; Rols, S.; Bendix, J.; Piligkos, S. *Inorg. Chem.* **2015**.

44. Thiele, S.; Vincent, R.; Holzmann, M.; Klyatskaya, S.; Ruben, M.; Balestro, F.; Wernsdorfer, W. *Phys. Rev. Lett.* **2013**, *111*, 037203.

45. Aulakh, D.; Pyser, J. B.; Zhang, X.; Yakovenko, A. A.; Dunbar, K. R.; Wriedt, M. *J Am Chem Soc* **2015**, *137*, 9254-9257.

46. Wang, Z. X.; Zhang, X.; Zhang, Y. Z.; Li, M. X.; Zhao, H.; Andruh, M.; Dunbar, K. R. *Angew Chem Int Ed Engl* **2014**, *53*, 11567-11570.

47. Dunbar, K. R. *Angew. Chem., Int. Ed.* **1996**, *35*, 1659-1661.

48. Clérac, R.; O'Kane, S.; Cowen, J.; Ouyang, X.; Heintz, R.; Zhao, H.; Bazile, M. J.; Dunbar, K. R. *Chem. Mater.* **2003**, *15*, 1840-1850.

49. Avendano, C.; Zhang, Z.; Ota, A.; Zhao, H.; Dunbar, K. R. *Angew Chem Int Ed Engl* **2011**, *50*, 6543-6547.

50. Mahajan, M.; Bhargava, S. K.; O'Mullane, A. P. *RSC Advances* **2013**.

51. Potember, R. S.; Poehler, T. O.; Cowan, D. O. *Appl. Phys. Lett.* **1979**, *34*, 405-407.

52. Ballesteros-Rivas, M.; Zhao, H.; Prosvirin, A.; Reinheimer, E. W.; Toscano, R. A.; Valdés-Martínez, J.; Dunbar, K. R. *Angew. Chem., Int. Ed.* **2012**, *51*, 5124-5128.

53. Lapidus, S. H.; McConnell, A. C.; Stephens, P. W.; Miller, J. S. *Chem. Commun.* **2011**, *47*, 7602-7604.

54. Abrahams, B. F.; Elliott, R. W.; Hudson, T. A.; Robson, R. *Cryst. Growth Des.* **2010**, *10*, 2860-2862.

55. Shimomura, S.; Kitagawa, S. *J. Mater. Chem.* **2011**, *21*, 5537-5546.

56. Manriquez, J. M.; Yee, G. T.; McLean, R. S.; Epstein, A. J.; Miller, J. S. *Science* **1991**, *252*, 1415-1417.

57. Aumüller, A.; Erk, P.; Klebe, G.; Hünig, S.; von Schütz, J. U.; Werner, H.-P. *Angew. Chem., Int. Ed.* **1986**, *25*, 740-741.

58. Anderson, P. W.; Lee, P. A.; Saitoh, M. *Solid State Commun.* **1973**, *13*, 595-598.

59. Mori, T.; Inokuchi, H. *Solid State Commun.* **1986**, *59*, 355-359.

60. Heintz, R. A.; Zhao, H.; Ouyang, X.; Grandinetti, G.; Cowen, J.; Dunbar, K. R. *Inorg. Chem.* **1999**, *38*, 144-156.

61. Zhang, Z.; Zhao, H.; Matsushita, M. M.; Awaga, K.; Dunbar, K. R. *J. Mater. Chem. C* **2014**, *2*, 399-404.

62. Zhang, X.; Zhang, Z.; Zhao, H.; Mao, J. G.; Dunbar, K. R. *Chem Commun (Camb)* **2014**, *50*, 1429-1431.

63. Zhang, Z.; Zhao, H.; Kojima, H.; Mori, T.; Dunbar, K. R. *Chem.Eur. J.* **2013**, *19*, 3348-3357.

64. Zhao, H.; Bazile, J. M. J.; Galán-Mascarós, J. R.; Dunbar, K. R. *Angew. Chem., Int. Ed.* **2003**, *42*, 1015-1018.

65. Yamaguchi, S.; Hanafusa, T. *Chem. Lett.* **1985**, *14*, 689-690.

66. Lopez, N.; Zhao, H.; Ota, A.; Prosvirin, A. V.; Reinheimer, E. W.; Dunbar, K. R. *Adv. Mater.* **2010**, *22*, 986-989.

67. Shimomura, S.; Matsuda, R.; Tsujino, T.; Kawamura, T.; Kitagawa, S. *J. Am. Chem. Soc.* **2006**, *128*, 16416-16417.

68. Saber, M. R.; Prosvirin, A. V.; Abrahams, B. F.; Elliott, R. W.; Robson, R.; Dunbar, K. R. *Chem.Eur. J.* **2014**, *20*, 7593-7597.

69. Zhao, H.; Heintz, R. A.; Dunbar, K. R.; Rogers, R. D. *J. Am. Chem. Soc.* **1996**, *118*, 12844-12845.

70. Shimomura, S.; Higuchi, M.; Matsuda, R.; Yoneda, K.; Hijikata, Y.; Kubota, Y.; Mita, Y.; Kim, J.; Takata, M.; Kitagawa, S. *Nat Chem* **2010**, *2*, 633-637.

71. Talin, A. A.; Centrone, A.; Ford, A. C.; Foster, M. E.; Stavila, V.; Haney, P.; Kinney, R. A.; Szalai, V.; El Gabaly, F.; Yoon, H. P.; Léonard, F.; Allendorf, M. D. *Science* **2014**, *343*, 66-69.

72. Kaim, W.; Moscherosch, M. *Coord. Chem. Rev.* **1994**, *129*, 157-193.

73. Miyasaka, H.; Campos-Fernández, C. S.; Clérac, R.; Dunbar, K. R. *Angewandte Chemie* **2000**, *39*, 3831-3835.

74. Ballesteros-Rivas, M.; Ota, A.; Reinheimer, E.; Prosvirin, A.; Valdes-Martinez, J.; Dunbar, K. R. *Angew Chem Int Ed Engl* **2011**, *50*, 9703-9707.

75. Kistenmacher, T. J.; Emge, T. J.; Bloch, A. N.; Cowan, D. O. *Acta Crystallogr., Sect. B* **1982**, *38*, 1193-1199.

76. Long, R. E.; Sparks, R. A.; Trueblood, K. N. *Acta Crystallographica* **1965**, *18*, 932-939.

77. Hoekstra, A.; Spoelder, T.; Vos, A. *Acta Crystallogr., Sect. B* **1972**, *28*, 14-25.

78. Miyasaka, H.; Izawa, T.; Takahashi, N.; Yamashita, M.; Dunbar, K. R. *J. Am. Chem. Soc.* **2006**, *128*, 11358-11359.

79. Motokawa, N.; Miyasaka, H.; Yamashita, M.; Dunbar, K. R. *Angewandte Chemie* **2008**, *120*, 7874-7877.

80. Blythe, A. R.; Boon, M. R.; Wright, P. G. *Discuss. Faraday Soc.* **1971**, *51*, 110-115.

81. Soos, Z. G. *Annual Review of Physical Chemistry* **1974**, *25*, 121-153.

82. O'Kane, S. A.; Clérac, R.; Zhao, H.; Ouyang, X.; Galán-Mascarós, J. R.; Heintz, R.; Dunbar, K. R. *J. Solid State Chem.* **2000**, *152*, 159-173.

83. Heintz, R. A.; Zhao, H.; Ouyang, X.; Grandinetti, G.; Cowen, J.; Dunbar, K. R. *Inorganic chemistry* **1998**, *38*, 144-156.

84. Johnson, E. C.; Callahan, R. W.; Eckberg, R. P.; Hatfield, W. E.; Meyer, T. J. *Inorg. Chem.* **1979**, *18*, 618-623.

85. Bunker, B. C.; Drago, R. S.; Hendrickson, D. N.; Richman, R. M.; Kessell, S. L. *J. Am. Chem. Soc.* **1978**, *100*, 3805-3814.

86. Aquino, M. A. S.; Lee, F. L.; Gabe, E. J.; Greedan, J. E.; Crutchley, R. J. *Inorg. Chem.* **1991**, *30*, 3234-3236.

87. Zhou, H. C.; Long, J. R.; Yaghi, O. M. *Chem Rev* **2012**, *112*, 673-674.

88. Shimomura, S.; Yanai, N.; Matsuda, R.; Kitagawa, S. *Inorg. Chem.* **2010**, *50*, 172-177.

89. Sharp, K. G. *Adv. Mater.* **1998**, *10*, 1243-1248.

90. Kagan, C. R.; Mitzi, D. B.; Dimitrakopoulos, C. D. *Science* **1999**, *286*, 945-947.

91. Draxl, C.; Nabok, D.; Hannewald, K. *Acc. Chem. Res.* **2014**, *47*, 3225-3232.

92. Judeinstein, P.; Sanchez, C. *J. Mater. Chem.* **1996**, *6*, 511-525.

93. Miller, J. S.; Epstein, A. J.; Reiff, W. M. *Science* **1988**, *240*, 40-47.

94. Zhang, W.-X.; Ishikawa, R.; Breedlove, B.; Yamashita, M. *RSC Advances* **2013**, *3*, 3772-3798.

95. Kazuya, K.; Hiroki, H.; Hitoshi, M.; Masahiro, Y. In *Multifunctional Molecular Materials*; Pan Stanford Publishing: 2013, p 61-103.

96. Osamu Sato, Z.-Y. L., Zi-Shuo Yao, Soonchul Kang, Shinji Kanegawa In *Spin-Crossover Materials: Properties and Applications*; Halcrow, M. A., Ed.; John Wiley & Sons, Ltd: 2013.

97. Xue, W.; Wang, B. Y.; Zhu, J.; Zhang, W. X.; Zhang, Y. B.; Zhao, H. X.; Chen, X. M. *Chem Commun (Camb)* **2011**, *47*, 10233-10235.

98. Pearson, A.; Ramanathan, R.; O'Mullane, A. P.; Bansal, V. *Advanced Functional Materials* **2014**, *24*, 7570-7579.

99. Nafady, A.; O'Mullane, A. P.; Bond, A. M. *Coord. Chem. Rev.* **2014**, *268*, 101-142.

100. Fukunaga, H.; Miyasaka, H. *Angew Chem Int Ed Engl* **2015**, *54*, 569-573.

101. Nishio, M.; Hoshino, N.; Kosaka, W.; Akutagawa, T.; Miyasaka, H. *J. Am. Chem. Soc.* **2013**, *135*, 17715-17718.

102. Knowles, K. E.; Malicki, M.; Parameswaran, R.; Cass, L. C.; Weiss, E. A. *J Am Chem Soc* **2013**, *135*, 7264-7271.

103. Garnica, M.; Stradi, D.; Barja, S.; Calleja, F.; Diaz, C.; Alcami, M.; Martin, N.; Vazquez de Parga, A. L.; Martin, F.; Miranda, R. *Nat Phys* **2013**, *9*, 368-374.

104. Miller, J. S. *Chem. Soc. Rev.* **2011**, *40*, 3266-3296.

105. Vickers, E. B.; Selby, T. D.; Thorum, M. S.; Taliaferro, M. L.; Miller, J. S. *Inorganic chemistry* **2004**, *43*, 6414-6420.

106. Miller, J. S.; Zhang, J. H.; Reiff, W. M.; Dixon, D. A.; Preston, L. D.; Reis, A. H.; Gebert, E.; Extine, M.; Troup, J.; et al. *J. Chem. Phys.* **1987**, *91*, 4344-4360.

107. Zhang, X.; Saber, M. R.; Prosvirin, A. P.; Reibenspies, J. H.; Sun, L.; Ballesteros-Rivas, M.; Zhao, H.; Dunbar, K. R. *Inorg. Chem. Front.* **2015**, *2*, 904-911.

108. Garito, A. F.; Heeger, A. J. *Acc. Chem. Res.* **1974**, *7*, 232-240.

109. Mori, T. *Chem. Rev.* **2004**, *104*, 4947-4970.

110. Halcrow, M. A. *Chem. Commun.* **2013**, *49*, 10890-10892.

111. Gütlich, P. *Eur. J. Inorg. Chem.* **2013**, *2013*, 581-591.

112. Takahashi, K.; Cui, H.-B.; Okano, Y.; Kobayashi, H.; Mori, H.; Tajima, H.; Einaga, Y.; Sato, O. *J. Am. Chem. Soc.* **2008**, *130*, 6688-6689.

113. Nihei, M.; Takahashi, N.; Nishikawa, H.; Oshio, H. *Dalton Trans.* **2011**, *40*, 2154-2156.

114. Koo, Y.-S.; Galán-Mascarós, J. R. *Adv. Mater.* **2014**, *26*, 6785-6789.

115. Chen, Y.-C.; Meng, Y.; Ni, Z.-P.; Tong, M.-L. *Journal of Materials Chemistry C* **2015**, *3*, 945-949.

116. Xue, W.; Wang, B.-Y.; Zhu, J.; Zhang, W.-X.; Zhang, Y.-B.; Zhao, H.-X.; Chen, X.-M. *Chem. Commun.* **2011**, *47*, 10233-10235.

117. Maddison, D. S.; Tansley, T. L. *Journal of Applied Physics* **1992**, *71*, 1831-1837.

118. Dorbes, S.; Valade, L.; Real, J. A.; Faulmann, C. *Chem. Commun.* **2005**, 69-71.

119. Faulmann, C.; Jacob, K.; Dorbes, S.; Lampert, S.; Malfant, I.; Doublet, M.-L.; Valade, L.; Real, J. A. *Inorg. Chem.* **2007**, *46*, 8548-8559.

120. Takahashi, K.; Cui, H.-B.; Okano, Y.; Kobayashi, H.; Einaga, Y.; Sato, O. *Inorg. Chem.* **2006**, *45*, 5739-5741.

121. Nakano, M.; Fujita, N.; Matsubayashi, G.-E.; Mori, W. *Mol. Cryst. Liq. Cryst.* **2002**, *379*, 365-370.

122. Phan, H.; Benjamin, S. M.; Steven, E.; Brooks, J. S.; Shatruk, M. *Angew Chem Int Ed Engl* **2015**, *54*, 823-827.

123. Alonso, C.; Ballester, L.; Gutiérrez, A.; Perpiñán, M. F.; Sánchez, Ana E.; Azcondo, M. T. *Eur. J. Inorg. Chem.* **2005**, *2005*, 486-495.

124. Murray, K.; Kepert, C. In *Spin Crossover in Transition Metal Compounds I*; Gütlich, P., Goodwin, H. A., Eds.; Springer Berlin Heidelberg: 2004; Vol. 233, p 195-228.

125. Olguín, J.; Brooker, S. In *Spin-Crossover Materials*; John Wiley & Sons Ltd: 2013, p 77-120.

126. Halcrow, M. A. *Chem. Lett.* **2014**, *43*, 1178-1188.

127. Kahn, O.; Martinez, C. J. *Science* **1998**, *279*, 44-48.

128. Carmen Muñoz, M.; Antonio Real, J. In *Spin-Crossover Materials*; John Wiley & Sons Ltd: 2013, p 121-146.

129. Weber, B.; Bauer, W.; Obel, J. *Angew. Chem., Int. Ed.* **2008**, *47*, 10098-10101.

130. Hayami, S.; Gu, Z.-z.; Yoshiki, H.; Fujishima, A.; Sato, O. *J. Am. Chem. Soc.* **2001**, *123*, 11644-11650.

131. Kubota, H.; Takahashi, Y.; Harada, J.; Inabe, T. *Cryst. Growth Des.* **2014**, *14*, 5575-5584.

132. Madalan, Augustin M.; Voronkova, V.; Galeev, R.; Korobchenko, L.; Magull, J.; Roesky, Herbert W.; Andruh, M. *Eur. J. Inorg. Chem.* **2003**, *2003*, 1995-1999.

133. Madalan, A. M.; Roesky, H. W.; Andruh, M.; Noltemeyer, M.; Stanica, N. *Chem. Commun.* **2002**, 1638-1639.

134. Dobrowolski, M. A.; Garbarino, G.; Mezouar, M.; Ciesielski, A.; Cyranski, M. K. *CrystEngComm* **2014**, *16*, 415-429.

135. Zhang, X.; Xie, H.; Ballesteros-Rivas, M.; Wang, Z.-X.; Dunbar, K. R. *J. Mater. Chem. C* **2015**, *3*, 9292-9298.

136. Melby, L. R.; Harder, R. J.; Hertler, W. R.; Mahler, W.; Benson, R. E.; Mochel, W. E. *J. Am. Chem. Soc.* **1962**, *84*, 3374-3387.

137. Winter, A.; van den Berg, A. M. J.; Hoogenboom, R.; Kickelbick, G.; Schubert, U. S. *Synthesis* **2007**, *2007*, 0642-0642.

138. Indumathy, R.; Radhika, S.; Kanthimathi, M.; Weyhermuller, T.; Unni Nair, B. *J. Inorg. Biochem.* **2007**, *101*, 434-443.

139. Sheldrick, G. *Acta Crystallogr A* **2015**, *71*, 3-8.

140. Sheldrick, G. *Acta Crystallogr A* **2008**, *64*, 112-122.

141. Dolomanov, O. V.; Bourhis, L. J.; Gildea, R. J.; Howard, J. A. K.; Puschmann, H. *J. Appl. Crystallogr.* **2009**, *42*, 339-341.

142. Reiff, A. L.; Garcia-Frutos, E. M.; Gil, J. M.; Anderson, O. P.; Hegedus, L. S. *Inorg. Chem.* **2005**, *44*, 9162-9174.

143. Miller, R. G.; Brooker, S. *Inorg Chem* **2015**, *54*, 5398-5409.

144. Hayami, S.; Komatsu, Y.; Shimizu, T.; Kamihata, H.; Lee, Y. H. *Coord. Chem. Rev.* **2011**, *255*, 1981-1990.

145. Oshio, H.; Ino, E.; Mogi, I.; Ito, T. *Inorg. Chem.* **1993**, *32*, 5697-5703.

146. Givaja, G.; Amo-Ochoa, P.; Gomez-Garcia, C. J.; Zamora, F. *Chem. Soc. Rev.* **2012**, *41*, 115-147.

147. Ikari, T.; Jandl, S.; Aubin, M.; Truong, K. D. *Phys. Rev. B* **1983**, *28*, 3859-3863.

148. Holczer, K.; Mihaly, G.; Janossy, A.; Gruner, G.; Kertesz, M. *J. Phys. C: Solid State Phys.* **1978**, *11*, 4707.

149. Coleman, L. B.; Cohen, M. J.; Sandman, D. J.; Yamagishi, F. G.; Garito, A. F.; Heeger, A. J. *Solid State Commun.* **1973**, *12*, 1125-1132.

150. Halcrow, M. A. *Chemical Society Reviews* **2011**, *40*, 4119-4142.

151. Guionneau, P. *Dalton Trans.* **2014**, *43*, 382-393.

152. Kershaw Cook, L. J.; Tuna, F.; Halcrow, M. A. *Dalton Trans.* **2013**, *42*, 2254-2265.

153. Piñeiro-López, L.; Arcís-Castillo, Z.; Muñoz, M. C.; Real, J. A. *Cryst. Growth Des.* **2014**, *14*, 6311-6319.

154. Aravena, D.; Castillo, Z. A.; Muñoz, M. C.; Gaspar, A. B.; Yoneda, K.; Ohtani, R.; Mishima, A.; Kitagawa, S.; Ohba, M.; Real, J. A.; Ruiz, E. *Chem.Eur. J.* **2014**, *20*, 12864-12873.

155. Southon, P. D.; Liu, L.; Fellows, E. A.; Price, D. J.; Halder, G. J.; Chapman, K. W.; Moubaraki, B.; Murray, K. S.; Létard, J.-F.; Kepert, C. J. *J. Am. Chem. Soc.* **2009**, *131*, 10998-11009.

156. Hostettler, M.; Törnroos, K. W.; Chernyshov, D.; Vangdal, B.; Bürgi, H.-B. *Angew. Chem., Int. Ed.* **2004**, *43*, 4589-4594.

157. Mishima, T.; Ojiro, T.; Kajita, K.; Nishio, Y.; Iye, Y. *Synth. Met.* **1995**, *70*, 771-774.

158. Tyeklar, Z.; Jacobson, R. R.; Wei, N.; Murthy, N. N.; Zubieta, J.; Karlin, K. D. *J. Am. Chem. Soc.* **1993**, *115*, 2677-2689.

159. Reger, D. L.; Grattan, T. C.; Brown, K. J.; Little, C. A.; Lamba, J. J. S.; Rheingold, A. L.; Sommer, R. D. *J. Organomet. Chem.* **2000**, *607*, 120-128.

160. Rizzuto, F. J.; Hua, C.; Chan, B.; Faust, T. B.; Rawal, A.; Leong, C. F.; Hook, J. M.; Kepert, C. J.; D'Alessandro, D. M. *Phys. Chem. Chem. Phys.* **2015**, *17*, 11252-11259.

161. Zhang, Y.-Z.; Gómez-Coca, S.; Brown, A. J.; Saber, M. R.; Zhang, X.; Dunbar, K. R. *Chem. Sci.* **2016**.

162. Li, J.-R.; Sculley, J.; Zhou, H.-C. *Chem. Rev.* **2012**, *112*, 869-932.

163. Getman, R. B.; Bae, Y.-S.; Wilmer, C. E.; Snurr, R. Q. *Chem. Rev.* **2012**, *112*, 703-723.

164. Yoon, M.; Srirambalaji, R.; Kim, K. *Chem. Rev.* **2012**, *112*, 1196-1231.

165. Kreno, L. E.; Leong, K.; Farha, O. K.; Allendorf, M.; Van Duyne, R. P.; Hupp, J. T. *Chem. Rev.* **2012**, *112*, 1105-1125.

166. Feng, D.; Chung, W.-C.; Wei, Z.; Gu, Z.-Y.; Jiang, H.-L.; Chen, Y.-P.; Darensbourg, D. J.; Zhou, H.-C. *J. Am. Chem. Soc.* **2013**, *135*, 17105-17110.

167. Katz, M. J.; Mondloch, J. E.; Totten, R. K.; Park, J. K.; Nguyen, S. T.; Farha, O. K.; Hupp, J. T. *Angew. Chem., Int. Ed.* **2014**, *53*, 497-501.

168. Narayan, T. C.; Miyakai, T.; Seki, S.; Dincă, M. *J. Am. Chem. Soc.* **2012**, *134*, 12932-12935.

169. Hendon, C. H.; Tiana, D.; Walsh, A. *Phys. Chem. Chem. Phys.* **2012**, *14*, 13120-13132.

170. Sun, L.; Hendon, C. H.; Minier, M. A.; Walsh, A.; Dinca, M. *J Am Chem Soc* **2015**, *137*, 6164-6167.

171. Kambe, T.; Sakamoto, R.; Hoshiko, K.; Takada, K.; Miyachi, M.; Ryu, J.-H.; Sasaki, S.; Kim, J.; Nakazato, K.; Takata, M.; Nishihara, H. *J. Am. Chem. Soc.* **2013**, *135*, 2462-2465.

172. Sheberla, D.; Sun, L.; Blood-Forsythe, M. A.; Er, S.; Wade, C. R.; Brozek, C. K.; Aspuru-Guzik, A.; Dinca, M. *J Am Chem Soc* **2014**, *136*, 8859-8862.

173. Lorusso, G.; Sharples, J. W.; Palacios, E.; Roubeau, O.; Brechin, E. K.; Sessoli, R.; Rossin, A.; Tuna, F.; McInnes, E. J. L.; Collison, D.; Evangelisti, M. *Adv. Mater.* **2013**, *25*, 4653-4656.

174. Kurmoo, M. *Chem. Soc. Rev.* **2009**, *38*, 1353-1379.

175. Chen, T.-H.; Popov, I.; Kaveevivitchai, W.; Miljanić, O. Š. *Chem. Mater.* **2014**, *26*, 4322-4325.

176. Almeida Paz, F. A.; Klinowski, J.; Vilela, S. M. F.; Tome, J. P. C.; Cavaleiro, J. A. S.; Rocha, J. *Chem. Soc. Rev.* **2012**, *41*, 1088-1110.

177. Leong, C. F.; Chan, B.; Faust, T. B.; D'Alessandro, D. M. *Chem. Sci.* **2014**, *5*, 4724-4728.

178. Miyasaka, H. *Acc Chem Res* **2013**, *46*, 248-257.

179. Nafady, A.; Le, T. H.; Vo, N.; Haworth, N. L.; Bond, A. M.; Martin, L. L. *Inorg Chem* **2014**, *53*, 2268-2275.

180. Abrahams, B. F.; Elliott, R. W.; Hudson, T. A.; Robson, R. *Cryst. Growth Des.* **2013**, *13*, 3018-3027.

181. Shimomura, S.; Horike, S.; Matsuda, R.; Kitagawa, S. *J. Am. Chem. Soc.* **2007**, *129*, 10990-10991.

182. Horike, S.; Sugimoto, M.; Kongpatpanich, K.; Hijikata, Y.; Inukai, M.; Umeyama, D.; Kitao, S.; Seto, M.; Kitagawa, S. *J. Mater. Chem. A* **2013**, *1*, 3675-3679.

183. Abrahams, B. F.; Elliott, R. W.; Robson, R. *Aust. J. Chem.* **2014**, *67*, 1871-1877.

184. Park, S. S.; Hontz, E. R.; Sun, L.; Hendon, C. H.; Walsh, A.; Van Voorhis, T.; Dinca, M. *J Am Chem Soc* **2015**, *137*, 1774-1777.

185. Aspuru-Guzik, A.; Dutoi, A. D.; Love, P. J.; Head-Gordon, M. *Science* **2005**, *309*, 1704-1707.

186. Graham, M. J.; Zadrozny, J. M.; Shiddiq, M.; Anderson, J. S.; Fataftah, M. S.; Hill, S.; Freedman, D. E. *J. Am. Chem. Soc.* **2014**, *136*, 7623-7626.

187. Leuenberger, M. N.; Loss, D. *Nature* **2001**, *410*, 789-793.

188. Kojima, H.; Zhang, Z.; Dunbar, K. R.; Mori, T. *J. Mater. Chem. C* **2013**, *1*, 1781-1790.

189. Cheruiyot, L. L.; Crutchley, R. J.; Thompson, L. K.; Greedan, J. E.; Liu, G. *Can. J. Chem.* **1995**, *73*, 573-580.

190. Kosaka, W.; Morita, T.; Yokoyama, T.; Zhang, J.; Miyasaka, H. *Inorg Chem* **2015**, *54*, 1518-1527.

191. Ruiz, E.; Rodr ǵuez-Fortea, A.; Alvarez, S. *Inorg. Chem.* **2003**, *42*, 4881-4884.

192. Dechambenoit, P.; Long, J. R. *Chemical Society Reviews* **2011**, *40*, 3249-3265.

193. Hao, Z.-M.; Zhang, X.-M. *Dalton Trans.* **2011**, *40*, 2092-2098.

194. Ohba, M.; Yoneda, K.; Kitagawa, S. *CrystEngComm* **2010**, *12*, 159-165.

195. Kahn, O.; Larionova, J.; Yakhmi, J. V. *Chemistry – A European Journal* **1999**, *5*, 3443-3449.

196. Lopez, N.; Zhao, H.; Prosvirin, A. V.; Chouai, A.; Shatruk, M.; Dunbar, K. R. *Chem. Commun.* **2007**, 4611-4613.

197. Shimomura, S.; Matsuda, R.; Kitagawa, S. *Chem. Mater.* **2010**, *22*, 4129-4131.

198. Acker, D. S.; Hertler, W. R. *J. Am. Chem. Soc.* **1962**, *84*, 3370-3374.

199. Kittel, C. *Introduction to solid state physics*; Wiley, 1986.

200. Lines, M. E. *J. Phys. Chem. Solids* **1970**, *31*, 101-116.

201. Triki, S.; Thetiot, F.; Galan-Mascaros, J.-R.; Pala, J. S.; Dunbar, K. R. *New J. Chem.* **2001**, *25*, 954-958.

202. Marshall, S. R.; Incarvito, C. D.; Manson, J. L.; Rheingold, A. L.; Miller, J. S. *Inorg. Chem.* **2000**, *39*, 1969-1973.

203. L. Manson, J.; D. Incarvito, C.; L. Rheingold, A.; S. Miller, J. *J. Chem. Soc., Dalton Trans.* **1998**, 3705-3706.

204. Manson, J. L.; Arif, A. M.; Incarvito, C. D.; Liable-Sands, L. M.; Rheingold, A. L.; Miller, J. S. *Journal of Solid State Chemistry* **1999**, *145*, 369-378.

205. Rodriguez-Martín, Y.; Ruiz-Pérez*, C.; Sanchiz, J. n.; Lloret*, F.; Julve, M. *Inorg. Chim. Acta* **2001**, *318*, 159-165.

206. Prosvirin, A. V.; Zhao, H.; Dunbar, K. R. *Inorganica Chimica Acta* **2012**, *389*, 118-121.

207. Snyder, L. R. *Journal of Chromatography A* **1974**, *92*, 223-230.

208. Long, J. R. In *The Chemistry of Nanostructured Materials*, p 291-315.

209. Sanvito, S. *Chem. Soc. Rev.* **2011**, *40*, 3336-3355.

210. Coronado, E.; Minguez Espallargas, G. *Chem. Soc. Rev.* **2013**, *42*, 1525-1539.

211. Zhang, X.; Wang, Z.-X.; Xie, H.; Li, M.-X.; Woods, T. J.; Dunbar, K. R. *Chem. Sci.* **2016**, *7*, 1569-1574.

212. DeRosa, M. C.; White, C. A.; Evans, C. E. B.; Crutchley, R. J. *J. Am. Chem. Soc.* **2001**, *123*, 1396-1402.

213. Evans, C. E. B.; Naklicki, M. L.; Rezvani, A. R.; White, C. A.; Kondratiev, V. V.; Crutchley, R. J. *J. Am. Chem. Soc.* **1998**, *120*, 13096-13103.

214. Naklicki, M. L.; Crutchley, R. J. *J. Am. Chem. Soc.* **1994**, *116*, 6045-6046.

215. Abrahams, B. F.; Hudson, T. A.; Robson, R. *Cryst. Growth Des.* **2010**, *10*, 1468-1470.

216. Aquino, M. A. S.; Lee, F. L.; Gabe, E. J.; Bensimon, C.; Greedan, J. E.; Crutchley, R. J. *J. Am. Chem. Soc.* **1992**, *114*, 5130-5140.

217. Hudson, T. A.; Robson, R. *Cryst. Growth Des.* **2009**, *9*, 1658-1662.

218. Abrahams, B. F.; Elliott, R. W.; Hudson, T. A.; Robson, R. *CrystEngComm* **2012**, *14*, 351-354.

219. Liu, Z.; Liu, G.; Wu, Y.; Cao, D.; Sun, J.; Schneebeli, S. T.; Nassar, M. S.; Mirkin, C. A.; Stoddart, J. F. *J Am Chem Soc* **2014**, *136*, 16651-16660.

220. Pedersen, K. S.; Bendix, J.; Clerac, R. *Chem Commun (Camb)* **2014**, *50*, 4396-4415.

221. Ding, M.; Wang, B.; Wang, Z.; Zhang, J.; Fuhr, O.; Fenske, D.; Gao, S. *Chemistry – A European Journal* **2012**, *18*, 915-924.

222. Schottel, B. L.; Chifotides, H. T.; Dunbar, K. R. *Chem. Soc. Rev.* **2008**, *37*, 68-83.

223. Dougherty, D. A. *Acc. Chem. Res.* **2013**, *46*, 885-893.

224. Wang, Q.-L.; Zhang, Y.-Z.; Southerland, H.; Prosvirin, A. V.; Zhao, H.; Dunbar, K. R. *Dalton Trans.* **2014**, *43*, 6802-6810.

225. Wang, X.-Y.; Prosvirin, A. V.; Dunbar, K. R. *Angew. Chem., Int. Ed.* **2010**, *49*, 5081-5084.

226. Wang, Q.-L.; Southerland, H.; Li, J.-R.; Prosvirin, A. V.; Zhao, H.; Dunbar, K. R. *Angew. Chem., Int. Ed.* **2012**, *51*, 9321-9324.

227. Venkatakrishnan, T. S.; Sahoo, S.; Bréfuel, N.; Duhayon, C.; Paulsen, C.; Barra, A.-L.; Ramasesha, S.; Sutter, J.-P. *J. Am. Chem. Soc.* **2010**, *132*, 6047-6056.

228. Paraschiv, C.; Andruh, M.; Journaux, Y.; Zak, Z.; Kyritsakas, N.; Ricard, L. *J. Mater. Chem.* **2006**, *16*, 2660-2668.

229. Wang, J.; Slater, B.; Alberola, A.; Stoeckli-Evans, H.; Razavi, F. S.; Pilkington, M. *Inorg. Chem.* **2007**, *46*, 4763-4765.

230. Zhang, X.; Zhao, H.; Palatinus, L.; Gagnon, K. J.; Bacsa, J.; Dunbar, K. R. *Cryst. Growth Des.* **2016**, *16*, 1805-1811.

231. Zhang, X.; Zhao, H.; Palatinus, L.; Gagnon, K.; Bacsa, J.; Dunbar, K. *Acta Crystallogr A* **2014**, *70*, C1265.

232. Li, H.; Zhong, Z. J.; Duan, C.-Y.; You, X.-Z.; Mak, T. C. W.; Wu, B. *J. Coord. Chem.* **1997**, *41*, 183-189.

233. Zhou, B. X.; Jiang, S. Q.; Zhou, D.; Zhao, Y. T. *Chin. Chem. Lett.* **1999**, *10*, 429-432.

234. White, C. A. Magneto-structural correlations of novel copper(II) molecular materials. Ph.D. NQ42812, Carleton University (Canada), Canada, 1999.

235. Jimenez-Sandoval, O.; Ramirez-Rosales, D.; Rosales-Hoz, M. D.; Sosa-Torres, M. E.; Zamorano-Ulloa, R. *J. Chem. Soc.-Dalton Trans.* **1998**, 1551-1556.

236. Palatinus, L.; Chapuis, G. *J. Appl. Crystallogr.* **2007**, *40*, 786-790.

237. Palatinus, L.; van der Lee, A. *J. Appl. Crystallogr.* **2008**, *41*, 975-984.

238. Petricek, V.; Dusek, M.; Palatinus, L. *Z Kristallogr* **2014**, *229*, 345-352.

239. Spek, A. *Acta Crystallographica Section C* **2015**, *71*, 9-18.

240. White, C. A.; Derosa, M. C.; Yap, G. P. A.; Raju, N. P.; Greedan, J. E.; Crutchley, R. J. *Mol. Cryst. Liq. Cryst. Sci. Technol., Sect. A* **2002**, *376*, 289-294.